The relationship between Active Galactic Nuclei and the star-forming properties of their host galaxies

Emmanuel P. W. Bernhard

Department of Physics & Astronomy
The University of Sheffield

The University Of Sheffield.

A dissertation submitted in candidature for the degree of Doctor of Philosophy at the University of Sheffield

February, 2018

Declaration

I declare that no part of this thesis has been accepted, or is currently being submitted, for any degree or diploma or certificate or any other qualification at this University or elsewhere.

This thesis is the result of my own work unless otherwise stated.

The following Chapters have been based on my own publications:

- Chapter 2 and Chapter 3 – Bernhard et al. (2016)
- Chapter 5, § 5.3 – Bernhard et al. (2014)

In Chapter 3, § 3.3.2 I did not run the multi-component spectral energy distribution fitting code to derive the stellar masses. Laure Ciesla, which is involved in the development of the code, kindly accepted to run it on our dataset.

Chapter 5 (aside from § 5.3) and the Chapter 6 are to be submitted for publication.

Further than the work presented in this thesis, I also actively contributed to the following publications:

- Ciesla et al. (2015) – *"Constraining the properties of AGN host galaxies with spectral energy distribution modelling"*
- Mullaney et al. (2015) – *"*ALMA *and* Herschel *reveal that X-ray-selected AGN and main-sequence galaxies have different star formation rate distributions"*

Abstract

It is now accepted that there is a co-evolution between galaxies and their central super massive black holes (SMBHs). Primarily, cosmological simulations suggest that accreting SMBHs (or Active Galactic Nuclei, AGN) must somehow quench their hosts' star-formation rates (SFRs). In contrast, empirical results report that there is no evidence of a strong (anti-)correlation between SFR and X-ray luminosity (a proxy for AGN power). In this thesis, we aim to investigate further this apparent contradiction between AGNs and their host star-forming properties.

The hypothesis we test is that a powerful AGN will have a higher impact on a low mass host galaxy than on a high mass one. Therefore, instead of the previously used X-ray luminosity, we investigate the relationship between the X-ray luminosity *relative to the host stellar mass* (a proxy for Eddington ratio, $\lambda_{\rm Edd}$) and the host SFR.

We first used a sample of 1620 X-ray selected AGNs, for which we measured $\lambda_{\rm Edd}$ and their host far-infrared luminosities (a proxy for SFR) that we corrected for AGN contamination. By doing this, we found a slight enhancement of SFR at higher $\lambda_{\rm Edd}$ when compared to the SFR of star-forming galaxies with similar stellar masses that do not host AGNs. Furthermore, the change in the star-forming properties at higher $\lambda_{\rm Edd}$ indicates that the $\lambda_{\rm Edd}$ distribution must change with the host star-forming properties.

To investigate further how the Eddington ratio distribution of AGNs changes with the star-forming properties of their hosts, we used a model for which we assumed the Eddington ratio distribution simply split between star-forming and quiescent galaxies. Overall, we find that our model is able to reproduce the X-ray luminosity function but fails to reproduce the flat relationship between SFR and X-ray luminosity. Finally, we found that this can be resolved if we introduce a mass-dependency into our model.

Acronyms used

AGN – Active Galactic Nuclei
AIC – Akaike Information Criterion
AICc – Corrected AIC
BIC – Bayesian Information Criterion
e.g. – exempli gratia (for the sake of example)
FIR – Far Infra-Red
FWHM – Full Width at Half Maximum
i.e. – id est (that is)
IMF – Initial Mass Function
IR – Infrared
MIPS – Multiband Imaging Photometer and Spectrometer
MS – Main Sequence
NIR – Near Infra-Red
PACS – Photo-detector Array Camera and Spectrometer
PSF – Point Spread Function
PSM – Population Synthesis Model
SED – Spectral Energy Distribution
SF – Star-Forming
SFR – Star Formation Rate
SMBH – Super Massive Black Hole
SNR – Signal-to-Noise Ratio
SPIRE – Spectral and Photometric Imaging Receiver
QSRS – Quasi Stellar Radio Sources
UV – Ultraviolet

Symbols used

κ – Opacity
σ – Standard Deviation
σ_{T} – cross-section (Thomson scattering)
λ_{Edd} – Eddington ratio
χ^2 – Chi-square
$\mathcal{A}_{\mathrm{w}}$ – Akaike weight
F_{grav} – Force of gravitation
F_{rad} – Force of radiation
m_{p} – Mass of the proton
Ms – Mega-second
$\mathcal{L}$ – Likelihood
L_{AGN} – AGN luminosity
keV – Kilo-electron-Volt
L_{Edd} – Eddington luminosity
L_{IR} – IR luminosity
L_{UV} – UV luminosity
L_X – X-ray luminosity
$L_{\odot}$ – Solar luminosity
L_{star} – Total luminosity from the stars
M_{BH} – SMBH mass
M_* – Stellar mass
$M_{\odot}$ – Solar mass
T1 – un-obscured AGN
T2 – obscured AGN
pc – parsec
kpc – Kilo-parsec
T – Temperature
t – Time
K – Kelvin
z – Redshift

Contents

List of Figures

List of Tables

Chapter 1

Introduction

1.1 Early insights into the AGN-galaxy connection

The study of Active Galactic Nuclei (hereafter AGNs) began in the early 20$^{\text{th}}$ century with the discovery of bright nuclear emission lines (typical of gaseous nebulae; e.g. planetary nebulae) within certain "spiral nebulae" (e.g. Fath, 1909). These lines were found superimposed onto a continuum spectrum which resembled a collection of unresolved stars, or a galaxy (i.e. Fath, 1909; Slipher, 1917; Hubble, 1926). Later, Seyfert (1943) started a systematic study of these peculiar objects (e.g. NGC1068, see Fig. 1.1) and reported important spectral features (i.e. emission lines that are broad, with velocity widths of several thousands of kilometres per second, or narrow, or, in some cases both) that are now used extensively to identify AGNs (e.g. Baldwin et al., 1981). Independently, in the 1950s, some studies reported the presence of strong radio emissions (called radio galaxies) observed in all-sky radio surveys, among which some prove to have compact optical structure, with optical spectra similar to the sources observed by Seyfert in 1943 (e.g. Bolton & Stanley, 1948; Ryle & Smith, 1948; Hanbury Brown et al., 1952; Jennison & Das Gupta, 1953; Matthews & Sandage, 1963). The latter were coined "Quasi Stellar Radio Sources" (QSRS), or Quasars, in recognition of their appearance similar to an "un-reddened bluish star". The discovery of fuzzy nebulae around Quasars strongly suggested that, like the sources that Seyfert studied in 1943, these are at the centres of distant galaxies (e.g. Matthews, 1963). (see Fig. 1.2)

Today, it is widely recognised that Quasars and the sources observed by Seyfert in 1943 are both the same phenomenon, collectively known as Active Galactic Nuclei. The name AGN refers to the presence of a central super massive black hole (here-

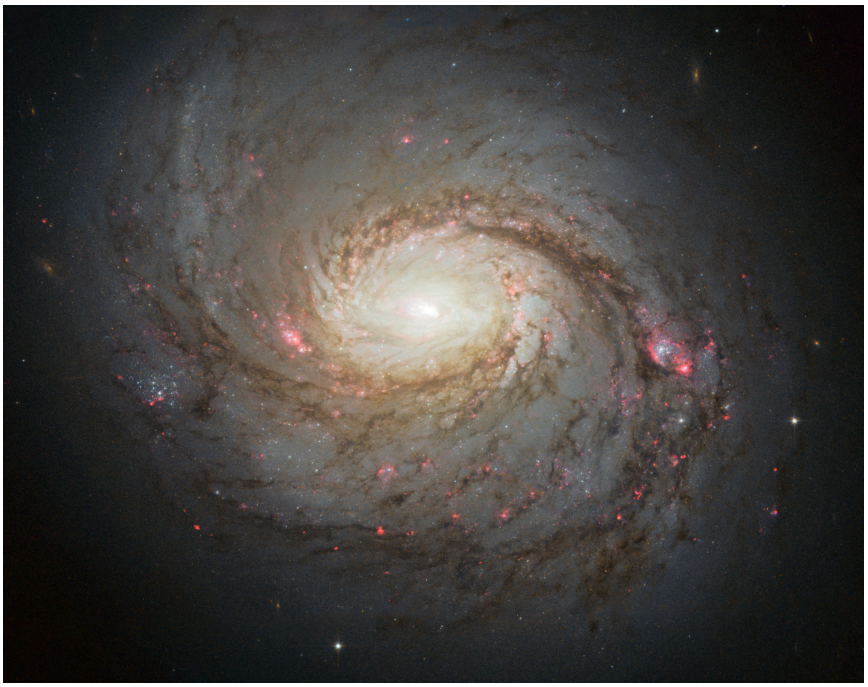

Figure 1.1: Optical image of NGC1068 in false colours, captured with the HUBBLE space telescope. The bright spot at the centre of the galaxy shows the bright AGN at optical wavelengths. The darker spiral arms host obscuring dust. Nests of new born stars are shown in bright red. The white "fuzzy" light in the disk of the galaxy is emission from the older population of stars. The AGN hosts by this galaxy is a Type 2 (i.e. obscured) AGN. *Credits:* NASA, ESA & A. van der Hoeven.

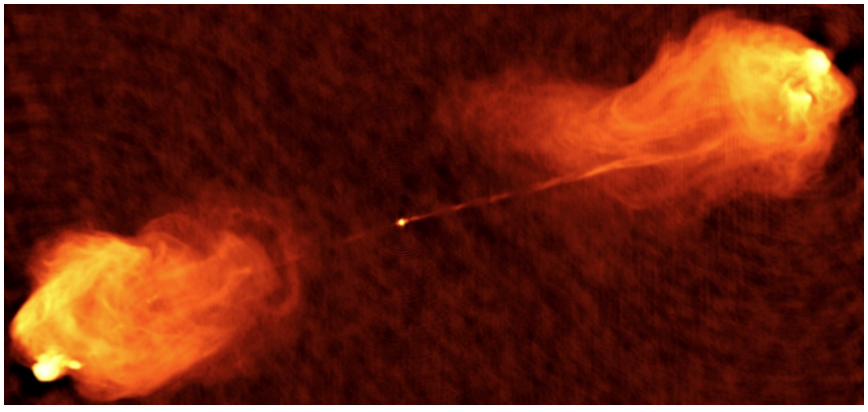

Figure 1.2: Radio image of Cygnus A with the thin jets from the AGN leading to two giant symmetrical lobes. These lobes extend ten times further from the nucleus than the stars in the galaxy. Cygnus A is the brightest extragalactic radio source in the sky. *Credits:* NRAO/AUI.

after SMBH) that is accreting a large amount of gas and dust from its surroundings (Novikov & Thorne, 1973; Shakura & Sunyaev, 1973). As well as increasing the mass of the central SMBH, this accretion mechanism also produces a tremendous amount of radiation which is emitted across the full observable electromagnetic spectrum (i.e. from radio to gamma-rays), with *typical* bolometric (i.e. total) AGN luminosities ($L_{\rm AGN}$) in the range 10^{40} to 10^{45} erg s^{-1} (e.g. Aird et al., 2017a). For comparison, the bolometric luminosity of all the stars in the Milky Way is $L_{\rm star} \approx 10^{43}$ erg s^{-1}.

Despite being known to reside in galaxies, prior to the mid-90's AGNs were largely considered in isolation and studied only because of their peculiarity. However, in the late 90's, some studies began to suggest that AGNs have a wider importance in galaxy formation than previously thought (e.g. Rees, 1996). In particular, the discovery of a tight correlation between the mass of SMBHs (hereafter $M_{\rm BH}$) and the velocity dispersion of the stars in the host galaxy bulges highlights that the growth of SMBHs is intimately linked to their host galaxies (see Fig. 1.3 left-hand panel; e.g. Kormendy & Richstone, 1995; Magorrian et al., 1998; Marconi & Hunt, 2003; Ferrarese & Merritt, 2000; Gebhardt et al., 2000; Merritt, 2000; Tremaine et al., 2002; Kormendy et al., 2011). In addition, SMBHs build their masses via multiple accretion episodes that can be observed as AGN activity, further supporting a relationship between AGNs and their host galaxies. However, this connection cannot be due to the gravitational influence of the SMBH, as galaxy bulges can extend to kilo-parsec (kpc) scales, whereas the gravitational sphere of influence of even the most massive SMBHs (i.e. $M_{\rm BH} \sim 10^9\ M_{\odot}$) only dominates over stars out to a few hundred parsecs (pc). Therefore, astronomers began to consider other means to connect SMBHs to their host galaxies.

As simple gravitational interactions are excluded, various studies based on cosmological simulations have explored the possible impact of the energy released by the AGNs upon their host galaxies. To date, this has predominantly focussed on how this energy impacts the star formation rate (SFR), as it is through star formation that galaxies build their stellar mass. This is supported by the similar observed redshift evolution between the density of the total SFR and that of the total SMBH accretion rate (see Fig. 1.3 right-hand panel; e.g. Silverman et al., 2008b; Aird et al., 2010; Assef et al., 2011). Many cosmological simulations have found that the AGN must somehow quench the host galaxy SFR in order for their results to be consistent with observations (e.g. Di Matteo et al., 2005; Springel et al., 2005; Hopkins et al., 2008; Dubois et al., 2013). However, there is still no clear consensus from an observational perspective supporting, or ruling-out, the quenching of SFR via the energy released by AGN activity.

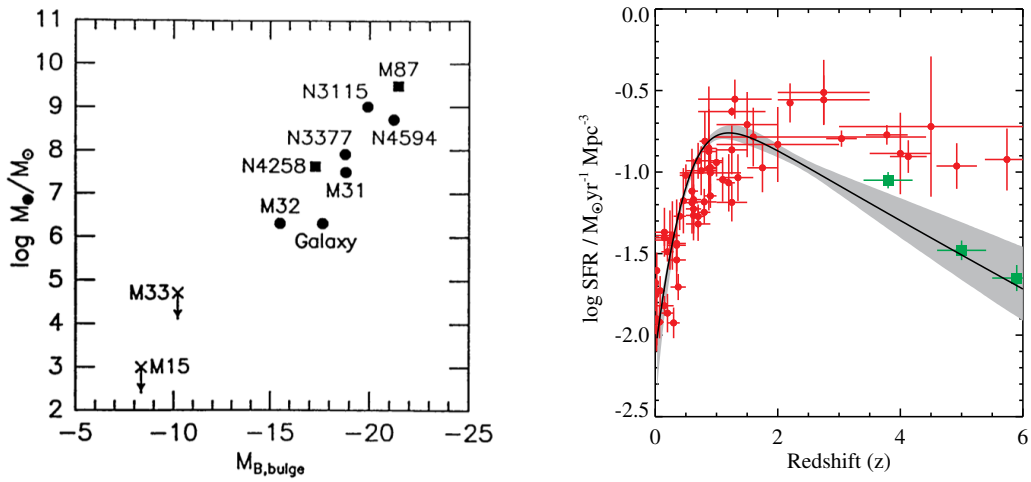

Figure 1.3: The two key pieces of evidence for a fundamental link between SMBHs and their host galaxies. *Left-hand panel:* The relationship between SMBH mass and galaxy bulge absolute magnitude. This strongly suggests a co-evolution of SMBHs and their host galaxies. *Credits:* This figure was originally published as Fig. 14 in Kormendy & Richstone (1995). *Right-hand panel:* The redshift evolution of the total SFR density (red and green dots) compared with the redshift evolution of the SMBH accretion rate density (solid line). The similarity between the redshift evolution of both SFR and SMBH growth densities is also seen as a key piece of evidence of a connection between SMBHs and their host galaxies. *Credits:* This figure was originally published as Fig. 13 in Aird et al. (2010).

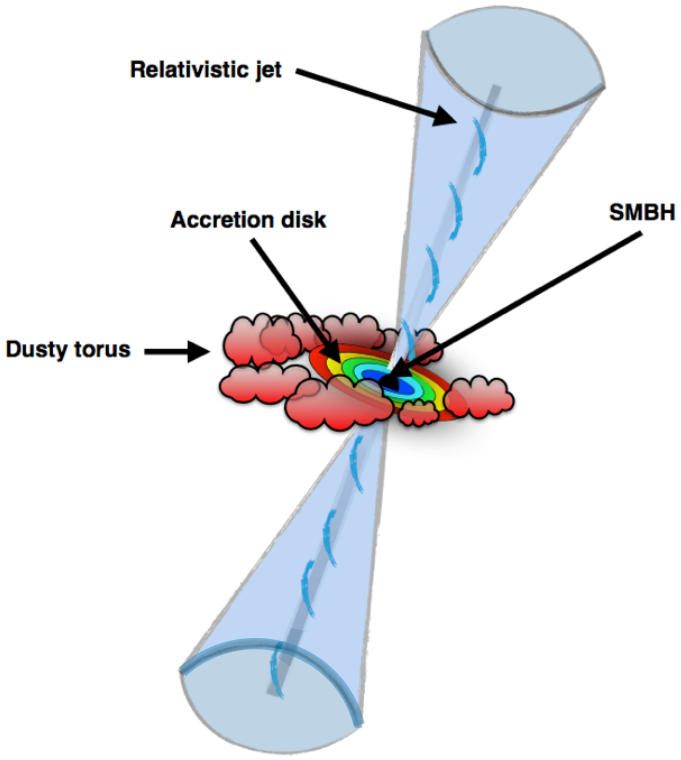

Figure 1.4: A sketch of the AGN structure. At the centre, shown with a black sphere, is the SMBH. The coloured disk shows the accretion disk colour-coded from the UV to the optical (from blue to red). In faint blue, we show the radio jets that can be seen in ≈ 10 per cent of the total AGN population. The torus is represented by an ensemble of red patchy clouds gathering around the AGN and made of dust and gas. Scales are not respected on this simplified sketch.

With the precise connection between the growth of SMBHs and that of the host galaxies unknown, astronomers began to appreciate that a comprehensive study of AGNs in the context of their host galaxies was necessary. This thesis examines one aspect of this complex interconnection: the relationship between AGN and SFR. As the process is initially triggered by the accretion mechanism occurring in the vicinity of central SMBHs, the next section focuses on explaining the basic AGN mechanism. Subsequently, in § 1.3, we describe the current understanding behind the AGN-galaxy SFR connection, before presenting the content of this thesis in § 1.4.

1.2 Active Galactic Nucleus mechanism

Since this thesis will focus on the connection between AGNs and their host galaxies, we need to be able to first measure the properties of these AGNs (e.g. AGN luminosity, accretion rate). Therefore, it is important that we first understand what an AGN is. As mentioned previously, at the centre of massive galaxies is a super-massive black hole with mass in the range $10^6 - 10^{10}$ $M_\odot$ (e.g. Schulze & Wisotzki, 2010; Kelly & Merloni, 2012). However, the lower limit remains unclear due to the difficulties of measuring SMBH masses below 10^6 $M_\odot$, although there has been evidences for lower mass SMBHs (Kormendy & McClure, 1993; Valluri et al., 2005; Lora et al., 2009; Jardel & Gebhardt, 2012).

During the AGN phase, gas and dust form an accretion disk (see Fig. 1.4) around the SMBH, the size of which is considered to extend out to roughly one parsec (e.g. Thorne & Price, 1975; Shields & Wheeler, 1978; Malkan, 1983; Czerny & Elvis, 1987). The majority of the thermally emitted photons from the accretion disk carry high energies (i.e. ultraviolet radiations, UV). The presence of free relativistic (i.e. high energy) electrons in the vicinity of the AGN allows a fraction of these UV photons (i.e. ≈ 5 per cent; Hopkins et al., 2007) to be reprocessed into X-rays (i.e. ~ 0.1 keV to several hundred keV) via inverse-Compton scattering (i.e. non-thermal; e.g. Haardt & Maraschi, 1991). Since not many sources can generate such extreme X-ray radiation – aside from ultra-luminous X-ray sources (e.g. Colbert & Ptak, 2002) – the central X-ray emission of galaxies (e.g. integrated 2-10 keV fluxes used in this work) is a very efficient way to detect AGNs. In addition to aiding detection, as the X-ray radiation is closely related to the accretion mechanism, X-rays are a reliable proxy to measure AGN properties (e.g. accretion power, accretion rate). As such, the central X-ray emissions of galaxies have also been extensively used in a number of studies investigating AGN properties (e.g. Alexander et al., 2005; Silverman et al., 2008b; Mullaney et al., 2011; Aird et al., 2015; Stanley et al., 2015).

Although X-rays are very efficient in tracing AGN properties, the softer X-ray emissions (i.e. below 10 keV) are absorbed by gas. Typically, for a gas column density of $\approx 10^{24}$ cm^{-2}, photons with energies below ~ 5 keV are fully absorbed (e.g. Maiolino et al., 1998; Matt et al., 2000). Therefore, X-ray surveys, especially when using instruments probing the soft X-ray emissions, are potentially biased toward less obscured X-ray sources. The obscuring gas material in AGNs is known to sit *mainly* in a torus located around the AGN at few tens of pc away from the SMBH, although it has been reported that gas clouds can be found at various locations around the AGN (see Fig. 1.4; see the review of Ramos Almeida & Ricci, 2017, for a complete

discussion on nuclear obscuration in AGNs).

In addition to gas, the torus also contains dust clouds (see Fig. 1.4) that are far enough from the hot accretion disk to avoid sublimation (i.e. roughly one-to-tens of pc away and with local temperature below ≈ 1000 K). Obscuration by the dusty torus is very efficient at absorbing the UV-to-optical photons emitted by the accretion disk. When we view the system edge-on, the dusty torus sits along our line of sight to the central component (i.e. accretion disk and SMBH), and therefore obscures the UV-to-optical emissions (hereafter Type 2 AGNs). The more our line of sight is aligned with the face-on axis of the torus (hereafter Type 1 AGNs), the more it unveils the central accretion disk at UV-to-optical wavelengths. Therefore, it is widely accepted that obscured and un-obscured AGNs are intrinsically the same, but observed at different orientations (i.e. whether observed through the torus or not). This is known as the Unification model of AGNs (Antonucci, 1993; Urry & Padovani, 1995).

More than obscuring the accretion disk at optical and UV wavelengths – and particularly pertinent for this thesis – the dusty torus also constitutes a source of contamination when measuring the SFR by using the infrared (IR) radiation of the host galaxy. This is due to the dust absorbing the UV photons from the accretion disk, which subsequently heats up, and re-emits at IR wavelengths (i.e. modified black-body behaviour). This must be taken into account when using IR radiation to measure host galaxy SFRs (e.g. Kennicutt, 1998), as there is potential for an overlap to occur between the IR emission arising from the dusty torus and that of the SFR (e.g. Mullaney et al., 2011; Symeonidis et al., 2016; Symeonidis, 2017).

Finally, roughly 10 per cent of the AGN population displays relativistic jets (see Fig. 1.4), also generated by the accretion mechanism and mostly perpendicular to the accretion disk. These jets can extend up to extra-galactic scales, and are often detected at radio wavelengths via their synchrotron emission (see Tadhunter, 2016, for a recent review on radio AGNs). However, since jetted AGNs constitute only a small fraction of the whole AGN population, they are not the main focus of this thesis.

1.3 Advances in the AGN-galaxy connection

As mentioned previously, this thesis aims to investigate the impact that AGNs have on star-formation within galaxies. Therefore, it is also important to appreciate how the non-AGN galaxy population evolves. In doing so, we are able to compare against AGN-hosting galaxies and assume that the AGN is responsible for any observed

differences, after taking other possible differences into account. As such, in this section, we first consider the properties of the non-AGN population, and subsequently present the latest results concerning our current understanding of where AGN and their host galaxies fit within this framework.

1.3.1 Evolution of galaxies without AGNs

Most star-forming galaxies have SFRs that are correlated with their stellar masses (e.g. Daddi et al., 2007; Elbaz et al., 2007; Noeske et al., 2007; Rodighiero et al., 2011; Schreiber et al., 2015; Ilbert et al., 2015). This has become known as the star-forming main sequence (hereafter, MS). In Fig. 1.5 we show the MS and its evolution out to $z{\approx}4$ as reported in Schreiber et al. (2015). The distribution of specific SFR (i.e. SFR relative to the galaxy stellar mass), which represents the intrinsic scatter around the MS, shows that ≈ 3 per cent of star-forming galaxies experience a burst of star formation (i.e. with SFRs on average five times above the MS; e.g. Sargent et al. 2012). These are called starburst galaxies, and many studies suggest that they are associated with on-going gas rich major mergers, known to favour the triggering of star-formation (e.g. Armus et al., 1987; Sanders & Mirabel, 1996; Ellison et al., 2008; Patton et al., 2011; Ellison et al., 2013). When a galaxy has exhausted its gas supply it becomes quiescent (i.e. with SFR below the MS), until new gas is provided (e.g. next merger) to bring it back up onto the MS, or the starburst sequence.

Because of the existence of the MS, in addition to other galaxy parameters (e.g. stellar mass, redshift), the SFR becomes a crucial parameter to derive. To measure the on-going SFR the UV luminosity of a galaxy is an efficient proxy since the UV photons are generated by young, rapidly evolving (i.e. $\approx$ 2–50 Myr), massive (i.e. above $\approx 10\ M_{\odot}$) stars (e.g. Kennicutt, 1998; Calzetti et al., 2007). However, in the presence of an AGN, the UV luminosity is highly contaminated by the UV radiation emitted by the accretion disk (via direct emission for an un-obscured AGN, or via scattered light for an obscured AGN; see § 1.2). This could be inaccurately interpreted as a higher SFR if not removed from the total UV luminosity of the galaxy. Whilst this correction for AGN contamination is necessary, it can lead to significant uncertainties regarding the SFR when measured using the UV luminosity. Furthermore, star-forming regions tend to be enshrouded within a dusty environment making them extremely obscured at UV wavelengths (e.g. Zahid et al., 2013). The dust in star-forming regions is known to absorb typically ≈ 90 per cent of the UV luminosity, for a galaxy with stellar mass of $10^{9.5}\ M_{\odot}$, and more than 99 per cent of the UV luminosity for a galaxy with stellar mass of $10^{11.5}\ M_{\odot}$ (e.g. Pannella et al., 2015).

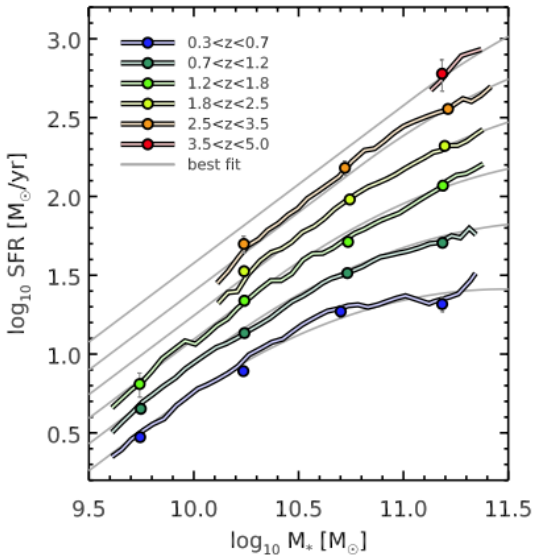

Figure 1.5: The main sequence of star-forming galaxies at various redshifts. The abscissa is the log of the stellar mass ($M_\odot$) and the ordinate is the log of the SFR ($M_\odot$/yr). We note a strong relationship between these two quantities out to $z\sim5$, known as the MS of star-forming galaxies. *Credits:* This figure was originally published as Fig. 10 in Schreiber et al. (2015).

These absorbed UV photons heat up the dust to temperatures of around $\approx$ 30–40 K (e.g. Hwang et al., 2010), reprocessing emission at far-infra-red (FIR) wavelengths. Therefore, instead of the UV luminosity, the IR luminosity (i.e. integrated luminosity between 8–1000 μm) is extensively used to measure SFRs (Kennicutt, 1998) primarily, in the study of non-AGN galaxies, but also of AGN host galaxies since the contamination at FIR wavelengths from the AGN (see § 1.2) is minimal (e.g. Netzer et al., 2007; Mullaney et al., 2011; Symeonidis et al., 2016; Symeonidis, 2017).

1.3.2 Recent insights into the AGN-galaxy connection

As mentioned previously, one way of connecting SMBH growth to galaxy growth, instead of a simple gravitational interaction, is for the AGN to directly impact the SFR on galactic scales. Indeed, simulations have found that AGNs should – somehow – have a negative impact on their host galaxy SFRs, i.e. AGN must quench SFR (e.g. Di Matteo et al., 2005; Springel et al., 2005; Hopkins et al., 2008; Dubois et al., 2013). In particular, if the quenching of SFR by AGNs is ignored, cosmological simulations tend to overestimate the number density of galaxies with stellar masses above $\sim 10^{10}$ $M_\odot$, when compared to what is observed (e.g. Dubois et al., 2016). Therefore, the SFR quenching by AGNs during an episode of SMBH accretion is widely utilised in simulations as the predominant impact that AGNs have on their

host galaxies. It should also be noted that the quenching of SFR by AGNs does not contradict the two key pieces of empirical evidence regarding the fundamental link between SMBH and galaxy growth: the $M_{\rm BH}$–galaxy bulge mass relationship, and the similar redshift evolution of the SFR and accretion rate densities (see § 1.1). However, the quenching of SFR by the AGN is often implemented in cosmological simulations via a variety of AGN feedback mechanisms that are far from fully understood (see the reviews of e.g. Fabian, 2012; Harrison, 2017, for details on the feedback mechanism).

Since cosmological simulations suggest that AGN feedback suppresses star formation in their hosts, many observational studies have attempted to observe this effect with large, statistically significant samples of AGNs. However, when examined from observational perspective, most studies report that AGN host galaxies mainly form a diverse population (e.g. Nandra et al., 2007; Böhm & Wisotzki, 2007; Schawinski et al., 2007; Silverman et al., 2008a; Xue et al., 2010; Cisternas et al., 2011; Kocevski et al., 2012). However, within this diverse population, AGNs tend to be found in more massive galaxies (i.e. $M_{*} > 10^{10}\ M_{\odot}$; e.g. Dunlop et al., 2003; Kauffmann et al., 2003; Best et al., 2005; Xue et al., 2010; Aird et al., 2012; Shimizu et al., 2015) with somewhat enhanced SFRs compared to the general population (e.g. Barvainis & Ivison 2002; Priddey et al. 2003; Page et al. 2004; Schweitzer et al. 2006; Lutz et al. 2008; Hickox et al. 2009; Silverman et al. 2009; Shao et al. 2010; Bonfield et al. 2011; Koss et al. 2011; Santini et al. 2012; Mullaney et al. 2012; Rosario et al. 2012; Rovilos et al. 2012; Harrison et al. 2012; Zinn et al. 2013; Shimizu et al. 2016, although see Page et al. 2012). Overall, these results are in contrast with the predictions of simulations in the sense that they do not show a suppression of SFR in AGN host galaxies.

To investigate the impact that AGNs have on their host galaxy SFRs, most observational studies aim to measure the differences between SFRs derived from a sample of AGN hosts to those of a sample of non-AGN galaxies. However, Shimizu et al. (2016) have demonstrated that the choice of the control sample (i.e. the sample of non-AGN galaxies) is crucial and can lead to opposing conclusions regarding the impact that AGNs have on their host SFRs. Using a mass-matched sample of non-AGN galaxies, Shimizu et al. (2016) found that the average SFR of AGN hosts is enhanced compared to that of their mass-matched sample. However, as a consequence of AGNs residing in more massive galaxies (e.g. Aird et al., 2012), the mass-matched control sample of non-AGN galaxies is more likely to contain massive, elliptical galaxies that are predominantly quiescent (i.e. with SFRs below the MS; e.g. Wuyts et al., 2011; Bell et al., 2012). Should AGNs in reality be mainly located in massive, late type spiral galaxies (e.g. Koss et al., 2011), that are more likely to be on the MS (i.e.

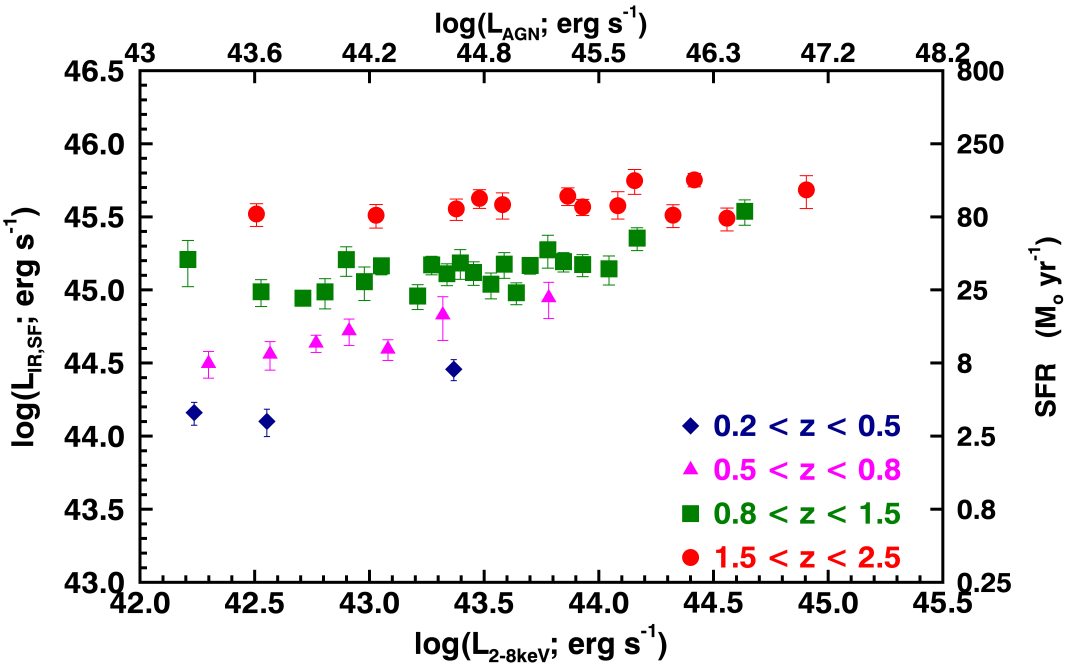

Figure 1.6: The relationship between the SFR and the 2-8keV X-ray luminosity of AGNs. This shows the mean average IR luminosity – or SFR – versus the 2-8 keV X-ray luminosity – or AGN luminosity – out to $z\sim2$ for a sample of X-ray selected AGNs. We note the absence of a strong (anti-)correlation between these two parameters. *Credits:* This figure was originally published as Fig. 3 in Stanley et al. (2015).

actively forming stars), the average SFR of the AGN host sample would naturally appear higher than that of the mass-matched sample, if using a mass-matched sample of massive elliptical quiescent galaxies. Previously, Shimizu et al. (2015), using the *same sample* of AGNs as Shimizu et al. (2016), but instead of using a mass-matched sample, only compared the AGN host SFRs to the MS of galaxies, reported a decrease of SFRs in galaxies hosting AGNs. These latter results are consistent with predictions from simulations. This demonstrates the importance in the choice of the control sample of non-AGN galaxies. In this work, we will use a mass-matched sample of galaxies which are exclusively star-forming (i.e. that follows the MS).

A second major difficulty in identifying the precise role that AGNs have on influencing the large scale SFR is the stochastic nature of the AGN (e.g. Aird et al., 2013; Hickox et al., 2014). While AGNs are known to significantly vary on a wide range of time-scales (i.e. hours to Myr), variations in SFR are expected to be steadier with a typical time-scale of $\sim$ 100 Myr. As a consequence, most studies that have aimed to measure the impact that AGNs have on SFR by exploring the relationship between

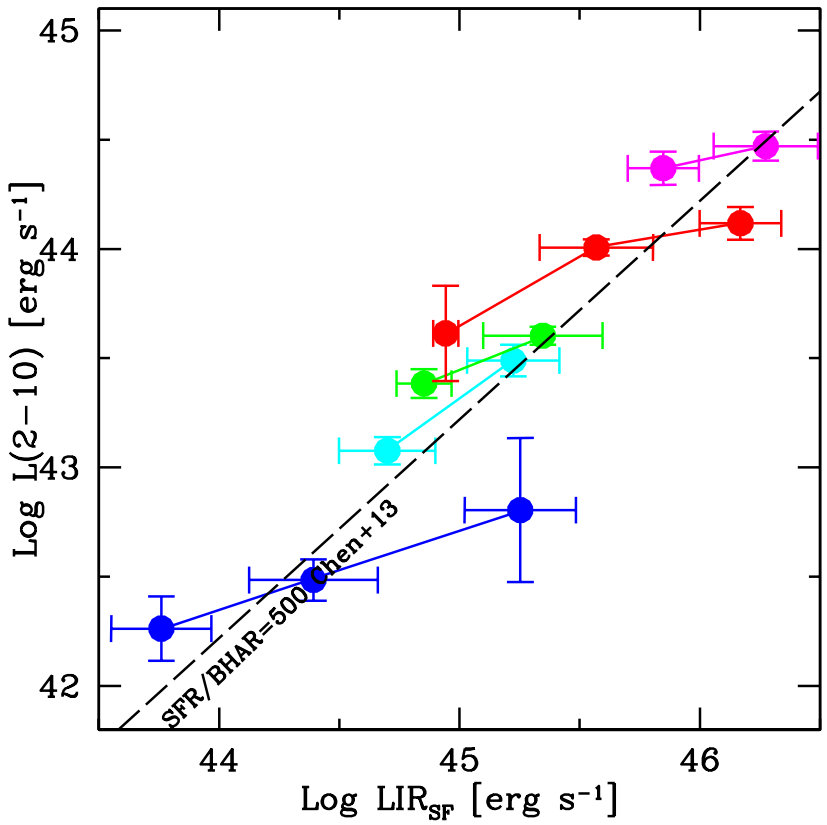

Figure 1.7: The relationship between the 2-10 keV X-ray luminosity and the SFR. This shows the 2-10 keV X-ray luminosity in bins of IR luminosity (i.e. inverting the abscissa and the ordinate of Fig. 1.6) for a sample of X-ray selected AGNs. Different colours are for different redshift bins out to $z\sim4$ (see Lanzuisi et al., 2017, for details). A slight correlation is reported between these two quantities. *Credits:* This figure was originally published as the right-hand panel of Fig. 5 in Lanzuisi et al. (2017).

AGN luminosity (a proxy for SMBH growth rate) and IR luminosity have found no clear evidence of a strong correlation – or anti-correlation – between these properties (see Fig. 1.6; e.g. Lutz et al., 2010; Shao et al., 2010; Mullaney et al., 2012; Rosario et al., 2012; Rovilos et al., 2012; Harrison et al., 2012; Stanley et al., 2015). Recently, Stanley et al. (2017) have found a small enhancement of SFR while expanding the previous studies at higher X-ray luminosities (i.e. $L_X > 10^{45}$ erg s^{-1}). However, they demonstrate that this is related to a slight increase in host mass at higher X-ray luminosities, resulting in an enhancement of SFR (i.e. following the MS of galaxies).

To mitigate the problem of variability, some studies have investigated how the average X-ray luminosity changes with SFR (i.e. inverting the abscissa and the ordinate from the above studies), aiming to average over the highly stochastic X-ray luminosity, and compare that to the steadier SFR (e.g. Mullaney et al., 2012; Chen et al., 2013; Dai et al., 2015; Delvecchio et al., 2015; Lanzuisi et al., 2017). Overall,

they report a correlation between average X-ray luminosity and SFR with slopes that vary with redshift (see Fig. 1.7; e.g. Lanzuisi et al., 2017). However, there may be a potential bias towards higher SFRs as these studies can only be carried out on AGNs for which we can individually measure the host SFRs (e.g. detected at FIR wavelengths). Overall, at present, there is no clear consensus on mechanisms that directly link AGN power and host galaxy star formation.

One aspect that many previous studies have failed to consider is that it is reasonable to assume that a luminous AGN (i.e. $L_X \gtrsim 10^{43-44}$ erg s^{-1}) will have a stronger impact on a lower mass host galaxy (i.e. $M_* \lesssim 10^{10}$ $M_\odot$) than on a higher mass one (i.e. $M_* \gtrsim 10^{11.5}$ $M_\odot$). This is simply due to the different depths of potential wells induced by different stellar masses. Therefore, in Chapter 2 and Chapter 3 of this thesis we aim to investigate how the AGN host SFRs change with *specific* X-ray luminosity (i.e. X-ray luminosity relative to the host stellar mass), instead of the often used X-ray luminosity. By measuring the SFRs of a large sample of AGN hosts at different specific X-ray luminosities, our hypothesis is that we should observe the quenching predicted in simulations at higher specific X-ray luminosities. Guided by our results, and by recent studies indicating that the specific X-ray luminosity distribution changes with the host star-forming properties (e.g. Georgakakis et al., 2014; Wang et al., 2017; Aird et al., 2017a), we then use in Chapter 5 and Chapter 6 a modelling approach to investigate in detail the specific X-ray luminosity distribution and how it relates to host SFRs.

1.4 This thesis

As mentioned above, the aim of this thesis is to investigate the co-evolution of SMBHs and their host galaxies. We first use a sample of 1620 X-ray selected AGNs, for which we measure AGN host SFRs (corrected for AGN contamination), and compare these to a sample of star-forming non-AGN galaxies that follow the MS. In Chapter 2, we describe how we reliably measure SFRs in the presence of AGNs, using multi-component spectral energy distribution fitting to separate the stellar emission from that of the AGN. We also describe the stacking analysis we use to incorporate undetected AGN host galaxies in the analysis. In Chapter 3 we show that, by doing this, we find an *enhancement* of the normalised average SFR (i.e. SFR relative to that of the MS) at higher specific X-ray luminosities, which is against our expectations based on a naive interpretation of results from simulations of an AGN quenching at these specific X-ray luminosities. We argue that these results indicate that the specific X-ray luminosity distribution changes with the star-forming properties of the

host galaxy, as suggested by other recent studies (e.g. Georgakakis et al., 2014; Aird et al., 2017b; Wang et al., 2017).

Since our results suggest a different specific X-ray luminosity distribution for star-forming and quiescent galaxies, we develop a model to investigate the specific X-ray luminosity distribution and how it relates to the star-forming properties of the host galaxies. To do this, we first attempt to fit the X-ray luminosity functions by assuming a model for the specific X-ray luminosity distributions split between star-forming and quiescent galaxies. In Chapter 4 we describe how we use an iterative (i.e. Markov Chain Monte Carlo approach) optimisation method to infer these specific X-ray luminosity distributions. In Chapter 5, we demonstrate that our model is able to reproduce the X-ray luminosity function, but fails at reproducing the flat relationship between SFR and X-ray luminosity when implementing a distribution for SFRs. In Chapter 6, we incorporate a mass dependency in the specific X-ray luminosity distribution for star-forming galaxies and show that, as well as reproducing the X-ray luminosity function, it predicts the flat relationship between SFR and X-ray luminosity. Finally, we provide a general conclusion of this thesis in Chapter 7.

Chapter 2

A reliable measure of SFR in the presence of an AGN

2.1 Introduction

In this thesis we aim to constrain the star-forming properties of AGN host galaxies to explore the connection between AGN power and their host SFRs. Therefore, SFRs of the AGN hosts is a crucial property that needs to be measured accurately. As mentioned in Chapter 1, § 1.3.1, to derive SFRs we use the IR luminosities (i.e. integrated 8–1000 μm fluxes, $L_{\rm IR}$) of galaxies that mainly trace the re-emission of dust heated by stars (Kennicutt, 1998). However, since the emission from the AGN heated dust can also significantly contribute at these wavelengths (see Chapter 1, § 1.2), it is crucial to account for AGN contamination in measuring SFRs (e.g. Mullaney et al., 2011; Symeonidis et al., 2016; Symeonidis, 2017). The Herschel telescope, with its Photo-detector Array Camera and Spectrometer (PACS, Griffin et al., 2010) and its Spectral and Photometric Imaging Receiver (SPIRE, Poglitsch et al., 2010) instruments, combined with the Multiband Imaging Photometer for Spitzer (MIPS) instrument on-board Spitzer, provides an unprecedented view of the spectral energy distribution (hereafter SED) at IR wavelengths (i.e. at 24 μm, 100 μm, 160 μm, 250 μm, 350 μm, and 500 μm). This is required to facilitate the decomposition of the SEDs into AGN and star-forming components.

Despite having the facilities to probe the IR SEDs of sources, there are observational limitations which increase the difficulties of obtaining the *full* IR SED coverage (i.e. detected at all the IR bands considered here) required to accurately measure SFRs on individual sources via the fit of their IR SEDs (e.g. the flux limit of the instrument, the larger PSF at longer wavelength; see Fig. 2.1 for an example of the effect of a larger PSF at longer wavelength). This fraction of IR-undetected sources

in a sample (i.e. for which we cannot measure SFR) can be as high as 56 per cent for sources out to $z\sim3$, as we will find when matching the IR counterparts of a sample of AGNs selected based on their central X-ray emission (see Chapter 3, § 3.2.2). This would lead to us missing more than half of the total AGN sample if these are rejected by the analysis, possibly generating strong selection effects (e.g. only brighter IR AGN hosts are accounted for). As a consequence, beyond measuring SFRs for IR detected sources, we also perform stacking to incorporate the IR-undetected ones in our analysis.

Stacking enhances the ratio of the signal to the noise by adding up together several frames centred on the source positions. This allows the measure of a total flux that, as well as containing the flux of individually detected sources, also contains the flux of the undetected ones that are present in the stack (Dole et al., 2006). Therefore, by performing stacking at each of the IR wavelengths considered in this analysis (i.e. at 24 μm, 100 μm, 160 μm, 250 μm, 350 μm, and 500 μm), and then averaging over the number of sources N used in the stack, we are able to derive an average SED for which we can extract an average SFR, incorporating the IR-undetected sources. Stacking has been used extensively in studies using the Herschel data (e.g. Dole et al., 2006; Béthermin et al., 2010; Schreiber et al., 2015; Stanley et al., 2015).

Once we have the full IR SED for a source (or at least an average IR SED for a stack of sources), we can measure the IR luminosity (i.e. the integrated flux over 8–1000 μm; $L_{\rm IR}$) and transform this into SFR (i.e. Kennicutt, 1998). To integrate the IR SED, we fit models which include possible AGN contamination to the IR SED (e.g. Mullaney et al., 2011). However, since we are using multiple models with different numbers of free parameters (i.e. whether including the AGN component or not), we cannot simply select the best model by minimising Chi-square (i.e. minimising the difference between the model and the observed data points). Instead, for one dataset (i.e. one IR SED) we perform a weighted average of all the possible models, the weights of which are related to the likelihood and the complexity of each model (i.e. penalising models with more degrees of freedom). This is known as multi-model inference.

In this chapter we present in § 2.2 the stacking analysis that we will apply in Chapter 3 on our sample of AGNs to incorporate the Herschel-undetected host galaxies. We then show in § 2.3 how we extract the SFRs from the IR SEDs using the multi-component SED fitting and the multi-model inference selection method. Finally, we summarise this chapter in § 2.4.

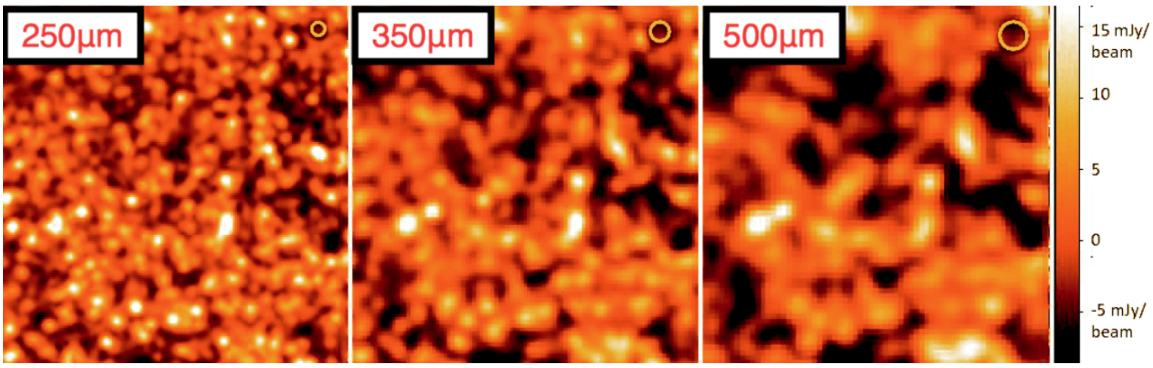

Figure 2.1: Visual example of the blending of sources due to confusion noise in HERSCHEL. Here are 3 maps of the same part of the sky, from left-to-right, at 250 μm, 350 μm and 500 μm. We note that there is a higher number of "resolved" sources at 250 μm compared to 500 μm. This is the effect of blending of the sources induced by a larger PSF at longer wavelengths. The top right yellow circle on each map shows the full width at half maximum (FWHM) of the beam. *Credits:* This figure was originally published as Fig. 1 in Nguyen et al. (2010).

2.2 Stacking analysis

2.2.1 Definition and application

As mentioned in § 2.1, stacking allows the measurement of an average flux for a sample of sources, incorporating undetected ones. The flux measured from a source can be decomposed into two main components, a true flux component super-imposed on noise arising from different effects (see below). The signal-to-noise ratio (SNR) can be expressed as,

$$\mathrm{SNR} = \frac{S_{\mathrm{src}}}{\sqrt{\sum_i \sigma_i^2}}, \tag{2.1}$$

where S_{src} is the flux of the source, and $\sum_i \sigma_i^2$ is the sum of all the "observational" noises, labelled i (e.g. shot noise, read-out noise, dark current, etc). Therefore, fainter sources (i.e. $S_{\mathrm{src}} << \sum_i \sigma_i^2$) are not detected since they have fluxes much lower than the noise. Since the noises sum-up in quadrature while the signal from the source sums-up linearly, for a set of N different images of a source, that are then co-added (i.e. stack), the total SNR can be written as,

$$\mathrm{SNR}_{\mathrm{tot}} = \frac{N \times S_{\mathrm{src}}}{\sqrt{N \times \sum_i \sigma_i^2}} = \sqrt{N} \times \mathrm{SNR}. \tag{2.2}$$

Therefore, the total SNR is enhanced by a factor of $\sqrt{N}$ compared to that of a single frame. We show in Fig. 2.2 a visual example of stacking by simulating N undetected individual sources (i.e. using two-dimensional Gaussian with amplitude much smaller than the noise) that we then stack a hundred (N=100), a thousand (N=1000), and ten thousand (N=10000) times. In this example, we observe that as we increase the number of sources, N, in the stack, the signal increases faster than the noise and the flux emerges, as predicted by Eq. 2.2.

We can perform stacking to incorporate in our analysis the AGNs that are not detected at IR wavelengths, by stacking cut-outs at known AGN positions to measure the total IR flux of the N AGNs that are considered in the stack. Dividing this number by N returns the mean flux of the sources in the stack. One of the major drawback of stacking is that we are only able to derive the mean properties of the sources (i.e. it does not provide a measure of the distribution). Such mean values might be dominated by a few very bright outliers. As a consequence, a mean SFR obtained from stacking does not necessarily reflect the mode (i.e. the most common value in the sample) of the distribution of SFRs (see Mullaney et al. 2015 for detailed discussion on this aspect).

As mentioned earlier, we are interested in measuring SFRs via the fit to IR SEDs (i.e. integrated 8–1000 μm emission), as such, we separately stack the six IR bands we use in this study, i.e. 24 μm, 100 μm, 160 μm, 250 μm, 350 μm, and 500 μm. To do this, we co-add sub-frames centred on the positions of the detected and the undetected (using the 24 μm or the X-ray positions when undetected) sources and measure the resulting flux of the sources contained in the stack (see § 2.2.2 for the flux extraction). By dividing this total number by the number of AGNs in the stack N, we obtain the average flux, and once applied at all the wavelengths, the average SED from which we can measure the average SFR (see § 2.3 for the extraction of SFRs from SEDs).

2.2.2 Flux extraction

To extract the flux from an image, should it be a cut-out around a detected source or a final stacked average cut-out, we performed aperture photometry. However, again, this flux (or average flux) is a linear combination of the true flux with the addition of noises (see Eq. 2.2). To improve the estimation of the flux, prior to extraction, we measure the residual background by averaging the pixel values in an annulus drawn around the source (see Table 2.1 for the annulus sizes) and subtract it from the frame. We then fit the observed point spread function (PSF) of the instrument at the centre

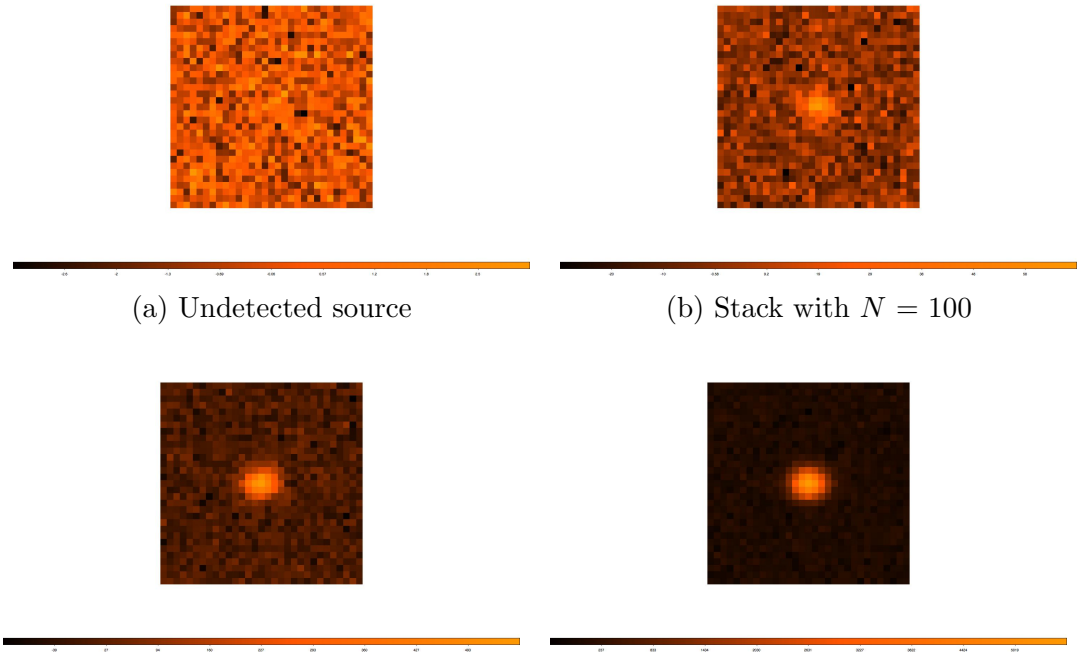

(a) Undetected source

(b) Stack with $N = 100$

(c) Stack with $N = 1000$

(d) Stack with $N = 10000$

Figure 2.2: Visual example of stacking. From the top-left to the bottom-right panel we stack an increasing number N of randomly generated sources. Each source was created using a two-dimension Gaussian function with FWHMs of 4.3 and 3.6 pixels in the X and Y directions, respectively, and amplitude following a uniform distribution. Each source is then added to a map of randomly generated Gaussian noise with standard deviation of 1 and mean of 0. The stacking is equivalent to averaging the N randomly generated sources, as shown here for $N = 100$, 1000 and 10000. We note that as the number of sources N involved in the stack increases the noise around the source gets suppressed and the detection at the centre becomes visually clearer.

of the frame, and measure the flux in a circular aperture of a given radius[1] (see Table 2.1). We apply an "aperture correction" factor to account for the missing flux lying outside of this finite circular aperture. This aperture correction factor depends on the shape of the PSF and the chosen finite radius from which the flux is extracted. Both these quantities depend on the wavelength. Finally, a correction is applied to account for the loss of flux due to the high-pass filtering (filter blocking frequencies below a cut-off value often used for image sharpening). Therefore, the measured flux, S (or average flux if stacked, $\langle S \rangle$), at a given wavelength can be expressed as,

$$S = (S_{\rm extracted} \times {\rm aper\_corr} \times {\rm HPF}) - \sigma_{\rm back}, \tag{2.3}$$

where $S_{\rm extracted}$ is the flux extracted within the finite circular aperture, "aper_corr" is the aperture correction factor, "HPF" is the correction factor for high pass filtering, and $\sigma_{\rm back}$ is the residual flux contained in the background, and measured in the annulus drawn around the source. All the aforementioned correction factors are reported in the observer manuals of the respective instruments [2] [3] [4] and given in Table 2.1. We show in Fig 2.3 an example of a stack for $N = 12$ sources at 24 μm and its corresponding PSF fit.

This method can be used to extract flux from an image of an individually detected source as well as to a frame that results from stacking. In the case of stacking, we took a bootstrapping approach to estimate the uncertainties on the flux by randomly re-sampling one third of the N sources included in the stack (with replacement) and re-performing the stacking and flux extraction analyses. This was repeated 100 times for a given stack, with the standard deviation of these 100 trials divided by the square root of three taken as the uncertainty on the flux.

2.2.3 Correction for clustering

There is a last source of contamination that must be accounted for, but that only applies while performing stacking to measure average fluxes. This is that any contributing flux from bright neighbours can boost the true flux of the stacked source via the flux contained in the wing of the neighbours PSF. This contribution will vary

[1] We note that fitting the observed PSF constitutes an extra step, as such, one can, directly from the map, measure the flux contained within the aperture, after removing the background emission.

[2] The IRAC instrument handbook is publicly available at:
`http://irsa.ipac.caltech.edu/data/SPITZER/docs/irac/`

[3] The PEP full public data release handbook is publicly available at:
`http://www.mpe.mpg.de/resources/PEP/DR1_tarballs/readme_PEP_global.pdf`

[4] The SPIRE instrument handbook is publicly available at:
`http://herschel.esac.esa.int/Docs/SPIRE/spire_handbook.pdf`

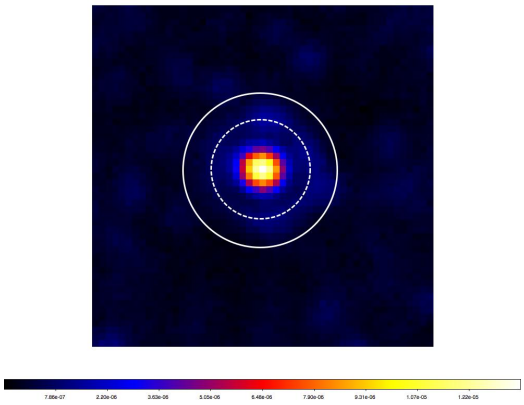

(a) Stack source with flux extraction rings

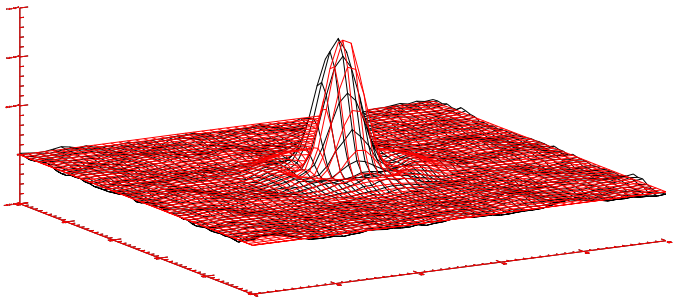

(b) fit of the PSF

Figure 2.3: Example of a stack of N = 12 sources at 24 μm and its corresponding PSF fit. *Top panel:* average cut-out of 12 stacked sources. The white dashed ring shows the finite circular aperture used for the flux extraction, and the annulus drawn between this dashed white ring and the plain white ring shows the area used to measure the background noise. *Bottom panel:* fit of the PSF (red) performed to extract the average 24 μm flux of the stacked source (black) using Eq. 2.3. The average 24 μm flux found for this particular stack was 0.64 milli-Jansky.

Table 2.1: Quantities used for our flux extraction. For each wavelength, "PSF radius" gives the encompassed area from which the flux is extracted, "Aper. corr." reports the multiplying coefficient to account for the missing flux (i.e. outside of the PSF radius area), "Back. annu." specifies the size of the annulus used to remove the background noise, and "H.P.F" is the multiplying coefficient used to account for the high-pass-band filtering. All these values are recommended by the observer manuals of the respective instrument[234].

λ	24μm	100μm	160μm	250μm	350μm	500μm
Aperture radius (arcsec)	7.0	7.2	12.0	22.0	30.0	40.0
Aper. corr.	2.05	1.50	1.48	1.3	1.2	1.2
Back. annu. (arcsec)	7 to 13	8 to 14	13 to 17	60 to 90	60 to 90	60 to 90
H.P.F	1.0	1.12	1.11	1.11	1.0	1.0

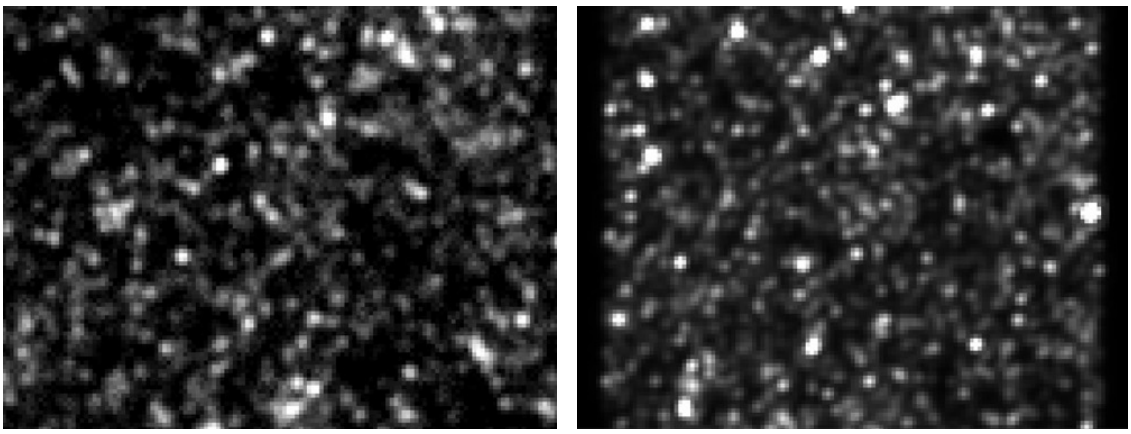

Figure 2.4: Real and simulated map of the central part of the COSMOS field at 350 μm. *Left-hand panel:* central part of the COSMOS field at 350 μm extracted from the science map released by the Herschel-SPIRE HerMes project (Oliver et al., 2012). *Right-hand panel:* same as left-hand panel but simulated using the prescriptions outlined in § 2.2.3. The colour scales of both maps are identical to allow the visual comparison.

from source to source such that if the sources are randomly distributed across the field then the level of boosting will be roughly the same in each stack (if the number of stacked sources is large to overcome shot noise). However, in the presence of clustering, the probability of finding neighbours close to the stacked sources increases (Chary & Pope, 2010), meaning the level of flux boosting related to this effect increases with the level of clustering. To account for this effect we adopt the approach of Schreiber et al. (2015), where the effects of clustering are measured by stacking on simulated maps with all the input fluxes known.

These maps are created using a complete sample of sources with positions, stellar masses and redshifts taken from the COSMOS catalogue of Ilbert et al. (2013). We allocate SFR to these sources randomly drawn from the specific SFR (i.e. SFR relative to the stellar mass) distribution of Sargent et al. (2012). For each source, SFR is then transformed into IR luminosity (Kennicutt, 1998), and to IR fluxes at 24 μm, 100 μm, 160 μm, 250 μm, 350 μm and 500 μm, using the redshift of the source (i.e. K-correction; Hogg et al., 2002), and the SED templates for star-forming galaxies reported in Mullaney et al. (2011). These mock sources are then placed on a mock noise map (generated from the publicly available root-mean-square map of the field) at the same positions as listed in the catalogue, as such, the simulated maps have the same level of clustering as that of the science maps, but with different fluxes. We show in Fig. 2.4 an example of a simulated map of the central part of COSMOS at 350 μm along with the real map.

We then stack sources on this simulated map in bins of redshift and stellar masses. The contamination due to clustering of a simulated map i, $\sigma^{i}_{\rm clus}$, is calculated as the difference between the stacked flux and the known mean flux of the simulated sources. We performed 100 realisations of this map (generating a new map each time), and the average value of the resulting distribution of clustering contamination, i.e. $\sigma_{\rm clus} = \sum_{1}^{100} \sigma^{i}_{\rm clus}/100$, gives the average contribution due to clustering (see Fig. 2.5 for an example at 350 μm). We find that the results of our simulation are in agreement with Schreiber et al. (2015; i.e. $\sigma_{\rm clus} = 0$ per cent, 0 per cent, 3 per cent, 8 per cent, 13 per cent, 25 per cent in the 24 μm, 100 μm, 160 μm, 250 μm, 350 μm and 500 μm band, respectively), which performed similar simulations but including narrower, hence deeper, fields (see Appendix B.2 of Schreiber et al. 2015). We apply these corrections to our stacked fluxes to take into account the clustering bias. Although we find identical corrections within a few per cent of Schreiber et al. (2015), we did not simply apply their values as we wanted to test the reliability of these by using different fields and catalogues.

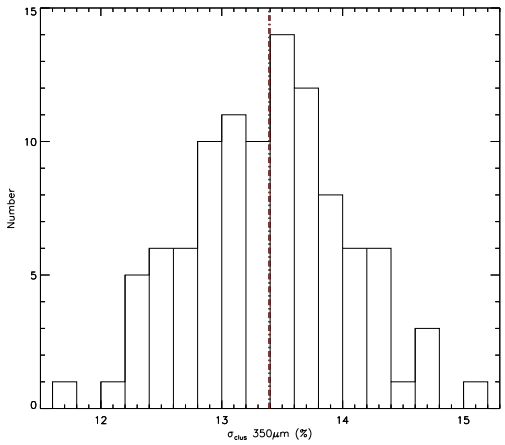

Figure 2.5: Histogram of the clustering contamination value in a series of 100 simulations. Shows the results of our simulation at 350 μm, with $\sigma_{\rm clus}$ the excess due to clustering in the stacked flux compared to the input flux. We have generated 100 simulated maps to plot this histogram and we have measured an average $\sigma_{\rm clus}$ of 13.39 per cent that we rounded to 13 per cent. This value is in agreement with $\sigma_{\rm clus}$ reported in Schreiber et al. (2015) at 350 μm.

2.3 Measuring star formation rates

2.3.1 Spectral energy distribution fitting

As mentioned above, we use the integrated 8–1000 μm emission (i.e. $L_{\rm IR}$) of the AGN host galaxies as a measure of their SFRs (Kennicutt, 1998) as it is largely unaffected by dust obscuration and AGN contamination (e.g. Mullaney et al., 2011; Netzer et al., 2007; Hatziminaoglou et al., 2010). However, it is known that powerful AGNs can contribute significantly at these wavelengths (in particular below 30 μm). To remove any AGN contamination into the IR luminosities we perform a two-component (i.e. a galaxy and an AGN component) SED fitting. For this, we used DECOMPIR[5] that fits the IR SED using chi-square minimisation with a combination of a galaxy component (taken from a library of five different galaxy templates) and an AGN component (Mullaney et al., 2011). The IR luminosity of the host galaxy can then be isolated from that of the AGN. We show in Fig. 2.6 an example of the best fit of an IR SED (taken from our sample of AGNs and after performing stacking, see Chapter 3) returned by DECOMPIR.

To test whether the AGN component is required, we use a multi-step approach to fit the IR SED using DECOMPIR. Firstly, we separately fit the SED with each

[5]Publicly available and can be downloaded at : `https://sites.google.com/site/decompir/`

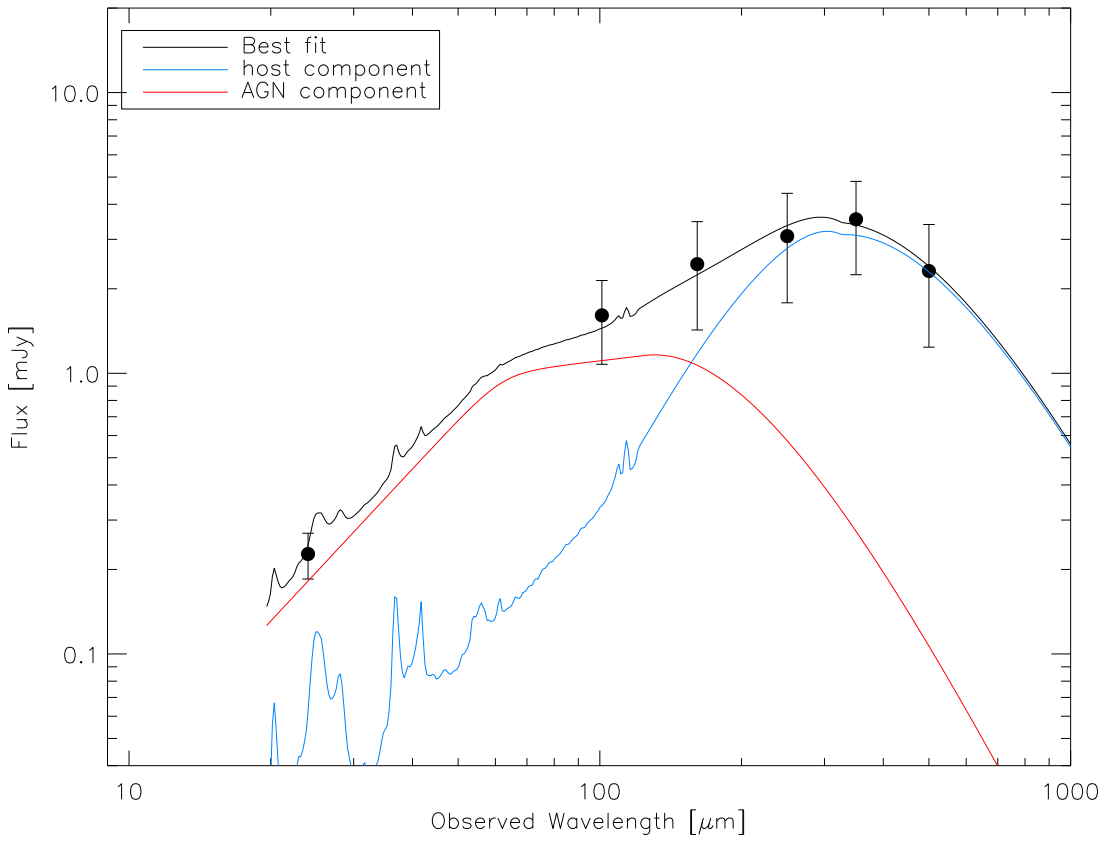

Figure 2.6: Example of a multi-component SED fit. The dots are the measured (stacked in this case) fluxes at 24 μm, 100 μm, 160 μm, 250 μm, 350 μm, and 500 μm, and their associated 1σ uncertainties. The host component is shown in blue, the AGN component in red, and the sum of both in black. We note that in this particular case, at wavelengths shorter than $\approx$160 μm the IR flux is dominated by the AGN emission. Whilst deriving SFRs, we only account for the flux contained within the host component.

of DECOMPIR's five different observed galaxy templates, and including an AGN component. Then, we repeat the fit but now excluding the AGN template (allowing the host galaxy template to renormalise). Thus, for each observed IR SED, we have ten different models (i.e. five with an AGN component, hereafter, "AGN+SF", and five host only, hereafter, "SF"). Since the five "AGN+SF" models have one degree of freedom more than the five "SF" ones, we cannot simply select the best one based on the chi-square of each fit. We need another way to compare these ten models that account for the differences in complexity (i.e. different number of degrees of freedom).

2.3.2 Multi-model inference

To compare the ten different models of the IR SEDs, we utilise multi-model inference. This enables us to balance under-and-over-fitting, also known as the *Occam's razor law of parsimony*, or more recently, the "model selection problem" (see e.g. Forster, 2000, 2002). To account for this we rely on the Akaike Information Criterion (Akaike, 1973, 1974, 1985, 1994, hereafter AIC) which measures the ability of the model at reproducing the observed data (i.e. quantified by the log-likelihood value returned by the fit), while incorporating a penalising factor that increases with increasing number of degrees of freedom (k). Therefore, contrary to Chi-square, the AIC allows the comparison of very different models (see Burnham & Anderson 2002 for a complete analysis, and see Appendix A for some insights on the demonstration of the AIC). It is advised to use the "corrected" AIC in a presence of a low number of data points, n, but there is no consensus on how low this number needs to be (e.g. Mutua, 1994). However, as pointed out by Burnham & Anderson (2002), for large n, the corrected AIC converges toward the AIC itself, as such, it is always better to use the corrected AIC (hereafter AICc). We use the following definition:

$$\mathrm{AICc} = -2\log(\mathcal{L}) + 2\ k\left(\frac{n}{n-k-1}\right), \tag{2.4}$$

where $\log(\mathcal{L})$ is the log-likelihood of the fit (i.e. the likelihood of observing the data given the model), n the number of observed data points (i.e. n=6 for a SED in our case), and k is the number of free parameters (i.e. $k_{\mathrm{AGN+SF}} = 2$ and $k_{\mathrm{SF}} = 1$ if we consider two or one fitting components, respectively). As mentioned in § 2.2.2, the uncertainties on the data are derived using a random iteration process, and as such, they are normally distributed. Therefore, the likelihood is defined as the product of a normal distribution associated with each data point, i.e.,

$$\mathcal{L} = \prod_{i=1}^{6} e^{-\frac{(x_i-\mu_i)^2}{2\sigma_i^2}}, \tag{2.5}$$

where σ is the standard deviation (or the errors on each data point), μ is the mean (or the expected value from the model), and x_i is the value of the data point i (or the observed value). Taking the natural logarithm of $\mathcal{L}$ gives us,

$$\log(\mathcal{L}) = -\sum_{i=1}^{6} \frac{(x_i-\mu_i)^2}{2\sigma_i^2} = -\frac{1}{2}\chi^2, \tag{2.6}$$

where $\chi^2 = \sum_{i=1}^{6}(x_i-\mu_i)^2/\sigma_i^2$ is the chi-square of the fit. Therefore, for normally distributed errors, as in our case, the log-likelihood is simply minus one and a half the chi-square of the fit. As such, we can write the corrected AIC as,

$$\mathrm{AICc} = \chi^2 + 2\ k\left(\frac{n}{n-k-1}\right). \tag{2.7}$$

For each of our ten models, we can measure the chi-square of the fit and use Eq. 2.7 to compute the AICc that allows their comparison. To do this, the model with the minimum AICc returns the best model. One can see that minimizing the AICc for constant k (models of same complexity) is equivalent to minimizing χ^2. However, it is well known that there is no true model, and as such, the best model is only an approximation of the true model (if it exists). Since we have a finite set of models, rather than selecting one "best" model we prefer to use a weighted mean of all of our ten models to account for the degeneracy. The weight of each model is defined using the Akaike weight (i.e. Akaike, 1973, 1974, 1985, 1994) which is based on their AICc, i.e.,

$$\mathscr{A}_{\mathrm{w}}^{i} = \frac{\mathrm{e}^{-0.5\times(\mathrm{AICc_i}-\mathrm{AICc_{min}})}}{\sum_1^m \mathrm{e}^{-0.5\times(\mathrm{AICc_i}-\mathrm{AICc_{min}})}}, \tag{2.8}$$

where $\mathscr{A}_{\mathrm{w}}^{i}$ is the Akaike weight of the model i, AICc_i is the AICc of the model i, $\mathrm{AICc_{min}}$ is the AICc of the best model (i.e. the one with minimum AICc), and m is the number of models (i.e. here m=10). The total IR luminosity of a given host galaxy, $L_{\mathrm{IR}}^{\mathrm{host}}$, is then computed as a sum of the ten possible modelled IR luminosities weighted by their Akaike weight, i.e.,

$$L_{\mathrm{IR}}^{\mathrm{host}} = \sum_{i=1}^{10}(L_{\mathrm{IR}\ i}^{\mathrm{host}} \times \mathscr{A}_{\mathrm{w}}^{i}), \tag{2.9}$$

and $L_{\mathrm{IR}}^{\mathrm{host}}$ is then converted to SFR using Eq. 4 of Kennicutt (1998), adjusted to a

Chabrier (2003) IMF. This can be applied to extract SFRs on individual FIR galaxy SEDs as well as on the average FIR SED produced when performing stacking to account for HERCHEL-undetected sources.

This method is very similar to that of Stanley et al. (2015), where they also derive SFRs via fit to the IR SEDs of AGN host galaxies using several combinations of AGN and galaxy host templates. However, in Stanley et al. (2015), they compare the various models using the Bayesian Information Criteria (BIC, Schwarz, 1978), instead of the AIC in this study. Although both criterion are used in model selection and are well known for their efficiency at penalising models on their degrees of freedom, there is a fundamental difference in these two criterion. While the BIC is searching for the best model, and therefore assumes that there is a *true* one among the finite set of models, AIC only assesses the goodness of a given model (e.g. Burnham & Anderson, 2002). Since we begin with the idea that there is no true model (i.e. we use a combination of five galaxy templates and one AGN template only), the AIC is more adapted for our study to measure the goodness of a model at representing our observed dataset (i.e. a SED), and to consequently allocate a weight. This weight can then be used to weight-average all the possible models. However, overall, AIC and BIC are known to give very similar results (e.g. Kuha, 2004).

2.3.3 Application to a sample of field galaxies

We have now presented our method of measuring SFRs from fits to the galaxy IR SEDs (i.e. from 8–1000 μm) accounting for AGN contamination when necessary. We also have explained that our measure of the SFR for a given galaxy (or the average SFR for a stack of galaxies) is a weighted mean of the SFRs returned by each of our ten models, and weighted according to their likelihood (i.e. using the AICc, see § 2.3.2).

One thing that remains to be checked is whether our method is somehow unnecessarily "imposing" the presence of an AGN component in the fit to the IR SEDs. To do this, we derive SFRs for a sample of galaxies that mainly contains star-forming galaxies (but might also contain some AGNs). By first excluding the AGN component to the fit of their IR SEDs, then including the AGN component, and comparing both estimates of the SFRs, we can assess by how much introducing the AGN component affects the measured SFRs. For a sample, we select sources from the multi-wavelength catalogue of Laigle et al. (2016). As we aim to perform multi-component IR SED fitting, we only select sources that are detected at the same IR wavelengths as those used in our study, i.e. 24 μm, 100 μm, 160 μm, 250 μm, 350 μm, and 500 μm. We

also require that they have available spectroscopic redshifts. Out of the 1,182,108 sources listed in the catalogue of Laigle et al. (2016), 447 satisfy these criteria (i.e. $\sim$0.04 per cent).

In Fig. 2.7 we show the comparison between the 447 SFRs when including an AGN component versus those when the AGN component is not included. The red dots indicate the galaxies for which our second estimate of SFRs returned an AGN contamination higher than 20 per cent of the total IR luminosity. Although most of the SFRs are consistent within each other, we find that only $\approx$5 per cent of the galaxies in this sample have IR SEDs that are significantly contaminated by AGN emission (i.e. at 20 per cent of their total IR luminosity). The low fraction of galaxies that need an AGN component to fit their IR SEDs suggests that our fitting method is accurate at recovering IR SEDs that are well reproduced using simply the star-forming templates. In other words, in the vast majority of cases there is no evidence that it needs an AGN component to the IR SEDs. Among the "AGN contaminated" galaxies (i.e. the five per cent that suggests a significant AGN contribution), SFRs are found to be on average $\approx$1.8 times higher than if the AGN contamination is accounted for. This also demonstrates the importance of accounting for the AGN contamination into the IR SEDs while deriving SFRs for a sample of AGN host galaxies (i.e. as for our forthcoming sample, see Chapter 3).

As we have measured the SFRs for these 447 field galaxies, we can compare these to those published in the Laigle et al. (2016) catalogue. We show in Fig. 2.8 this comparison. Overall, our SFRs are consistent with those of Laigle et al. (2016). As accounting for AGN contamination decreases the SFR, we expect a small fraction of our SFRs to be lower than those provided by Laigle et al. 2016 which do not account for any AGN contamination. Instead, we find that our SFRs (after accounting for AGN contribution) are on average $\approx$2 times higher than that of those reported in Laigle et al. (2016). However, in Laigle et al. (2016), measuring SFRs was not the primary goal of their study, such that they use the UV-to-optical part of the SED. Hence, their SFRs are subject to very large uncertainties arising from errors associated with correcting for dust obscuration. This can explain the discrepancies observed between the SFRs derived using our method and the SFRs reported in Laigle et al. (2016) for this particular sample of 447 sources.

2.4 Conclusion

In this chapter we outline our method to accurately measure SFRs for galaxies hosting AGNs by using their FIR luminosities to trace the emission of the dust heated by

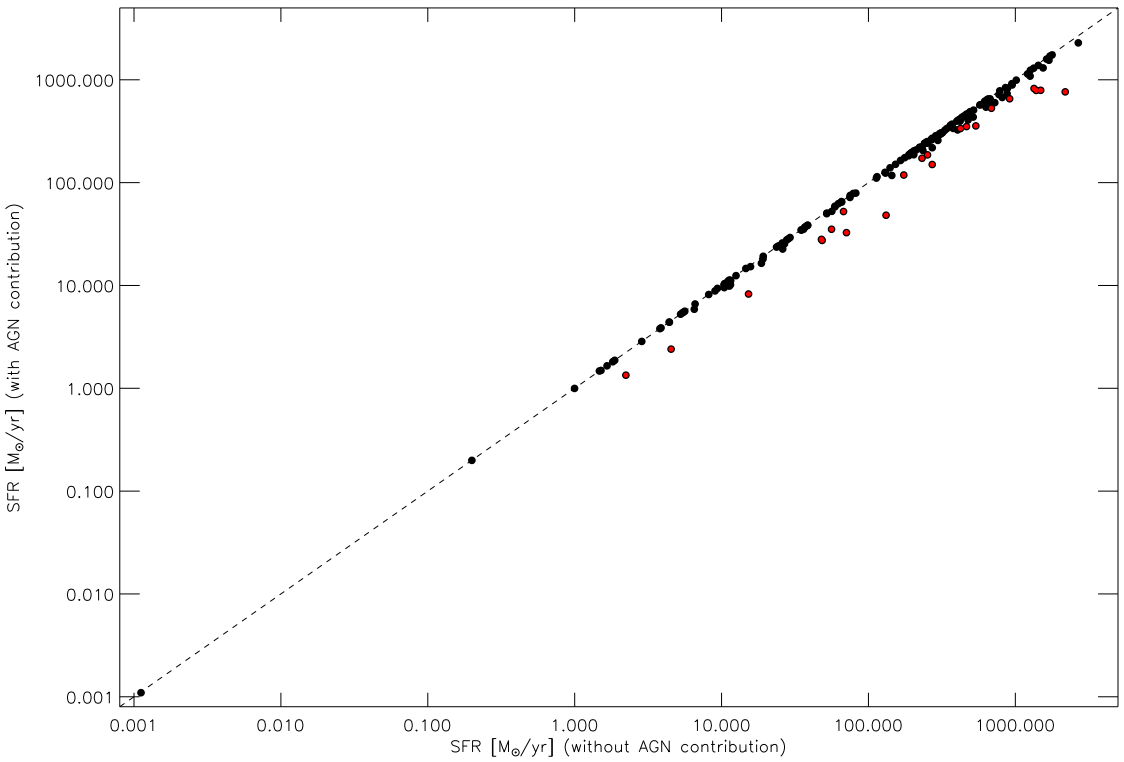

Figure 2.7: Comparison of SFRs derived whether considering an AGN contribution to the IR SED or not, for a sample of 447 sources taken from the COSMOS catalogue of Laigle et al. (2016). The red dots indicate the 5 per cent of the sources for which our fitting routine returns an AGN contamination of more than 20 per cent to the total IR luminosity. The dashed line indicates the 1:1 correlation.

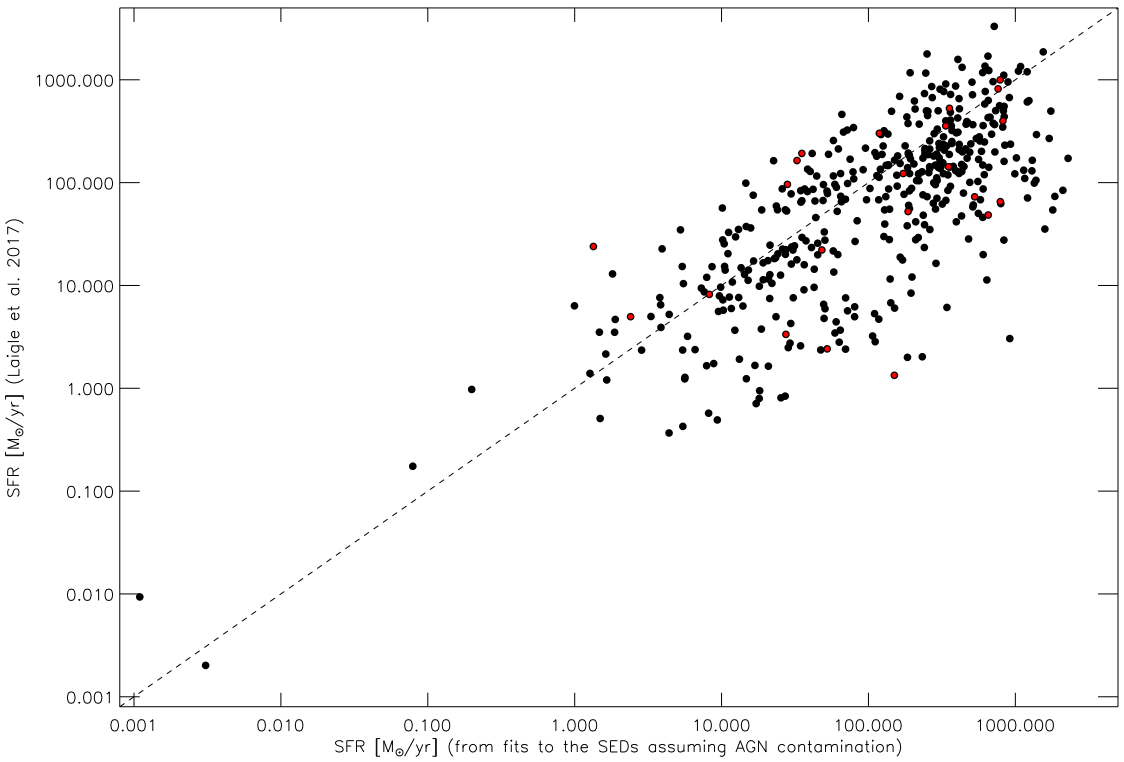

Figure 2.8: Comparison of SFRs derived using our method to those reported in Laigle et al. (2016) for a sample of 447 sources taken from the COSMOS catalogue of Laigle et al. (2016). The red dots indicate the 5 per cent of the sources for which our fitting routine returns an AGN contamination of more than 20 per cent of the total IR luminosity. The dashed line indicates the 1:1 correlation.

stars.

We first introduce the stacking analysis that we will perform to incorporate HERSCHEL-undetected AGN host galaxies into our analysis. We also show how we extract the flux from a frame containing the result of the stack, and how we use simulations to correct this flux for the boosting due to the clustering of the sources. In doing this, we find results which correspond exactly to those of Schreiber et al. (2015), i.e. $\sigma_{\rm clus} = 0$ per cent, 0 per cent, 3 per cent, 8 per cent, 13 per cent, 25 per cent in the 24 μm, 100 μm, 160 μm, 250 μm, 350 μm and 500 μm band, respectively.

We then present how we extract the FIR luminosities and therefore the SFRs out to the FIR SEDs, by performing a multi-component SED fitting, allowing for any AGN contribution when necessary. We highlight our model selection method based on multi-model inferences, that measures the corrected Akaike Information Criterion (AICc) to accurately account for model degeneracies.

Finally, we measure SFRs for a sample of 447 sources, all selected from the COSMOS catalogue of Laigle et al. (2016) based on their complete SED at IR wavelengths and on their available spectroscopic redshifts. Using this sample of 447 field galaxies, we compare the change in SFRs when adding an AGN component to the fit of the IR part of their SEDs to that of ignoring the AGN contamination. As expected for field galaxies, we find that only five per cent of the sources have SFRs that are AGN contaminated (above 20 per cent of the total FIR luminosity) suggesting that out method to fit IR SEDs is not unnecessarily imposing an AGN component to the IR SEDs of star-forming galaxies. These potential AGN sources have SFRs on average $\approx$1.8 times higher than if removing the AGN contamination.

Chapter 3

An enhanced fraction of starburst galaxies among high Eddington ratio AGNs

3.1 Introduction

In this thesis we aim to study the impact that AGNs have on the star formation rates (SFRs) of their host galaxies. As discussed in Chapter 1, § 1.3.2 many recent studies exploring this topic have found no evidence of a strong correlation between SFR and X-ray luminosity (a proxy for AGN power) out to $z\sim2$ (e.g. Rosario et al., 2012; Stanley et al., 2015). However, unlike previous studies that focus on the total AGN luminosity to trace AGN power, we use the total AGN luminosity *per unit host stellar mass* (i.e. specific AGN luminosity). This may be more pertinent since it is reasonable to consider that a powerful AGN (i.e. with X-ray 2-10keV luminosity of $L_X \sim 10^{44-45}$ erg s^{-1}) will have a larger impact on a low-mass galaxy compared to a high-mass galaxy. This is simply due to the deeper potential well of the later. Thus, by measuring the SFR of AGN hosts across several orders of magnitudes in specific AGN luminosity, we expect to observe a suppression of SFRs (quenched by AGN feedback) at higher specific AGN luminosities, as predicted in simulations (e.g. Di Matteo et al., 2005; Springel et al., 2005; Hopkins et al., 2008; Zubovas & King, 2012; Dubois et al., 2013). Should we observe an enhancement of the SFR at higher specific AGN luminosities, it will suggest a more complex relationship between AGN and star-forming activity than the one proposed in simulations, and it will support many of the observational studies finding that AGNs form a diverse population with somewhat enhanced SFRs compared to the general population (e.g. Barvainis &

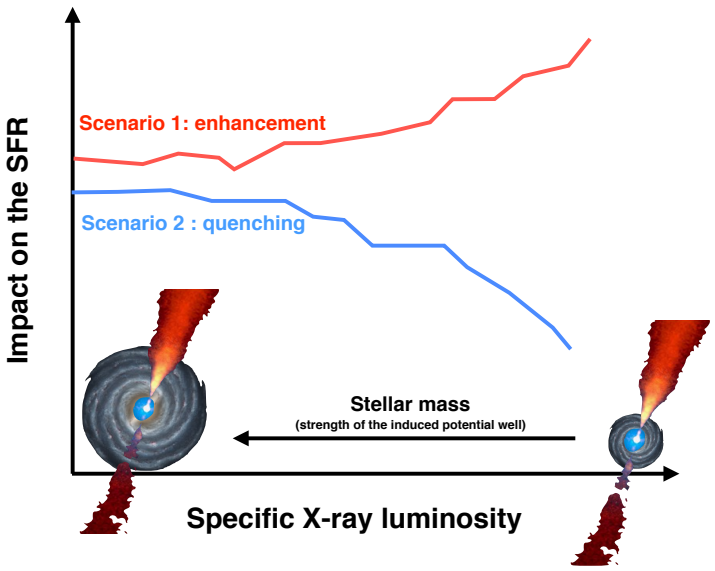

Figure 3.1: Two scenarios for the relationship between the specific X-ray luminosity and the SFR, i.e. enhancement or quenching of SFR at higher specific X-ray luminosities. We also point out in this figure that on average stellar mass decreases with increasing specific X-ray luminosity. The quenching scenario is favoured by simulations.

Ivison 2002; Priddey et al. 2003; Page et al. 2004; Schweitzer et al. 2006; Lutz et al. 2008; Hickox et al. 2009; Silverman et al. 2009; Shao et al. 2010; Bonfield et al. 2011; Santini et al. 2012; Mullaney et al. 2012; Rosario et al. 2012; Rovilos et al. 2012; Harrison et al. 2012; Zinn et al. 2013, although see Page et al. 2012). In figure 3.1 we show a sketch of the two scenarios that we aim to discriminate.

Using rest-frame UV and optical observations to measure the star-forming properties of X-ray AGN hosts, Azadi et al. (2015) recently reported that there is no evidence of a strong correlation (or anti-correlation) between specific AGN luminosity and average SFR, at least up to $z{\sim}1$. Instead, they reported that the fraction of star-forming galaxies increases with increasing specific AGN luminosity, suggesting a change in the underlying SFR distribution. However, Azadi et al. (2015) only probed low-to-moderate redshifts (i.e. $z{<}1$), thus missing the peak epoch of SMBH accretion and SFR densities (i.e. $z{\sim}2$). Furthermore, since Azadi et al. (2015) rely on optical-to-UV photometry to measure SFRs, and because of the potential high contamination at these wavelengths from the AGN, they were unable to consider the most luminous AGNs (i.e. $L_X{>}\ 10^{44}$ erg s^{-1}), which are also more likely to have the highest specific luminosities. Finally, by relying on the optical-to-UV part of the spectrum, Azadi et al. (2015) had to make considerable corrections for dust attenuation. As the problems of both AGN contamination and dust attenuation are minimal

at FIR wavelengths, there is significant scope to build upon the Azadi et al. (2015) study by exploiting data from the ESA Herschel Space Telescope to consider more closely the relationship between SFR and specific X-ray luminosity.

In this chapter we first present the datasets used for this study in § 3.2. We then detail in § 3.3 the data analysis performed on these datasets to extract AGN and host galaxy properties. The main results of this analysis are presented in § 3.4 and the implications of these results are discussed in § 3.5. Finally we conclude in § 3.6. Throughout, we assume a WMAP-7 year cosmology (i.e. $H_0 = 71$ km/s/Mpc, $k = 0.00974$, $\Omega_{\rm m} = 0.266$, $\Omega_\Lambda = 0.734$; Larson et al., 2011). For this chapter, we use a Chabrier (2003) initial mass function (hereafter, IMF) when calculating galaxy stellar masses and SFRs.

3.2 Datasets

Our datasets are extracted from multi-wavelength observations of three extragalactic fields: GOODS-North (hereafter, GN), GOODS-South (hereafter, GS), and the wider but shallower COSMOS fields. This combination allows us to probe modest AGN luminosities (i.e. $L_X \sim 10^{42-43}$ erg s^{-1}; the dominant AGN population in terms of numbers) out to $z \approx 3$, whilst also covering the wide areas needed to include rare AGNs with more extreme specific luminosities (i.e. $L_X/M_* \sim 100\ L_\odot/M_\odot$). A further benefit of using these fields is that they are the most intensely surveyed regions of the sky, with comprehensive multi-wavelength coverage spanning X-ray-to-radio regimes. In this section, we describe the datasets that we use to investigate the relationship between specific AGN luminosity and the star-forming properties of their host galaxies.

3.2.1 X-ray data

We use X-ray luminosities derived from the Chandra observations of our three fields as a proxy for bolometric AGN luminosity (using the average bolometric conversion factor from Vasudevan & Fabian 2007; see § 3.3.1). For COSMOS we use the 1.8 Mega-seconds (hereafter, Ms) Chandra-COSMOS (hereafter, C-COSMOS) survey of Civano et al. (2012) that covers the central 0.9 deg^2 of the COSMOS field (1761 X-ray detections in the 0.5–10 keV band down to limiting depths of $5.7{\times}10^{-16}$ erg cm^{-2} s^{-1}). For GN, we use the 2Ms point-sources catalogue of Alexander et al. (2003) from the Chandra Deep Field North (hereafter, CDFN) survey (503 X-ray detections in the 0.5–8 keV band), while for GS we use the main 4Ms catalogue

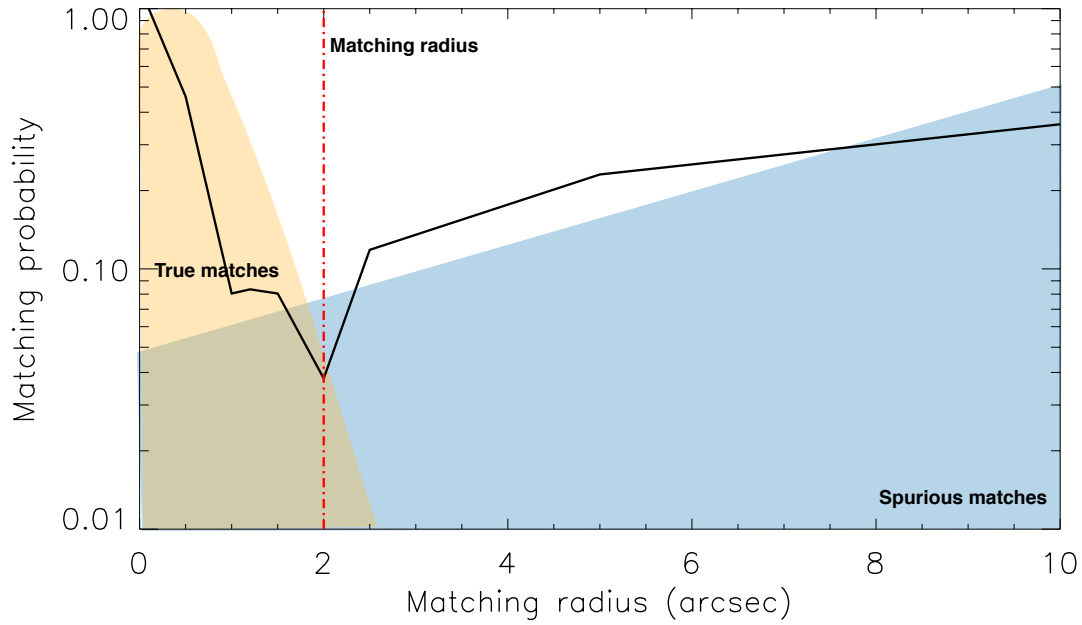

Figure 3.2: Example of a matching fraction of HERSCHEL sources, this case at 24 μm. The black curve shows the probability of matching a source at different radius. The red dashed line indicates the matching radius maximising the number of real matches (expected within the orange area) while minimising the number of spurious ones (expected within the blue area).

of Xue et al. (2011) from the CHANDRA Deep Field South (hereafter, CDFS) survey (740 X-ray detections in the 0.5–10 keV band). Combining catalogues from all three fields gives a total of 3004 X-ray-detected sources, which we refer to as our "X-ray detected" catalogue.

3.2.2 Far-infrared data

As mentioned in Chapter 2, § 2.3, we use the FIR emission of the host galaxy as a tracer of its SFR by using the Kennicutt (1998) relationships to convert FIR luminosities into SFRs. Our FIR data are from instruments on board the HERSCHEL space observatory (Pilbratt et al., 2010). The COSMOS field has been covered by HERSCHEL's PACS instrument (Poglitsch et al., 2010) at 100 μm and 160 μm as part of the PACS Evolutionary Probe (PEP, Lutz et al. 2011) programme. For GN and GS we use the HERSCHEL-PACS data that combine the PEP and the GOODS-HERSCHEL (Elbaz et al., 2011) programmes, and which provide the deepest surveys of these fields at wavelengths of 100 μm and 160 μm (Magnelli et al., 2013). For each field we use the de-blended catalogues based on the positions of SPITZER-MIPS 24 μm prior, which provide 100 μm and 160 μm fluxes for all 24 μm sources, irrespec-

tive of whether they are formally detected at the longer wavelengths. We complement the PACS data with the deep HERSCHEL-SPIRE (Griffin et al., 2010) observations (at 250 μm, 350 μm and 500 μm) of our fields carried out by (1) the HerMES programme for COSMOS and GS (Roseboom et al., 2010; Oliver et al., 2012), and (2) the GOODS-HERSCHEL programme for GN (Elbaz et al., 2011).

For the COSMOS field, the PEP observations cover all of our 1761 X-ray sources. However, as GOODS-HERSCHEL did not cover the entire CDFN and CDFS we only consider X-ray sources with PACS coverage that is over 30 per cent of the maximum value in each field. This results in 365 out of the 503 X-ray detected sources in CDFN, and 410 out of the 740 in CDFS that have HERSCHEL coverage. Thus, of the 3004 X-ray sources in the three fields combined, 2536 are covered by HERSCHEL. These form our "HERSCHEL-covered" sample.

To obtain the 24 μm, 100 μm, and 160 μm flux counterparts for each X-ray source in our HERSCHEL-covered sample, we cross-matched against the HERSCHEL catalogue using a two arc-second matching radius between the X-ray and the 24 μm positions. This radius was chosen to maximise the number of true matches, while minimising the number of spurious ones (see Fig. 3.2 for an example of a matching function). As illustrated in Fig. 3.2, by using the minimum of the matching function (corresponding to two arc-seconds in this case), we expect roughly 92 per cent of our counterparts to be true matches. For SPIRE data (i.e. 250 μm, 350 μm, and 500 μm) in COSMOS we cross-matched against the SPIRE–HERSCHEL catalogue, but based on the 250 μm positions instead (since the 24 μm positions are not provided in this catalogue), using a matching radius of seven arc-seconds between either the previously matched 24 μm positions if detected, or the X-ray positions if undetected at 24 μm and the 250 μm positions. We note that the matching radius increases as we match our X-ray detected sample to longer wavelengths. This is a consequence of having a larger PSF at longer wavelengths (see Fig. 2.1) which increases the uncertainties on the source position at these longer wavelengths, hence broadening the distribution of true matches (see Fig. 3.2 for the distribution of true matches). Therefore, for SPIRE data, we expect a fraction of roughly 85 per cent of true counterparts to our X-ray detected catalogue. For GN, SPIRE fluxes are provided in the table of Elbaz et al. (2011), so are automatically included when we match to the PACS data. For GS we cross-matched against the HERSCHEL catalogue using a matching radius of two arc-seconds again between the X-ray and the 24 μm positions (since provided in the SPIRE catalogue). Out of the 2536 X-ray sources in our HERSCHEL-covered sample, 1178 (i.e. $\sim$ 56 per cent) sources are detected in at least one HERSCHEL band, which we refer as to our "X-ray FIR" catalogue.

3.2.3 Ancillary data

As the primary goal of this study is to measure how the star-forming properties of galaxies relate to the *specific* AGN luminosity (i.e. luminosity per unit host stellar mass), it is crucial that we have accurate host stellar masses for the galaxies in our sample. The most commonly used means to derive galaxy stellar masses is through fits to their broad-band spectral energy distributions (SEDs). However, since in our case the SED can be heavily contaminated by the light from the AGN, we used a multi-component SED fitting code (i.e. CIGALE, see § 3.3.2) to account for this. As demonstrated in Ciesla et al. (2015), CIGALE requires UV to mid-IR photometry in order to reliably extract the stellar mass of AGN host galaxies.

Since needed to measure the stellar masses, we extend our datasets to include data from the UV, the optical and the near-infrared (NIR) part of the spectrum. For the COSMOS field, the UV-to-NIR data (i.e. u^*, $B_{\rm J}$, $V_{\rm J}$, *ACS606,* r^+,i^+, *ACS814W, z+, UVISTA-Y, WFC3-F125W, UVISTA-J, WFC3-F140W, UVISTA-H, UVISTA-*$K_{\rm S}$*, IRAC1, IRAC2, IRAC3*, and *IRAC4* bands) are from a combination of the Ilbert et al. (2013) catalogue and, for the central region covered by the CANDELS survey, the 3dHST catalogue compilation of Skelton et al. (2014). For CDFN and CDFS, we use the 3dHST catalogue of Skelton et al. (2014), that also covers the UV to the NIR wavelengths (i.e. *U, B, V, ACS606, R, i, z, WFC3-F125W, J, WFC3-F140W, H,* $K_{\rm S}$*, IRAC1, IRAC2, IRAC3*, and *IRAC4* bands). We cross-matched these catalogues with our Herschel-covered sample using a radius of two arc-seconds on the 24 μm positions when available and the X-ray positions otherwise. To ensure a robust mass measurement we derive stellar masses only for sources with enough broad band photometry coverage (see left column of Fig. 11 of Ciesla et al. 2015 that shows the accuracy on the stellar mass measurement depending on the available wavelength coverage). As a consequence, we are able to derive stellar masses for 1852 sources out of the 2536 (i.e. 73 per cent) sources in our Herschel-covered sample.

3.3 Data analysis

Our main focus for this chapter is to investigate the SFR of AGN host galaxies across several orders of magnitudes at specific AGN luminosities. As stressed in Chapter 2, § 2.3, it is crucial that we disentangle the AGN emission from that of the host galaxy. Throughout this section, we first describe in § 3.3.1 how we derive the intrinsic X-ray luminosities from the observed 2-10 keV ones. We then show how we measure the host stellar masses in § 3.3.2, accounting for AGN contamina-

tion. Furthermore, as explained in Chapter 2, we perform stacking to incorporate HERSCHEL-undetected sources into our analysis and multi-model inferences to accurately extract the SFRs. In § 3.3.3 we show how we apply theses techniques to our science datasets. To ensure that our full analysis is not dominated by the way we select our sources, we use a mass-matched sample for which we derive similar properties. This mass-matched sample is presented in § 3.3.4.

3.3.1 AGN properties

Intrinsic X-ray luminosities

One of the most direct ways to quantify the power of an AGN is to derive its absorption-corrected (i.e. intrinsic) X-ray luminosity since it is arising from the accretion process into the SMBH (see Chapter 1, § 1.2). For COSMOS and GS we obtained the 2–10 keV intrinsic X-ray luminosities by cross-matching our HERSCHEL-covered sample with the catalogue of Brightman et al. (2014) which provides this information for respectively 100 per cent and ≈70 per cent of our sources in these two fields. To ensure consistency throughout, we also adopted the redshifts provided in Brightman et al. (2014) for these matched sources (of which ≈60 per cent are spectroscopic redshifts). For those sources that are not covered by Brightman et al. (2014), we derived an analytic solution to convert observed X-ray fluxes to intrinsic X-ray luminosities. We use a second-order polynomial to relate the ratio of un-obscured to obscured fluxes (i.e. the flux that would be observed if there were no obscuring material relative to the actual observed flux, or $F_{\rm unobs}/F_{\rm obs}$) to the band ratios (i.e. Hard X-ray band/Soft X-ray band in counts) and the redshifts (z) of X-ray sources in Brightman et al. (2014):

$$\log_{10}\left(\frac{\mathrm{F_{unobs}}}{\mathrm{F_{obs}}}\right) = \sum_{\mathrm{i}=0}^{2} \alpha_{\mathrm{i}} \times \log_{10}\left(\frac{\text{Hard band}}{\text{Soft band}}\right)^{\mathrm{i}} + \sum_{\mathrm{i}=0}^{2} \beta_{\mathrm{i}} \times \mathrm{z}^{\mathrm{i}} \qquad (3.1)$$

where $\alpha_{\rm i}$ and $\beta_{\rm i}$ are polynomial coefficients. The best calibration is given for $\alpha_0 = 0.23$, $\alpha_1 = 0.61$, $\alpha_2 = 0.041$, $\beta_0 = 0.01$, $\beta_1 = -0.11$, and $\beta_2 = -0.02$. In Fig. 3.3 we show the goodness of the analytical solution for AGNs detected in COSMOS and where $L_{\rm B14}$ is provided. We find that the same coefficients reproduce the intrinsic luminosities reported in Brightman et al. (2014) in both GS and COSMOS with a median of $L_{\rm Poly}/L_{\rm B14} = 1.05$ (where $L_{\rm B14}$ are the intrinsic X-ray luminosities reported in Brightman et al. 2014) and a standard deviation of $\sigma_{L_{\rm Poly}/L_{\rm B14}} = 0.51$. The large standard deviation is increased by the few outliers (see Fig. 3.3) and we find that 95 percent of the sources have similar X-ray intrinsic luminosities within 33 per cent.

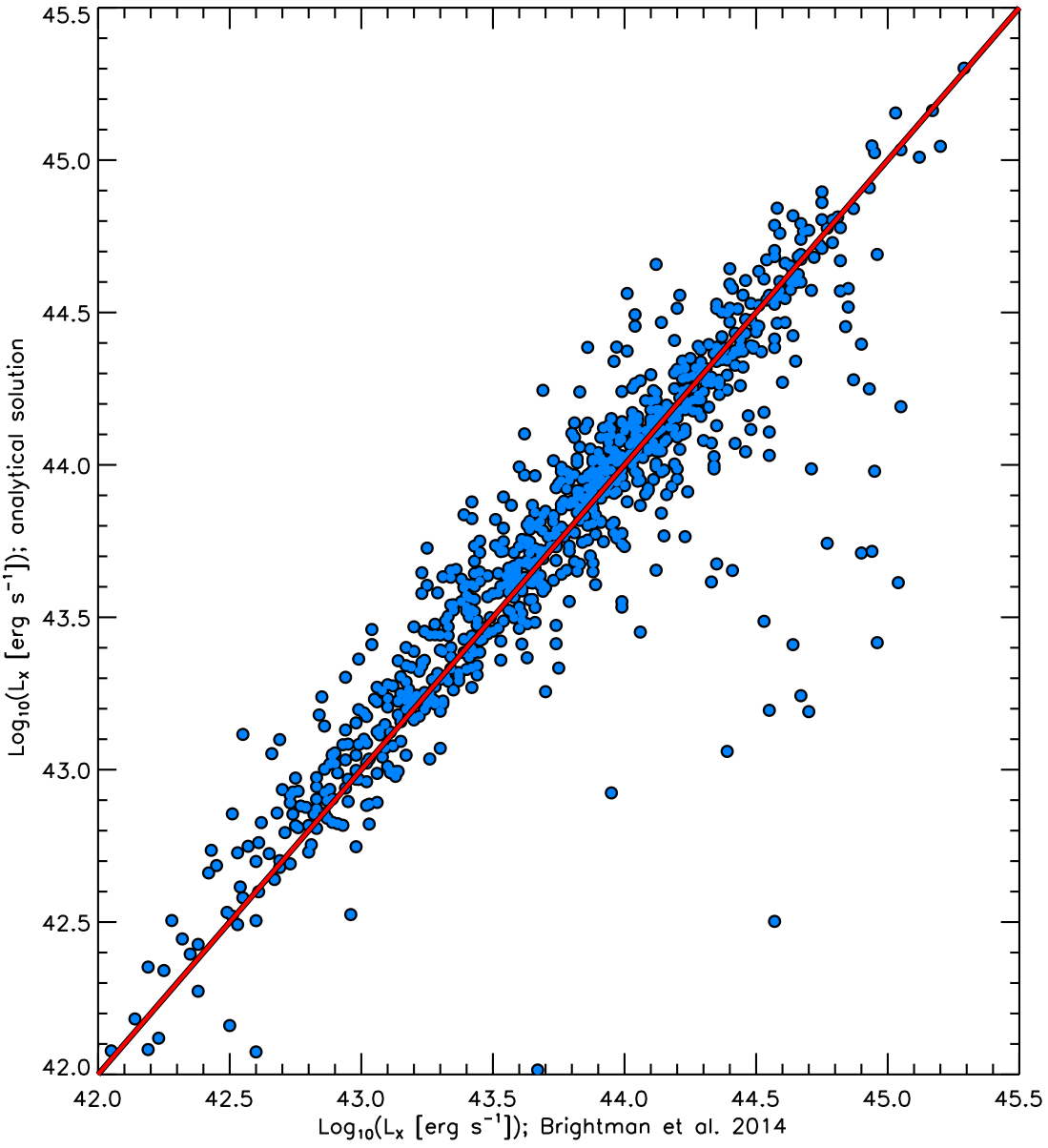

Figure 3.3: Comparison of the intrinsic X-ray luminosities derived using our analytical solution and those of Brightman et al. (2014) for the COSMOS field. The red line indicates the 1:1 relationship. We find a good agreement between the two luminosities, validating Eq. 3.1 to derive intrinsic X-ray luminosities on our full sample of AGNs.

Using Eq. 3.1 together with the redshifts from Bauer et al. (2004) for the sources in GN, and the redshifts from Hsu et al. (2014) to complete the ≈30 per cent of the GS sources that are not covered by Brightman et al. (2014), we derive intrinsic 2–10 keV luminosities for all of the 2536 sources in our HERSCHEL-covered sample.

To minimise contamination from non-AGN, we only retain sources with intrinsic X-ray luminosity greater than 10^{42} erg s^{-1}. This has no impact on our results, as we are primarily interested in high specific luminosity AGNs. Thus, we expect little contamination (i.e. typically less than 20 per cent for galaxies with $M_*\gtrsim 10^{10.5}\ M_\odot$ at $z\gtrsim$2; Aird et al. 2017b) from the host galaxy to the measured X-ray flux. Among our 2536 HERSCHEL-covered sample, 1980 are selected as true AGNs, and are referred to as our "AGN sample".

Specific L_X as a tracer of Eddington ratio

In this chapter, we wish to measure the star-forming properties of AGN hosts as a function of specific AGN luminosity (i.e. AGN luminosity relative to the host stellar mass). For convenience, we express the specific AGN luminosity in terms of the more familiar Eddington ratio of the AGN ($\lambda_{\rm Edd}$), i.e. the ratio of AGN bolometric luminosity ($L_{\rm AGN}$) to the Eddington luminosity of its SMBH ($L_{\rm Edd}$). To convert 2-10 keV intrinsic X-ray luminosity to $L_{\rm AGN}$ we use a bolometric correction factor of 22.4 which is the median value found in Vasudevan & Fabian (2007; based on a sample of local AGN with L_X= 10^{41-46}erg s^{-1}). As $\lambda_{\rm Edd}$ is to be used merely as a guide, we prefer to use a single bolometric correction factor over more complicated luminosity-dependent corrections (e.g. Hopkins et al., 2007). All our analyses are performed on the basis of specific X-ray luminosities, rather than $\lambda_{\rm Edd}$, such that the choice of bolometric correction factor has no effect on our results. The Eddington luminosity, $L_{\rm Edd}$, is defined as the theoritical luminosity a SMBH of mass M cannot exceed. Beyond this $L_{\rm Edd}$, the force of radiation (i.e. repulsive force) overcomes that of the gravity (i.e. attractive force), as such the in-falling material is pushed away and the accretion is stopped. To derive $L_{\rm Edd}$, we equate the force of radiation ($F_{\rm rad}$) to that of the gravity ($F_{\rm grav}$) for a SMBH of mass $M_{\rm BH}$ on a cloud of gas (or anything else falling into the SMBH) with mass m. When assuming spherical symmetry, we have that,

$$F_{\rm grav} \equiv \frac{GM_{\rm BH}m}{R^2} = \frac{L}{4\pi R^2 c} \times \kappa m \equiv F_{\rm rad}, \tag{3.2}$$

where R is the distance between the SMBH and the cloud, κ is the opacity of the cloud (i.e. cross-section area per unit mass), L is the luminosity, and G is the gravitational

constant. For ionised hydrogen, interactions are essentially between the photons and the free particles (i.e. Thomson scattering) and $\kappa = \sigma_{\rm T}/m_{\rm p}$, where $\sigma_{\rm T}$ is the Thomson scattering cross-section and $m_{\rm p}$ is the mass of the proton. Therefore, replacing this into Eq. 3.2 and rearranging, we have that,

$$L_{\rm Edd} = \frac{4\pi c G m_{\rm p}}{\sigma_{\rm T}} M_{\rm BH} = 1.26 \times 10^{38} \left(\frac{M_{\rm BH}}{M_{\odot}}\right) {\rm erg\ s^{-1}}. \tag{3.3}$$

Furthermore, we can use the relationship between the SMBH masses and the host galaxy stellar masses (M_*, see § 3.3.2 for the derivation of the stellar masses for our sample of AGNs), assuming a constant of proportionality of 0.002 (Marconi & Hunt, 2003) to transform $M_{\rm BH}$ into M_* in Eq. 3.3. Finally combining these definitions for $L_{\rm AGN}$ and $L_{\rm Edd}$, we have that the Eddington ratio is defined as,

$$\lambda_{\rm Edd} = \frac{L_{\rm AGN}}{L_{\rm Edd}} = \frac{22.4\ L_X}{1.26 \times 10^{38}\ {\rm erg\ s^{-1}} \times 0.002 \frac{M_*}{M_{\odot}}}. \tag{3.4}$$

The distribution of our $\lambda_{\rm Edd}$ sample with the redshift is shown in Fig. 3.4, with the sources that are HERSCHEL detected (i.e. at least in one of the HERSCHEL band) shown as red points. We reiterate that we convert specific X-ray luminosities into Eddington ratios purely for convenience because of its greater familiarity, and $\lambda_{\rm Edd}$ should not be regarded as a true measure of the Eddington ratio of the SMBH (which could explain the large numbers of AGNs with $\log(\lambda_{\rm Edd}) > 0$ in Fig. 3.4).

3.3.2 Host galaxy stellar masses

Our main goal is to study how star-forming properties of AGN hosts change as a function of specific AGN luminosity – or Eddington ratio. As we define specific luminosity as luminosity *per unit host stellar mass*, it is crucial that we accurately derive host stellar masses. In the presence of an AGN the optical to NIR wavelengths – from which stellar masses are normally derived – can suffer contamination by light from the AGN (e.g. Stern et al., 2005; Donley et al., 2012). To account for this contamination we used the multi-component SED fitting code CIGALE [1] that includes an AGN component to the fit (Burgarella et al., 2015; Ciesla et al., 2015). Recently, using models, Ciesla et al. (2015) demonstrated that CIGALE is able to reproduce the stellar masses of mock galaxies (generated using the GALFORM code; Cole et al. 2000) to within 40 per cent for galaxies where up to 70 per cent of the optical to NIR emission is due to the AGN (only ≈ 1 per cent of our AGNs are above an AGN contamination of 70 per cent at those wavelengths).

[1] CIGALE is publicly available at `http://cigale.lam.fr/`

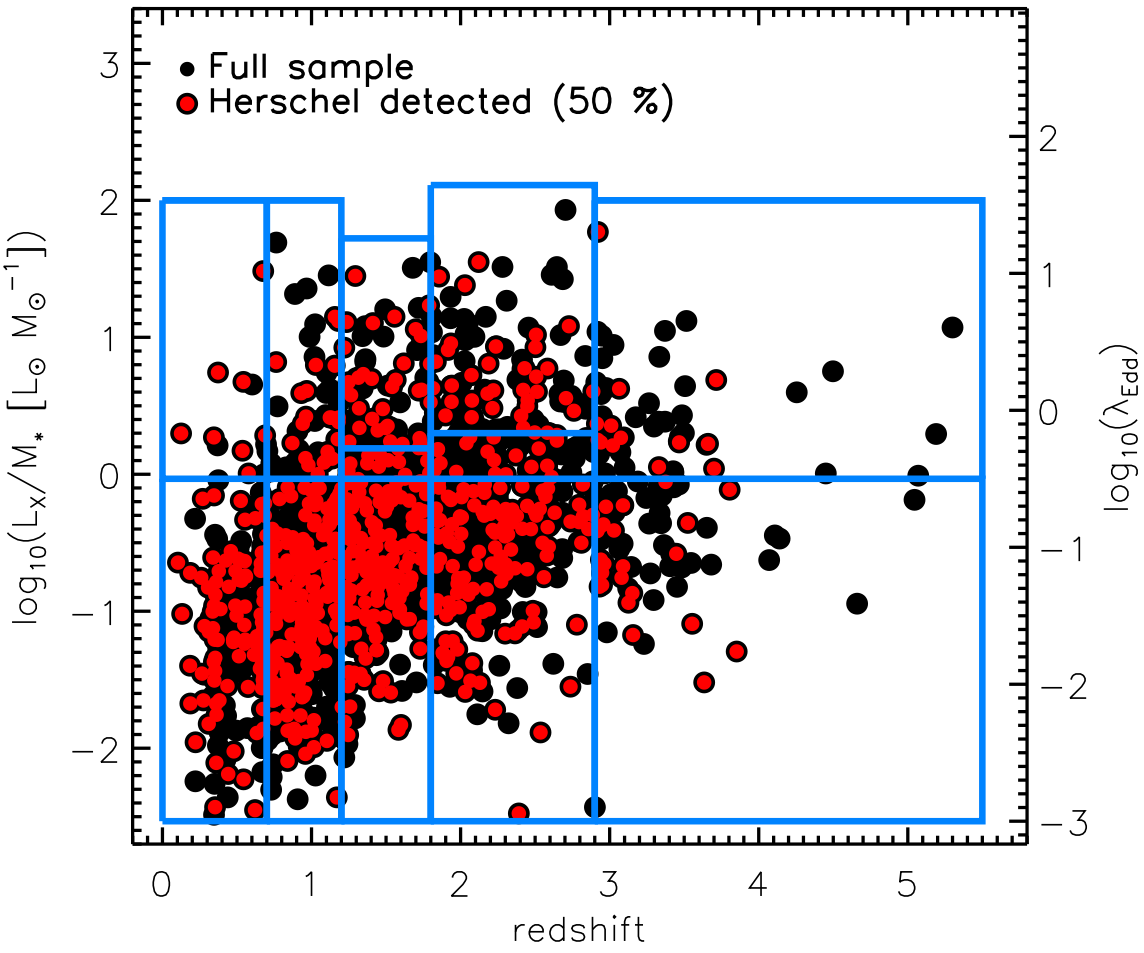

Figure 3.4: Distribution of our full AGN sample across redshift and $\lambda_{\rm Edd}$. Red circles indicate sources that are detected in at least one of the HERSCHEL band (i.e. $\approx$ 50 per cent). The blue rectangles indicate the position of each of our bin for which we measured average AGN and galaxy properties (i.e. performing stacking to include HERSCHEL-undetected sources).

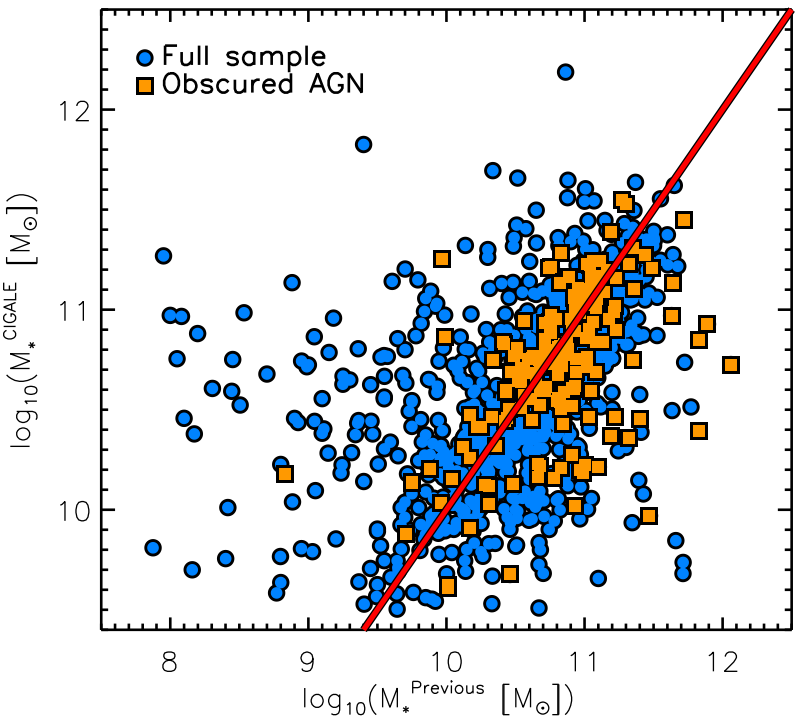

Figure 3.5: Comparison of stellar masses derived using CIGALE to those of Ilbert et al. (2013) for COSMOS and Elbaz et al. (2011) for GN and GS. The blue circles show the full sample and the orange squares show that of obscured AGNs only. The red line shows the 1:1 relationship between the two.

The parameters that control CIGALE's fitting process were selected based on those that Ciesla et al. (2015) found best reproduced the stellar masses of their mock galaxy samples (see Table 3.1). Ciesla et al. (2015) found that the uncertainty on stellar mass increases with decreasing host stellar mass due to a combination of faintness and possibly higher relative AGN contributions. Therefore, we only select AGNs with host galaxy stellar masses satisfying $M_* > 10^{9.5}$ $M_\odot$. Within our AGN sample of 1980 sources, 1620 satisfy this criterion. Although the level of AGN contamination spans the range 5–85 per cent, 95 per cent of the sample have AGN contamination of less than 50 per cent (within which Ciesla et al., 2015, report that the uncertainty on the stellar mass is less than 20 per cent). We also note that the 5 per cent of AGNs in our sample with AGN contamination above 50 per cent are distributed across our $\lambda_{\rm Edd}$ range and thus do not adversely effect one region of parameter space relative to another.

As a consistency check, we compared the AGN host stellar masses derived using CIGALE ($M_*^{\rm CIGALE}$) to those reported in Ilbert et al. (2013) for COSMOS and in Elbaz et al. (2011) for GN and GS ($M_*^{\rm Previous}$). Both these other studies take steps

to account for AGN contamination, but use more simplistic approaches than our SED-fitting based method. Specifically, for galaxies whose SPITZER-IRAC bands are AGN dominated (flagged by being characterised by a power-law; i.e. Donley et al., 2012), Ilbert et al. (2013) ignore these bands when deriving stellar masses, whereas Elbaz et al. (2011) remove them from their sample entirely. Thus, by comparing our masses with those of Ilbert et al. (2013), we obtain a measure of the discrepancy between different approaches of accounting for AGN contamination when calculating host stellar masses. This comparison is shown in Fig. 3.5 with filled blue circles. The standard deviation of the $\log(M_{*}^{\rm CIGALE}/M_{*}^{\rm Previous})$ ratios of the full sample is 0.5 dex and there is a systematic offset of 0.31 dex (i.e. a factor of ~ 2). However, we also separate obscured (type 2) and un-obscured (type 1) AGNs in this Figure using optical classifications for GN and GS. When we do this, we find a smaller standard deviation and systematic offset (i.e. 0.4 dex and 0.09 dex, respectively) for obscured AGNs. This suggests that the offset in the full sample arises from our different treatments of AGN contamination, which will be stronger for un-obscured AGNs. Therefore, we do not correct for any offset, believing that our treatment of AGN contamination by including AGN templates in our SED fits is more robust than those used by Elbaz et al. (2011) and Ilbert et al. (2013), i.e. studies where AGN were not the primary focus.

3.3.3 Host galaxy star formation rates

As detailed in Chapter 2, § 2.3 we use the integrated 8–1000 μm emission (i.e. $L_{\rm IR}$) of the AGN host galaxies as a measure of their SFRs (Kennicutt, 1998), performing multi-component SED fitting to account for any AGN contamination to $L_{\rm IR}$. Furthermore, we also mentioned that despite using the deepest FIR data available for our fields, only ≈20 per cent of our AGN sample is detected in enough HERSCHEL bands to perform SED fitting (i.e. in at least three bands; see § 3.2.2). As described in Chapter 2, § 2.2, to incorporate the remaining 80 per cent of sources, we perform stacking at IR wavelengths (i.e. 24 μm, 100 μm, 160 μm, 250 μm, 350 μm, and 500 μm) to derive average SEDs that include the HERSCHEL-undetected sources.

Prior to stacking, we split our sample into bins of specific AGN luminosity and redshift (see Table 3.2). This is to enable us to determine how the average star-forming properties of the host galaxies change with these parameters. To minimise shot noise we aim to have over 400 AGNs in each of our redshift bins. However, this is impossible for our lowest and highest redshift bins, but which still contain over 100 AGNs (i.e. still a statistically significant number). Within each of our

Table 3.1: Modules and parameter ranges used with CIGALE to derive the stellar masses of our AGN host galaxies.

Parameter	Value
CIGALE modules	
Star formation history	Delayed
Stellar population synthesis model	Bruzual & Charlot (2003)
Initial mass function	Chabrier (2003)
Attenuation law	Calzetti (2001)
Dust emission model	Dale & Helou (2002)
AGN	Fritz et al. (2006)
Range of parameters	
Stellar population synthesis	
e-folding time of the main stellar population (Myr)	100, 1000, 3000, 10000, 10^{10}
Age of the oldest stars in the galaxy (Gyr)	0.1, 1, 2, 3, 4, 5, 6, 7, 8, 9, 10, 11
Metallicity	0.02
Age separation between the young and the old populations (Myr)	10
Dust attenuation	
E(B-V)* for the young population	0.01, 0.05, 0.1, 0.2, 0.3, 0.4, 0.5, 0.6, 0.7, 0.8, 0.9, 1., 1.1, 1.2, 1.4
E(B-V)* reduction factor between the old and the young populations	0.44
Central wavelength of the UV bump (nm)	217.5
Width of the UV bump (nm)	35
AGN	
Ratio of dust torus radii	60
Optical depth at 9.7 microns	1.0, 6.0
Beta	-0.5
Gamma	0
Full opening angle of the dust torus (degrees)	100
Angle between equatorial axis and line of sight (degrees)	0, 90
Fraction of $L_{\rm IR}$ due to the AGN	0, 0.05, 0.1, 0.2, 0.3, 0.4, 0.5, 0.7, 0.9

Table 3.2: Description of our redshift and $\lambda_{\rm Edd}$ bins.

(1) Index	(2) Bin description		(3) N	(4) z	(5) M_* ($\times 10^{10}$ $M_\odot$)	(6) $\lambda_{\rm Edd}$	(7) L_X/M_* ($L_\odot$ M_*^{-1})
	All		1620	1.57	4.16	0.10	0.70
1	z = 0–0.7	$\log(\lambda_{\rm Edd})$<-0.5	170	0.50	4.68±0.05	0.05±0.01	0.13±0.01
2		$\log(\lambda_{\rm Edd})$>-0.5	11	0.51	2.17±0.13	1.64±0.01	4.81±0.29
3	z = 0.7–1.2	$\log(\lambda_{\rm Edd})$<-0.5	398	0.94	6.22±0.04	0.06±0.01	0.18±0.01
4		$\log(\lambda_{\rm Edd})$>-0.5	47	1.00	3.12±0.09	1.97±0.07	5.76±0.21
5	z = 1.2–1.8	$\log(\lambda_{\rm Edd})$<-0.5	323	1.47	6.47±0.05	0.11±0.01	0.31±0.01
6		-0.5<$\log(\lambda_{\rm Edd})$<-0.28	47	1.48	4.63±0.11	0.41±0.01	1.20±0.04
7		$\log(\lambda_{\rm Edd})$>-0.28	67	1.51	2.68±0.06	2.18±0.10	6.38±0.28
8	z = 1.8–2.9	$\log(\lambda_{\rm Edd})$<-0.5	285	2.22	9.64±0.07	0.13±0.01	0.37±0.01
9		-0.5<$\log(\lambda_{\rm Edd})$<-0.17	74	2.27	4.99±0.14	0.47±0.01	1.37±0.04
10		$\log(\lambda_{\rm Edd})$>-0.17	84	2.33	2.62±0.08	2.95±0.12	8.63±0.34
11	z>2.9	$\log(\lambda_{\rm Edd})$<-0.5	69	3.29	14.3±0.17	0.12±0.01	0.33±0.01
12		$\log(\lambda_{\rm Edd})$>-0.5	45	3.36	4.66±0.13	1.70±0.08	3.96±0.22

Notes: (1) Bin index. (2) redshift and $\lambda_{\rm Edd}$ ranges probed in the bin. (3) Number of AGNs. (4) Average redshift. (5) Average stellar mass. (6) Average Eddington ratio. (7) Corresponding average specific X-ray luminosity.

redshift bins, we also bin according to Eddington ratio (or, in reality, specific X-ray luminosity). In each redshift bin, all AGNs with -3.0<log($\lambda_{\rm Edd}$)<-0.5 are binned together to represent the low $\lambda_{\rm Edd}$ regime. We group these together because this low $\lambda_{\rm Edd}$ regime has already been explored in Azadi et al. (2015), at least at $z < 1$. This low $\lambda_{\rm Edd}$ bin includes most of our X-ray selected AGNs at all redshifts (i.e. 95 per cent, 91 per cent, 78 per cent, 67 per cent and 60 per cent for $z = 0 - 0.7, 0.7$-$-1.2, 1.2-1.8, 1.8-2.9$, and $z > 2.9$, respectively). The high Eddington ratio regime (i.e. log($\lambda_{\rm Edd}$) > -0.5) is then split into one or two bins, depending on the number of AGNs in each redshift bin (i.e. the two redshift bins containing over 100 AGNs with log($\lambda_{\rm Edd}$) >-0.5, i.e. z = 1.2 – 1.8 and 1.8 – 2.9, have two high Eddington ratio bins). Our various bin boundaries are shown in Fig. 3.4 and summarised in Table 3.2. We perform the stacking on each of our redshift and $\lambda_{\rm Edd}$ bins.

The average SFR in each redshift and $\lambda_{\rm Edd}$ bin is calculated from the stacked SEDs using fits that involves various models (including an AGN component when necessary) and performing model inferences to estimate the best average SFR (see Chapter 2, § 2.3 for details on our stacking and model inference method). The uncertainties on average SFRs are calculated by adopting a Monte Carlo approach, i.e. adding Gaussian noise to the stacked fluxes (according to the size of uncertainty on the fluxes) and re-performing the SED fits. Average SFRs and their associated errors are given in the column 2 of the Table 3.3.

When using FIR wavelengths to derive SFRs, we assume that the dust re-processes all the UV at the FIR wavelengths. However, a non-negligible amount of UV light could also be directly emitted (i.e. not re-processed by dust), thus possibly missing a fraction of the total SFR when using the re-processed FIR emission of the galaxy only. To estimate this direct UV component ($L_{\rm UV}$) emitted by our AGN host galaxies in each stack, we use the average relationship between the attenuation (i.e. $L_{\rm IR}/L_{\rm UV}$) and the stellar mass reported in Heinis et al. (2014). $L_{\rm UV}$ is then converted into $\rm SFR_{UV}$ using the Kennicutt (1998) relation (modified for a Chabrier 2003 IMF) and added to the $\rm SFR_{IR}$ to give the total SFR of the galaxy. Taking this approach, we find that the UV component represents only between 1-to-10 per cent of the total SFR, depending on the average stellar mass of the bin. In what follows, all the SFRs are the total SFRs (i.e. $\rm SFR_{IR} + SFR_{UV}$).

Finally, we also verified that any contamination to the X-ray luminosities from the host galaxies is negligible; by using Eq. 15 of Ranalli et al. (2003) to calculate the 2–10 keV flux arising from star-formation in the host galaxy in each of our bin we find a contamination which is less than 1 per cent.

Table 3.3: Average SFRs, normalised SFRs and minimum and maximum fractions of starbursts in each of our redshift and $\lambda_{\rm Edd}$ bins.

(1)	(2)	(3)	(4)
Index	SFR ($M_\odot$ yr^{-1})	SFR/SFR$_{\rm MS}$	Fraction[minimum - maximum](per cent)
1	16.73±2.30	0.43±0.06	2 – 3
2	22.67±10.2	1.07±0.54	8 –8
3	27.61±3.71	0.36±0.05	1 – 6
4	26.46±9.25	0.64±0.23	33 – 10
5	73.50±13.6	0.61±0.12	6 – 29
6	42.98±20.2	0.58±0.28	6 – 33
7	69.31±20.9	1.25±0.40	14 – 66
8	108.3±23.9	0.45±0.10	3 – 50
9	66.28±23.8	0.52±0.19	7 – 60
10	134.4±29.1	2.30±0.53	10 – 84
11	255.6±115.0	0.63±0.29	–
12	71.10±46.9	0.35±0.23	–

Notes: (1) Bin index (as in Column 1 of Table 3.2). (2) Average SFR measured after removing the AGN contamination. (3) Normalised average SFR accounting for the stellar mass bias.(4) Minimum and maximum fraction of AGN host that are starburst.

3.3.4 Control sample of non-AGN galaxies

To explore the dependence of star formation on the specific X-ray luminosity of AGNs, and how this may have evolved with redshift, we bin our sample in terms of these parameters (see § 3.3.3). This results in the AGN hosts in each of our bins to follow a different stellar mass distribution as shown in Fig. 3.6. We note that AGNs with low $\lambda_{\rm Edd}$ will tend to have higher stellar masses compared to the high $\lambda_{\rm Edd}$ AGNs. This results from using an X-ray flux limited sample of AGNs. With SFR related to stellar mass via the galaxy main sequence (MS; e.g. Salim et al., 2007; Daddi et al., 2007; Rodighiero et al., 2011; Elbaz et al., 2011; Sargent et al., 2012; Schreiber et al., 2015), this change in average mass from bin-to-bin leads to a change in SFR that could be misinterpreted as being related to AGN-feedback (see Stanley et al., 2017). Therefore it is important to take into account any differences in the stellar mass distributions of AGNs and MS galaxies when comparing the galaxy star-forming properties between bins.

To account for the different mass distributions across our redshift and Eddington ratio bins, we calculate the difference between the measured average SFR of the AGNs in each bin and the average the sample would have if all the host galaxies lay on the MS. As mentioned in Chapter 1, § 1.3.2, the choice of the control sample of non-AGN galaxies is crucial and can lead to very different conclusions. Ideally, we would use a large sample of mass-matched non-AGN galaxies that belongs to the MS. However, because luminous AGNs (i.e. of the type explored here) tend to reside in higher mass galaxies (e.g. Dunlop et al., 2003; Kauffmann et al., 2003; Best et al., 2005; Aird et al., 2012), a sufficiently large enough sample of real high mass star-forming galaxies with the same level of Herschel coverage does not exist. Instead, following an updated model outlined first in Bernhard et al. (2014) we generate a population of 25,002,047[2] mock star-forming galaxies (see Chapter 5, §5.3 for details on the updated model). This sample of mock galaxies has exactly the same SFR distribution as a sample of real MS galaxies, but is significantly larger than any observed ones. Thus, for each of our AGN, we can match five mock galaxies with the same stellar mass and redshift (to within Δz=0.1 and $\Delta\log(M)$=0.005). We then calculate the mean SFR of the mock sample in each of our bins, with the uncertainty on the mean calculated by randomly re-sampling one third (i.e. to mimic the bootstrapping approach used for our data) of the mock population 100 times and measuring the spread of resulting distributions of means. The dotted histograms in Fig. 3.6 show the corresponding mass-matched sample for each of our redshift and $\lambda_{\rm Edd}$ bins.

[2]The model is defined by the volume within which the generated mock galaxies are placed (i.e. a 50 square degrees field out to redshift 3 in this case), hence the odd number of mock galaxies.

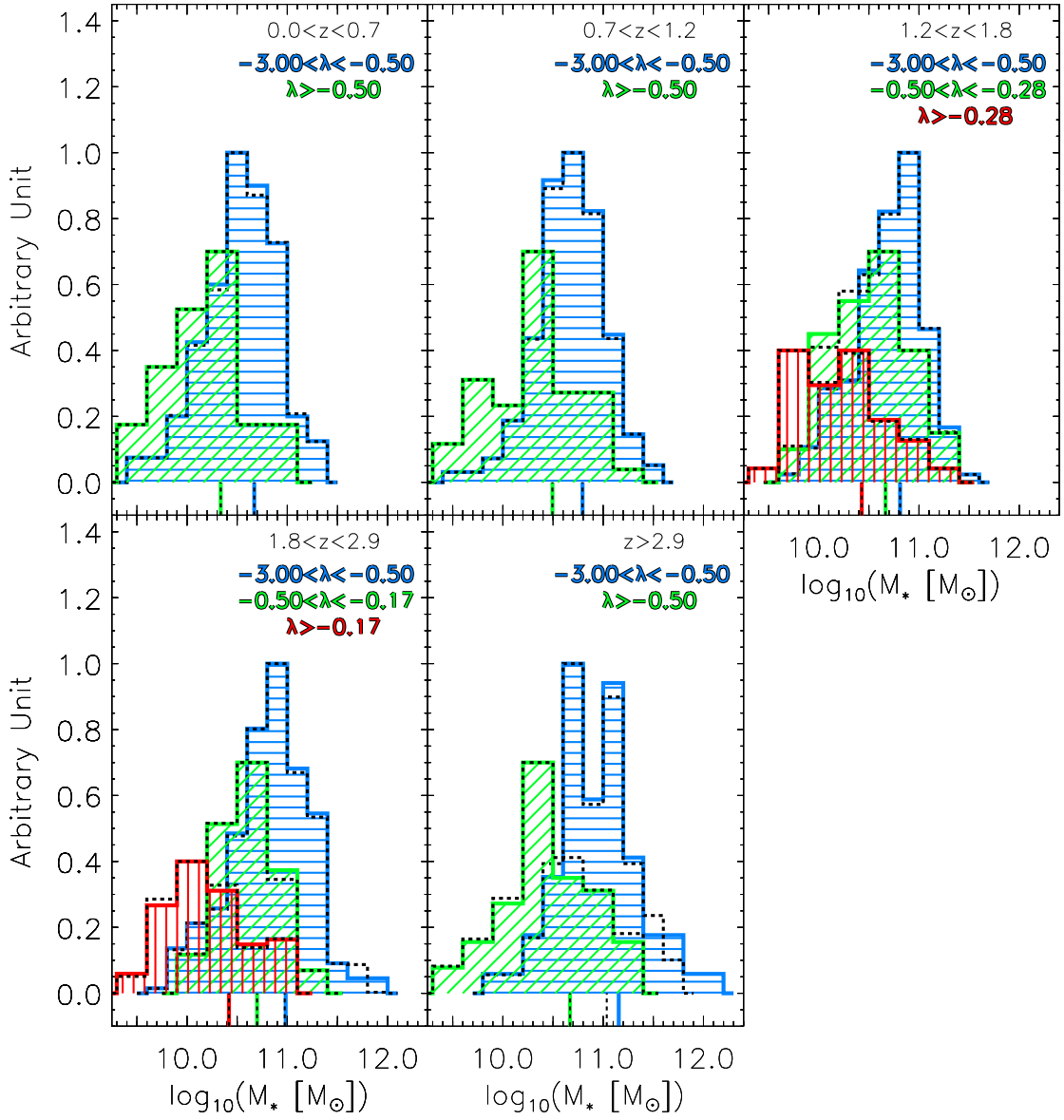

Figure 3.6: Stellar mass distributions of the full AGN sample and of the mass-matched sample in each of our bins. Each panel corresponds to a different redshift bin, within which each coloured-hatched histogram shows the AGN host stellar mass distribution for each $\lambda_{\rm Edd}$ bin (see keys). Black-dashed histogram shows that of the mass-matched sample. The tick mark underneath each histogram indicates the average stellar mass of the bin. The coloured tick marks are for the AGN host sample and the black-dashed tick marks are for that of the mass matched sample.

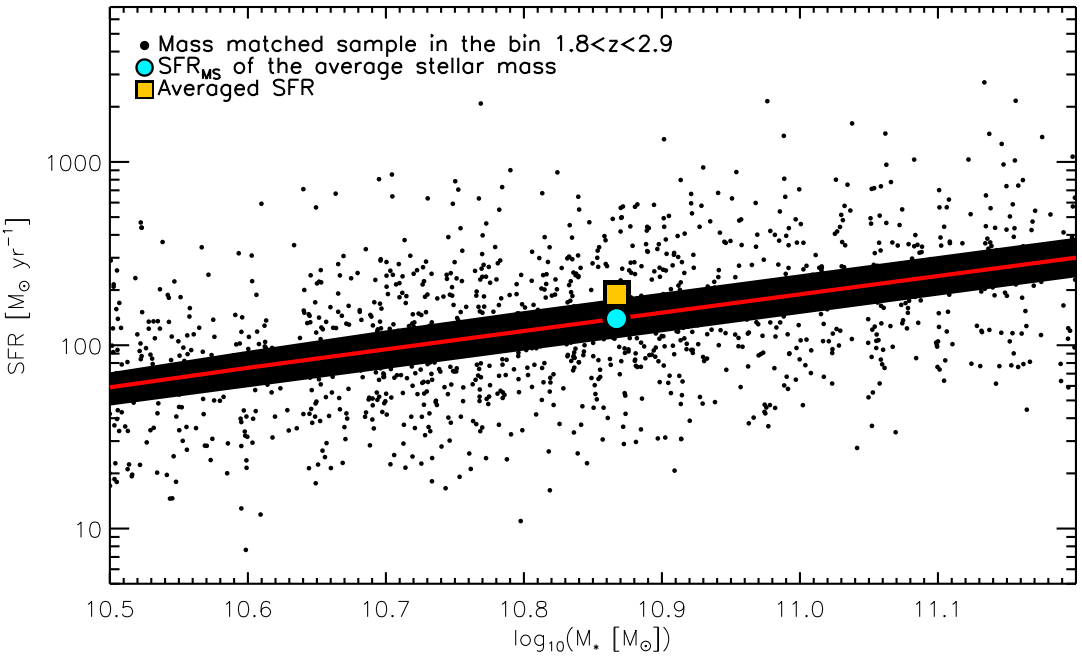

Figure 3.7: SFR versus stellar mass for the mass-matched sample in the $1.8<z<2.9$ bin. The black dots show the individual mock galaxy SFRs while the orange square shows the average of these. The average MS is shown by a red line and the black area illustrates its evolution from z=1.8 to z=2.9. The blue circle shows averaged SFR that corresponds to the average stellar mass in the bin (i.e. not using a mass-matched galaxy for each AGN host). We find that the latter is a factor of ≈1.5 below that calculated from using a mass-matched sample.

The benefits of using a mass-matched sample over simply assuming the average stellar mass of the observed AGNs to calculate the average MS SFR is demonstrated in Fig. 3.7 for the bin $1.8 < z < 2.9$. Here, it is clear that simply taking the average stellar mass and converting that to an average MS SFR (using Eq. 9 in Schreiber et al. 2015) results in an average SFR that is a factor of ≈1.5 below that calculated from using a mass-matched sample. This is a result of the asymmetrical distribution of specific SFR (i.e. SFR divided by the stellar mass), with the few outliers (i.e. starburst galaxies) boosting the true average SFR compared to that of the MS.

3.4 Results

In the previous sections, we described how we arrived at our final sample of 1620 AGNs with Herschel coverage and reliable host stellar masses, and how we measured the average SFRs of their host galaxies, employing stacking to include Herschel-undetected AGN hosts. In this section, we describe how we used this

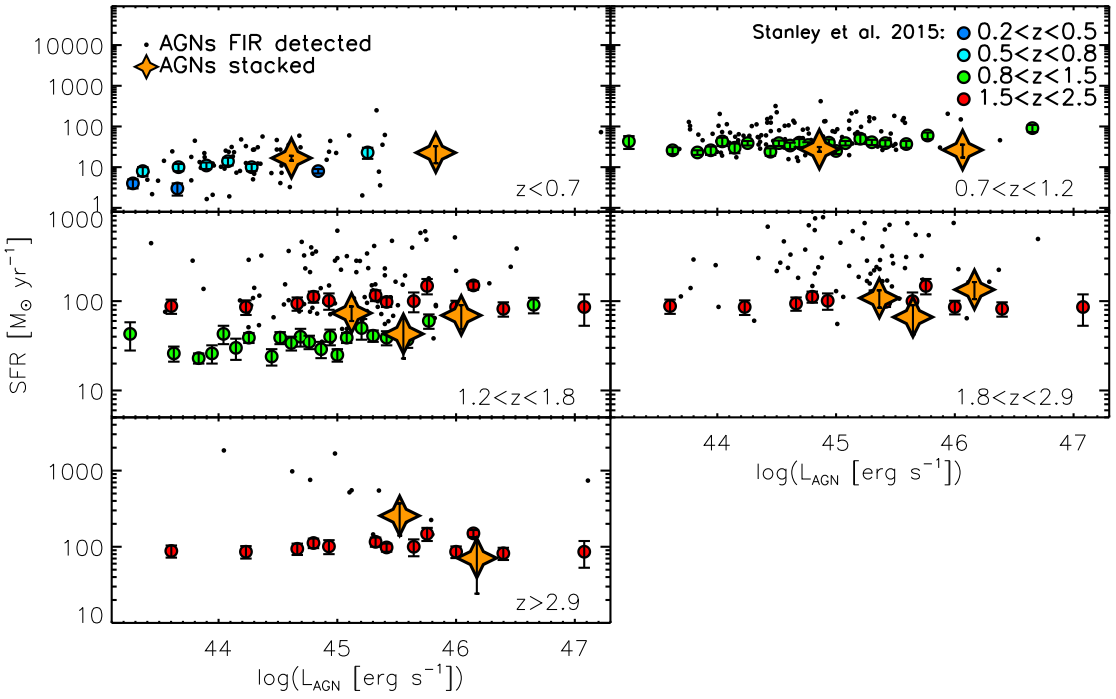

Figure 3.8: Average SFR for our X-ray selected AGN hosts binned in terms of their AGN luminosities. Each panel represents a different redshift bin indicated at their bottom right-hand side. The black dots show the AGN hosts that are Herschel-detected and for which we are able to individually derive the SFR. The orange stars indicate the average SFR in each bin (including Herschel-undetected sources via stacking). We compare our results to those of Stanley et al. (2015), colour-coded according to their redshift bins (see key). We report that our average SFRs are broadly consistent with theirs.

dataset to explore the star-forming properties of the AGN hosts as a function of specific X-ray luminosity (equivalently, $\lambda_{\rm Edd}$; see § 3.3.1), and whether any relation between these properties has evolved with redshift. First, however, we check that our average SFRs are consistent with those reported in previous studies.

3.4.1 SFR as a function of total X-ray luminosity

Most previous studies that have explored the connection between SMBH and galaxy growth have found no clear evidence for a strong correlation between the total X-ray luminosity and the SFR of the host galaxy, particularly for the dominant population of moderate luminosity AGNs (i.e. $10^{42} < L_X < 10^{45}$ erg s^{-1} ; e.g. Lutz et al., 2010; Shao et al., 2010; Mullaney et al., 2012; Rosario et al., 2012; Rovilos et al., 2012; Harrison et al., 2012; Stanley et al., 2015, 2017). To check whether our data analyses are producing reliable results, we compare our measured SFRs against those reported in one of the most recent of such studies (i.e. Stanley et al., 2015). This

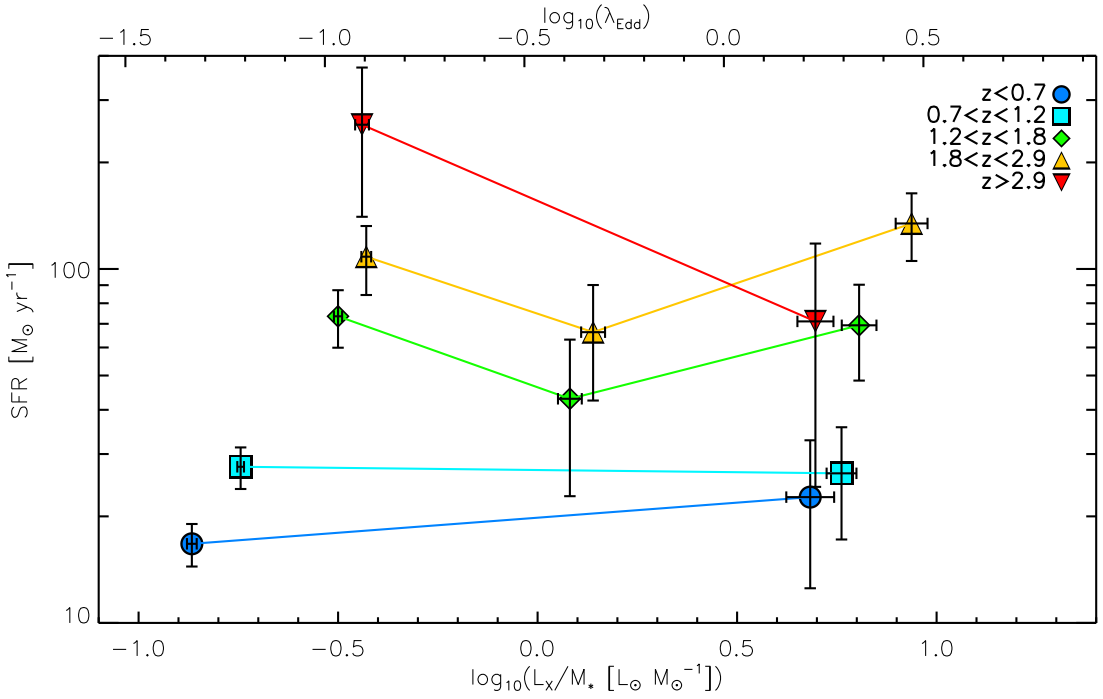

Figure 3.9: SFR for our X-ray selected AGN hosts versus specific X-ray luminosity (bottom axis) or Eddington ratio (top axis). Different coloured symbols indicate different redshift bins (see keys). The error bars are the 1σ uncertainties of the mean. We do not find any evidence of a positive or negative relationship between SFR and Eddington ratio.

comparison is shown in Fig. 3.8, where we plot our measured SFRs alongside those from Stanley et al. (2015). We have fewer bins than Stanley et al. (2015) as we bin in terms of $\lambda_{\rm Edd}$ rather than L_X as used in their study. However, we calculate the average AGN luminosity of each of our bins using Eq. 3.4, to enable us to perform a direct comparison. For all of our redshift bins, our measured average SFRs are in agreement with Stanley et al. (2015) over the range of AGN luminosities covered by our study (i.e. $10^{43} < L_{\rm AGN} < 10^{45}$ erg s^{-1}). As found in Stanley et al. (2015), our results indicate that there is no evidence of a strong correlation between average SFR and total X-ray luminosity. Our results also reconfirm that average SFRs of AGN host galaxies increase with redshift, consistent with suggestions that average SFRs of AGN hosts are similar to those of non-AGN MS galaxies (e.g. Mullaney et al., 2012, 2015).

3.4.2 SFR as a function of Eddington ratio

Motivated by the absence of a strong correlation between total X-ray luminosity and SFR of the host galaxy (see § 3.4.1), we test whether any correlation exists between

the specific X-ray luminosity – or Eddington ratio, $\lambda_{\rm Edd}$ – and the average SFR. We present in Fig. 3.9 how the mean-averaged SFR for our X-ray selected AGN sample changes with Eddington ratio. We find that there is no evidence of a correlation between SFR and $\lambda_{\rm Edd}$ at a given redshift. This expands upon the findings of Azadi et al. (2015), who also report the lack of correlation between these two parameters for AGNs with $\lambda_{\rm Edd}$<0.1 and z<1.2. However, we also find that the average SFRs of the AGN hosts increase with increasing redshifts at a given $\lambda_{\rm Edd}$, following the z evolution of the MS, and as observed when comparing average SFR to the X-ray luminosity (see § 3.4.1).

Not shown in Fig. 3.9, however, are the effects of the stellar mass gradient along the abscissa. As mentioned previously, due to the X-ray flux limit of our sample, AGNs with low $\lambda_{\rm Edd}$ will tend to have, on average, higher stellar masses compared to the high $\lambda_{\rm Edd}$ AGNs (see the stellar mass histograms in Fig. 3.6). Since SFR is related to stellar mass via the MS, this gradient may have an effect on the observed relationship between SFR and $\lambda_{\rm Edd}$, such that higher $\lambda_{\rm Edd}$ AGNs (i.e. in galaxies with preferentially lower stellar masses) should tend to have lower SFRs (i.e. by roughly a factor of five according the observed stellar mass gradient). Thus, the observed flat relationship between SFR and $\lambda_{\rm Edd}$ suggests that the hosts of high $\lambda_{\rm Edd}$ AGNs have boosted SFRs (relative to the MS) compared to low $\lambda_{\rm Edd}$ AGNs.

In light of the above, we use our mock mass-matched sample of MS galaxies to normalise for the effects of the mass gradient within our samples. To do this we take the measured mean SFRs of each of our bins and divide them by the mean SFR of the corresponding mass-matched MS sample (i.e. $\rm SFR_{MS}$; see § 3.3.4). Uncertainties on this ratio were derived by propagating the errors on the mean SFR and $\rm SFR_{MS}$ (see § 3.3.3 and § 3.3.4). In Fig. 3.10 we display how the normalised average SFR changes with Eddington ratio at various redshifts. In this figure we also show the 3σ range of non-AGN MS galaxies as reported in Schreiber et al. (2015). Our results indicate that at low $\lambda_{\rm Edd}$ (i.e. $\log(\lambda_{\rm Edd})< -0.5$) AGN hosts display SFRs toward the lower edge of the MS range at all redshifts. By contrast, our results suggest that AGNs with $\log(\lambda_{\rm Edd})> 0$ show slightly enhanced normalised average SFRs compared to $\log(\lambda_{\rm Edd})< -0.5$ AGNs, by factors of 2.25±1.18, 1.75±0.67, 2.04±0.75, 5.11±1.63 for the redshift bins $z < 0.7, 0.7 < z < 1.2, 1.2 < z < 1.8$ and $1.8 < z < 2.9$, respectively. However, it must be noted that it is only in the $1.8< z <2.9$ redshift bin that this increase is measured at a significance of $> 3\sigma$ (3.13σ). Since this represents the bin containing the largest number of high Eddington ratio AGNs (i.e. 84 AGNs in the bin -0.17<$\log(\lambda_{\rm Edd})$<1.64), increasing the number of AGNs in other bins (i.e. having a larger sample) may also unveil a relationship between normalised

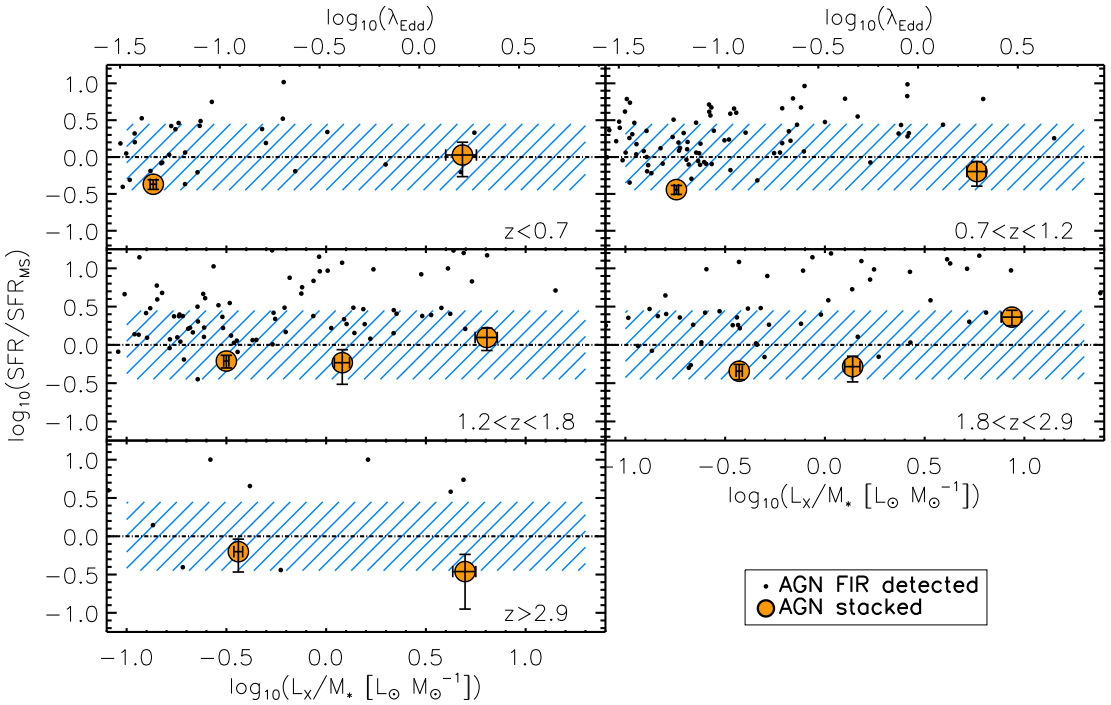

Figure 3.10: MS normalised average SFR versus specific X-ray luminosity (bottom axis) or Eddington ratio (top axis). Each panel shows a different redshift bin as indicated at their bottom right-hand side. Black dots represent AGNs that are individually detected by Herschel and for which we are able to derive normalised SFRs, while the orange circles indicate the normalised average SFR derived from stacking. The black dashed line indicates the position of the MS and the blue shaded area its 1σ scatter. Error bars indicate the 1σ uncertainties on the mean values. We find that AGNs in our highest $\lambda_{\rm Edd}$ bin and for $1.8<z<2.9$ have higher normalised average SFR than that of their lower $\lambda_{\rm Edd}$ counterparts with a 3.13σ significance.

average SFR and $\lambda_{\rm Edd}$ in these bins. However, it should be noted that the significance of any difference drops to $< 3\sigma$ in all our redshift bins if we exclude galaxies with $M_* < 10^{10} M_\odot$. This demonstrates that it is crucial to probe stellar mass down to that limit, since it also corresponds to the highest $\lambda_{\rm Edd}$ AGNs. Furthermore, we also note that the average uncertainties on stellar masses observed in our sample is roughly 15 per cent, which is always smaller than the uncertainties measured on the normalised average SFRs at higher $\lambda_{\rm Edd}$ (i.e. the uncertainties on averaged normalise SFRs are close to 30 per cent at higher $\lambda_{\rm Edd}$). Therefore, the observed enhancement of averaged normalise SFR at higher $\lambda_{\rm Edd}$ is not a consequence of the uncertainties on the stellar masses.

3.4.3 Fraction of starburst galaxies among AGN hosts

The main goal of this chapter is to investigate how the star forming properties of AGN host galaxies relate to the specific X-ray luminosity using a large sample of X-ray selected AGNs. In § 3.4.2, we found that there is no correlation between average SFR and specific AGN luminosity, at least up to redshift ≈ 3 and for $0.1 < L_X/M_* < 10\ L_\odot\ M_\odot^{-1}$ (see also Fig. 3.9). However, when we instead compare the SFRs of AGN host galaxies to a mass-matched sample of MS galaxies, we found that high $\lambda_{\rm Edd}$ AGNs have slightly higher normalised average SFRs compared to low $\lambda_{\rm Edd}$ AGNs (at 3.13σ for z$\sim$2; see Fig. 3.10). This finding suggests that the *distribution* of SFRs for AGN hosts must be different between the lowest and the highest $\lambda_{\rm Edd}$ bin (i.e. it is impossible to have two different average values from two identical distributions).

To explore this further we attempt to compare the distribution of SFRs of AGN hosts across each of our bins, as well as against the distribution of non-AGN star-forming galaxies (i.e. Sargent et al., 2012; Schreiber et al., 2015). Due to the low Herschel detection rate of individual AGNs (i.e. only $\approx$20 per cent of the sample for which we are able to derive SFRs) the faint end of the SFR distribution cannot be directly probed. Instead, we focus on the higher end of the SFR distribution (i.e. where most of our detected galaxies lie) to measure the fraction of AGN hosts with SFRs that are five times above the MS, which probes the so-called "starburst" region of the SFR distribution. Although we are probing the higher end of the SFR distribution, it is possible that some of the Herschel-undetected galaxies in our sample are actually starbursts, hence affecting the number of AGNs located in these galaxies. To account for this we derive upper limits on the SFRs for the undetected sources, which we then use to place upper and lower limits on the fraction of starburst galaxies. To measure the upper limits on the SFRs, we first calculate the 3σ upper

limits on the fluxes at 100 μm for HERSCHEL-undetected sources at $z \leq 1$, and at 160 μm for those at $z > 1$. To do this, we extract the flux on 100 positions, selected at random, around the undetected source (i.e. between twice and 4 times the full width at half maximum of the PSF) and take three times the standard deviation of the resulting flux distribution as the 3σ upper-limit on the flux. These upper limits on the fluxes are then converted into upper limits on the SFRs using the templates for star-forming galaxies of Mullaney et al. (2011).

By taking the above approach to calculate upper limits on the HERSCHEL-undetected AGNs, we are able to infer the fraction of starbursts in each of our redshift and $\lambda_{\rm Edd}$ bins, accounting for both detected and undetected hosts. To do this, since some of the undetected AGNs in our sample show upper limits above our starburst threshold (i.e. with SFR at least five times above the MS), the *maximum* fraction of starbursts is defined by assuming that all these upper limits represent genuine starburst AGNs. Conversely, the *minimum* fraction of starbursts is defined by assuming that all upper limits above the starburst threshold are, in fact, non-starburst galaxies. Therefore for each of our redshift and $\lambda_{\rm Edd}$ bins we have a *conservative* range of possible values for the fraction of starbursts (i.e. from the minimum to the maximum). Since the $z > 2.9$ redshift bin contains only 114 AGNs, of which 91 per cent have only upper limits on their SFRs, we do not consider this bin for studying the evolution of the fraction of starbursts with $\lambda_{\rm Edd}$.

The results are displayed in Fig. 3.11, in which we show the range of possible fraction of starbursts as a function of Eddington ratio and redshift. For two of our redshift bins (i.e. $z < 0.7$ and $0.7 < z < 1.2$), we measure a significant increase of the fraction of starbursts, with the minimum fraction in our $\log(\lambda_{\rm Edd}) > 0.5$ bin, which is higher by $\approx$5 percentage points than the maximum fraction in our $\log(\lambda_{\rm Edd}) < 0.5$ bin (i.e. ≈ 8 per cent versus ≈ 4 per cent for $z < 0.7$, and ≈ 6 per cent versus ≈ 10 per cent for $0.7 < z < 1.2$). Again, this suggests that the distribution of normalised SFRs changes with $\lambda_{\rm Edd}$, such that AGNs of higher $\lambda_{\rm Edd}$ have, on average, marginally higher normalised SFRs. However, for the redshift bins $1.2 < z < 1.8$ and $1.8 < z < 2.9$, the range of possible starburst fractions is too broad to be able to claim any significant change in the fraction of starbursting hosts as a function of $\lambda_{\rm Edd}$.

In Fig. 3.11 we also show the fraction of non-AGN galaxies that we would expect to see as starbursts in the general star-forming galaxy population. This is calculated from the normalised SFR distribution of Schreiber et al. (2015) and is ≈ 3 per cent. We use our mass-matched sample to confirm that this fraction is appropriate for our sample (i.e. is not subject to effects arising from binning in $\lambda_{\rm Edd}$). In all of our redshift bins, we find that the *minimum* fraction of starburst galaxies in our highest

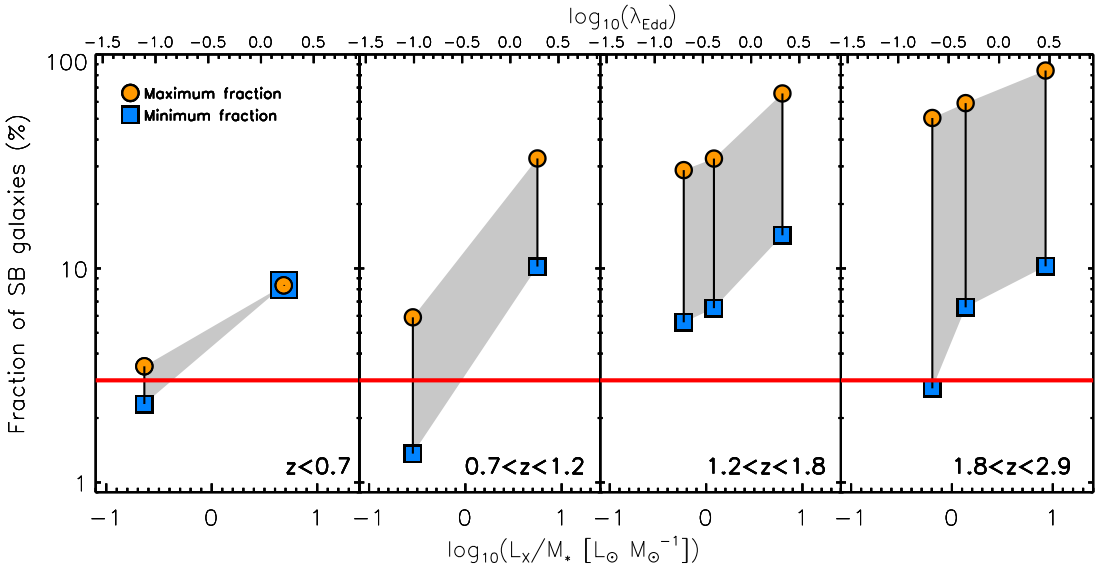

Figure 3.11: Fraction of starbursting hosts in each of our redshift and specific X-ray luminosity (bottom axis) or $\lambda_{\rm Edd}$ (top axis) bins. The blue squares show the minimum fraction of starbursts (i.e. all upper limits measured in the starburst regime are assumed to be non-starburst) and the orange circles show the maximum fraction of starbursts (i.e. all upper limits measured in the starburst regime are assumed to be starbursts) in each of our bins. The grey area shows the range of possible values. The red line represents the expected fraction of starbursts for a non-AGN star-forming population composed of MS and starburst galaxies only (i.e. 3 per cent; from Schreiber et al. 2015). In three of our redshift bins, we find that the minimum fraction of starbursts among high $\lambda_{\rm Edd}$ AGNs is significantly higher than that of the general population of star-forming galaxies.

$\lambda_{\rm Edd}$ bins is higher than in the general star-forming galaxy population, with fractions of 8.3 per cent, 10.2 per cent, 14.3 per cent and 10.2 per cent in our $z \sim 0.4, 1, 1.5$ and 2.5 bins. We calculate the Poisson uncertainty on these percentages, which allows us to measure the significance of the difference between the fraction of starburst galaxies in each of our redshift and highest $\lambda_{\rm Edd}$ bins and the expected 3 per cent, using

$$P(k|\lambda) = \frac{\lambda^k e^{-\lambda}}{k!}, \tag{3.5}$$

where k is the *minimum* number of starburst galaxies in each bin (calculated from our minimum fraction) and λ is the number that we would expect if 3 per cent of the AGNs in that bin were starbursts. Thus $1 - P(k|\lambda)$ gives the probability of measuring the observed fraction by chance if AGNs and star-forming galaxies had the same fraction of starbursts. The highest $\lambda_{\rm Edd}$ bins in our $z \sim 0.4, 1, 1.5$ and 2.4 bins all have starburst fractions that are higher (at 72.9 per cent, 98.5 per cent, 99.99 per cent and 99.8 per cent confidence, respectively) than the star-forming galaxy population. These results are similar to those of reported in Azadi et al. (2015) for AGN hosts at $z \lesssim 1$, but also extend to much higher redshifts.

3.5 Discussion

In this chapter we have explored the star-forming properties of AGN hosts as a function of their specific X-ray luminosity – used as a proxy measure of Eddington ratio ($\lambda_{\rm Edd}$) – out to redshift $\approx$3. This work expands upon that of Azadi et al. (2015) by considering AGNs with higher $\lambda_{\rm Edd}$ and at higher redshifts. Consistent with that study, we find that there is no evidence of a strong correlation between average SFR and $\lambda_{\rm Edd}$ up to $z \approx 1$ and to $\log(\lambda_{\rm Edd}) \sim -0.5$. However, by including more extreme redshifts and $\lambda_{\rm Edd}$ AGNs in our sample, we can now also report that there is no evidence of enhanced or suppressed star-formation rates among AGNs with $\log(\lambda_{\rm Edd}) > -0.5$ compared to lower $\lambda_{\rm Edd}$ AGNs, at least up to $z \approx 3$.

When we compare the mean SFR of AGN hosts relative to that of mass and redshift-matched samples of non-AGN star-forming galaxies (from the SFR distribution of Schreiber et al., 2015) we find that the highest $\lambda_{\rm Edd}$ AGNs (i.e $\log(\lambda_{\rm Edd}) > 0$) in four of our five redshift bins show marginally enhanced SFRs relative to their lower $\lambda_{\rm Edd}$ counterparts, up to redshift ≈ 3. However, this enhancement is only significant at a level of $> 3\sigma$ in one of our redshift bins (i.e. $1.8 < z < 2.9$). We also find that the *minimum* fraction of starburst galaxies in the highest $\lambda_{\rm Edd}$ bin at all redshifts is higher than what would be expected if AGN hosts followed the same SFR distri-

bution as the general star-forming population presented in Schreiber et al. (2015). These results suggest that the SFR distribution of AGNs changes as a function of specific AGN luminosity and that, at least at high $\lambda_{\rm Edd}$ values, differs from that of normal (i.e. non-AGN) star-forming galaxies. Recently, there has been similar reports of discrepant AGN SFR distributions relative to normal galaxies (e.g. Shimizu et al., 2015; Mullaney et al., 2015). However, these studies found that the mode of the SFR distribution of AGN hosts is roughly a factor of $\sim$2 *lower* than that of the MS galaxies, whereas our results indicate a *higher* fraction of starbursts among high $\lambda_{\rm Edd}$ AGNs. These results are reconciled by appreciating that Shimizu et al. (2015) and Mullaney et al. (2015) both report that the SFR distribution of AGN hosts is also significantly *broader* compared to normal, star-forming galaxies (as defined by e.g. Schreiber et al. 2015). This broadened distribution means that there is still an increased likelihood of AGNs residing in strongly starbursting systems, despite the majority of AGNs residing in lower SFR galaxies (i.e. MS host galaxies and below). Indeed, while we report a higher fraction of starbursts among high $\lambda_{\rm Edd}$ AGNs compared to normal, star-forming galaxies, we also note that roughly 20 per cent of our AGNs in COSMOS are classified as optically quiescent (i.e. using a colour-colour diagram) by Ilbert et al. (2013). While this is only a very approximate estimate of the quiescent fraction, it still underlines the broad diversity of the star-forming properties of AGN hosts. The findings reported here build upon this by suggesting a link between the SFR distribution and the $\lambda_{\rm Edd}$ of the AGN.

Recently, Rodighiero et al. (2015) and Delvecchio et al. (2015) took the opposite, yet complementary, approach to that described here to probe the link between average star-formation and black hole growth rates. Rather than calculate the average star-forming properties of a sample of AGNs, as we do here, they instead calculate the average SMBH growth rate of either a sample of mass-selected (Rodighiero et al., 2015) or infrared-selected (Delvecchio et al., 2015) galaxies (see also Rafferty et al., 2011; Mullaney et al., 2012; Chen et al., 2013, for earlier studies that take a similar approach). Both of these studies report higher average SMBH growth rates among AGNs with higher SFRs, including those with starburst-like SFRs. Because of the different approaches used, it is difficult to directly interpret our results in terms of these studies. However, there appears to be a certain level of consistency insofar as enhanced SMBH growth rates follow enhanced SFR (or vice-versa). Whether this is a causal relationship, or if there is another more fundamental property linking the two (e.g. the availability of cold gas; Vito et al., 2014), remains unclear.

The higher starburst fraction among high $\lambda_{\rm Edd}$ AGNs compared to that expected from the SFR distribution of normal star-forming galaxies suggests that some aspect

of the starbursting process is conducive to triggering some high $\lambda_{\rm Edd}$ AGNs. A number of studies have reported that strongly starbursting systems are triggered by major galaxy mergers (e.g. Noguchi, 1988; Hernquist, 1989; Barnes & Hernquist, 1991; Duc & Mirabel, 1997; Elbaz & Cesarsky, 2003; Barnes, 2004; Tadhunter et al., 2011, 2012; Davies et al., 2015). As such, our results could be interpreted that the merger process also plays a role in triggering a proportion of high $\lambda_{\rm Edd}$ AGNs. This is consistent with previous finding that report heightened numbers of powerful AGNs among merging systems (e.g. Treister et al., 2012, 2013; Ellison et al., 2015). However, it remains unclear whether the merger plays a direct role in triggering powerful AGNs, or whether it is the resultant star-formation that is the more important fuelling mechanism (e.g. Thompson et al., 2005; Cuadra et al., 2006, 2008; Vollmer et al., 2008; Cen, 2015). Again, we stress that our results do not imply that the majority of high $\lambda_{\rm Edd}$ AGNs reside in starbursts (which *may* be merger-induced), simply that high $\lambda_{\rm Edd}$ AGNs are slightly more predisposed to starbursting systems compared to the normal galaxy population.

A caveat of using the IR emission of the host galaxy to derive the SFR is that it measures the integrated SFR on a time-scale of several hundreds of million years. By contrast, although a typical average lifetime of an AGN phase is of the order of 10^7–10^9 years (e.g. Martini & Weinberg, 2001; Marconi et al., 2004), the accretion rate of the SMBH likely fluctuates by several order of magnitudes on shorter time-scales (e.g. Alexander & Hickox, 2012; Neistein & Netzer, 2014; Hickox et al., 2014). Since we use the X-ray emission of the nucleus to derive the instantaneous power of the AGN it may be difficult to interpret the impact that AGNs have on the SFRs of host galaxies by directly comparing this to the IR output of the galaxies. However, using hydrodynamical simulations, Volonteri et al. (2015) were able to track the time evolution of the black hole accretion rate versus the SFR for different stages of a major merger (i.e. before, during and after the merger), including the rapid variability of AGNs, and averaging the SFR over 100 million years to mimic the FIR estimates. They found that during the merger phase (i.e. enhanced SFR), SMBHs spend a greater fraction of time accreting at high Eddington ratios compared to during non-merger phases. They also found that high accretion rate phases are often concurrent with a starburst, but that the ensuing supernova feedback arising from this starburst suppresses AGN activity. In these simulations, the distribution of SFR, averaged over 100 million years, for high Eddington ratio AGNs is broader, and it also peaks at larger SFR than for low Eddington ratio AGN. In such a scenario, it may be more *likely* that we find high Eddington ratio AGNs during a merger phase than in a non-merger phase, depending on the relative times spent within those phases.

Considering that major mergers are thought to help induce starbursts (e.g. Noguchi, 1988; Hernquist, 1989; Barnes & Hernquist, 1991; Duc & Mirabel, 1997; Elbaz & Cesarsky, 2003; Barnes, 2004; Davies et al., 2015), these results could therefore be considered as being consistent with our findings of a higher fraction of starbursting galaxies among high $\lambda_{\rm Edd}$ AGNs. Whether or not our highest $\lambda_{\rm Edd}$ bins are dominated by galaxies undergoing major mergers is, however, beyond the scope of our study.

3.6 Conclusion

From the outset, the primary motivation of this study was to determine whether there is any evidence for a suppression of star formation among galaxies hosting the highest Eddington ratio AGNs, which could be interpreted as evidence of so-called "AGN feedback". To this aim, we used deep Herschel data to measure the star-forming properties of a sample of 1620 X-ray selected AGNs in the COSMOS, GOODS-N, and GOODS-S fields. Our AGN sample spans $10^{42} < L_X < 10^{46}$ erg s^{-1} and $z \lesssim 3$ (see § 3.2). Rather than measuring the Eddington ratio directly, we calculate AGN luminosity relative to the stellar mass of the host galaxy (i.e. the specific $L_{\rm AGN}$); in some respects, this is more pertinent than the actual Eddington ratio, as it provides a measure of the AGN power relative to the gravitational potential of its host. Stacking analyses were employed to account for Herschel-undetected sources, and broad-band SED fitting was used to account for any AGN contamination when deriving host stellar masses and star-formation rates.

In agreement with previous studies (e.g. Lutz et al., 2010; Shao et al., 2010; Mullaney et al., 2012; Rosario et al., 2012; Rovilos et al., 2012; Harrison et al., 2012; Stanley et al., 2015), we found no clear evidence of any strong (anti-)correlation between AGN luminosity and the star-forming properties of their hosts, at least for the luminosity and redshift ranges considered here. When we instead consider specific $L_{\rm AGN}$ (i.e. L_X/M_*), however, we find a small increase in the star-formation rates among the highest specific $L_{\rm AGN}$ AGNs; although this increase is only significant at a $> 3\sigma$ level in one of our redshift bins. One means of investigating this further will be to derive the distribution of star-forming properties of AGN hosts compared to the non-AGN population. A full exploration of this is not possible with our AGN sample, and the relationship between the Eddington ratio distribution and the host star-forming properties is the focus of the following chapters. However, we do find that the fractions of strongly starbursting galaxies are at least a factor of ~ 3 times larger among our highest $\lambda_{\rm Edd}$ AGNs compared to the non-AGN population. From this, we argue that the distribution of SFRs among the AGN population is broader

than that observed for MS galaxies, which is consistent with the findings of other recent studies (e.g. Mullaney et al., 2015; Shimizu et al., 2015).

Chapter 4

Our method to infer the Eddington ratio distribution of AGNs

4.1 Introduction

In this thesis, we explore the link between the accretion activity of SMBHs and the star-forming properties of their host galaxies. In the previous chapter, we used a sample of 1620 AGNs (spanning X-ray luminosities between $L_X \sim 10^{42-45}$ erg s^{-1}) for which we derived their specific X-ray luminosities (L_X/M_*). Whilst measuring their host galaxy SFRs, we found that, at least out to $z \sim 3$, there is a slight enhancement of normalised average SFR (i.e. the SFR of the host divided by the SFR if lying on the MS) at higher specific X-ray luminosity – or Eddington ratio, $\lambda_{\rm Edd}$. This result is reinforced by our finding of a higher fraction of starbursting galaxies at higher Eddington ratios (see Chapter 3, § 3.6).

The enhancement of normalised average SFR with Eddington ratio indicates that the Eddington ratio distribution *must* change with the star-forming properties of the host galaxies. This is in agreement with many recent studies that find a difference in the Eddington ratio distribution of star-forming and quiescent host galaxies (e.g. Georgakakis et al., 2014; Aird et al., 2017a; Wang et al., 2017). To investigate this further, we would ideally measure how the Eddington ratio distribution changes as a function of SFR (or MS-normalised SFR). However, observational limits (e.g. flux limited catalogues, blending between the AGN and star emissions) prevent us from directly constraining the Eddington ratio distribution of AGNs to this level of detail. Instead, for the remainder of this thesis, we will take an indirect approach (i.e. a modelling approach) to infer how the Eddington ratio distribution depends upon the host galaxy properties, including SFR.

By using a modelling approach, many recent studies find that the Eddington ratio

distribution for AGNs is well described by a universal (i.e. star-forming and quiescent galaxies combined) broken power-law out to $z{\approx}1$ (e.g. Aird et al., 2012; Hickox et al., 2014; Veale et al., 2014; Caplar et al., 2015; Jones et al., 2017). Many studies have also demonstrated that combining a universal broken power-law for the Eddington ratio distribution of AGNs with the distribution of SFR for MS galaxies (for the MS see e.g. Sargent et al., 2012; Schreiber et al., 2015) reproduces the observed flat relationship between SFR and X-ray luminosity (e.g Veale et al., 2014; Stanley et al., 2015). However, while expanding to higher redshifts, Jones et al. (2017) found that a simple universal broken power-law for the Eddington ratio distribution cannot reproduce the observed X-ray luminosity function of Aird et al. (2010) beyond $z{\sim}1.2$. They suggest that a more complicated model needs to be considered beyond that redshift. This suggestion is aligned with our results which indicate that the Eddington ratio distribution must change with the host star-forming properties, and with recent studies that find a difference in the Eddington ratio distribution for star-forming and quiescent galaxies (e.g. Georgakakis et al., 2014; Aird et al., 2017a; Wang et al., 2017). Therefore, we propose to investigate a model in which the Eddington ratio distribution is split between star-forming and quiescent galaxies. Consequently, we must model the Eddington ratio distribution using two functions, the parameters of which need to be optimised in order to match observations.

In this chapter we describe the method that we use to infer our Eddington ratio distribution split between star-forming and quiescent galaxies. We first introduce in § 4.2 population synthesis models (hereafter PSMs) often adopted to infer the Eddington ratio distribution. In the same section, we also clarify why PSMs, where one generates a large sample AGNs, are not the best approach to infer the Eddington ratio distribution of AGNs. We then present in § 4.3 our analytical approach considered instead of the PSMs and explain how we use Markov Chain Monte Carlo to estimate the parameters that define our Eddington ratio distribution. Finally, we summarise in § 4.4.

4.2 Population synthesis models

Population synthesis models (PSMs) have proven very helpful for investigating the Eddington ratio distribution of AGNs (e.g. Aird et al., 2012; Hickox et al., 2014; Stanley et al., 2015; Jones et al., 2017). To do this, PSMs randomly draw galaxy properties from probability distribution functions (PDFs). For example, PSMs can be used to generate a population of N mock galaxies with masses drawn from a mass function (can be interpreted as a PDF), and for which we randomly allocate $\lambda_{\rm Edd}$

following an Eddington ratio distribution (can also be interpreted as a PDF). As the stellar masses are known, each $\lambda_{\rm Edd}$ can then be converted into an X-ray luminosity, the histogram of which is proportional to the X-ray luminosity function, given that Eddington ratio distribution. In our case, the Eddington ratio distribution is unknown, but can be defined by a function with free parameters, $\Theta = \{\theta_1, \theta_2, ..., \theta_n\}$, where θ_j is a parameter of the model Eddington ratio distribution (e.g. a normalisation, a slope, etc). Then, by using an observed mass function (e.g. Davidzon et al., 2017) and an observed X-ray luminosity function (e.g. Aird et al., 2015), we can iterate over the set of parameters Θ until the model X-ray luminosity function matches the observed one.

To optimise the parameters that define the Eddington ratio distribution, one can use Chi-square minimisation (i.e. minimising the difference between the model and the observed X-ray luminosity function). However, since PSMs *randomly* draw properties from PDFs, two independent simulations of N mock galaxies drawn from an identical PSM (i.e. changing neither the mass function nor the Eddington ratio distribution) will produce two slightly different model X-ray luminosity functions (i.e. PSMs are stochastic). Therefore, when PSMs are incorporated into an iterative process for optimisation, commonly used algorithms such as the Levenberg–Marquardt least-squares fit (i.e. Levenberg, 1944; Marquardt, 1963) fail at comparing the goodness of the fit between two consecutive iterations.

An alternative to the classic optimisation algorithms is to use Markov Chain Monte Carlo simulations (hereafter MCMCs). The gain of using MCMCs is that they obtain probability distributions of each parameter which can account for the stochastic nature of the variables. Furthermore, should our solution be degenerate (i.e. different set of parameters Θ for the Eddington ratio distribution result in undistinguishable model X-ray luminosity functions), MCMCs allow the multiple solutions to be unveiled, in contrast to alternative classic optimisation methods (e.g. Levenberg–Marquardt least-squares fit) that only converge toward one solution which might be a local minimum in the presence of a degenerate solution.

Another drawback of using PSMs for iterative processes is that they are computationally expensive. The reason for this is that, after updating the set of parameters Θ that defines the Eddington ratio distribution with a set of new parameters, we must generate a new population of N galaxies to produce the updated model X-ray luminosity function. Furthermore, N needs to be large enough (e.g. $\mathcal{O}(10^9)$) for the sample of mock galaxies to also contain rare extreme sources (e.g. galaxies with $M_*> 10^{11}$ $M_\odot$, or AGNs with $L_X> 10^{46}$ erg s^{-1}), otherwise the bright end of the X-ray luminosity function (i.e. low probability) will be dominated by Poisson noise.

This increases the difficulty of comparing two different sets of parameters, Θ, that define the Eddington ratio distribution. Therefore, instead of using a PSM to infer the Eddington ratio distribution, we use an analytical approach similar to the convolution method used in several recent studies (e.g. Veale et al., 2014; Caplar et al., 2015; Weigel et al., 2017).

4.3 Method to optimise the Eddington ratio distribution

As mentioned above, to infer the Eddington ratio distribution we use MCMC on an analytical model. In this section, we first describe in § 4.3.1 our analytical approach. We then present in § 4.3.2 the MCMC that we use to optimise the parameters of this model to best match the observed X-ray luminosity function.

4.3.1 Analytical approach

For our model, instead of relying on PSMs, we analytically relate the mass function to the Eddington ratio distribution to model the X-ray luminosity function. Our method is similar, but developed independently, to the convolution methods sometimes considered in studies which also investigate the Eddington ratio distribution (e.g. Veale et al., 2014; Caplar et al., 2015; Weigel et al., 2017). The main difference is that we use definitions from statistics instead of using the definition of the convolution.

As we define an AGN's X-ray luminosity to be proportional to its Eddington ratio multiplied by its host stellar mass (i.e. $L_X \propto \lambda \times M_*$), the X-ray luminosity function corresponds to the "joint probability distribution" between the mass function and the Eddington ratio distribution. The joint probability of a given L_X is the sum of all the possible combinations of M_* and $\lambda_{\rm Edd}$ that return this L_X, but weighted by their own probabilities. To obtain the joint probability *distribution* (i.e. not only for a given L_X) we repeat this for different values of L_X in the range of $L_X \in [10^{38} - 10^{47}]$ erg s^{-1}.

To mathematically derive the joint probability distribution, we write the probability of having a given X-ray luminosity, k, given $\lambda_{\rm Edd}$ and M_*, $P(L_X = k|\lambda_{\rm Edd}, M_*)$, (hereafter $P(L_X = k)$ for short hand) as,

$$P(L_{\rm X} = k) \propto P(\lambda_{\rm Edd} = \frac{k}{M_*}), \tag{4.1}$$

where we simply use our definition for $\lambda_{\rm Edd}$, i.e. $\lambda_{\rm Edd} \propto L_X/M_*$. Hence the probability

of having an AGN with X-ray luminosity 'k' is equivalent to that of having an AGN with Eddington ratio 'k/M_*'. The probability of observing an AGN with L_X=k in *all* galaxies is the sum of these individual probabilities over all the possible stellar masses (i.e. law of total probabilities), i.e.

$$P(L_{\rm X} = k) \propto \sum_{j=M_{\rm min}}^{M_{\rm max}} P(\lambda_{\rm Edd} = \frac{k}{j}\ ,\ M_* = j), \tag{4.2}$$

where $P(\lambda_{\rm Edd} = \frac{k}{j}\ ,\ M_* = j)$ is the probability of $\lambda_{\rm Edd}$= $\frac{k}{j}$ *and* M_*= j. $M_{\rm min}$ and $M_{\rm max}$ are the boundaries within which the mass function is defined (e.g. $j \in [10^8$- $- 10^{15}]$; in unit of $M_\odot$). For statistically independent variables we have that,

$$P(L_X = k) \propto \sum_{j=M_{\rm min}}^{M_{\rm max}} P(\lambda = \frac{k}{j}) \times P(M_* = j), \tag{4.3}$$

where $P(\lambda = \frac{k}{j})$ is the Eddington ratio distribution evaluated at 'k/j', and $P(M_* = j)$ is the mass function evaluated at 'j'. Since Eq. 4.3 is for a given L_X (i.e. L_X= k), we define $k \in [10^{38} - 10^{47}]$ (in unit of erg s^{-1}) and iterate over k to obtain the full X-ray luminosity function. We chose broad – non-physical – boundaries to the stellar mass (i.e. $M_*$$\in [10^8 - 10^{15}]$ $M_\odot$) and the X-ray luminosity (i.e. $L_X$$\in [10^{38} - 10^{47}]$ erg s^{-1}) to ensure that our results are not affected by any boundary effects within the sensible range of parameters (e.g. $L_X = 10^{42} - 10^{45}$ erg s^{-1} for the X-ray luminosities, and $M_* = 10^9 - 10^{12}$ $M_\odot$ for the stellar masses).

By taking this analytical approach, we avoid having to model N galaxies (where we have seen that $N \sim \mathcal{O}(10^9)$ in order to generate sufficient numbers of massive luminous galaxies), and can simply split our mass function into $\mathcal{O}(10^3)$ bins between $M_{\rm min} = 10^8$ $M_\odot$ to $M_{\rm max} = 10^{15}$ $M_\odot$. Since we adopt an iterative process to identify the best fitting parameters, this factor of $\mathcal{O}(10^6)$ reduction in the number of required calculations *per iteration* dramatically reduces the time taken to converge.

4.3.2 Markov Chain Monte-Carlo simulation

In the previous subsection we demonstrate how we analytically combine the mass function with the Eddington ratio distribution to model the X-ray luminosity function. We now explain how we use MCMC to optimise the parameters that define our model Eddington ratio distribution, in order for our model X-ray luminosity function to match the observed one, after assuming a mass function.

The MCMC sampler is an algorithm that performs a random walk within the parameter space and which, over time, converges *around* the best fitting solution.

The dimension of the full parameter space is given by the number of free parameters that define the model (e.g. for a power law with a normalisation and a slope, this is a two-dimension parameter space). The initial position, $X_{\rm t} = X_0$, in the parameter space is randomly allocated (i.e. draw a random set of model parameters). A new position, $X_{\rm t+1}$, is then proposed. This new position is drawn such that an adjacent location to $X_{\rm t}$ (the current position) is more likely to be proposed than a distant one. This is done by randomly drawing a set of new parameter values from Gaussian functions centred on each of the parameters defining the actual position $X_{\rm t}$. The widths of these Gaussian functions are often fixed but can be re-defined if necessary. If the new proposal provides a better fit to the data than that of the previous set of parameters, it is accepted, and the proposed position in the parameter space becomes the actual position. However, if the proposed set of new parameters provides a worse fit to the data, the proposed location *is not* automatically rejected. To decide whether or not a worst proposal is accepted or rejected, the MCMC sampler measures the relative likelihood (see below) of the two positions, α, (i.e. between the proposed new position and the actual one). The new position is then accepted with probability α. Therefore, by repeating this process a fixed number of steps, in addition to converging toward the best fitting parameters (i.e. better fit always results in moving to the new position), the MCMC sampler also provides a mapping of how likely each point of the parameter space is, relative to the maximum likelihood (i.e. the location of the best fitting solution). Once projected along each axes of the parameter space (i.e. for each parameter), this gives the likelihood distribution of each parameter (or posterior distribution). The peak of a parameter's likelihood distribution indicates the best fitting solution, whilst the standard deviation determines the uncertainties. We show in Fig. 4.1 a sketch of the MCMC process for two cases, one in which the proposed set of new parameters gives a worse fit to the data, and one in which they gives a better fit to the data.

As mentioned above, the decision to accept or reject the proposed set of new parameters is based on the relative likelihood of the two models, generated by the two set of parameters. Therefore, we need to be able to measure the likelihood at each step. Again, this is the likelihood of measuring the observed data given the model. Assuming that the uncertainties on the data follow a Gaussian distribution, we use the same definition for the (log-)likelihood as the one defined in Chapter 2, § 2.3.2, i.e.,

$$\log(\mathcal{L}) = -\frac{1}{2}\chi^2, \tag{4.4}$$

where χ^2 is the Chi-square between the model and the observed X-ray luminosity

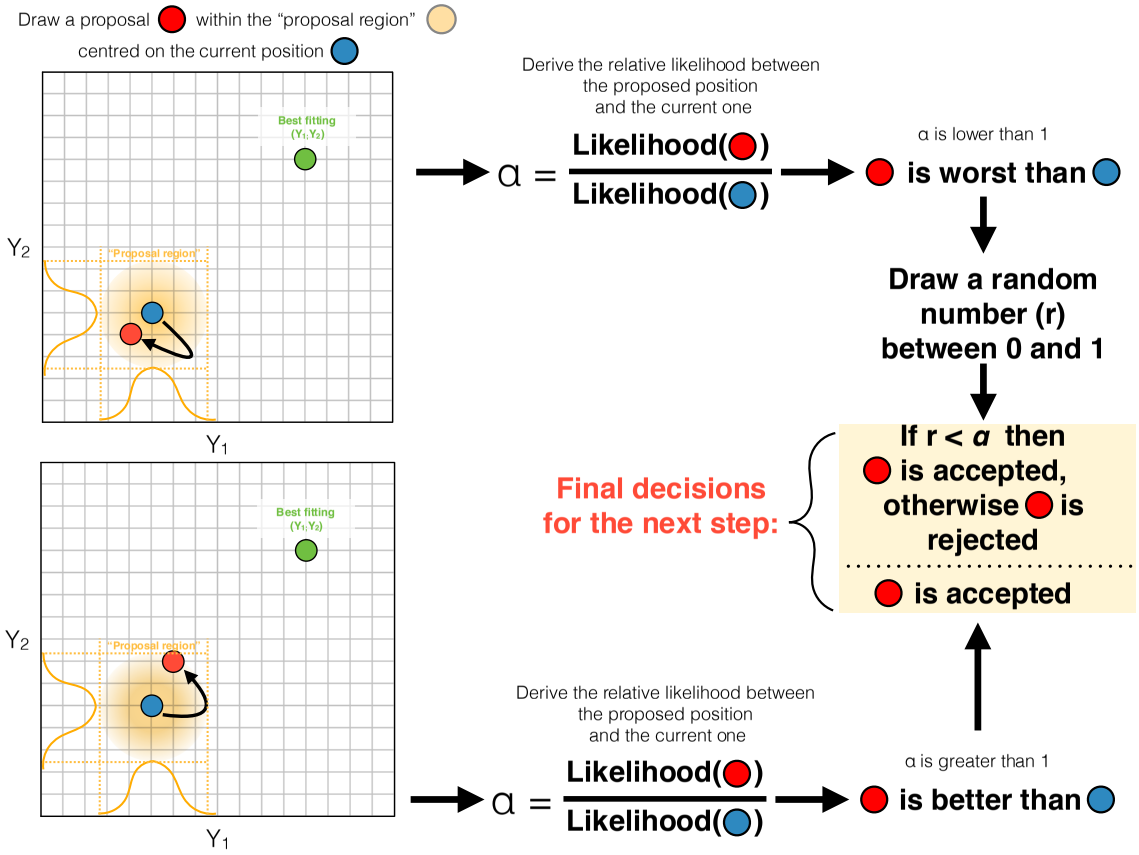

Figure 4.1: Sketch of the MCMC process. Top pathway indicates the MCMC process for a proposed new position in the parameter space that provides a worse fit to the data, whilst the bottom pathway is that of a proposal that provides a better fit to the data. The light yellow box on the right-hand side indicates all the possible final decisions for the proposed new step, whether it gives a better or a worse fit to the data. The rectangle grids on the left-hand side shows the parameter space defined by the two parameters Y_1 and Y_2. The two yellow Gaussian functions centred on the actual Y_1 and Y_2 positions shows the probability distributions from which the new proposal is drawn.

function. With our definition of the log-likelihood, we are essentially performing Chi-square minimisation, however, since implemented into a MCMC process, it provides uncertainties on each parameter based on the likelihood distribution, and is more robust to local minima.

The MCMC algorithm described above is one of the most commonly used, and is referred to as the Metropolis-Hasting algorithm (Metropolis et al., 1953). However, this algorithm is highly dependent on the proposal functions (i.e. the Gaussians from which steps are drawn), such that, if not set up properly, it encounters difficulties at sampling large parameter spaces (i.e. it takes a large number of iterations to converge). Since we aim to optimise the Eddington ratio distribution split between star-forming and quiescent galaxies (i.e. each with a function defined by independent free parameters), our parameter space is likely to be large. Therefore, for this work, we use a more powerful MCMC algorithm recently developed for optimisation in large parameter spaces. It is based on the "parallel tempered affine invariant" ensemble sampler of Goodman & Weare (2010). A complete description of this ensemble sampler is beyond the scope of this work. However, briefly, it allows the parallel computation of several MCMC chains (i.e. walkers), leading to a faster convergence and a better exploration of larger, more complex parameter spaces. We use an application-programming interface (API), written in PYTHON, EMCEE (Foreman-Mackey et al., 2013), that implements the Goodman & Weare (2010) MCMC algorithm[1].

For the remainder of this thesis, when referring to the use "MCMC optimisation" to infer parameters of the Eddington ratio distribution, we refer to running the aforementioned algorithm for a fixed number of 15000 steps on a collection of 200 walkers. Of these 15000 steps, the first 10000 are discarded (i.e. a burn-in phase) and only the last 5000 are kept for the analysis. This is to ensure that the final solution is not dependent on the random positions from which walkers are dropped into the parameter space (i.e. initial conditions). We make sure that the chain has reached the stationary distribution by using the convergence diagnostic of Gelman–Rubin that compares the "within chain" variance to the "between chain" variance (Gelman & Rubin, 1992). We find that for all the science runs we performed, we have a Gelman–Rubin coefficient always strictly above 0.99, which is very close to the value of 1 that indicates the convergence of the chains.

The result of the MCMC is a distribution (i.e. likelihood or posterior distribution) of a sample of 5000 (number of iterations) times 200 (number of walkers) in number for each parameter that defines our model Eddington ratio distribution. The peak of each distribution indicates the best solution for each corresponding parameter

[1] EMCEE is publicly available at `http://dan.iel.fm/emcee/current/`

(i.e. Eddington ratio distribution that best fit the X-ray luminosity function, once combined to a mass function), and the 1σ uncertainties are given by the standard deviation of these posterior distributions. To extract these quantities (i.e. best solutions and their uncertainties), we fit a one dimensional Gaussian function to each distribution. However, for some cases the posterior distribution does not resemble to a Gaussian. Instead, it raises and flattens above or below a given value. This indicates that the parameter is not defined above or below this value, and constitutes an upper or lower limit, respectively. We take as a limit the inflection of the distribution (i.e. where it flattens).

4.4 Conclusion

In this chapter we present our method to infer the Eddington ratio distribution for AGNs. We first introduce PSMs that can be used to generate a population of N galaxies (with $N \sim \mathcal{O}(10^9)$ to generate enough massive and luminous galaxies) with masses following the mass function, and with Eddington ratio following the Eddington ratio distribution. Combining Eddington ratio with stellar mass, we can derive X-ray luminosity for each mock galaxy, the histogram of which is related to the X-ray luminosity function. We argue that PSMs are stochastic and computationally expensive, such that an analytical approach is more suitable while using an iterative process to infer the Eddington ratio distribution. We then define our analytical approach that directly models the X-ray luminosity function by taking the joint probability distribution between the mass function and the Eddington ratio distribution. Finally, we detail our MCMC optimisation method that we will apply in the following chapters to infer the Eddington ratio distribution split between star-forming and quiescent galaxies.

Chapter 5

A different model Eddington ratio distribution for star-forming and quiescent galaxies

5.1 Introduction

In this thesis we propose to explore the link between accretion activity of SMBHs and their host galaxy SFRs. In previous chapters we focused on a sample 1620 AGNs for which we have measured accretion activities via their specific X-ray luminosities (i.e. the X-ray luminosity relative to the host stellar mass; or Eddington ratio, $\lambda_{\rm Edd}$), and compared that to their host SFRs (after removing AGN contamination). Our results indicate a slight enhancement beyond $z{\sim}1.2$ of normalised average SFR (i.e. the SFR relative to that of the MS) at higher Eddington ratios (i.e. $\lambda_{\rm Edd}> -0.5$). We also find a higher fraction (i.e. above the 3 per cent observed for non-AGN galaxies) of starbursting galaxies among higher Eddington ratio AGNs (see Chapter 3, § 3.4). Since normalised average SFR changes with $\lambda_{\rm Edd}$, we concluded that the Eddington ratio distribution must change with the host star-forming properties. This is in agreement with results reported in various recent studies (e.g. Georgakakis et al., 2014; Aird et al., 2017a; Wang et al., 2017). We now aim to investigate this distribution further. However, with the current samples, we are unable to directly measure this distribution without considerable corrections for completeness (i.e. too many Herschel-undetected hosts; see Chapter 2, § 3.2.2).

As mentioned in Chapter 4, § 4.1, many studies that investigate the Eddington ratio distribution have adopted a modelling approach (e.g. Aird et al., 2012; Conroy & White, 2013; Veale et al., 2014; Caplar et al., 2015). Overall, these studies find

that below $z{\sim}1$ the Eddington ratio distribution is well represented by a universal (i.e. the same distribution, irrespective of SFR, stellar mass, etc) broken power-law, the normalisation of which increases with redshift (e.g. Aird et al., 2013; Jones et al., 2017). Furthermore, once incorporated into a population synthesis model (PSM; see Chapter 4, § 4.2 for a description of PSMs) that includes host star-forming properties, some of these models are successful at reproducing the observed flat relationship between SFR and X-ray luminosity (Hickox et al., 2014; Stanley et al., 2015). However, as mentioned previously, Jones et al. (2017) have recently found that using a single universal broken power-law model for the Eddington ratio distribution cannot reproduce the X-ray luminosity function of Aird et al. (2010) beyond $z{\sim}1.2$. They argue the need for a more complicated model for the Eddington ratio distribution of AGNs.

In addition to the difficulties in reproducing the X-ray luminosity function using a single universal broken power-law beyond $z{\sim}1.2$, many recent observational studies have demonstrated that the Eddington ratio distribution for star-forming galaxies significantly differs from that of the quiescent[1] ones (e.g. Georgakakis et al., 2014; Aird et al., 2017a; Wang et al., 2017). In particular, using a sample of X-ray selected AGNs split between star-forming and quiescent galaxies (based on their host colour-colour diagram), Georgakakis et al. (2014) found that, below $z{\sim}1$, AGNs in blue star-forming galaxies dominate the high-$\lambda_{\rm Edd}$ end of the Eddington ratio distribution (i.e. $\lambda_{\rm Edd}{\gtrsim}\,10^{-2}$). They also report that, in contrast, the lower tail of the Eddington ratio distribution is dominated by red quiescent galaxies. These results are in agreement with those recently reported in Wang et al. (2017) who conducted a similar study but extended out to $z{\sim}2$. This emphasises the need of a more advanced model for the Eddington ratio distribution of AGNs that accounts for these observed differences between the Eddington ratio distributions of star-forming and quiescent galaxies.

Motivated by our observational results, in addition to the recent findings of a different Eddington ratio distribution for star-forming and quiescent galaxies, we propose in this chapter to explore a model where the Eddington ratio distribution of AGNs split between star-forming and quiescent galaxies. We use two independent model Eddington ratio distributions, the sum of which corresponds to the total model Eddington ratio distribution. We follow our analytical approach fully described in Chapter 4, § 4.3.1 to combine the Eddington ratio distribution with the mass function to model the X-ray luminosity function. The optimisation of each parameter that defines the model Eddington ratio distribution is performed following the MCMC process outlined in Chapter 4, § 4.3.2. In this chapter, we demonstrate that a simple

[1]Hereafter quiescent refers to the SFR. These galaxies still have a strong central activity (AGN).

model which assumes the Eddington ratio distribution is split between star-forming and quiescent galaxies is not sufficient, and fails to consistently reproduce both the X-ray luminosity function at $z\gtrsim2$ and the observed flat relationship between SFR and X-ray luminosity.

We first describe in § 5.2 our model Eddington ratio distribution. We then introduce in § 5.3 the PSM used to generate a population of host galaxies, and how we incorporate AGNs following our Eddington ratio distribution. The results regarding the model relationships between the AGN accretion properties and the host SFRs are shown in § 5.4, and their implications are discussed in § 5.5. Finally, we conclude in § 5.6.

5.2 Inferring the Eddington ratio distribution and its redshift evolution

As mentioned above, we aim to investigate the Eddington ratio distribution of AGNs split between star-forming and quiescent galaxies. This can be done by optimising a model Eddington ratio distribution that, when combined with an observed mass function, reproduces the observed X-ray luminosity function. Throughout, we use the up-to-date mass function for star-forming and quiescent galaxies reported in Davidzon et al. (2017), and the total (i.e. not split in term of star-forming and quiescent population) X-ray luminosity function of Aird et al. (2015). To separate between star-forming and quiescent galaxies, Davidzon et al. (2017) used a (NUV - r) versus (r - J) colour-colour plot, instead of the often used UVJ diagram, since it is more sensitive to recent SFR (e.g. Salim et al., 2005; Arnouts et al., 2007; Davidzon et al., 2017). The limit used in Davidzon et al. (2017) defines galaxies with specific SFR (i.e. SFR/M_*) sSFR$< 10^{-11}$ yr^{-1} as fully quiescent. This value is in agreement with studies splitting galaxies in terms of star-forming and quiescent galaxies based on the location of the MS of galaxies, at least out to z=3 (e.g. Rodighiero et al., 2011; Schreiber et al., 2015). As our results will strongly depend on the shape of the mass function, we show in Fig. 5.1 the mass functions as reported in Davidzon et al. (2017). For this model, we assume a Salpeter (1955) IMF (instead of Chabrier (2003) which was assumed so far).

5.2.1 Modelling the Eddington ratio distributions

Using our analytical approach, we demonstrate in Chapter 4, § 4.3.1 how we model the X-ray luminosity function by combining the mass function with the Eddington ratio

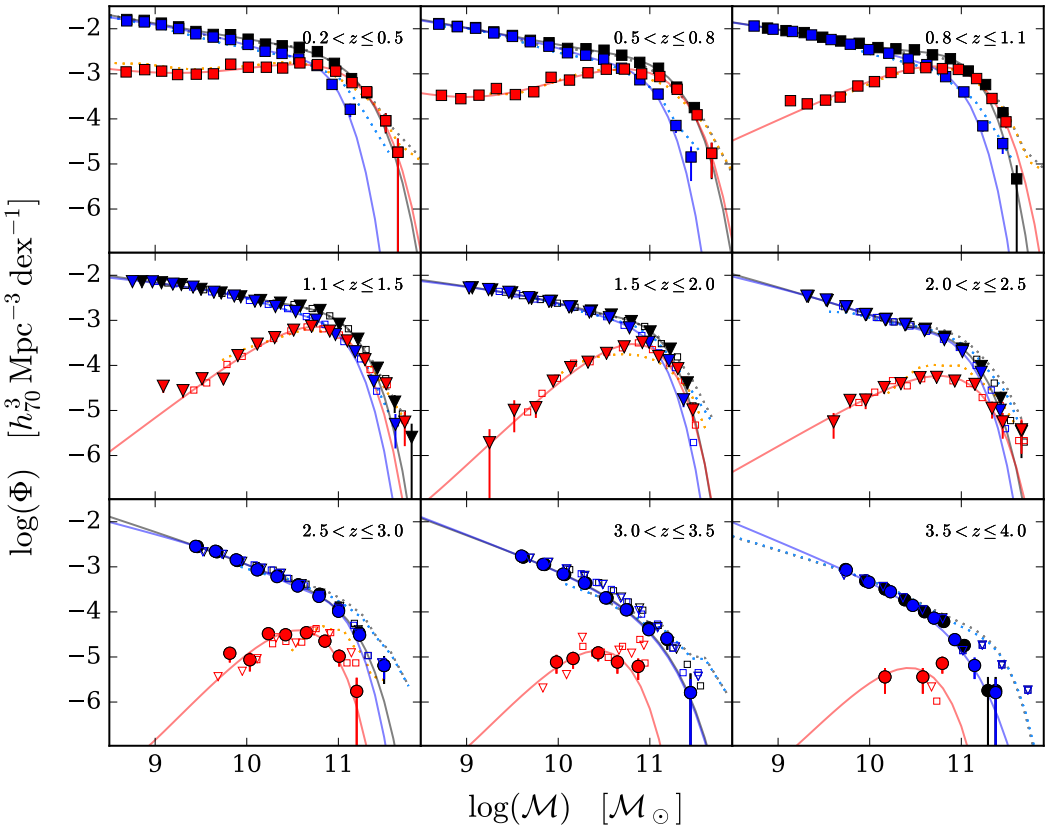

Figure 5.1: Mass function split between star-forming and quiescent galaxies out to $z{\sim}4$. The redshift is indicated in each panel on the top right-hand side. Blue colour is for star-forming and red colour is for quiescent galaxies. The various lines indicate multiple employed fitting methods. *Credits:* this figure was originally published as Fig. C.2 in Davidzon et al. (2017).

distribution. However, in our case, the Eddington ratio distribution is unknown and needs to be derived. In order to do this, we define two functions of Eddington ratio, each representing the Eddington ratio for either the star-forming or the quiescent component. Adding up these two functions (weighted by their relative numbers) gives the total Eddington ratio distribution. Many studies use a broken power-law to model the Eddington ratio distribution (e.g. Aird et al., 2013; Veale et al., 2014; Caplar et al., 2015; Jones et al., 2017). We first adopt a conservative approach by assuming that each component of our model Eddington ratio distribution is also represented by a broken power-law, which we write as,

$$p(\lambda_{\rm Edd}) = \frac{A}{\left(\frac{\lambda_{\rm Edd}}{\lambda_{\rm break}}\right)^{\gamma_1} + \left(\frac{\lambda_{\rm Edd}}{\lambda_{\rm break}}\right)^{\gamma_2}}, \tag{5.1}$$

where $p(\lambda_{\rm Edd})$ is the probability of $\lambda_{\rm Edd}$, A is the normalisation, $\lambda_{\rm break}$ is the position of the break, and γ_1 and γ_2 are the slopes at low $\lambda_{\rm Edd}$ (i.e. below the break) and high $\lambda_{\rm Edd}$ (i.e. above the break), respectively. As such, each of our broken power law components has four free parameters, giving a total of eight free parameters for this model. A sketch of our model Eddington ratio distribution split between two broken power-laws, i.e. one for the star-forming and one for the quiescent galaxies is shown in Fig. 5.2.

Assuming the two broken power-laws and their eight free parameters, we are able to use our optimisation method (see Chapter 4, § 4.3.2) to extract the parameters that best fit the observed X-ray luminosity function. However, prior to optimisation, we employ some assumptions (all based on observations) to ease the extraction of the best fitting parameters. Following results reported in e.g. Georgakakis et al. (2014); Aird et al. (2017a); Wang et al. (2017), we assume that both the normalisation, $A_{\rm SF}$, and the position of the break, $\lambda^{\rm SF}_{\rm break}$, of the star-forming component are each always higher than their quiescent analogues, $A_{\rm Qui}$ and $\lambda^{\rm Qui}_{\rm break}$. This also has the benefit of reducing the degeneracy of the model. It is important to stress, however, that we do not assume any specific parameter values for these, we simply incorporate this information by excluding some parts of the parameter space. We show in Fig. 5.3 a sketch of the boundaries used for each of the eight free parameters (i.e. defining the parameter space).

We use our optimisation method, fully described in Chapter 4, § 4.3.2 to explore the parameter space defined by the eight free parameters and extract those that, when combined with the mass functions, best fit the observed X-ray luminosity function of Aird et al. (2015). To investigate any redshift evolution, we repeat this optimisation at z=0.3, z=0.5, z=0.7, z=1.0, z=1.2, z=1.5, z=1.7, z=2.0, z=2.3, z=2.5, z=2.7,

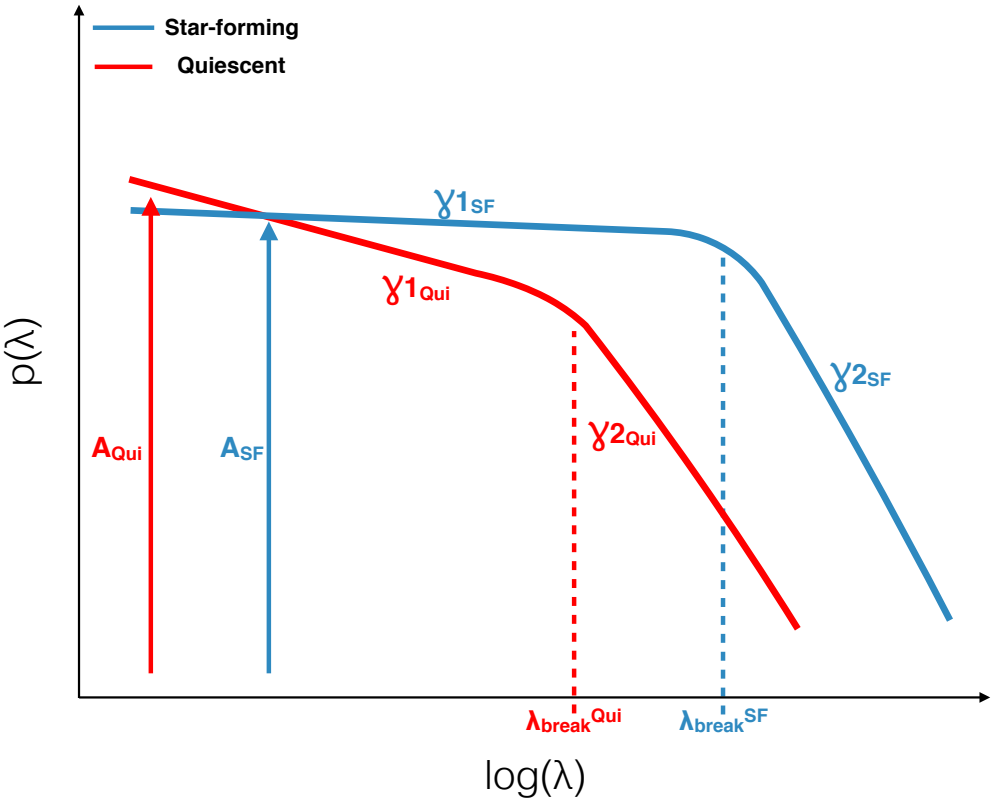

Figure 5.2: Sketch of our model Eddington distribution split between a star-forming (in blue) and a quiescent (in red) component. Each of these is represented by a broken power-law with, A, a normalisation, $\lambda_{\rm break}$, a position of the break, γ_1, a slope at low Eddington ratio, and, γ_2, a slope at high Eddington ratio. The scripts "SF" and "Qui" stand for star-forming and quiescent, respectively.

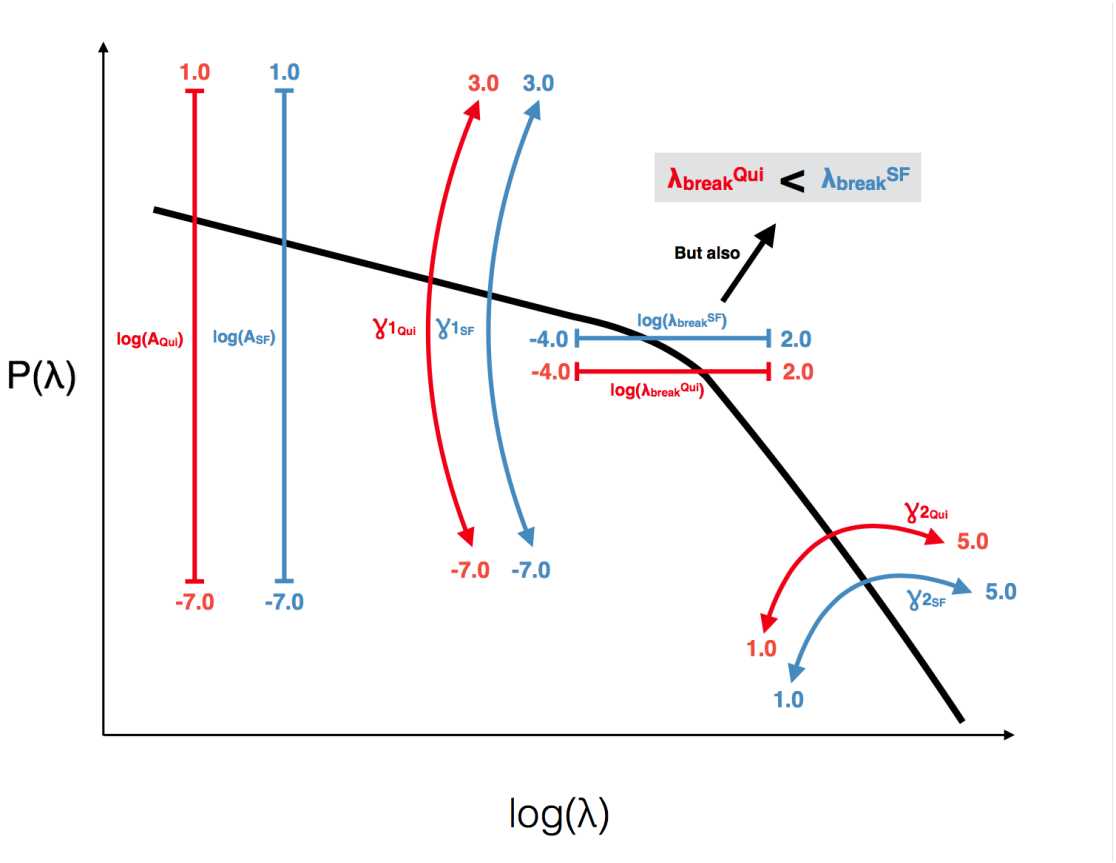

Figure 5.3: Sketch of the boundaries within which the best fitting solution is explored. Blue colour is for the star-forming component and red colour is for the quiescent one. Values at the end of each arrow and range indicate the boundaries in which our optimisation method operates (i.e. define the parameter space).

z=3.0, and z=3.5. We fit the X-ray luminosity functions of Aird et al. (2015) interpolated at these redshifts, using the redshift evolution provided in their study (i.e. we do not fit their observed data points given for different redshift bins). We show in Appendix B, Fig. B.1 an example of the posterior distribution at z=1.0 from which the parameters were extracted (see Chapter 4, 4.3.2 for extraction from the posterior distribution).

5.2.2 X-ray luminosity functions

In Fig. 5.4 we show the fit to the X-ray luminosity function for our model. Up to $z\sim$1.75 our total X-ray luminosity functions are in very good agreement with those of Aird et al. (2015). However, beyond this redshift, our model is unable to reproduce the observed X-ray luminosity function. We find that at these redshifts our model under-predicts the knee of the observed X-ray luminosity function (i.e. between $10^{43.5} \lesssim L_X \lesssim 10^{44.5}$ erg s^{-1}). Fig. 5.4 also illustrates the model X-ray luminosity function split between star-forming and quiescent galaxies. Overall, we find that the star-forming galaxies always dominate the X-ray luminosity functions at $L_X \gtrsim 10^{42.5}$ erg s^{-1} which corresponds to the bulk of the AGN population. The contribution from quiescent galaxies, in our model, to the total X-ray luminosity function, however, is only significant at lower X-ray luminosities (i.e. $L_X \lesssim 10^{42}$ erg s^{-1}).

Beyond $z\sim$2, our model cannot reproduce the observed X-ray luminosity function. We find that the contribution from quiescent galaxies to the total X-ray luminosity function is very low compared to that of the star-forming galaxies. To explain the reasons for this, we examine the stellar mass function of Davidzon et al. (2017). They report that the contribution from quiescent galaxies to the mass function decreases as the redshift increases (the knee of the mass function for quiescent galaxies is at least a factor of ten in normalisation below that of the star-forming galaxies at $z\gtrsim$2; see Fig. 5.1). This lower contribution from the quiescent galaxies to the total mass function at higher redshifts can be compensated in our model by an increase in the normalisation of the model Eddington ratio distribution for quiescent galaxies (as our model relates the mass function to the Eddington ratio distribution). However, in our model, the normalisation of the quiescent galaxy component cannot exceed that of the star-forming component. As illustrated in Fig. 5.5, top left-hand panel, the normalisation of the Eddington ratio distribution for quiescent galaxies reaches its maximum value for our model beyond $z\sim$2 (i.e. $A_{\rm SF} \sim A_{\rm Qui}$). For that reason, the contribution from quiescent galaxies to the total X-ray luminosity function cannot increase enough to match the observed X-ray luminosity function. Should we relax

this assumption (see § 5.2.5), our model would find that beyond $z{\sim}2$ a significant fraction of AGNs live in quiescent galaxies compared to star-forming hosts. However, this is against observational studies that find that AGNs predominantly reside in MS star-forming galaxies (e.g. Mullaney et al., 2015; Stanley et al., 2015).

As beyond $z{\sim}2$ our model cannot increase the contribution from quiescent galaxies to the total X-ray luminosity function, it attempts to use only star-forming galaxies, but fails. We find that the faint-end of the model X-ray luminosity function for star-forming galaxies is too steep to reproduce the observed flat faint-end of the X-ray luminosity function at these redshifts. Caplar et al. (2015) have demonstrated that the faint-end slope of the X-ray luminosity function is determined by whichever is the steeper of either the low-mass end of the mass function or the low-$\lambda_{\rm Edd}$ end of the Eddington ratio distribution. Davidzon et al. (2017) report a steepening with redshift of the slope at the low-mass end of their mass function (see Fig. 5.1). Conversely, Aird et al. (2015) find a flattening of the faint-end slope of the X-ray luminosity function. For that reason, our model is unable to reproduce the total X-ray luminosity function beyond $z{\sim}2$ by using only star-forming galaxies (i.e. the low mass-end of the mass function is too steep). This motivates a mass-dependent model for the Eddington ratio distribution of star-forming galaxies where the contribution from low mass galaxies to the total Eddington ratio is lower compared to that of higher mass galaxies. We will explore this further in Chapter 6.

Finally, as a further check, we include in Fig. 5.4 the measured X-ray luminosity function separated into star-forming and quiescent galaxies at $z{<}1$ reported in Georgakakis et al. (2014). Despite not including this information during our optimisation, we find good agreement between our model and these observed X-ray luminosity functions of star-forming and quiescent galaxies, increasing our confidence in the model at these redshifts.

Our model is able to provide a realistic fit to the X-ray luminosity function out to $z \sim 2$. Beyond this redshift, we find that our model under-predicts the knee of the X-ray luminosity function (i.e. between $10^{43.5} {<} L_X {<} 10^{44.5}$ erg s^{-1}), and fails at reproducing the observed X-ray luminosity function. We now explore how the Eddington ratio distribution evolves with redshift.

5.2.3 Redshift evolution of our Eddington ratio distributions

To investigate how the Eddington ratio distribution evolves with redshift, we examine how each of the eight parameters which define our Eddington ratio distribution evolves with redshift. As our model fails at reproducing the X-ray luminosity func-

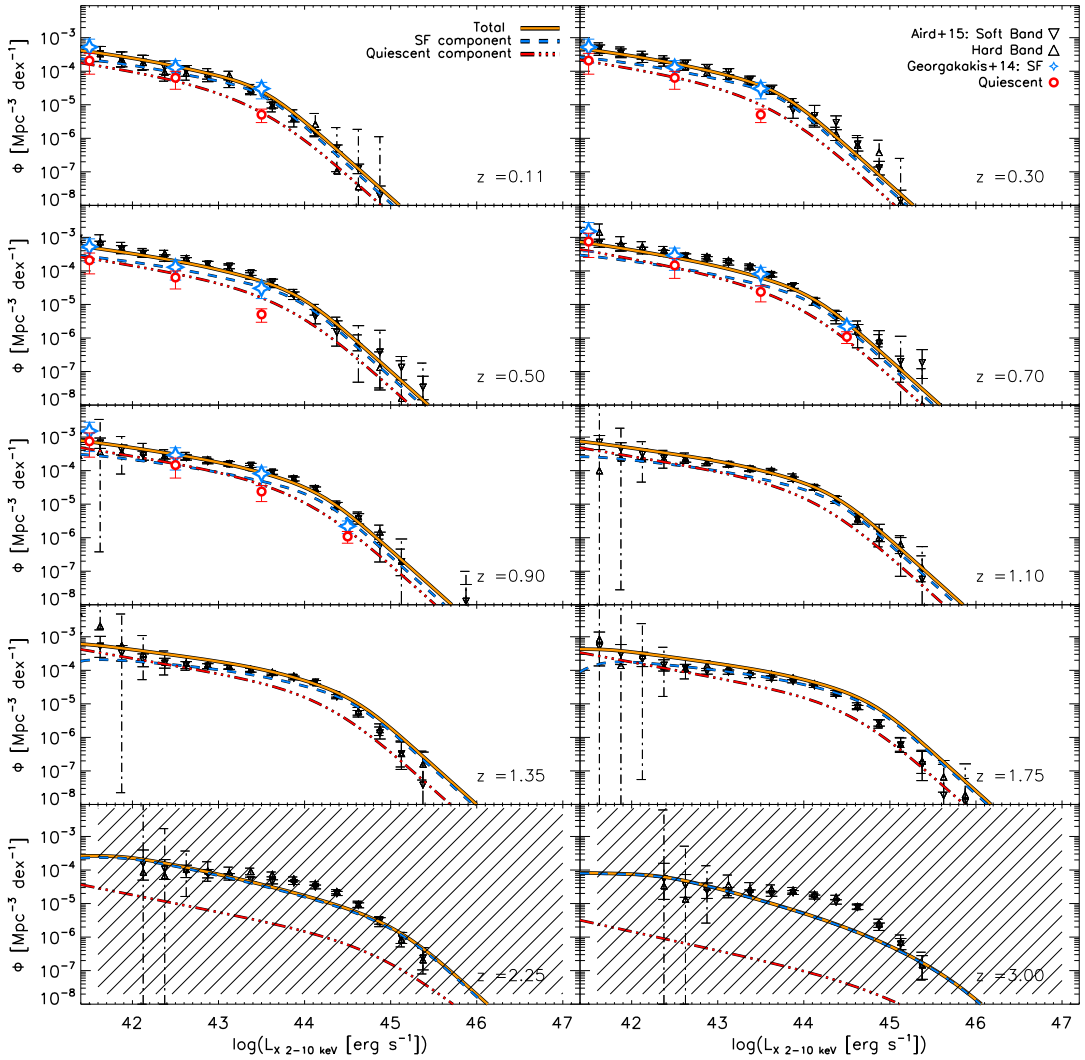

Figure 5.4: Fit to the X-ray luminosity functions out to $z\sim3$. Each panel represents a different redshift bin, as indicated at the bottom right-hand side. These redshift bins correspond to those of Aird et al. (2015). The orange line shows the total model X-ray luminosity function, the blue dashed line shows the star-forming galaxy component, and the red triple-dashed line shows the quiescent galaxy component. Upward and downward triangles are observed values from Aird et al. (2015) for the soft band and the hard band, respectively. Blue empty stars are the observed X-ray luminosity function for star-forming galaxies as reported in Georgakakis et al. (2014), and red empty circles are the same but for quiescent galaxies. We find a good agreement between our model X-ray luminosity function and the observed one out to $z\sim2$, including when split between star-forming and quiescent galaxies at least up to $z\sim1$. However, our model is unable to reproduce the observed X-ray luminosity function beyond $z\sim2$.

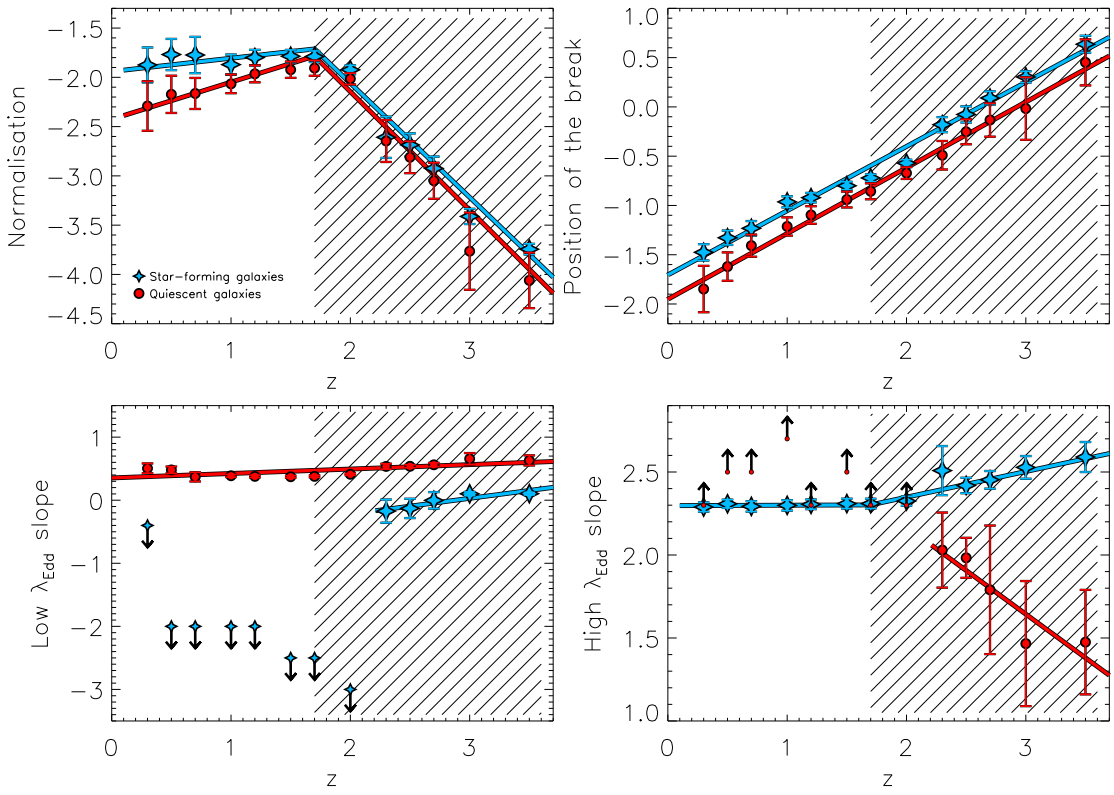

Figure 5.5: Redshift evolution of the parameters that define our model Eddington ratio distribution. Blue stars are for the parameters that define the Eddington ratio for star-forming galaxies and red circles are the same but for quiescent galaxies. The top left-hand panel shows the normalisations, the top right-hand panel displays the positions of the breaks, the bottom left-hand panel exhibits the low $\lambda_{\rm Edd}$ slope, and the bottom right-hand panel shows the high $\lambda_{\rm Edd}$ slope. Upward and downward arrows indicate lower and upper-limits, respectively. The shaded area in each panel indicates the redshifts for which our model is unable to give a good fit to the observed X-ray luminosity function (see Fig 5.4).

tion beyond $z{\sim}2$, we first investigate the redshift evolution of our Eddington ratio distribution below this redshift, before considering higher redshifts.

In Fig. 5.5, we present the redshift evolution of each of the optimised parameters. As expected (i.e. assumed in our model, see § 5.2.1), the normalisation of the star-forming component is higher than that of the quiescent one. We report that the normalisation of the star-forming and the quiescent component both slightly increases with increasing redshift to $z{\sim}2$, and we note a slightly faster increase for that of the quiescent component (see top left-hand panel in Fig. 5.5). This suggests that the relative number of AGNs in quiescent galaxies increases with redshift, compared to the number of AGNs in star-forming galaxies. We also find that the position of the break for the star-forming and the quiescent component both strongly increase with increasing redshift at a very similar rate (i.e. slope of ∼0.6; see top right-hand panel in Fig. 5.5), indicating a higher AGN activity at higher redshifts. More importantly, we report that the low-$\lambda_{\rm Edd}$ end of the Eddington ratio distribution for star-forming galaxies is consistent with a rising slope (i.e. negative γ_1 in Eq 5.1). However, we note we are only able to provide upper-limits for this parameter (see bottom left-hand panel in Fig. 5.5). A consequence of the rising slope is that the Eddington ratio distribution for star-forming galaxies in our model is best described by a "peaky" distribution, similar to the light-bulb distributions sometimes used in recent studies (e.g. Hickox et al., 2014; Veale et al., 2014; Stanley et al., 2015). This suggests that the star-forming galaxies exclusively host AGNs with $\lambda_{\rm Edd}$ typical of the higher-end of the Eddington ratio distribution (i.e. $\log(\lambda_{\rm Edd}){\gtrsim}$-1.5). In contrast, the low-$\lambda_{\rm Edd}$ slope of the Eddington ratio distribution for quiescent galaxies is consistent with a decreasing slope (i.e. positive γ_1 in Eq 5.1), and does not evolve significantly with redshift. This indicates that lower accretion rate AGNs tend to reside in less star-forming galaxies. Finally, we find that the high-$\lambda_{\rm Edd}$ slopes of the Eddington ratio distribution for both star-forming and quiescent galaxies are consistent, although we only have lower-limits for the slope of the quiescent component (see bottom right-hand panel in Fig. 5.5). We do not find any significant redshift evolution of these last parameters out to $z{\sim}2$.

Beyond $z{=}1.7$ we see a significant break toward lower values in the redshift evolution of the normalisation of both star-forming and quiescent component, with both normalisations almost identical, suggesting a similar number of AGNs in quiescent hosts relative to star-forming host galaxies. We further note a mild break in the slope at high $\lambda_{\rm Edd}$ for the star-forming component toward higher values (i.e. steeper slope). We do not notice any similar behaviour of the position of the break for both star-forming and quiescent galaxies, with a redshift evolution beyond $z{=}1.7$ consis-

tent with the redshift evolution at lower redshift. We also see no break in the redshift evolution of the slope at lower Eddington ratio. However, beyond z=1.7, the slope at low Eddington ratio for the star-forming component becomes consistent with a flat (or very mildly rising) slope, in contrast to the strong rising slope reported below this redshift. However, this must be related to the attempt of our model to fit the total X-ray luminosity function using only star-forming galaxies (see § 5.2.2). Finally, the slope at higher $\lambda_{\rm Edd}$ for the quiescent component decreases with redshift beyond z=1.7 (i.e. shallower slope). However, we reiterate that our model *is unable* to satisfactorily reproduce the X-ray luminosity function at these higher redshifts (see § 5.2.2). We argue that it is related to the low contribution from the quiescent galaxies to the total X-ray luminosity function. We can observe this in the top left-hand panel of Fig. 5.5 where the normalisation of the Eddington ratio distribution of the quiescent population beyond $z{\sim}2$ reaches its maximum value allowed in our model (i.e. cannot exceed that of the star-forming component).

We performed a linear fit to see how each parameter changes with redshift, assuming a break at z=1.7 when necessary (i.e. the normalisation and the high-$\lambda_{\rm Edd}$ slope for the star-forming component). We estimated the 1σ uncertainties on the fitting parameters by measuring the standard deviation of 1000 Monte-Carlo realisations. All the fitting parameters and their associated uncertainties are given in Table 5.1.

Each of the aforementioned trends can be seen in the evolution of the overall $\lambda_{\rm Edd}$ distributions, which we plot in Fig. 5.6. Here, each distribution has been normalised such that it integrates to unity after applying a cut at $\lambda_{\rm Edd}= 10^{-7}$ when diverging. Arrows in this figure indicate the overall effects of parameters that are upper and lower-limits to the Eddington ratio distribution.

One of our main findings is that, although it was not implemented prior to optimisation, the Eddington ratio distribution for star-forming galaxies is consistent with a "peaky" distribution, similar to the "light-bulb" distributions sometimes used in similar studies (e.g. Hickox et al., 2014; Veale et al., 2014; Stanley et al., 2015). This suggests, interestingly, that star-forming galaxies exclusively prefer AGNs with higher Eddington ratios (i.e. $\lambda_{\rm Edd}{\sim}0.1$), while quiescent host AGNs span a wide range of $\lambda_{\rm Edd}$ (i.e. $0.001{\lesssim}\lambda_{\rm Edd}{\lesssim}1$). However, we are only able to derive upper-limits on the slope at low-$\lambda_{\rm Edd}$, γ_1, for the star-forming component. As a consequence, prior to investigating further how the Eddington ratio distribution relates to the star-forming properties of the host galaxies, we attempt a different model where the Eddington ratio distribution for star-forming galaxies is explicitly represented by a "peaky" distribution (instead of a broken power law). This aims to give a tighter constraint to the low-$\lambda_{\rm Edd}$ slope of the Eddington ratio distribution for star-forming

Table 5.1: Redshift evolution of the parameters that describe the Eddington ratio distribution for star-forming and quiescent galaxies, described by Eq. 5.1. SF and Qui labels stand for star-forming and quiescent, respectively. The slopes and intercepts are given for an evolution in $(1+z)$. Uncertainties on the parameters are the standard deviation of a 1000 Monte-Carlo realisations (i.e. 1σ).

Parameters	Intercepts	Slopes	
$\log(A_{\rm SF})$	$-2.07^{\pm0.19}$	$0.13^{\pm0.07}$	for $z<1.7$
		$-1.15^{\pm0.03}$	for $z>1.7$
$\log(A_{\rm Qui})$	$-2.80^{\pm0.23}$	$0.37^{\pm0.10}$	for $z<1.7$
		$-1.20^{\pm0.11}$	for $z>1.7$
$\log(\lambda_{\rm break}^{\rm SF})$	$-2.36^{\pm0.06}$	$0.65^{\pm0.02}$	
$\log(\lambda_{\rm break}^{\rm Qui})$	$-2.62^{\pm0.16}$	$0.66^{\pm0.06}$	
$\gamma_1^{\rm SF}$	$\lesssim -3.0$	0.0	for $z<1.7$
	$-0.96^{\pm0.51}$	$0.25^{\pm0.12}$	for $z>1.7$
$\gamma_1^{\rm Qui}$	$0.28^{\pm0.05}$	$0.07^{\pm0.02}$	
$\gamma_2^{\rm SF}$	$2.29^{\pm0.04}$	$0.01^{\pm0.02}$	for $z>1.7$
		$0.15^{\pm0.03}$	for $z>1.7$
$\gamma_2^{\rm Qui}$	$\gtrsim 2.7$	0.0	for $z<1.7$
	$3.75^{\pm2.33}$	$-0.53^{\pm0.63}$	for $z>1.7$

Notes: Slopes and intercepts are given for an evolution as a function of $(1+z)$. The intercept for $z>1.7$, when assuming a break in the z evolution of the parameter, is given by the continuity at $z=1.7$ (i.e. [intercept for $z > 1.7$] = $(1 + 1.7) \times$ ([slope for $z < 1.7$] − [slope for $z > 1.7$]) + [intercept for $z < 1.7$]).

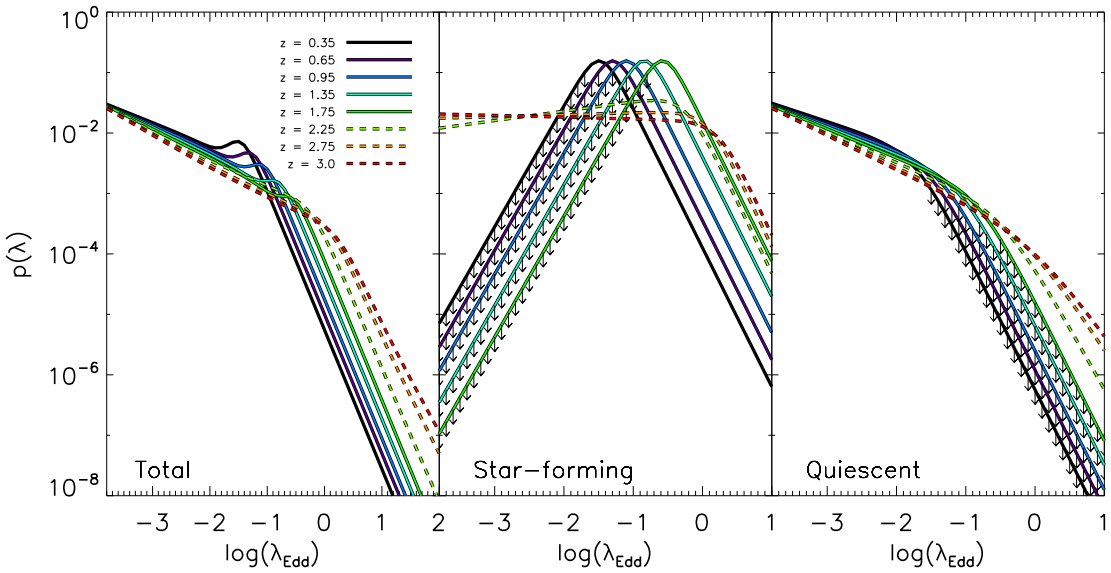

Figure 5.6: Model Eddington ratio distribution out to z=3. The left-hand panel shows the total model Eddington ratio distribution returned by our optimisation method out to z=3. The middle and right-hand panels are for that of the star-forming and the quiescent component, respectively. Colours are for different redshifts (see keys). Downward arrows indicate the effects of the upper and lower-limits found in the parameters that define these Eddington ratio distributions (see Fig. 5.5). The dashed lines are the Eddington ratio distributions for which our model cannot reproduce the observed X-ray luminosity function (i.e. beyond $z\sim$2; see Fig 5.4). Each distribution has been normalised such that it integrates to unity after applying a cut at $\lambda_{\rm Edd}= 10^{-7}$ when diverging.

galaxies, and to improve the fit to the X-ray luminosity function beyond $z{\sim}2$.

5.2.4 A "Peaky" distribution for the star-forming component

On fitting the X-ray luminosity function with the double broken power-law for the Eddington ratio distribution we found that, at least for $z{\lesssim}2$, the best-fitting results *always* required that the distribution for star-forming galaxies peaked at the position of the break (i.e. a positive slope below the break and a negative slope above the break). This is qualitatively similar in shape to the "light-bulb" distributions considered in some models (e.g. Hickox et al., 2014; Veale et al., 2014; Stanley et al., 2015). Following this finding, we replaced the broken power-law for star-forming galaxies with an inverted Gamma function (i.e. shape similar to that of the "light-bulb"; see Fig. 5.7) defined as,

$$p(\lambda_{\rm Edd}) = \frac{A_{\rm SF}}{\Gamma(k)\ \theta^k} \left(\frac{1}{\lambda_{\rm Edd}}\right)^{k-1} \exp\left(-\frac{1}{\lambda_{\rm Edd}\ k}\right), \tag{5.2}$$

where $p(\lambda_{\rm Edd})$ is similar to that of Eq. 5.1, $A_{\rm SF}$ is the normalisation, k is the "shape", and θ is the "scale" ($\Gamma(k)$ is the Gamma function evaluated at k). We chose an inverted Gamma distribution instead of a Gaussian since the higher-$\lambda_{\rm Edd}$ slope of the inverted Gamma distribution is similar in shape to that of a broken power-law. This component has three free parameters. We retain the broken power-law model for the quiescent galaxies, giving a total of seven free parameters for this new model. We show in Fig. 5.7 a sketch of this second model for the Eddington ratio distribution (i.e. assuming the "peaky" distribution for star-forming galaxies) indicating the meaning of the seven free parameters.

We repeat the optimisation for these seven free parameters (see Chapter 4, § 4.3.2), keeping the prior information stating that the Eddington ratio distribution for star-forming galaxies *must peak* at higher values than the break of the distribution for the quiescent ones (e.g. Georgakakis et al., 2014; Aird et al., 2017a; Wang et al., 2017). The different boundaries defining the parameter space to explore are sketched in Fig. 5.8. To investigate any redshift evolution, we again repeat the optimisation at z=0.3, z=0.5, z=0.7, z=1.0, z=1.2, z=2.0, z=2.2, and z=2.5. We show in Appendix B, Fig. B.2 an example of the posterior distribution at z=2.2 from which the parameters have been extracted.

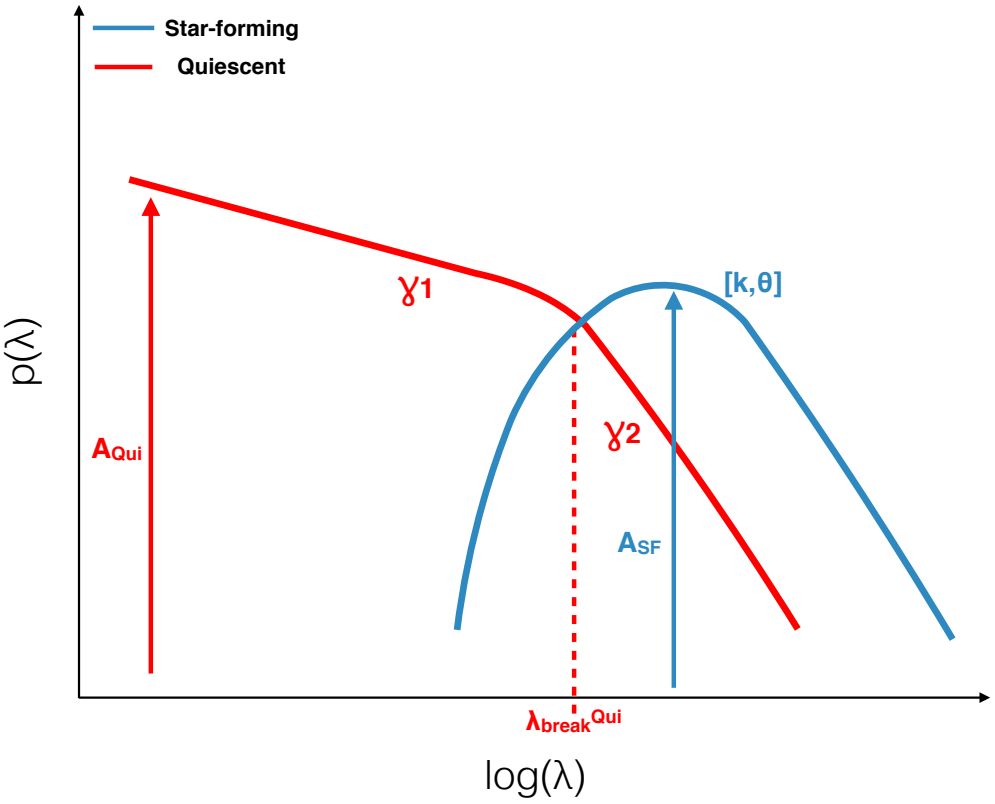

Figure 5.7: Sketch of our model Eddington ratio distribution that assumes a "peaky" function for the star-forming galaxies, instead of the previously used broken power-law. The component of the Eddington ratio distribution for star-forming galaxies is shown in blue, while that of quiescent galaxies is shown in red. The distribution used for the star-forming component is an inverse-Gamma distribution with a normalisation ($A_{\rm SF}$), a shape (k), and a scale (θ). For quiescent galaxies we keep the broken power-law distribution with similar parameters than these of Fig. 5.2. "SF" and "Qui" subscripts stand for star-forming and quiescent, respectively.

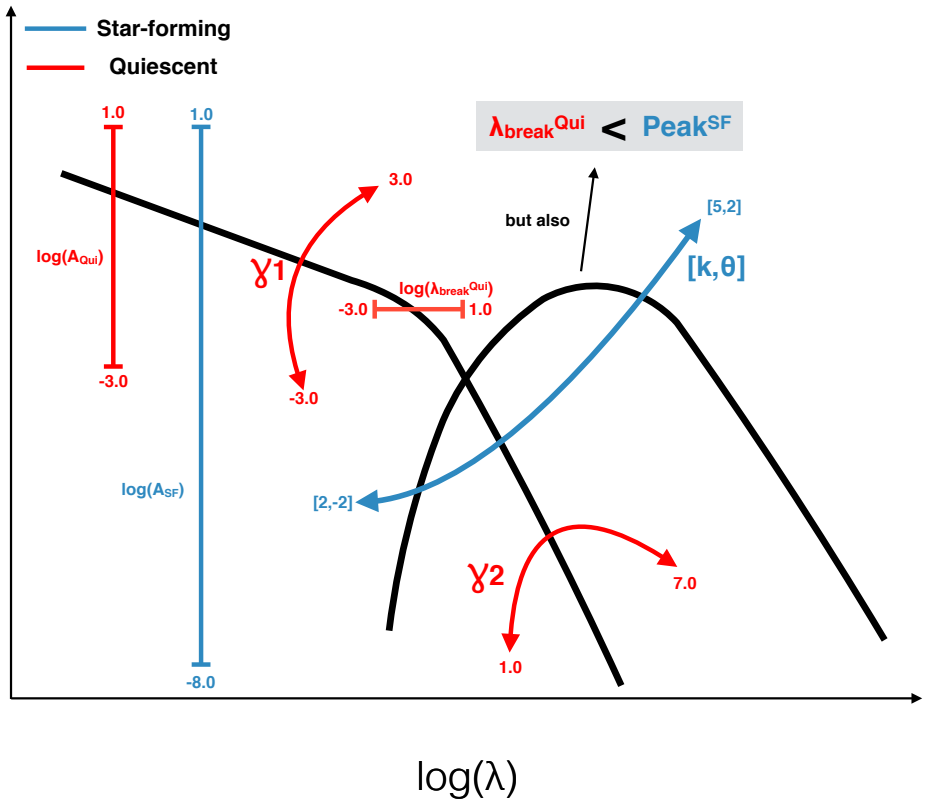

Figure 5.8: Sketch of the boundaries used to define the parameter space for our model that assumes a "peaky" distribution for the star-forming component of the Eddington ratio distribution. The black lines indicate the shape of each component, the "peaky" one being the star-forming galaxy one. The arrows and ranges indicate the boundaries in which our optimisation method operates (i.e. showing the parameter space). Parameters are as described in Fig. 5.7. The grey box indicates our assumption that the Eddington ratio distribution for star-forming galaxies ($\rm Peak^{SF}$) must peak at higher $\lambda_{\rm Edd}$ values than the knee of the distribution of the quiescent galaxies ($\lambda^{\rm Qui}_{\rm break}$).

5.2.5 Updated X-ray luminosity functions

We show in Fig. 5.9 the results of the fit to the X-ray luminosity function for our second model (i.e. assuming the "peaky" distribution for the star-forming component of the Eddington ratio distribution). Up to $z{\sim}3$ our model total X-ray luminosity function is in very good agreement with the observed one of Aird et al. (2015). This constitutes an improvement from our previous model that was unable to reproduce the X-ray luminosity function beyond $z{\sim}2$. This is a consequence of relaxing the assumption on the normalisations (i.e. in our previous model, we specify that the normalisation of the star-forming component must be higher than that of the quiescent one). We also show in Fig. 5.9 the model X-ray luminosity function split between star-forming and quiescent galaxies. We find that, up to $z{\sim}2$, the star-forming galaxies dominate the brightest end of the X-ray luminosity function (i.e. $L_X{\gtrsim}\ 10^{44}$ erg s^{-1}), whereas the contribution from quiescent galaxies to the total X-ray luminosity function is only significant at lower X-ray luminosities (i.e. $L_X{\lesssim}\ 10^{43}$ erg s^{-1}). These results are consistent with those reported in our previous model (see § 5.2.2). In contrast, beyond $z{\sim}2$, this model predicts that the X-ray luminosity function is dominated by quiescent galaxies to very high luminosities (i.e. at $L_X{<}\ 10^{45.5-46}$ erg s^{-1}), as suggested in the previous model, should we have relaxed the assumption on the normalisations. We note, however, that this is still inconsistent with observations (e.g. Mullaney et al., 2015; Stanley et al., 2015) as it implies that beyond $z{\sim}2$ the vast majority of AGNs are hosted in quiescent galaxies. This behaviour of our model is again a consequence of the steep negative slope of the stellar mass function of star-forming galaxies at high redshifts (i.e. at $z \gtrsim 2$) and low masses (see Fig. 5.1), which contrasts against the much flatter low luminosity end of the X-ray luminosity function at these same redshifts (Aird et al., 2015). Faced with this situation, it is impossible for this model to reproduce the X-ray luminosity function using predominantly star-forming galaxies. A similar situation was also encountered in Jones et al. (2017) while using a universal broken power-law for the Eddington ratio distribution of all galaxies (i.e. not split in term of star-forming and quiescent populations). They reported that, beyond $z{\sim}1.2$, their model was unable to reproduce the flat faint-end of the X-ray luminosity function. Since our model has more degrees of freedom (i.e. two components instead of one in Jones et al. 2017), and that the mass function for quiescent galaxies is narrower than that of the star-forming galaxies beyond $z{\sim}2$ (see Fig. 5.1), we are able to reproduce the total X-ray luminosity function at these redshifts, but at the cost of having ≈100 per cent of AGNs in quiescent galaxies at higher redshifts. This further motivates the need for a mass-dependent Eddington ratio distribution for star-forming galaxies, as recently

reported in Aird et al. (2017a). This will be fully explored in Chapter 6.

Finally, as a further check, we include in Fig. 5.9 the measured X-ray luminosity functions separated into star-forming and quiescent galaxies at $z<1$ reported in Georgakakis et al. (2014). Despite not including this information during our optimisation, we find good agreement between our second model and these observed X-ray luminosity functions of star-forming and quiescent galaxies, increasing our confidence in this second model at these redshifts.

The main difference between the model that assumes a "peaky" distribution for star-forming galaxies to that of our previous model (i.e. assuming a broken power-law for the Eddington ratio distribution of star-forming galaxies) is the behaviour at $z\gtrsim2$. While our first model was unable to reproduce the X-ray luminosity function at these redshifts, our second model is able to do so, but still produces results that are inconsistent with observations when examining the split in term of star-forming and quiescent galaxies.

5.2.6 Updated redshift evolution of our Eddington ratio distributions

As we have seen, this second model gives reasonable fit of the X-ray luminosity function at all redshifts, but puts too many AGNs in quiescent galaxies at $z\gtrsim2$. To investigate how the Eddington ratio distribution evolves with redshift in this second model, we now explore how the seven free parameters describing our model evolve with redshift to $z\sim2$.

In Fig. 5.10, we present the redshift evolution of each of the optimised parameters that define our Eddington ratio distribution for our second model. The top panel shows the ratio of the star-forming over the quiescent normalisation (i.e. $A_{\rm SF}/A_{\rm qui}$), the left-hand panels show parameters that define the Eddington ratio distribution for star-forming galaxies (i.e. θ and k in Eq. 5.2) while the right-hand panels are for those of the quiescent population (i.e. $\lambda_{\rm break}$, γ_1, γ_2 in Eq. 5.1). As expected, the normalisation of the star-forming component is higher than that of the quiescent component up to $z\sim2$. This indicates that AGNs are predominantly found in star-forming galaxies. We find very little evolution in the shape parameter (k) of the inverse-Gamma distribution used for star-forming galaxies, but note that the scale parameter decreases with increasing redshift (which corresponds to a shift in the distribution toward *higher* $\lambda_{\rm Edd}$ with increasing redshift; see Fig. 5.11 central panel). This again suggests a higher accretion activity at higher redshifts. For quiescent galaxies, we find that the position of the break shifts to higher $\lambda_{\rm Edd}$ values with

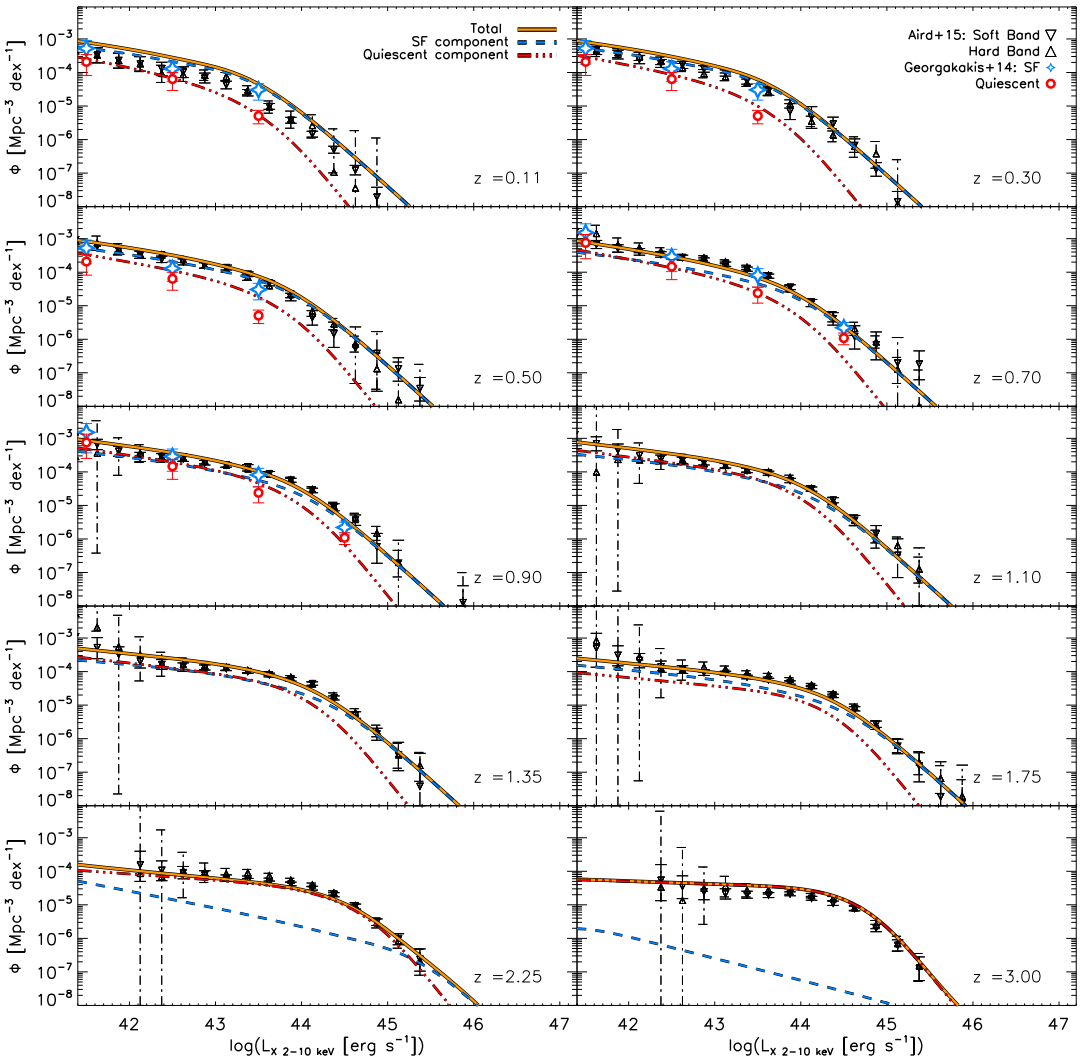

Figure 5.9: Fit to the X-ray luminosity functions out to z=3 while using a "peaky" Eddington ratio distribution for the star-forming component. Each panel represents a different redshift bin, as indicated on the bottom right-hand side. These redshift bins correspond to those of Aird et al. (2015). The orange line shows the total model X-ray luminosity function, the blue dashed line shows the star-forming galaxy component, and the red triple-dashed line shows the quiescent galaxy component. Upward and downward triangles are observed values from Aird et al. (2015) for the soft band and the hard band, respectively. Blue empty stars are the observed X-ray luminosity functions for star-forming galaxies as reported in Georgakakis et al. (2014), and red empty circles are the same but for quiescent galaxies. We find a very good fit to the observed total X-ray luminosity function out to z=3. However, our model places too many AGNs in quiescent galaxies beyond $z\sim$2.

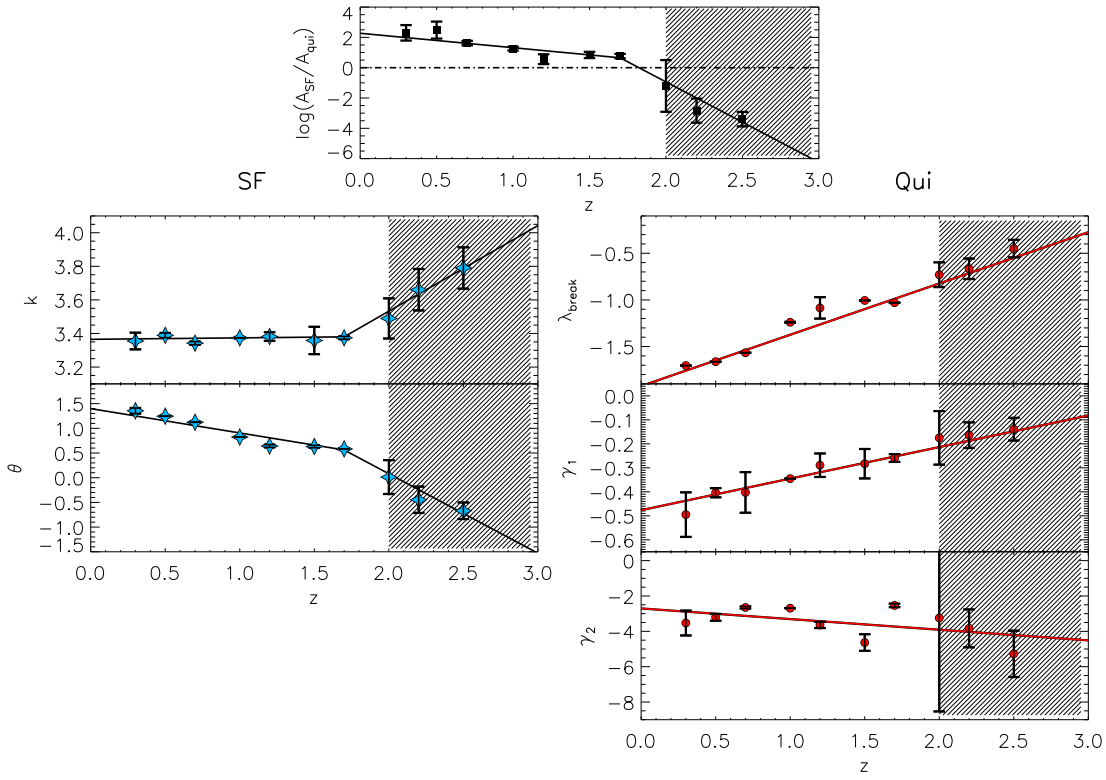

Figure 5.10: Redshift evolution of each parameter that defines the model Eddington ratio distribution when assuming a "peaky" distribution for the star-forming component. The top panel shows the ratio between the normalisation of the star-forming component and the quiescent one ($\log(A_{\rm SF}/A_{\rm Qui})$). The left-hand side panels are for the parameters that define the Eddington ratio distribution for star-forming galaxies (i.e. k and θ), and the right-hand side panels are for these of the quiescent galaxies (i.e. $\lambda_{\rm break}$, γ_1 and γ_2). Lines are for the best linear fit, allowing a break at z=1.7 when necessary (i.e. $\log(A_{\rm SF}/A_{\rm Qui})$, k, and θ). The shaded area beyond z=1.7 is to indicate that our model fails at splitting the X-ray luminosity function between star-forming and quiescent galaxies at these redshifts (see Fig. 5.9).

Table 5.2: Redshift evolution of the parameters that define our Eddington ratio distribution for our model that assumes a "peaky" distribution. The slopes and intercepts are given for an evolution in $(1+z)$. Uncertainties on the parameters are the standard deviation of a 1000 Monte-Carlo realisations (i.e. 1σ).

Parameters	Intercepts	Slopes	
$\log(A_{\rm SF}/A_{\rm qui})$	$3.71^{\pm0.33}$	$-0.95^{\pm0.33}$	for $z<1.7$
		$-5.31^{\pm0.01}$	for $z>1.7$
k	$3.36^{\pm0.04}$	$0.009^{\pm0.01}$	for $z<1.7$
		$0.51^{\pm0.01}$	for $z>1.7$
θ	$1.89^{\pm0.06}$	$-0.49^{\pm0.07}$	for $z<1.7$
		$-1.60^{\pm0.01}$	for $z>1.7$
$\lambda_{\rm break}$	$-2.47^{\pm0.01}$	$0.54^{\pm0.01}$	
γ_1	$-0.61^{\pm0.03}$	$0.13^{\pm0.01}$	
γ_2	$-2.10^{\pm0.03}$	$-0.60^{\pm0.01}$	

Notes: Slopes and intercepts are given for an evolution as a function of $(1+z)$. The intercept for $z>1.7$ when assuming a break in the z evolution of the parameters is given by the continuity at $z=1.7$ (i.e. [intercept for $z > 1.7$] $= (1+1.7) \times$ ([slope for $z < 1.7$] $-$ [slope for $z > 1.7$]) $+$ [intercept for $z < 1.7$]).

increasing redshift (which is similar to the shift in the peak of the $\lambda_{\rm Edd}$ distribution for star-forming galaxies), together with a flattening of the low-end slope (γ_1) to less negative values. In contrast, the high-end slope of the $\lambda_{\rm Edd}$ distribution for quiescent galaxies (γ_2) steepens (i.e. gets more negative) with increasing redshift.

Beyond $z=1.7$ we see a break in the evolution of all the parameters associated with star-forming galaxies, yet the evolution in the parameters for quiescent galaxies remains consistent with that at $z<1.7$. However, we reiterate the problems our model encounters at these high redshifts (see § 5.2.5).

We also performed a linear fit of each parameter with redshift to parametrise the evolution with redshift for this second model, assuming a break at $z=1.7$ when necessary (i.e. for $A_{\rm SF}/A_{\rm qui}$, θ, and k). Again, we estimated the 1σ uncertainties on the fitting parameters by measuring the standard deviation of 1000 Monte-Carlo realisations. All the fitting parameters and their associated uncertainties are given in Table 5.2.

As with the previous model, each of the aforementioned trends for our second model can be seen in the evolution of the overall Eddington ratio distributions, which we plot in Fig. 5.11. Here, again, each distribution has been normalised such that it integrates to unity after applying a cut at $\lambda_{\rm Edd}= 10^{-7}$ when diverging.

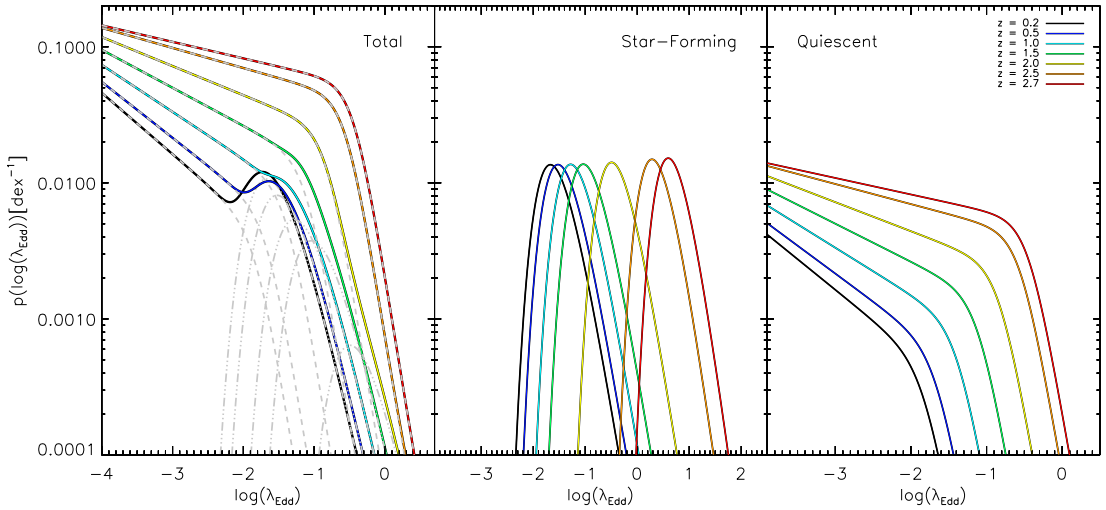

Figure 5.11: Model Eddington ratio distributions when assuming a "peaky" distribution for the star-forming component. The left-hand panel shows the total Eddington ratio distributions out to z=2.7. Also in the left-hand panel, shown with grey dashed lines are the star-forming and quiescent components of the total Eddington ratio distributions. The central panel shows that of the star-forming galaxies and the right-hand panel that of the quiescent galaxies. Each distribution is normalised such that it integrates to unity after applying a cut at $\lambda_{\rm Edd}$=10^{-7} when diverging. Colours indicate different redshifts (see keys).

Overall, we find that there is no significant change between our previous model and this second model in terms of the Eddington ratio distribution shape and its redshift evolution. However, a benefit of defining a "peaky" distribution for the Eddington ratio distribution of star-forming galaxies is that all the parameters are now defined, meaning we no longer have upper and lower-limits. Furthermore, we find that the second model can better fit the total X-ray luminosity function to higher redshift than our first model, although it still provides an inconsistent split between star-forming and quiescent galaxies. In the following subsection we adopt the second model to investigate how the Eddington ratio distribution relates to the star-forming properties of their host galaxies as it gives better results overall.

5.3 AGN-host galaxies population synthesis model

By fitting the X-ray luminosity function of Aird et al. (2015), we now hold a solution for the Eddington ratio distributions split between star-forming and quiescent galaxies and their evolution with redshift (see § 5.2). We also provide the X-ray lu-

minosity function split in terms of star-forming and quiescent galaxies, however, we find that our model is unable to give a realistic split between these populations at $z\gtrsim2$ regarding the relative numbers of AGNs in star-forming and quiescent galaxies. Since we aim to investigate the AGN-galaxy connection, we must implement these Eddington ratio distributions in a PSM containing host galaxies to test whether our model reproduces the observed relationships between AGN and host properties.

As a starting point, we use a PSM that I developed during my Masters thesis that creates a population of star-forming galaxies (Bernhard et al., 2014). This model successfully reproduces the luminosity function at FIR and UV wavelengths out to $z\sim6$, as well as the observed relationship between attenuation (i.e. the ratio between the IR to the UV luminosity, $\rm L_{IR}/L_{UV}$) and UV luminosity (see Bernhard et al., 2014, for the details on the model, hereafter B14). Briefly, in B14, we first generate – in a fixed volume – a population of galaxies with stellar masses that follow the star-forming galaxy mass function of Ilbert et al. (2013). For each galaxy in the mock catalogue we then allocate SFR following the MS reported in Rodighiero et al. (2011). From the main sequence SFRs, we generate realistic SFRs by randomly adding scatter following the specific SFR (i.e. SFR/M_*) distribution of Sargent et al. (2012), including the observed 3 per cent of Starburst galaxies. We then use the mass-dependent attenuation relation of Heinis et al. (2013) to split each SFR into a direct (i.e. un-attenuated) and a dust re-emitted (i.e. attenuated) component (i.e. $\rm SFR_{UV}$ and $\rm SFR_{IR}$, respectively). The IR and UV luminosities are then derived using the Kennicutt (1998) relationships assuming a Salpeter (1955) initial mass function.

Before incorporating AGNs via their Eddington ratio distribution, we updated B14. We changed the definition of the stellar mass function to that of Davidzon et al. (2017), instead of Ilbert et al. (2013). We also updated the MS to reflect the more recent reported by Schreiber et al. (2015), instead of Rodighiero et al. (2011). Finally, we updated the attenuation relation – used to derived IR and UV luminosities in B14 – to that of Pannella et al. (2015), instead of Heinis et al. (2013). The new mass function and attenuation relation used here are very similar to the ones reported in previous studies (i.e. used in B14), as such it corresponds to minor differences between B14 and the updated version. However, as shown in Fig. 5.12, the new definition of the MS reported in Schreiber et al. (2015) is rather different than that of Rodighiero et al. (2011). The main differences are the steeper slope for the M_*–SFR relationship and the flattening of the MS reported in Schreiber et al. (2015) at higher masses (i.e. M$> 10^{11} M_\odot$) and for $z< 1$.

As a result of these updates, we find that a number of refinements introduced in B14 are obsolete (see § 2.4 in Bernhard et al. (2014) for more details on the re-

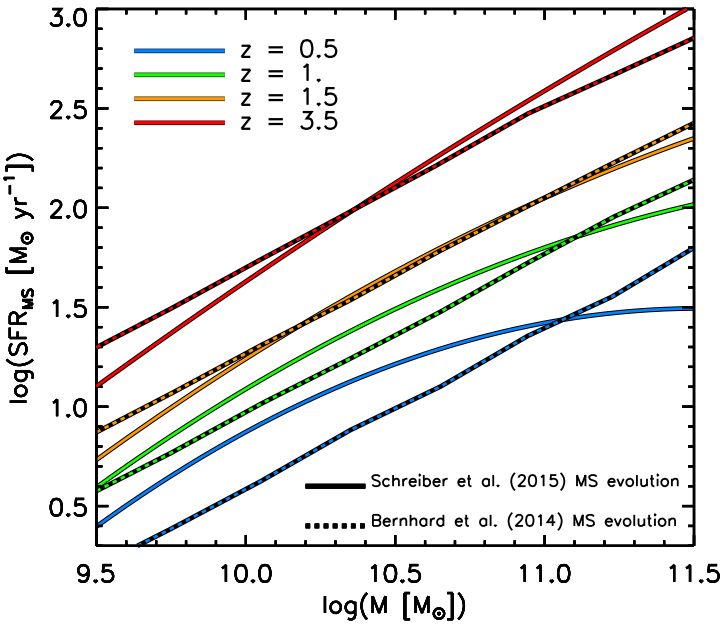

Figure 5.12: Differences in the MS between B14 and the updated B14 model out to z=3.5. The dotted lines show the MS used in B14 (i.e. Rodighiero et al., 2011) whilst the plain lines show the MS updated for this work (i.e. Schreiber et al., 2015). We note some changes in the slopes between the previous and the updated version, including the flattening at higher stellar masses and low redshifts (i.e. z<1), as reported in Schreiber et al. (2015).

finements). Briefly, the Starburst and the MS galaxies now follow exactly the same attenuation relation, in contrast to what was presented in B14; the scatter around the attenuation relation is kept at 0.4 dex (1 mag) as predicted in B14 and now confirmed in Pannella et al. (2015); and the evolving normalisation of the attenuation relation at low redshifts is now unnecessary to reproduce the UV and the IR luminosity functions. As a sanity check, we show in Fig. 5.13 and Fig. 5.14 a comparison of the model UV and the IR luminosity functions (generated using the updated B14 model), respectively, against observed UV and IR luminosity functions. These demonstrate that the model is still consistent with observed luminosity functions at UV and IR wavelengths, at least out to $z{\sim}4$.

The B14 model was primarily developed to investigate star-forming galaxies only. However, a significant fraction of AGNs are also detected in quiescent galaxies (e.g. Georgakakis et al., 2015; Aird et al., 2017a; Wang et al., 2017). Therefore, we also update our model to include a population of quiescent galaxies in the updated B14 model (using the quiescent galaxy mass functions of Davidzon et al. 2017) with specific SFRs (i.e. SFRs divided by stellar masses) at least a factor of 10 below that of the MS (Ilbert et al., 2013).

We now use the Eddington ratio distribution presented in § 5.2.4 to incorporate AGNs within our model for star-forming and quiescent galaxies. To do this, we simply randomly allocate an Eddington ratio between $-3 < \log(\lambda_{\rm Edd}) < 3$ to each mock galaxy, depending on if it is a star-forming or a quiescent galaxy and following their respective Eddington ratio distribution. Since galaxies (star-forming or quiescent) outnumber AGNs, we randomly select $N_{\rm AGN}$ among the full population of mock galaxies for which we allocate an Eddington ratio. Excluded galaxies are not considered AGNs (or with $\log(\lambda_{\rm Edd})<-3$). $N_{\rm AGN}$ is chosen such that the X-ray luminosity function for star-forming and quiescent galaxies matches the one derived in our model (see § 5.2.5). To summarise, in Fig 5.15 we show a cartoon of this PSM, along with the important parameters and relationships that define it.

Using this PSM, we generate a population of 33,925,192 galaxies (i.e. 32,939,834 star-forming and 985,358 quiescent galaxies) with stellar masses spanning $8 < \log(M_*/M_\odot) < 14$. This corresponds to a 50 square degree blank-field survey out to z=3. Out of the 33,925,192 galaxies, 2,017,420 are AGNs with $-3 < \log(\lambda_{\rm Edd}) < 3$ (i.e. 1,034,408 are in star-forming galaxies, and 983,012 are in quiescent galaxies). We note that in our model, almost all quiescent galaxies contains AGNs (i.e. 99.8 per cent). This contradicts observations that suggest that AGNs reside in MS star-forming galaxies (e.g. Rosario et al., 2012; Mullaney et al., 2015; Stanley et al., 2015). This discrepancy is a consequence of the low relative numbers of quiescent-to-star-forming

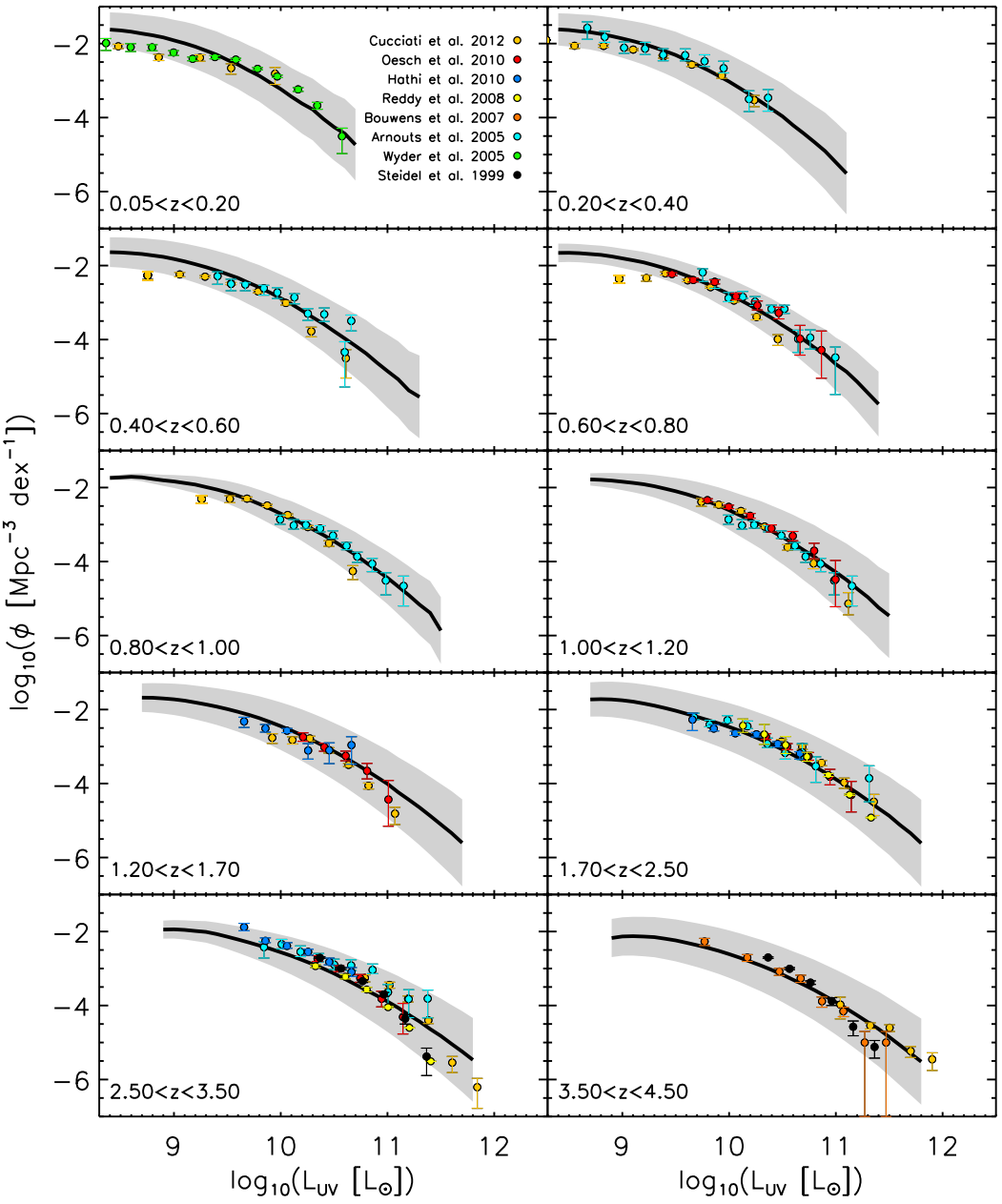

Figure 5.13: Model UV luminosity functions using the updated B14 out to $z\sim4$. We find that our UV luminosity function generated using the updated B14 is still consistent with various empirical studies (i.e. Steidel et al., 1999; Wyder et al., 2005; Arnouts et al., 2005; Bouwens et al., 2007; Reddy et al., 2008; Hathi et al., 2010; Oesch et al., 2010; Cucciati et al., 2012). The black line shows the model UV luminosity function and the light grey area shows the corresponding 3σ uncertainties (derived from 200 Monte-Carlo realisations to account for uncertainties on the parameters that define the mass function, the SFR distribution, and the attenuation relation).

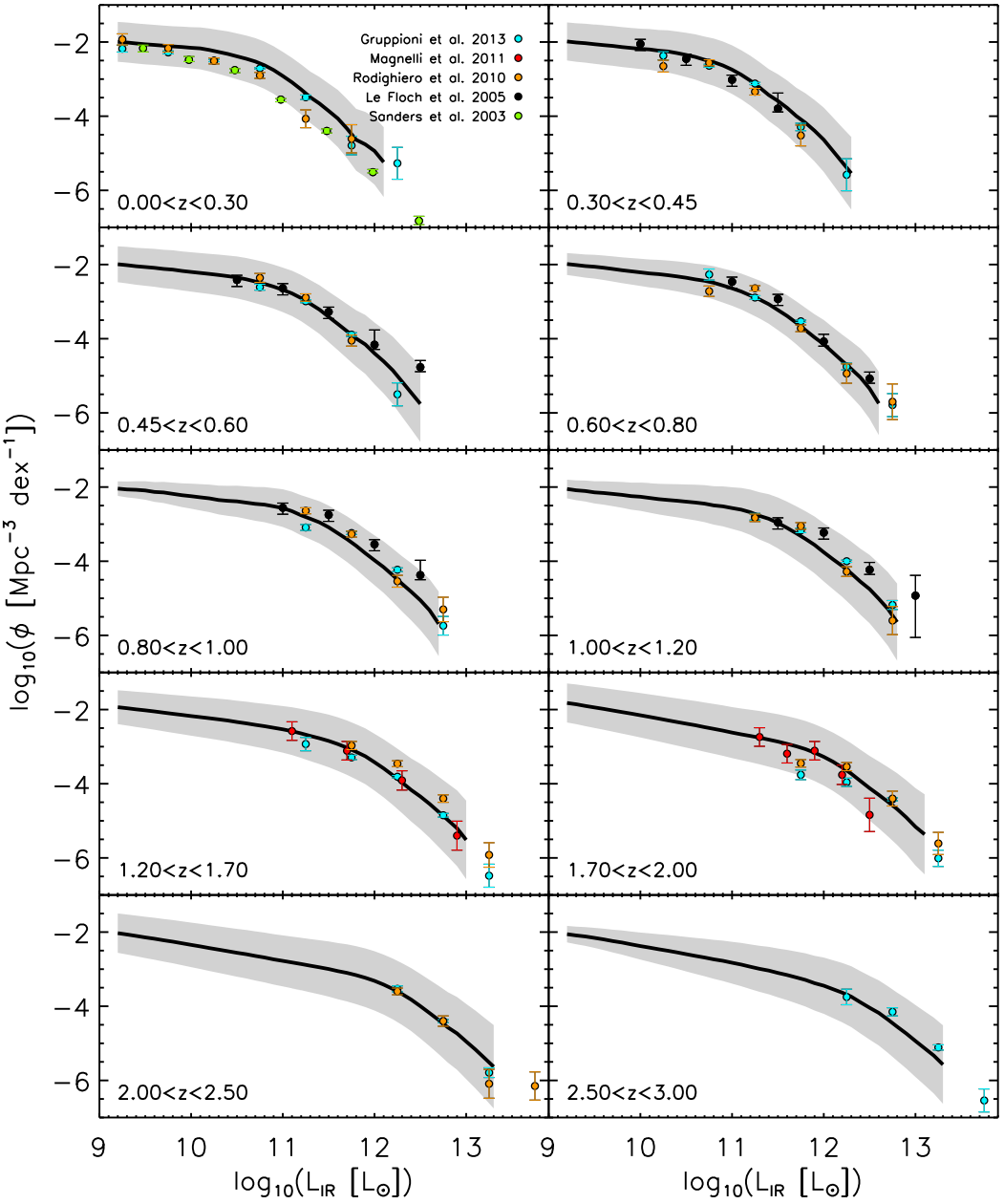

Figure 5.14: Model IR luminosity functions using the updated B14 out to $z{\sim}3$. We find that our IR luminosity function is still consistent with various empirical results (i.e. Sanders et al., 2003; Le Floc'h et al., 2005; Rodighiero et al., 2010; Magnelli et al., 2011; Gruppioni et al., 2013). The black line shows the model IR luminosity function and the light grey area shows the corresponding 3σ uncertainties (derived from 200 Monte-Carlo realisations which accounts for uncertainties on the parameters that define the mass function, the SFR distribution, and the attenuation relation).

galaxies, as shown by the mass function (see Fig. 5.1), in comparison to the contribution from quiescent galaxies to the total X-ray luminosity function, which is found to be roughly 50 per cent (e.g. Georgakakis et al., 2015). Most of our model AGNs in quiescent galaxies have a low accretion rate (i.e. $\lambda_{\rm Edd}\sim0.001$) such that they might be observationally undetected (i.e. X-ray luminosity of $L_X=10^{41}$ erg s^{-1} for a $\lambda_{\rm Edd}=0.001$ and a stellar mass of 10^{11} $M_{\odot}$). In our PSM, if we consider galaxies with stellar masses above $M_*=10^{10.5}$ $M_{\odot}$ (i.e. where quiescent and star-forming galaxies are found in similar numbers; see Fig. 5.1), we find that there are 307,048 star-forming galaxies, among which 64,905 are AGNs (i.e. 20 per cent), and 103,288 quiescent galaxies, among which 102,930 are AGNs (i.e. 99 per cent). As expected, the relative numbers of quiescent galaxies is higher (i.e. quiescent galaxies tend to be more massive) but again, contrary to observations, almost all of them are AGNs. As before, this is a direct consequence of the fewer number of quiescent galaxies compared to that of star-forming galaxies, along with the high contribution from quiescent galaxies to the X-ray luminosity function.

5.4 Results

In the previous section we showed how we developed a simple model that combines our analytic method of deriving the Eddington ratio distribution with a PSM to describe their host properties. AGNs are incorporated via their Eddington ratio distribution split between star-forming and quiescent galaxies (see § 5.2). We show that we are able to reproduce the observed X-ray, UV and FIR luminosity functions at least up to $z\sim3$. In this section we test our model against recent observed relationships between AGN and host galaxy properties.

5.4.1 SFR in bins of X-ray luminosities

A key test of any model that describes the Eddington ratio distribution is whether it can reproduce other observed features of the AGN population besides just the X-ray luminosity functions. Here, we test our PSM by assessing whether it can reproduce the observed flat relationship between SFR and X-ray luminosity as reported in many observational studies (e.g. Mullaney et al., 2012; Rosario et al., 2012, 2013; Stanley et al., 2015; Bernhard et al., 2016). We do this by calculating the mean-average SFRs of the AGNs in our PSM in bins of 0.5 dex in X-ray luminosity, taking into account both star-forming and quiescent galaxies.

As shown in Fig. 5.16, our model predicts a strong correlation between average

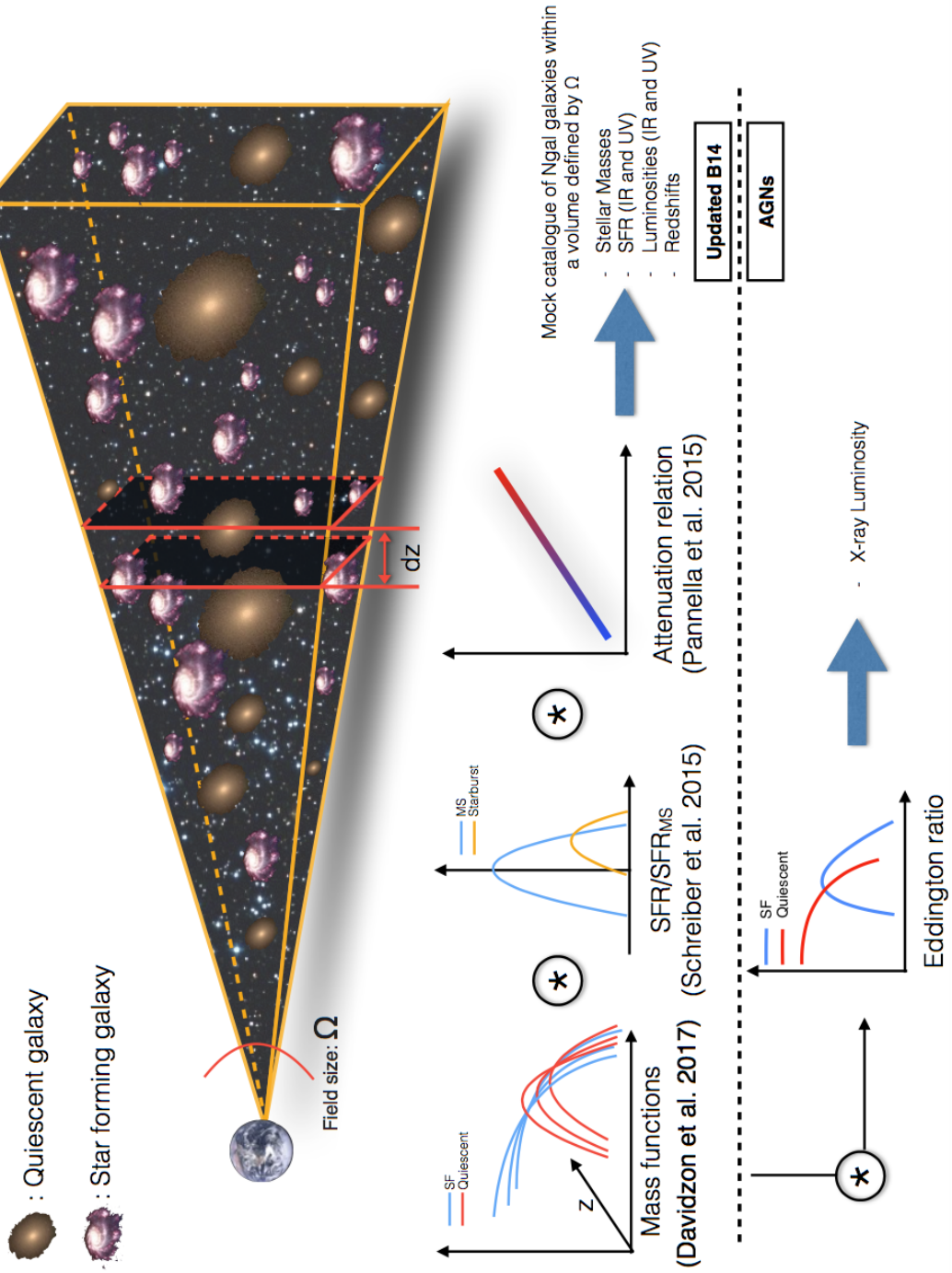

Figure 5.15: Illustration presenting the updated B14 model. We generate mock catalogues of quiescent and star-forming galaxies at different redshifts, z, within a volume defined by the field size, Ω, and the maximum redshift. Our model is based on a mass function, a distribution for SFR relative to that of the MS, an attenuation relation, and an Eddington ratio distribution.

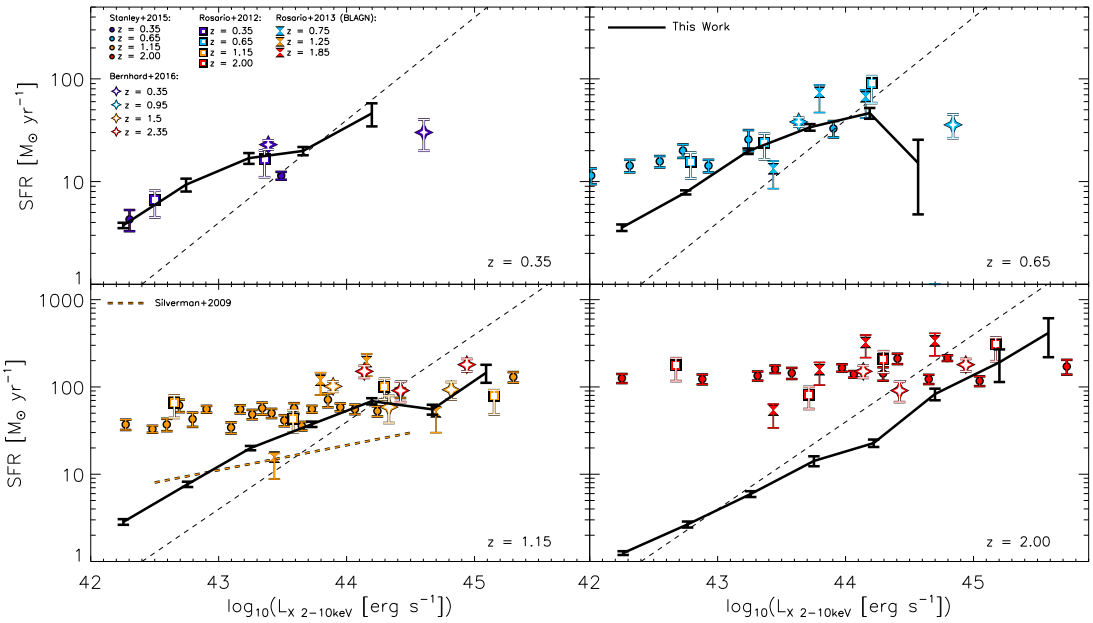

Figure 5.16: Relationship between averaged SFR and X-ray luminosity out to z=2. The black line shows the predicted relationship between averaged SFR and X-ray luminosity using our model. Data points are from various studies (i.e. Rosario et al., 2012, 2013; Stanley et al., 2015; Bernhard et al., 2016). The dashed black line shows the correlation found in Netzer (2009) for AGN-dominated system. Our model predicts a strong correlation between SFR and X-ray luminosity, at odds with the observed flat relationship between these two parameters.

SFR and X-ray luminosity (with an average slope of ∼0.6), at least up to z∼2. This agrees with empirical results for our lowest redshift bin (i.e. $z = 0.35$), but strongly contradicts the flat observed relationship between SFR and X-ray luminosity at higher redshifts (e.g. Rosario et al., 2012; Stanley et al., 2015).

It is important to note that other recent studies that are also based on PSMs find a similar strongly increasing relationship between SFR and X-ray luminosity when employing a "peaky" shaped Eddington ratio distribution for star-forming galaxies (e.g. Veale et al., 2014; Stanley et al., 2015). We will show in § 5.5 that this strong correlation is likely due to the AGN host mass distribution and the SFR-mass relationship (i.e. MS) induced by the use of a "peaky" Eddington ratio distribution in PSMs (and not the presence of a large number of quiescent galaxies).

5.4.2 X-ray luminosity in bins of SFRs

The flat relationship observed between SFR and X-ray luminosity is often attributed to the stochastic nature of AGNs compared to that of the hosts SFR (e.g. Aird et al., 2013; Hickox et al., 2014). This is supported by studies that find a correlation by

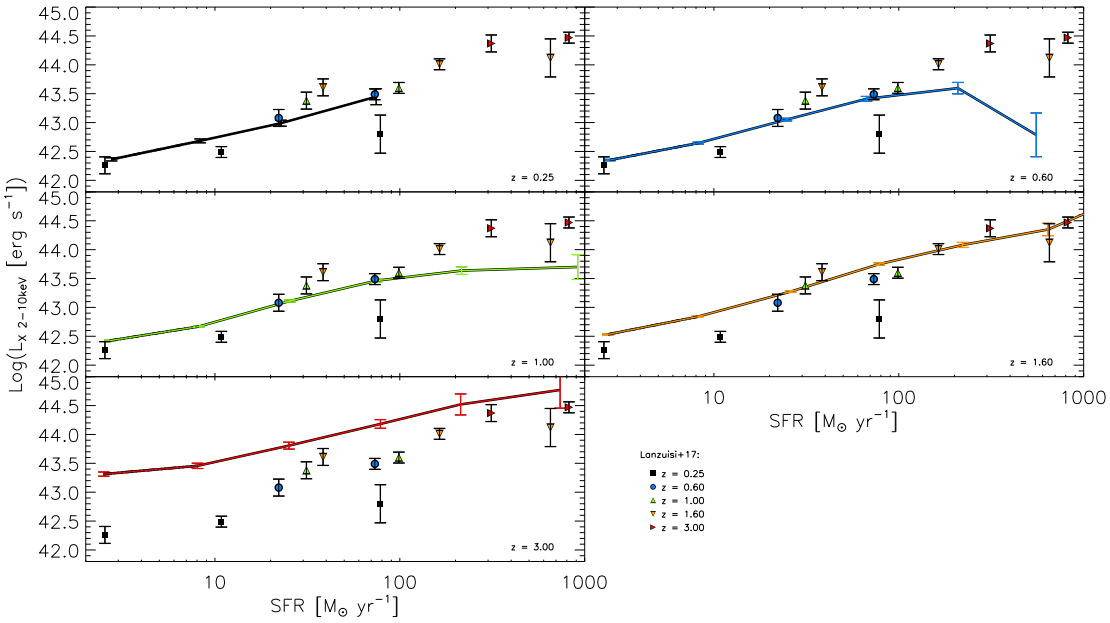

Figure 5.17: Relationship between averaged X-ray luminosity and SFR out to z=3. The lines show the predicted relationship between averaged X-ray luminosity and SFR at different redshifts (see keys on the bottom right-hand side of each panel). Data points are from Lanzuisi et al. (2017). We find good agreements between our predicted relationship and published data out to z=3, although our model fails at reproducing the observed flat relationship between SFR and X-ray luminosity.

taking the mean-average X-ray luminosity (i.e. averaging over the variability) in bins of SFRs (e.g. Chen et al., 2013; Delvecchio et al., 2015; Dai et al., 2015; Lanzuisi et al., 2017).

We investigate whether our model reproduces this relationship between average X-ray luminosity and SFR. We show in Fig. 5.17 the prediction of our model when measuring the mean-average X-ray luminosities in bins of SFRs. However, we only consider in our model AGNs with $L_X > 10^{42}$ erg s^{-1}, as often used in observational studies to avoid contamination to the X-ray luminosities from hosts SFR. In doing this, we also find a correlation between average X-ray luminosity and SFR (i.e. average slope of roughly $\approx$0.5) which is in good agreement with results recently reported in Lanzuisi et al. (2017) out to $z\sim$3 (i.e. average slope of 0.52). Therefore, although our model fails at reproducing the flat relationship between average SFR and X-ray luminosity, it does succeed at recreating the relationship between average X-ray luminosity and SFR.

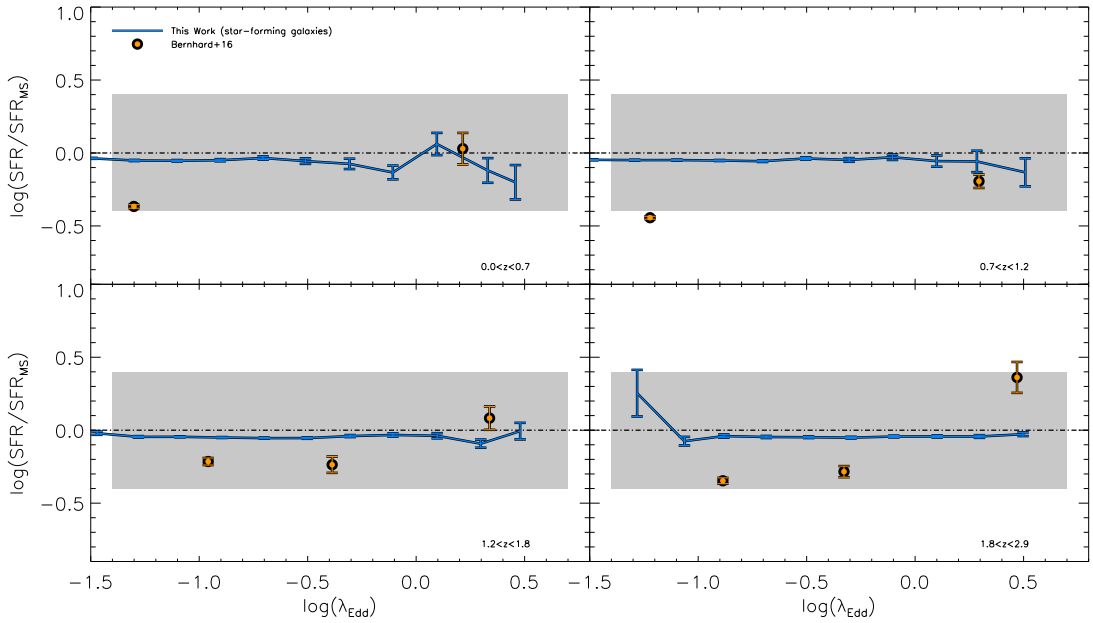

Figure 5.18: Normalised average SFR versus Eddington ratio out to $z\sim$2.5. The blue line shows the normalised average SFR in bins of Eddington ratio as predicted in our model, and only considers star-forming galaxies. The orange data points are from Bernhard et al. (2016). The dashed black line shows the position of the MS, and the grey area shows its scatter. We find that our model fails to reproduce the slight enhancement of averaged normalised average SFR observed in Bernhard et al. (2016).

5.4.3 MS normalised SFR versus Eddington ratio

We also investigate the relationship between normalised average SFR (i.e. SFR relative to that of the MS) in bins of Eddington ratios predicted by our model. As mentioned in Chapter 3, using a large observed sample of X-ray selected AGNs, we find a slight enhancement to the normalised average SFR at higher Eddington ratio (i.e. $\log(\lambda_{\rm Edd})>0$) when compared to their lower Eddington ratio counterparts and for $z>1.2$. In contrast, as shown in Fig. 5.18 our model predicts no correlation between these two quantities, with normalised average SFR fully consistent with the MS. For this, we only consider star-forming galaxies for our model since we do not have a good prescription for the normalised average SFRs of quiescent galaxies.

5.4.4 Comparison to empirical Eddington ratio distribution at z=1

One of our main findings is that a model of the Eddington ratio distribution simply split between star-forming and quiescent galaxies demands a "peaky" distribution for

the star-forming component in order to reproduce the total observed X-ray luminosity function out to $z{\sim}3$. Conversely, the Eddington ratio distribution for quiescent galaxies is found to be consistent with a broken power-law (see § 5.2). In Fig. 5.19 we compare our model Eddington ratio distribution to empirical results of Wang et al. (2017) at $z{=}1$. We find a good agreement between our model Eddington ratio distribution of quiescent galaxies and that of Wang et al. (2017). Furthermore, our model Eddington ratio distribution for star-forming galaxies at $z{=}1$ is consistent with empirical results for $\lambda_{\rm Edd}{\gtrsim}0.1$. However, at lower $\lambda_{\rm Edd}$, our model predicts that the Eddington ratio distribution for star-forming galaxies rapidly raises (as a consequence of the "peaky" distribution), in contradiction with empirical results from Wang et al. (2017) which indicate a power-law shape at these $\lambda_{\rm Edd}$. Should that be the case, it would strongly suggests a mass-dependent Eddington ratio distribution. The reason is that the Eddington ratio distribution for star-forming galaxies needs to be "peaky" for our model to reproduce the flat faint-end of the observed X-ray luminosity function (see § 5.2). We explore the mass-dependent Eddington ratio distribution in Chapter 6.

5.5 Discussion

5.5.1 Why does our model fail?

We first attempted to model the Eddington ratio distribution split between star-forming and quiescent galaxies by assuming that each component is defined by a broken power-law. While optimising the parameters that define this model, we found that the Eddington ratio distribution for star-forming galaxies is best represented by a "peaky" distribution (i.e. a rising slope before the position of the break). However, this model cannot reproduce the X-ray luminosity function beyond $z{\sim}2$. We argue that it is related to a decrease in the normalisation of the quiescent galaxy mass function with increasing redshift that cannot be compensated for by an increase in the normalisation of the Eddington ratio distribution for quiescent galaxies. This is a direct consequence of our model as we specify that the normalisation of the Eddington ratio distribution for star-forming galaxies must be always higher than that of the quiescent galaxies. Relaxing this assumption would lead to a higher contribution from quiescent galaxies that would be at odds with observations (e.g. Mullaney et al., 2015; Stanley et al., 2015). To investigate further, we then define a new model where the Eddington ratio distribution for star-forming galaxies is defined as a "peaky" distribution.

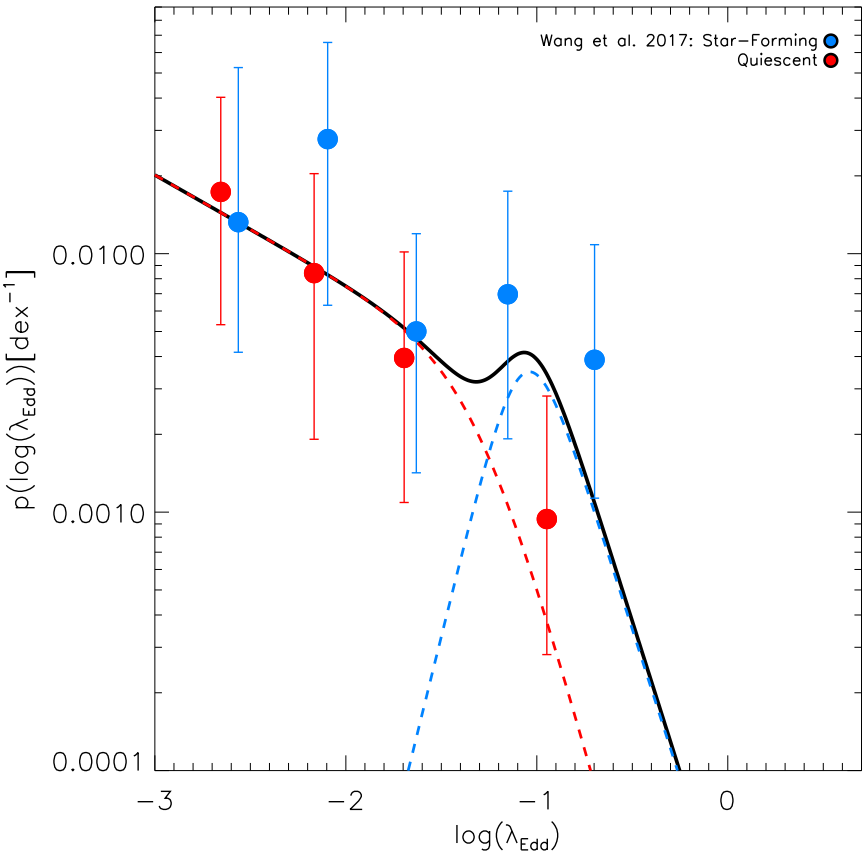

Figure 5.19: Comparison of our model Eddington ratio distribution at z=1 to empirical results of Wang et al. (2017). The thick black line shows the total model Eddington ratio distribution at z=1, while the blue and red dashed lines indicate its star-forming and its quiescent component, respectively. Red circles are the empirical Eddington ratio distribution for quiescent galaxies at $z\sim$1 as reported in Wang et al. (2017), and blue circles are that of the star-forming galaxies. While we find a good agreement between our model and the empirical Eddington ratio distribution for quiescent galaxies, there is a large discrepancy at lower values of $\lambda_{\rm Edd}$ between our model and the empirical Eddington ratio distribution for star-forming galaxies. We later solve this by assuming a mass-dependent Eddington ratio distribution.

By employing this "peaky" distribution, we saw that the second model also failed on two key accounts: firstly, it predicts that almost all AGNs at $z>2$ are hosted by quiescent galaxies (see § 5.2.5), which is at odds with recent observations (e.g. Mullaney et al., 2015; Stanley et al., 2015). Secondly, it fails to reproduce the flat relationship between SFR and X-ray luminosity reported in many observational studies (see Fig. 5.16; e.g. Mullaney et al., 2012; Rosario et al., 2012; Stanley et al., 2015). The first point of failure is resulting from the steep mass function of star-forming galaxies (at masses below the break) at $z>2$, in contrast to the very flat faint end of the X-ray luminosity function at these redshifts (e.g. Aird et al., 2015). This inconsistency in the shapes of the star-forming mass function and X-ray luminosity function makes it extremely difficult to reproduce the latter without any mass dependency in the Eddington ratio distribution, while still maintaining a high proportion of AGNs in star-forming galaxies.

To help explain why the model cannot reproduce the flat relationship between SFR and X-ray luminosity, we show in Fig. 5.20 which galaxy masses populate different parts of the SFR/X-ray plane. This plot shows that our model produces a strong correlation between X-ray luminosity and stellar mass. This is a direct result of the "peaky" Eddington ratio distribution for star-forming galaxies, which this model demands in order to reproduce the observed luminosity functions. The narrowness of this Eddington ratio distribution means that a galaxy of a given mass can only produce an AGN within a limited range of luminosities. When we then include the correlation between SFR and stellar mass for MS galaxies (e.g. Schreiber et al., 2015), the consequence is a correlation between SFR and X-ray luminosity. This correlation was also noticed by Veale et al. (2014) when using their "light-bulb" Eddington ratio model, which is similar in shape to our "peaky" distribution.

As demonstrated by Veale et al. (2014), reproducing the flat SFR/X-ray relationship requires a broader Eddington ratio distribution than either their light-bulb or our "peaky" distributions. However, in our model, the large numbers of low $\lambda_{\rm Edd}$ AGNs arising from a broad distribution, combined with the large numbers of low mass galaxies arising from the steep mass function, causes a severe over-prediction of the numbers of low luminosity AGNs. This leads to a steep gradient at the faint end of the X-ray luminosity function, in conflict with the observed X-ray luminosity functions of Aird et al. (2015). One way to solve this problem is to have a model with a mass-dependent Eddington ratio distribution for star-forming galaxies that essentially suppresses low Eddington ratios in low mass galaxies. This would then allow it to maintain a broad Eddington ratio distribution in high mass, star-forming galaxies, thus reproducing the flat SFR/X-ray relationship. We fully explore the

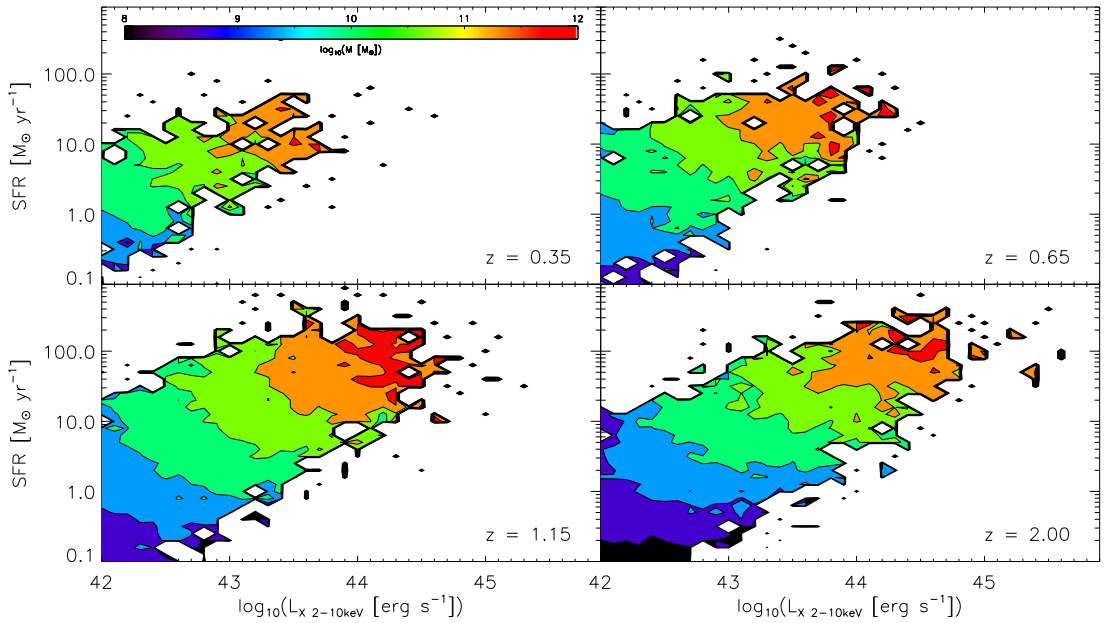

Figure 5.20: Stellar mass distribution in the SFR/X-ray luminosity plane out to z=2. The different colours indicate different average masses, in the range $8<\log(M_*/M_\odot)<12$ (see colour-bar). We find that our model predicts a correlation between X-ray luminosity and stellar mass. Therefore, once we implement the SFR-M_* relationship for star-forming galaxies, our model also predicts a correlation between SFR and X-ray luminosity, at odds with empirical results.

mass-dependent Eddington ratio distribution in Chapter 6.

5.5.2 Recovering the flat SFR/X-ray luminosity relationship in our model

In the previous sub-section we discussed the role of the MS and the "peaky" distribution used for the Eddington ratio distribution for star-forming galaxies in the failure to reproduce the flat SFR/X-ray relationship in our model. We argue that a mass-dependent Eddington ratio distribution for star-forming galaxies would solve this problem. However, several studies have reported that the Eddington ratio distribution is potentially mass-independent out to $z\sim1$ (e.g. Aird et al., 2013; Jones et al., 2017).

One factor that we have not yet considered when comparing against observations is the effects of observational bias. It is possible that the discrepancy is introduced by observational biases rather than a mass-independent model for the Eddington ratio distribution. At higher redshifts, only galaxies with higher masses, and therefore higher SFRs are detected at FIR wavelengths, hence creating a bias toward higher

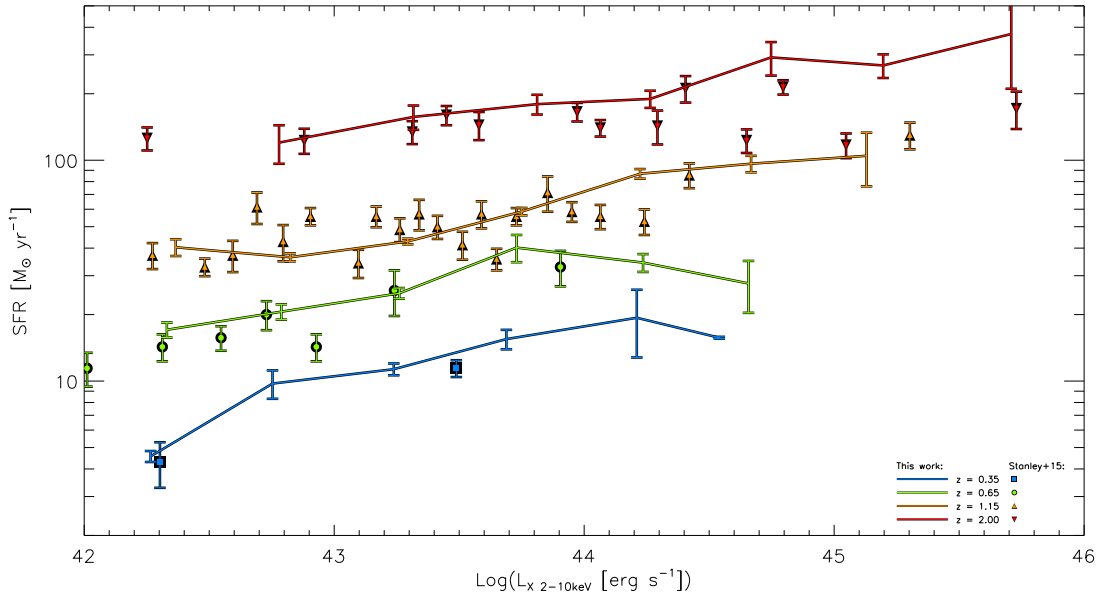

Figure 5.21: Relationship between SFR and X-ray luminosity after accounting for potential observational biases for SFRs. The lines are the predicted relationships between SFR and X-ray luminosity at various redshifts, after applying the SFR detection limits of Schreiber et al. (2015). Data points are from Stanley et al. (2015). We find a net improvement of our model predictions out to $z\sim2$ when accounting for detection limit biases in SFRs.

values of average SFRs. We show in Fig. 5.21 the average SFRs in bins of X-ray luminosities for our model, but only accounting for galaxies that would be detected in each of our redshift bin. To do this, we assume the SFR detection limits (or equivalently the IR luminosity detection limits) reported in Schreiber et al. 2015: SFR$\gtrsim$1, 8, 13, 70, 250 $M_{\odot}$/yr at $z\sim$0.35, 0.65, 1.15, 2, respectively. Although these values have not been chosen to match the flat relationship between SFR and X-ray luminosity, we find a net improvement of the results when comparing these with the observed relationship of Stanley et al. (2015) at all redshifts (see Fig. 5.21).

Accounting for an observational bias toward higher star-forming galaxies at higher redshifts seems to reproduce the flat SFR/X-ray relationship in our model. However, most observational studies account for this bias by including un-detected galaxies via various methods (e.g. stacking). Therefore, it is not likely that the flat relationship observed by these studies is due to an observational bias.

5.5.3 Caveats

When deriving the Eddington ratio distribution, our model is limited by the functional form chosen for each component of the Eddington ratio distribution and the

associated assumptions used to avoid degeneracies during fitting (see § 5.2). An obvious caveat to our model is that we cannot explore the full range of possible Eddington ratio distributions. However, as stressed in § 5.2.1, all our assumptions are motivated by the findings of recent studies (e.g. Georgakakis et al., 2014; Aird et al., 2017a; Wang et al., 2017). Furthermore, the X-ray luminosity function predicted by our model is in good agreement with that observed out to $z{\sim}2$, including when split in terms of star-forming and quiescent galaxies (e.g. Georgakakis et al., 2014; Aird et al., 2015). However, we do find some discrepancies: the X-ray luminosity function split between star-forming and quiescent galaxies beyond $z{\sim}2$; the low-$\lambda_{\rm Edd}$ tail of the distribution for star-forming galaxies when compared to that of Wang et al. (2017); and the failure to reproduce the observed flat relationship between SFR and X-ray luminosity. Therefore, while we do not claim that our Eddington ratio distributions are universal, they provide a simple means by which to explore the AGN-galaxy connection. Furthermore, we employ the MCMC fitting process, which explores the full available parameter space and is thus able to find both local and global maxima.

5.6 Conclusion

Motivated by recent results reporting a different Eddington ratio distribution for star-forming and quiescent galaxies (Aird et al., 2017a; Wang et al., 2017), as well as our observations of an enhancement of the star-forming properties of AGN hosts at higher $\lambda_{\rm Edd}$, we attempt to constrain these distributions by using a model to fit the observed X-ray luminosity function of Aird et al. (2015). We first find that our model demands a "peaky" distribution for star-forming galaxies to be able to fit the total X-ray luminosity function at higher redshifts. Whilst implementing this, we find that our model is able to reproduce the total observed X-ray luminosity function up to $z{\sim}3$. However, when split between a star-forming and quiescent component, it places too many AGNs in quiescent galaxies at $z{\gtrsim}2$. We also find that our model predicts a strong correlation between SFR and X-ray luminosity, which contradicts observations. We argue that this is a result of the combination of our "peaky" distribution for star-forming galaxies and the relationship between SFR and the stellar mass (i.e. MS).

Overall, there is a large discrepancy with our model that demands a "peaky" distribution for the Eddington ratio of star-forming galaxies in order to reproduce the X-ray luminosity function, but also requires a broader Eddington ratio distribution to reproduce the flat SFR/X-ray relationship. In Chapter 6, we argue that a mass-dependent Eddington ratio distribution for star-forming galaxies (as recently

observed in Aird et al. 2017a) is able to rectify this conflict. This constitutes the main focus of Chapter 6.

Chapter 6

A mass-dependent Eddington ratio distribution for star-forming galaxies

6.1 Introduction

The aim of this thesis is to explore the relationship between SMBH accretion and the properties of their host galaxies. In Chapter 3 we investigated this relationship using a sample of 1620 X-ray selected AGNs for which we measured average host SFRs (accounting for contamination from the AGN) in bins of specific X-ray luminosity (i.e. X-ray luminosity relative to host stellar mass) – or Eddington ratio $\lambda_{\rm Edd}$ – and redshift. We found a slight enhancement in the normalised average SFR (i.e. SFR relative to that of the MS) at higher $\lambda_{\rm Edd}$ (i.e. $\lambda_{\rm Edd} > -0.5$), a result reinforced by our finding of a higher fraction of starburst galaxies at these higher $\lambda_{\rm Edd}$. As we measured a change in the average host star-forming properties with $\lambda_{\rm Edd}$, this implies that the distribution of Eddington ratios must change with the host star-forming properties (see Chapter 3).

Our results of a changing Eddington ratio distribution with host star-forming properties is in agreement with recent observational studies that report a different Eddington ratio distribution for star-forming and quiescent galaxies (e.g. Georgakakis et al., 2014; Aird et al., 2017a; Wang et al., 2017). Motivated by this, in Chapter 5, we considered a modelling approach to infer the Eddington ratio distribution split between star-forming and quiescent galaxies. To do this, we used the mass function of Davidzon et al. (2017) and optimised the Eddington ratio distribution to fit the total observed X-ray luminosity function of Aird et al. (2015) out to $z\sim3$ (see

§ 5.2). We then incorporated these Eddington ratio distributions into a population synthesis model (PSM; see Chapter 4, § 4.2) for galaxies (i.e. a mock catalogue of star-forming and quiescent galaxies) to determine whether they reproduce the observed flat SFR/X-ray luminosity relationship.

On fitting the total X-ray luminosity function, assuming a model Eddington ratio distribution split between star-forming and quiescent galaxies, we found that the best fit is given by assuming a "peaky" distribution for the Eddington ratio of star-forming galaxies. We argue that our model demands a "peaky" distribution (i.e. narrower than a broken power-law) for star-forming galaxies to reconcile the steep low-mass end of their mass function with the flat faint-end slope of the X-ray luminosity function (see Chapter 5, § 5.2.5). Conversely, the Eddington ratio distribution for quiescent galaxies is found to be consistent with a broken power-law. We also report that, although our model is able to fit the total X-ray luminosity function of Aird et al. (2015) out to $z\sim3$, it places too many AGNs in quiescent galaxies beyond $z\sim2$ (at least when using the model that incorporates the "peaky" Eddington ratio distribution for star-forming galaxies; see Chapter 5, § 5.2.5). This is at odds with observations (e.g. Rosario et al., 2012; Stanley et al., 2015; Azadi et al., 2015). Finally, we found that, using the PSM outlined in Chapter 5, § 5.3, our model fails to reproduce the observed flat relationship between average SFR and X-ray luminosity. Instead we predict a strong correlation between these parameters. We have demonstrated that the "peaky" distribution for the Eddington ratio of star-forming galaxies generates a correlation between X-ray luminosity and stellar mass. This leads to a correlation between SFR and X-ray luminosity when including the MS for star-forming galaxies (see Chapter 5, § 5.5), as also reported in Veale et al. (2014).

Overall, we find that there is a strong tension within our model that demands a narrow (i.e. "peaky") Eddington ratio distribution for star-forming galaxies to be able to reproduce the total X-ray luminosity function of Aird et al. (2015) out to $z\sim3$, yet a broad Eddington ratio distribution for star-forming galaxies to obtain a flat relationship between SFR and X-ray luminosity.

One way to solve this discrepancy is to assume a mass-dependent Eddington ratio distribution that essentially suppresses low $\lambda_{\rm Edd}$ in low mass galaxies (see Chapter 5, § 5.5.1). A similar Eddington ratio distribution for star-forming galaxies has recently been reported in Aird et al. (2017a) using a semi-empirical approach. Therefore, in this section, we model the Eddington ratio distribution for star-forming galaxies, but this time introducing a mass dependency. For this model we only change the Eddington ratio distribution of star-forming galaxies, and keep that of the quiescent ones. To do this, we extract the X-ray luminosity function for star-forming galaxies

out to $z\sim2$ given by our previous model (see Chapter 5, § 5.2.5), then fit this using a model that incorporates a mass-dependent Eddington ratio distribution. Our new model (hereafter referred to as "mass-dependent") is constrained to below $z=2$ since our previous model produces inconsistent results for quiescent galaxies beyond that redshift.

In this chapter, we first describe in § 6.2 our mass-dependent model for the Eddington ratio distribution of star-forming galaxies. We then show the new results, among which the new relationship between SFR and X-ray luminosity predicted by this mass-dependent model in § 6.3, and demonstrate that our mass-dependent model is able to reproduce the flat SFR/X-ray relationship. We discuss the implications of these results in § 6.4, and finally, conclude in § 6.5.

6.2 Mass-dependent Eddington ratio distributions

6.2.1 Mass dependency in the model Eddington ratio distributions

We found that a model which assumes an Eddington ratio distribution for AGNs split between star-forming and quiescent galaxies is unable to reproduce the flat relationship between SFR and X-ray luminosity. Motivated by our findings, as well as some recent studies reporting that the Eddington ratio distribution for star-forming galaxies is mass-dependent (e.g. Aird et al., 2017a), we have developed a final model that can accommodate a mass dependency. To do this, we define three different Eddington ratio distributions (adopting broken power-laws for each) in three different mass bins the sum of which represents the Eddington ratio distribution for star-forming galaxies. We define our mass bins as: low mass ($8<\log(M_*/M_\odot)<10$), medium mass ($10<\log(M_*/M_\odot)<11$), and high mass ($11<\log(M_*/M_\odot)<12$). We again use our optimisation method (see Chapter 4) to extract each "mass component" of the Eddington ratio distribution for star-forming galaxies.

Since assuming three broken power laws has the potential of generating 12 free parameters, we rely on a few assumptions based on the empirical results of Aird et al. (2017a) to help prevent degeneracies. First, we require that the break of each broken power law peaks at different $\lambda_{\rm Edd}$ values in such a way that a higher mass bin peaks at a *lower* value of $\lambda_{\rm Edd}$ than its lower mass neighbour. Secondly, we assume that the three Eddington ratio distributions share the same slope at high Eddington ratios. Finally, we assume the normalisation of each of the three broken power laws is such that the Eddington ratio distribution above the break is always coincident.

Again, we stress that all these features have been reported in Aird et al. (2017a), and thus are based on observations. We show in Fig. 6.1 a sketch of the Eddington ratio distribution assumed for this mass-dependent model. In making these assumptions, we reduce the parameter space to eight free parameters (see also Fig 6.1):

- one normalisation, $A_{\rm SF}$, (from which the others are derived via our third assumption);
- three break positions, $\lambda_{\rm break}$, (one for each mass bin and ordered according to our first assumption);
- three power law slopes below the break, γ_1, (which are unconstrained within the given limits of the parameter space);
- a single shared power law slope above the break, γ_2.

We optimise the eight free parameters of this new model, using our MCMC optimisation method (see Chapter 4), and adopting the mass function of Davidzon et al. (2017), to fit the X-ray luminosity function of star-forming galaxies derived by the previous model (interpolated at z=0.1, z=0.3, z=0.5, z=0.7, z=1.0, z=1.3, z=1.5, and z=1.7). We present in Fig. 6.2 a sketch of the limits used for each parameters (i.e. defining the parameter space). We performed a fit of the star-forming component of the X-ray luminosity function as derived while using our previous model in each of our redshift bin with z<2. We then interpolate these X-ray luminosity function for star-forming galaxies at the redshifts used in our mass-dependent model. We show in Appendix B, Fig. B.3 an example of the posterior distribution at z=0.5 from which the parameters have been extracted.

6.2.2 X-ray luminosity functions

The first thing we must determine with this mass-dependent model is whether it can reproduce the observed X-ray luminosity function. We show in Fig. 6.3 the fit to the star-forming component of the X-ray luminosity function using our mass-dependent Eddington ratio distribution model to $z\sim$2. Our mass-dependent model does a good job at fitting the star-forming X-ray luminosity functions in all our redshift bins. Since our mass-dependent model assumes an Eddington ratio distribution split into three different mass bins, we are also able to derive the X-ray

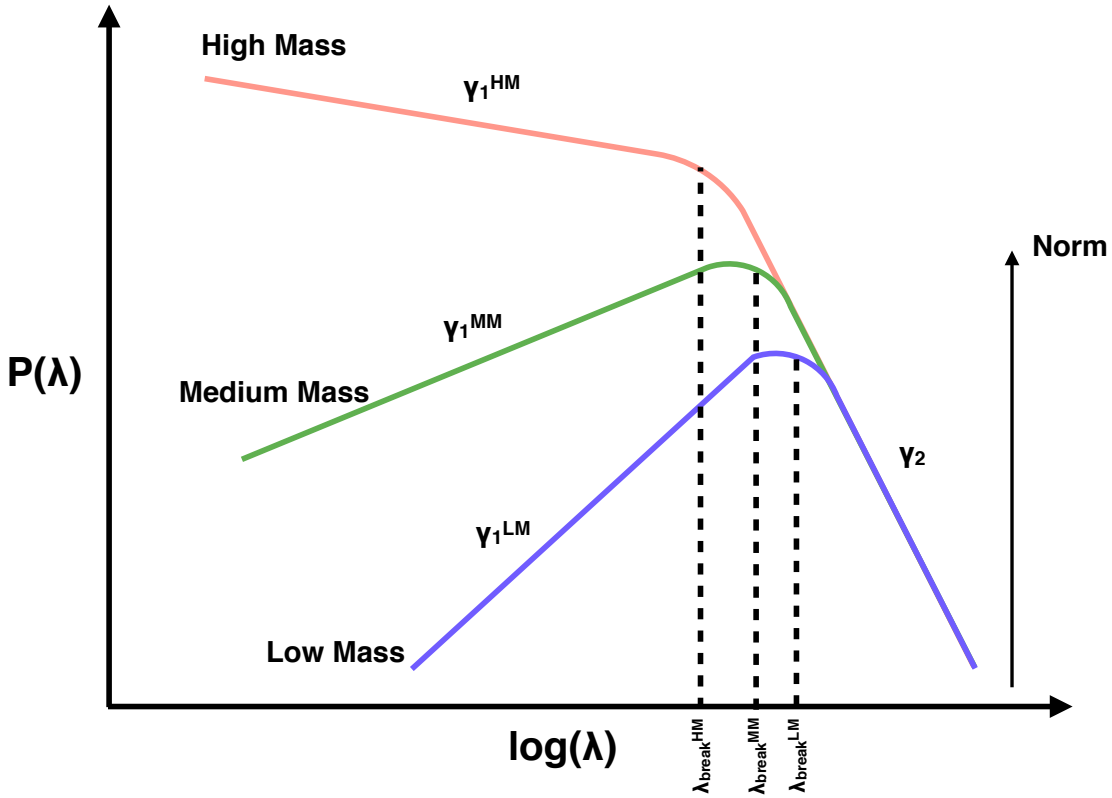

Figure 6.1: Sketch of our mass-dependent Eddington ratio distribution that defines our mass-dependent model. Different colours indicates different mass bins. γ_1 is the slope at low Eddington ratio, γ_2 is the slope at high Eddington ratio, $\lambda_{\rm break}$ is the position of the break, and "Norm" is the normalisation. The super-scripts HM, MM and LM stand for high mass, medium mass, and low mass, respectively.

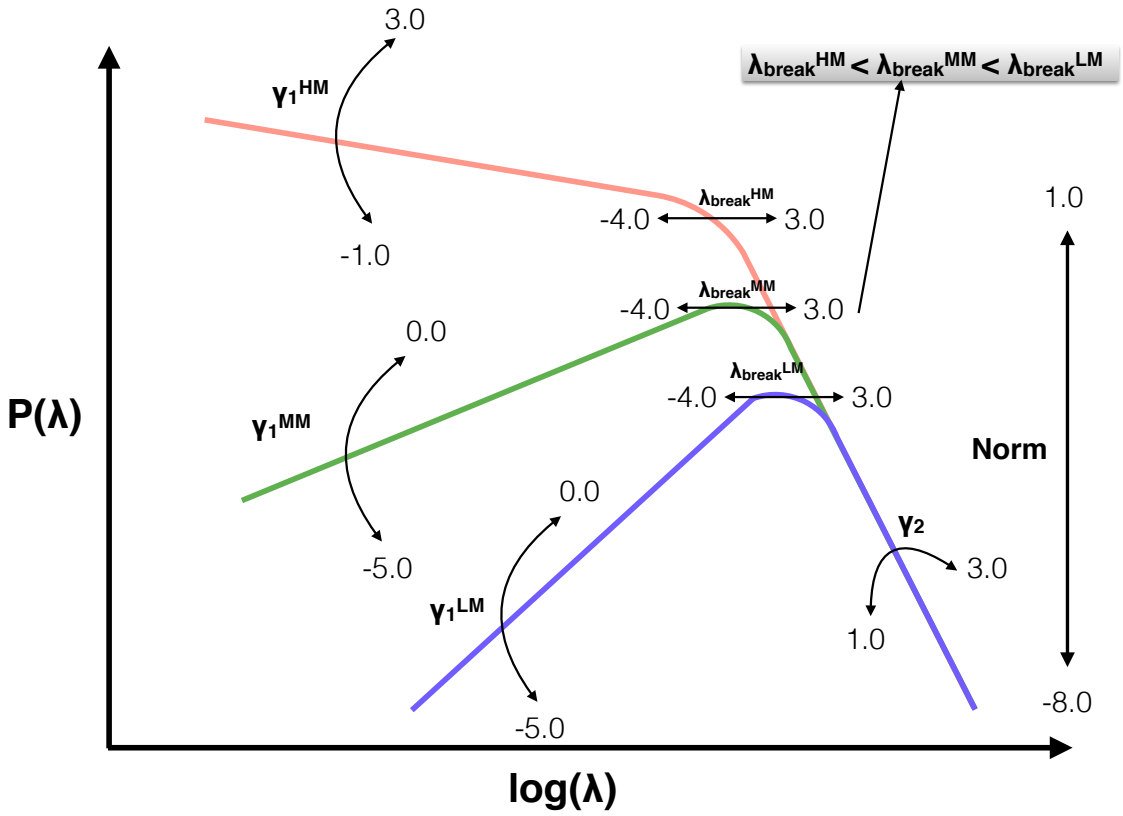

Figure 6.2: Sketch of the boundaries within which our optimisation process operates. Colours and parameters are similar to those of Fig. 6.1. Each arrow and value indicates the boundaries used to search the parameters that best fit the X-ray luminosity function (i.e. parameter space). We sketch our assumptions on the positions of the breaks (i.e. $\lambda_{\rm break}^{\rm HM} < \lambda_{\rm break}^{\rm MM} < \lambda_{\rm break}^{\rm LM}$). We also show that the normalisation is shared between the three distributions (i.e. defined by the normalisation of the Eddington ratio distribution of the highest mass bin), and the γ_2 is shared among all the mass bins.

luminosity function of each mass bin (see Fig. 6.3). In doing so, our model predicts that the highest mass galaxies (i.e. $M_*> 10^{11}$ $M_\odot$) dominate the star-forming X-ray luminosity functions across almost the full range of X-ray luminosities (i.e. 10^{41} $<L_X<$ 10^{46} erg s^{-1}). The exception being in our lowest redshift bin (i.e. $z \sim 0.11$) where 10^{10} $<M_*/M_\odot<$ 10^{11} galaxies contribute marginally more than our highest mass galaxies at $L_X \gtrsim 10^{43.5}$ erg s^{-1}. In general, however, these medium mass galaxies only contribute significantly (i.e. > 10 per cent) at luminosities above the knee of the X-ray luminosity functions (i.e. $L_X> 10^{44}$ erg s^{-1}). By contrast, the lowest mass galaxies (i.e. $M_*< 10^{10}$ $M_\odot$) have almost no contribution to the X-ray luminosity function of star-forming galaxies (i.e. $<<1$ per cent) at $L_X> 10^{43}$ erg s^{-1}. Indeed, we are only able to derive upper and lower-limits (overall leading to a lower contribution of the low mass galaxies to the total X-ray luminosity function) for the parameters defining the low-mass component of our Eddington ratio distribution (see § 6.2.3).

While conducting empirical studies, the difficulties in measuring stellar masses for AGN host galaxies create a bias against lower mass galaxies (i.e. with $M_* \lesssim 10^{9.5-10}$ $M_\odot$). Therefore, observed samples of AGNs tend to probe higher mass host galaxies. As our model predicts that the X-ray luminosity function are essentially dominated by massive galaxies at all redshifts, empirical studies would potentially miss the contribution from lower mass galaxies and then naturally lead toward a *mass-independent* Eddington ratio distribution (since likely to be biased toward higher stellar masses), as often reported (e.g. Aird et al., 2012; Jones et al., 2017; Weigel et al., 2017). Carefully combining empirical results with statistics modelling leads to a mass-dependent Eddington ratio as recently found by Aird et al. (2017a), and as supported by our models.

6.2.3 Redshift evolution of the Eddington ratio distributions

Before exploring whether our mass-dependent model reproduces the SFR/X-ray relationship we first investigate how the eight parameters that define our mass-dependent model change with redshift. We show in Fig. 6.4 the redshift evolution of these parameters. We report that the overall normalisation of the star-forming component ($A_{\rm SF}$) increases very slightly with increasing redshift. The position of the break ($\lambda_{\rm break}$) in each mass bin shifts toward higher $\lambda_{\rm Edd}$ values. This is consistent with the overall increase of the position of the break observed in the previous model (i.e. all mass bins collapsed together; see Chapter 5, § 5.2.6), suggesting a higher accretion for AGNs at higher redshifts. Furthermore, we find that the slope at low $\lambda_{\rm Edd}$ for

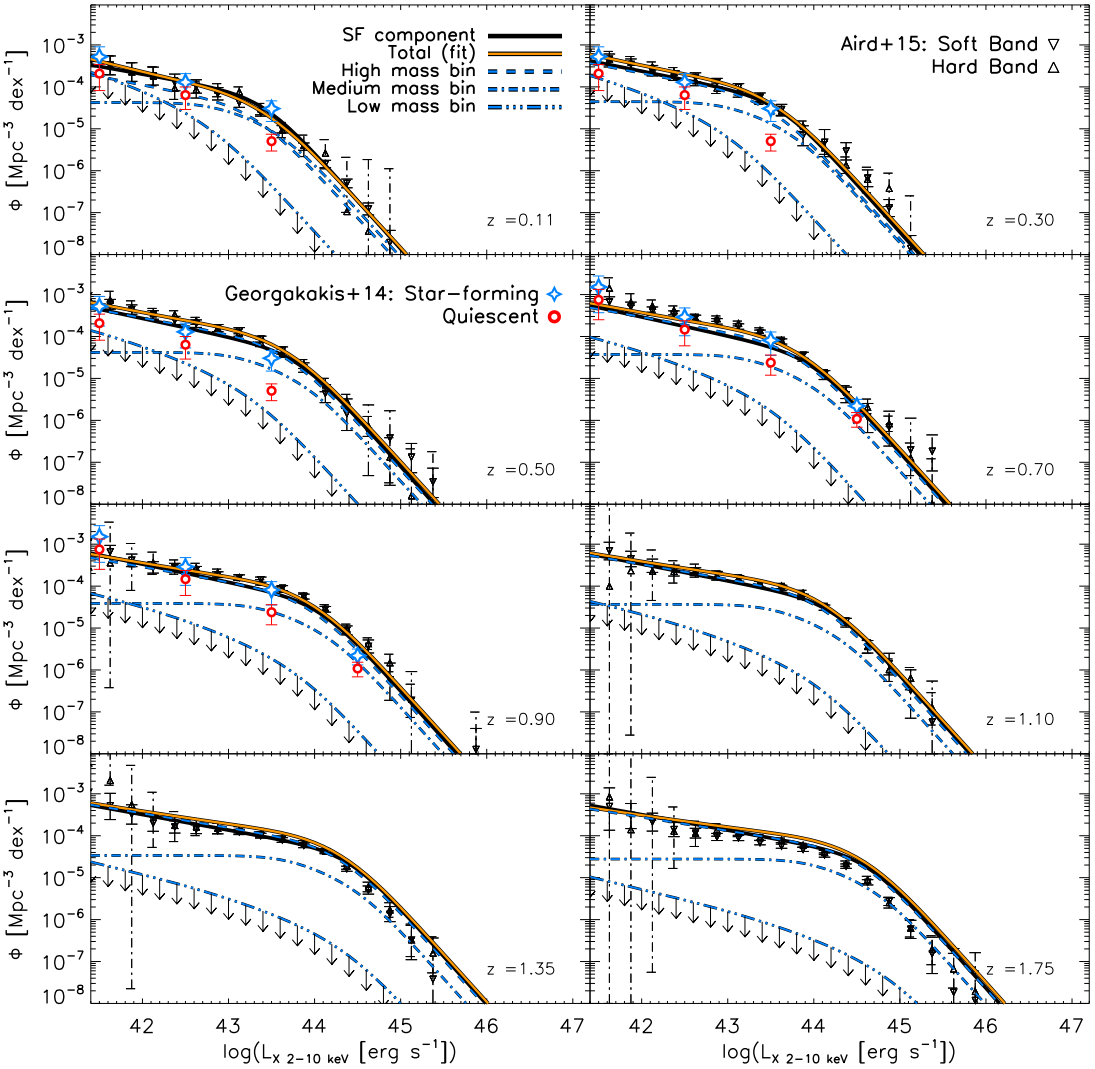

Figure 6.3: Fit to the star-forming component of the X-ray luminosity function using our mass-dependent model. The black lines show the star-forming component of the X-ray luminosity function (derived from our previous model; see Chapter 5, § 5.2.5), and the orange lines show the best fit given by our model. The dashed, double-dot dashed, and triple-dot dashed lines show the X-ray luminosity function for our low ($8<\log(M_*/M_\odot)<10$), medium ($10<\log(M_*/M_\odot)<11$), and high mass bin ($11<\log(M_*/M_\odot)<12$), respectively. Black arrows indicate the effect of upper and lower-limits in the parameters that define the Eddington ratio distribution. The blue stars and the red circles show the X-ray luminosity function for the star-forming and quiescent galaxies, respectively, as reported in Georgakakis et al. (2014), and up to $z\sim1$. The black downward and upward triangles show the total X-ray luminosity function of Aird et al. (2015) for the soft and the hard band, respectively.

our higher mass bin (γ_1) flattens with increasing redshift. Since our highest mass bin dominates the faint-end of the X-ray luminosity function, the flattening of γ_1 for our highest mass bin is a consequence of the flattening observed for the faint-end of the X-ray luminosity function with redshift. By contrast, we find that the slope at high $\lambda_{\rm Edd}$ (γ_2) for all our mass bins and the slopes at low $\lambda_{\rm Edd}$ for our medium and lower mass bins do not change significantly with redshift.

We note that for our lowest mass galaxies we can only place lower and upper-limits on the position of the break (i.e. $\lambda_{\rm break}$) and the faint-end slope (i.e. γ_1), respectively, of their Eddington ratio distribution. This suggests that the lowest mass galaxies in our mass-dependent model do not play a major role in defining the Eddington ratio distribution for star-forming galaxies, as was hinted by their low contribution to the total X-ray luminosity functions (see § 6.2.2). Finally, we also performed a linear fit of the redshift evolution of each parameter, using the standard deviation of 1000 Monte-Carlo realisations for the uncertainties on the fitting parameters. We report the results of this fit in Table 6.1.

Each of the aforementioned trends can be seen in the evolution of the overall Eddington ratio distributions, which we plot in Fig. 6.5. Each distribution has been normalised such that it integrates to unity after applying a cut at $\lambda_{\rm Edd}= 10^{-7}$ when diverging.

6.3 Results

6.3.1 Relationship between average SFR and X-ray luminosity

One of the key problems of our previous mass-independent model is that it was unable to reproduce the flat relationship between SFR and X-ray luminosity (see § 5.4.1). We demonstrated that this is a direct result of the need for a narrow distribution for the Eddington ratio of star-forming galaxies, and, as discussed in Chapter 5, § 5.5.1, hints toward a mass-dependent model for that Eddington ratio distribution.

Having confirmed that our mass-dependent model is still able to reproduce the X-ray luminosity function for star-forming galaxies up to $z\sim2$, we now consider whether the corresponding PSM reproduces the observed flat relationship between SFR and X-ray luminosity (e.g. Rosario et al., 2012; Stanley et al., 2015). We incorporate AGNs into the PSM using the same prescriptions as for our previous model. However, beyond splitting galaxies based on their star-forming properties only, we also separate them in terms of their stellar masses to account for the mass dependency

Table 6.1: Redshift evolution of the parameters that describe the Eddington ratio distribution of star-forming galaxies for our mass-dependent model. The slopes and intercepts are given for an evolution as a function of $(1+z)$. Uncertainties on the fitting parameters are extracted via 1000 Monte Carlo realisations (i.e. 1σ).

Parameters	Intercepts	Slopes
$\log(A_{\rm SF})$	$-1.57^{\pm 0.08}$	$0.03^{\pm 0.04}$
$\log(\lambda_{\rm break}^{\rm low\ mass})$	>-2.53	1.27
$\log(\lambda_{\rm break}^{\rm medium\ mass})$	$-2.05^{\pm 0.15}$	$0.68^{\pm 0.08}$
$\log(\lambda_{\rm break}^{\rm high\ mass})$	$-2.60^{\pm 0.08}$	$0.70^{\pm 0.04}$
$\gamma_1^{\rm low\ mass}$	<0.5	0.0
$\gamma_1^{\rm medium\ mass}$	$-1.0^{\pm 2.67}$	$-0.12^{\pm 1.30}$
$\gamma_1^{\rm high\ mass}$	$0.45^{\pm 0.05}$	$-0.04^{\pm 0.02}$
γ_2	$2.21^{\pm 0.06}$	$-0.03^{\pm 0.03}$

Notes: Slopes and intercepts are given for an evolution as a function of $(1+z)$. The intercept for $z>1.7$ when assuming a break in the z evolution of the parameters is given by the continuity at z=1.7 (i.e. [intercept for $z > 1.7$] = $(1 + 1.7) \times$ ([slope for $z < 1.7$] − [slope for $z > 1.7$]) + [intercept for $z < 1.7$]).

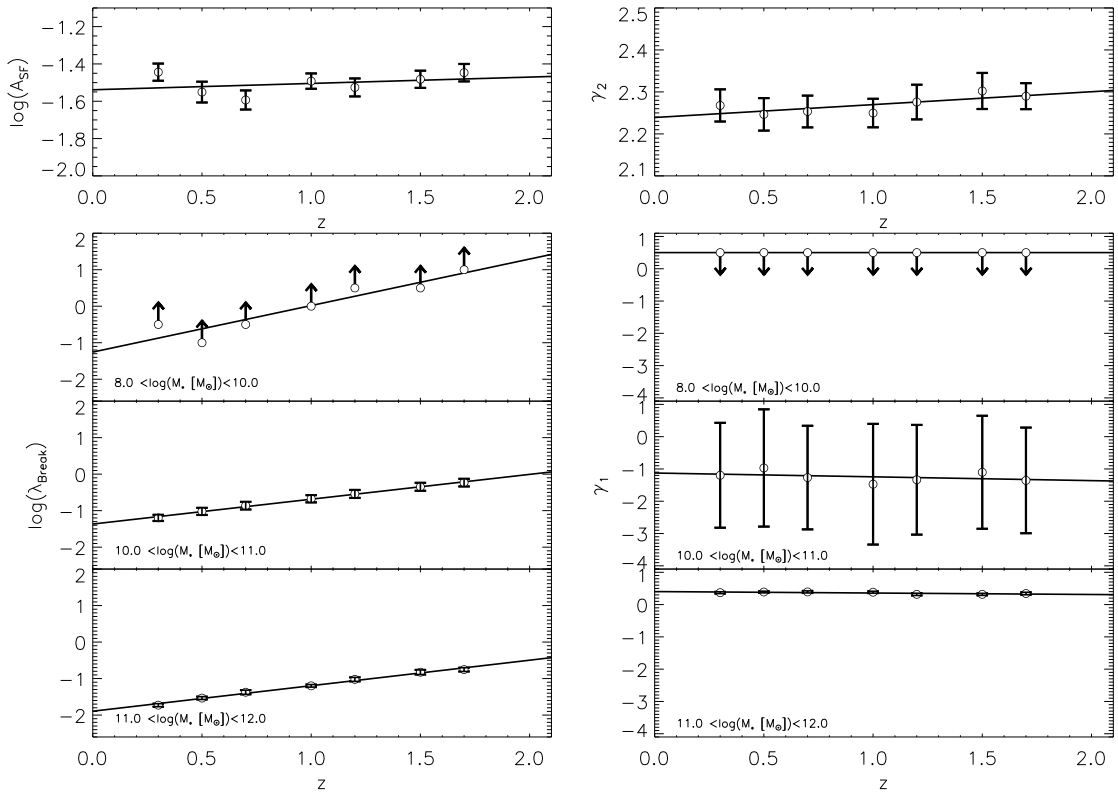

Figure 6.4: Redshift evolution of the parameters that define our mass-dependent Eddington ratio distribution at z=0.1, z=0.3, z=0.5, z=0.7, z=1.0, z=1.3, z=1.5, and z=1.7. Error bars show the 3σ uncertainties, and upward and downward arrows are for lower and upper-limits, respectively. The two top panels present the shared parameters among the different mass bins, i.e. the normalisation $\log(\mathrm{A_{SF}})$ and the slope at high Eddington ratio γ_2, the left-hand side panels are the three different break positions λ_{break}, one for each mass bin, and the right-hand side panels are the same but for that of the lower Eddington ratio slope γ_1. The black lines show the best fit of each parameters.

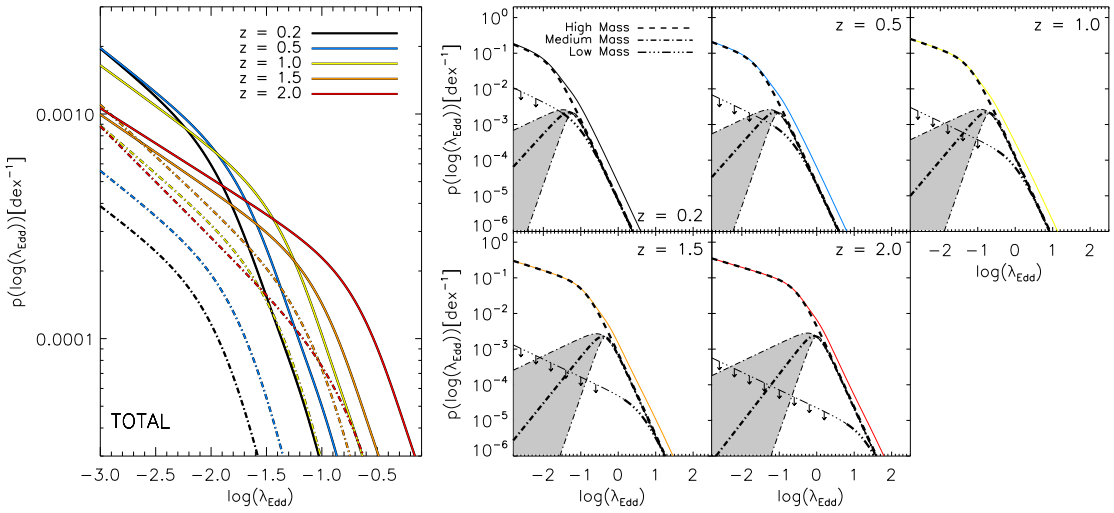

Figure 6.5: Eddington ratio probability distributions of star-forming and quiescent galaxies in our mass-dependent model at z=0.2, z=0.5, z=1.0, z=1.5, and z=2.0. The left hand side panel shows the total Eddington ratio probability distributions for star-forming (solid lines) and quiescent (dashed lines) galaxies. The right hand side panels are, for each redshift, the contribution of the different mass bins to the total Eddington ratio distribution for star-forming galaxies. In each of these panels, the dashed line is for the highest mass bin (i.e. $11<\log(M_*[M_\odot])<12$), the single-dotted dashed line is for the medium mass bin (i.e. $10<\log(M_*[M_\odot])<11$), and the triple-dotted dashed line is for the lowest mass bin (i.e. $8<\log(M_*[M_\odot])<10$). Arrows indicate the effect of upper limits found in the slope at low Eddington ratio for our lowest mass bin. The grey area illustrates the large uncertainties found in the slope at low Eddington ratio for our medium mass bin. We normalised each of the Eddington ratio distributions to integrate to unity applying a cut at $\lambda_{\rm Edd}=10^{-7}$.

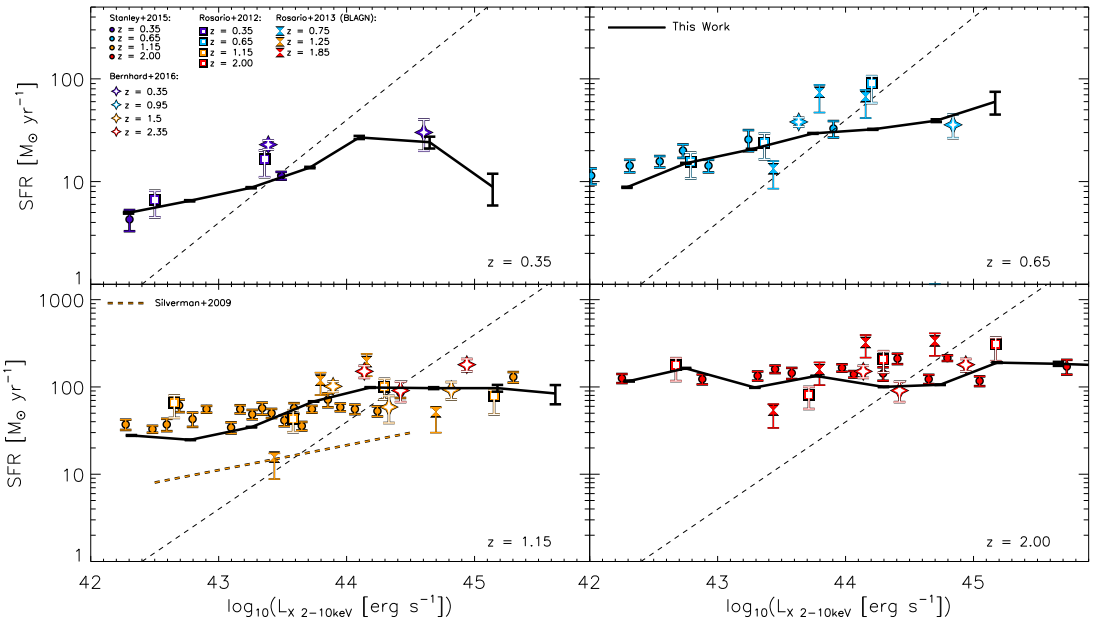

Figure 6.6: Average SFR in bins of X-ray 2-10 keV luminosities predicted by our mass-dependent model (black thick line). The error bars represent the uncertainties on the mean for average SFR. The various symbols are a compilation of published relationships (i.e. Rosario et al., 2012, 2013; Stanley et al., 2015; Bernhard et al., 2016, see keys). The orange dashed line is showing the relationship found in Silverman et al. (2009), and the black dashed line is representing the relationship for AGN-dominated systems, as reported in Netzer (2009).

of the Eddington ratio distribution. We show in Fig. 6.6 the mean-average SFR of AGNs split into 0.5 dex-wide bins of X-ray luminosity at similar redshifts as those of Stanley et al. (2015). Again, we include quiescent galaxies in our model when calculating these averages. Contrary to our previous model, we find that our mass-dependent model predicts a flat relationship between SFR and X-ray luminosity in very good agreement with observations (see Fig. 6.6). It is important to stress that the model was *not* optimised to recreate the flat SFR/X-ray luminosity relationship. Therefore, we conclude that the mass-dependent model is able to reproduce the X-ray luminosity functions for star-forming galaxies (with a good agreement with observations at least up to $z\sim1$) while also *independently* reproducing the observed flat relationship between SFR and X-ray luminosity out to $z\sim2$. This suggests that the flat relationship between SFR and X-ray luminosity is a good discriminator for models.

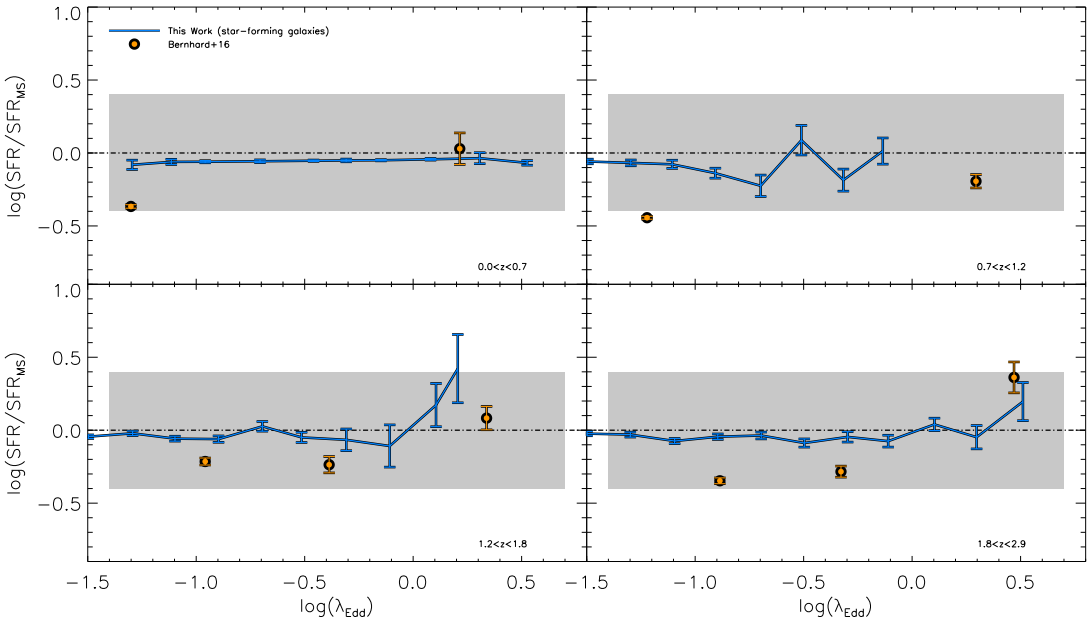

Figure 6.7: Normalised average SFR versus Eddington ratio up to $z\sim3$. The blue lines show the prediction for our mass dependent model. The orange circles show the results report in Bernhard et al. (2016). The grey area represent the scatter around the MS as reported in Schreiber et al. (2015), the dashed black line being the MS.

6.3.2 Relationship between $\lambda_{\rm Edd}$ and MS normalised SFR

To further test our mass-dependent model, we show in Fig. 6.7 how the normalised average SFR (i.e. SFR relative to that of the MS) changes with $\lambda_{\rm Edd}$ in our mass-dependent model. Although it is not incorporated in the optimisation, we predict a slight enhancement of normalised average SFR at higher $\lambda_{\rm Edd}$ (i.e. $\lambda_{\rm Edd}\gtrsim1$) compared to that of their lower $\lambda_{\rm Edd}$ counterpart (at least at $z\gtrsim1.2$), which is in good agreement with our empirical results (see Chapter 3, § 3.4.2). In Fig. 6.7 we only consider star-forming galaxies for our model since we do not have a good prescription for the MS normalisation of quiescent galaxies, hence the discrepancy at lower $\lambda_{\rm Edd}$ between our model and the observed data (i.e. that does contain quiescent galaxies). We also stress that in Fig. 6.7 our highest redshift bin, i.e. $1.8<z<2.9$ constitutes an extrapolation of our model. However, the results are still consistent with observations (i.e. a slight enhancement of the normalised average SFR at higher $\lambda_{\rm Edd}$).

6.3.3 Comparison to empirical Eddington ratio distributions

As in Chapter 5, §5.4.4 we can compare our model mass-dependent Eddington ratio distribution at z=1 to the empirical one reported in Wang et al. (2017). As our various assumptions are based on observations from Aird et al. (2017a), comparing our

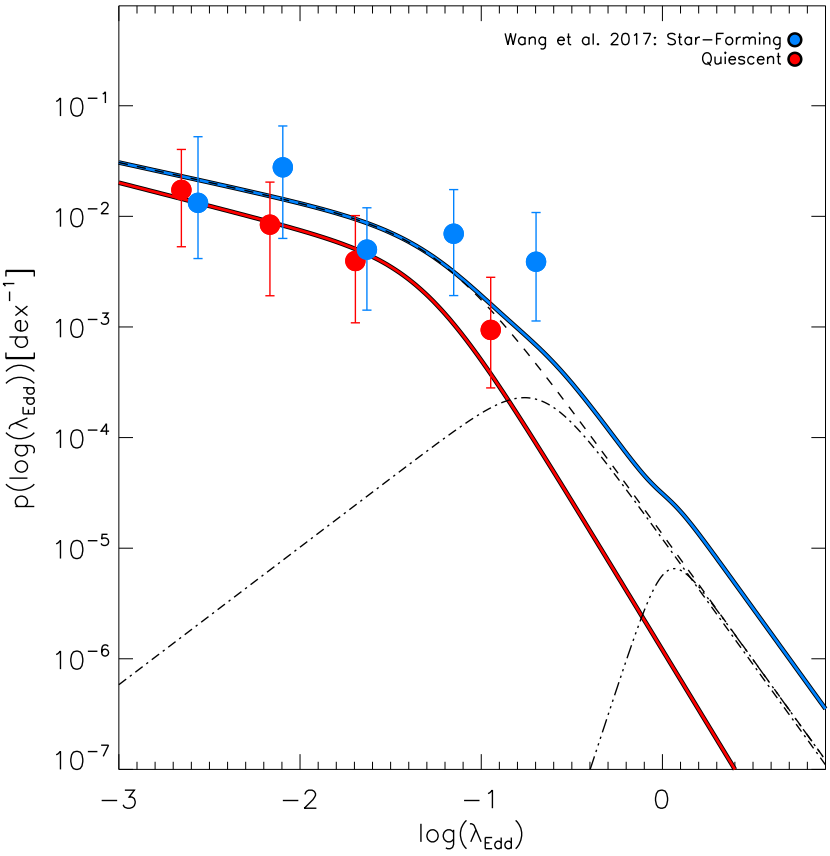

Figure 6.8: Comparison of our mass-dependent model Eddington ratio distribution to empirical results at z=1. The blue thick line is the total model Eddington ratio distribution for star-forming galaxies, while the dashed line, dotted-dashed line, and the triple dotted-dashed line indicate our higher, medium, and lowest mass bin contributions, respectively. The blue circles are empirical data of the star-forming component from Wang et al. (2017) at $z\sim$1, while the red circles are that of the quiescent component.

mass-dependent Eddington ratio distribution to that empirical of Wang et al. (2017) – instead of Aird et al. (2017a) – constitutes a more independent test for our model. We show this comparison in Fig. 6.8. Since we do not change the prescriptions on the quiescent galaxies, we still find a good agreement between our model and the empirical Eddington ratio distribution for quiescent galaxies at z=1. Furthermore, using our mass-dependent Eddington ratio distribution, we also find very good agreement between the model and the empirical Eddington ratio distribution of star-forming galaxies at z=1 (contrary to our previous model that was inconsistent at lower $\lambda_{\rm Edd}$ values). This strongly supports our mass-dependent model for the Eddington ratio distribution of star-forming galaxies. We predict that the low-$\lambda_{\rm Edd}$ end of the Eddington ratio distribution for star-forming galaxies is dominated by galaxies with $M_*\gtrsim 10^{11}$ $M_\odot$. However, Wang et al. (2017) reported that their sample of AGNs have typical stellar masses between $10^{10.5}$ $<M_*/M_\odot<$ 10^{11} (once corrected for the differences in the IMFs between Salpeter (1955) for this work and Chabrier (2003) for Wang et al. 2017), which is half a dex below our highest mass bin.

6.3.4 Predicted mass distribution

To further test our mass-dependent Eddington ratio distribution model, we show in Fig. 6.9 the predicted mass distributions for our mass-dependent model in bins of redshifts and Eddington ratios, that we compare to the mass distributions we obtained for our empirical sample (see Chapter 3, § 3.3.4 and Fig. 3.6). Overall, there is a good agreement between both our observed and predicted mass distributions out to $z\sim$2 and for a wide range of Eddington ratios (i.e. 10^{-3} $<\lambda_{\rm Edd}<$ 10^{2}). We note that for $z<$1.25, the predicted mass distributions show a strong break at $M_*=$ 10^{10} $M_\odot$. This is a direct consequence of our modelling approach that uses bins of stellar masses (see § 6.2.1), within which a boundary has been defined at $M_*=$ 10^{10} $M_\odot$. The general agreement between the predicted and the observed mass distributions at various redshifts and Eddington ratios supports our mass-dependent model, and is in agreement with recent observations of Aird et al. (2017a).

6.3.5 Comparison to the mass dependence of the sSFR

As a final test for our mass-dependent model, we compare the mass dependence of our Eddington ratio distribution to that of the specific SFR (sSFR) at z=1. We show in Fig. 6.10 for our mass-dependent model the average Eddington ratio measured in each of our stellar mass bin at z=1 and for star-forming galaxies. The upward arrow in Fig. 6.10 for our lowest mass bin illustrates the effect of the upper limit found for

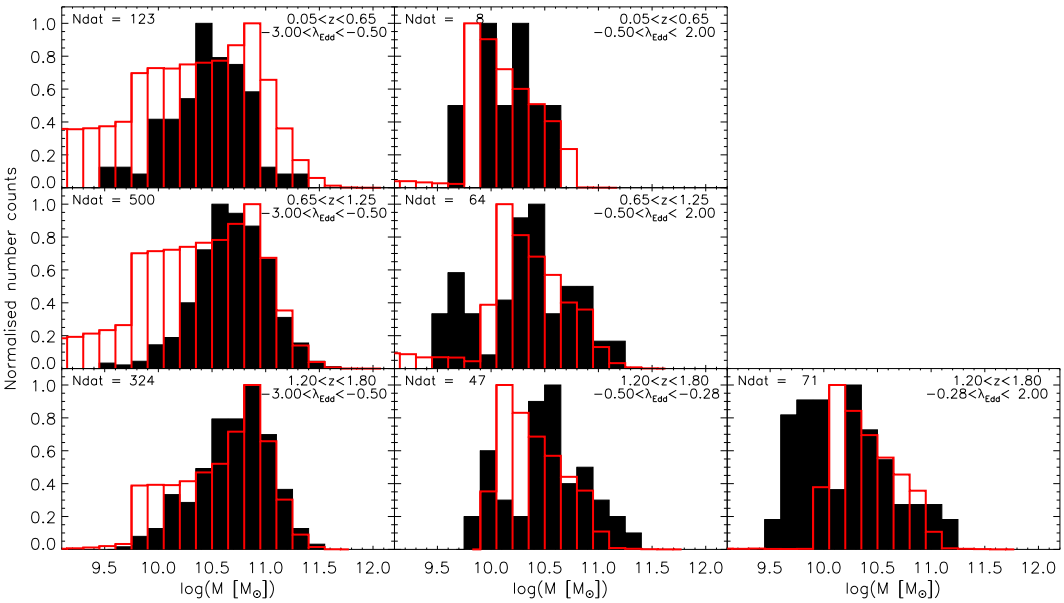

Figure 6.9: Comparison of the predicted mass distributions for our mass-dependent model to empirical mass distributions. The black filled histograms show the empirical mass distributions as reported in Chapter 3, Fig. 3.6 at various redshifts and $\lambda_{\rm Edd}$ (see top right-hand ranges in each panel). The top left-hand number (Ndat) in each panel indicates the number of AGNs present in this empirical histogram. The overlaid red histograms are the same but shows the predicted mass distributions from our mass-dependent model.

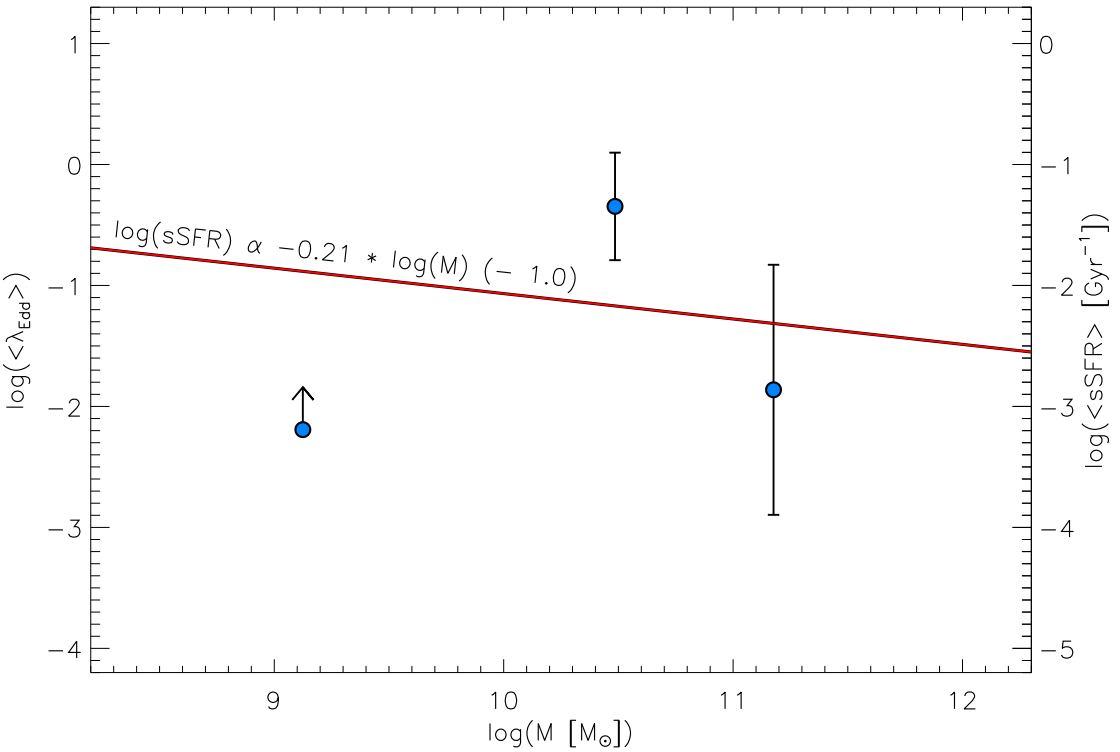

Figure 6.10: Evolution of average Eddington ratio in bins of stellar masses at z=1 (left hand axis), compared to that of sSFR (right hand axis). The thick blue points correspond to the average $\lambda_{\rm Edd}$ measured using our mass-dependent model in each of our mass bin. The upward arrow indicates the effect of the upper limit found in the slope at low $\lambda_{\rm Edd}$ in our lowest mass bin (see § 6.2.3). The red line corresponds to the sSFR evolution with stellar mass reported in Ilbert et al. (2015), renormalised by a factor of ten.

the slope at low Eddington ratio for our lowest mass bin (i.e. see § 6.2.3). In Fig. 6.10, we also show the mass dependence of average sSFR at z=1 given by Eq. 1 in Ilbert et al. (2015), and renormalised by a factor of ten. Although we only have a lower limit for average $\lambda_{\rm Edd}$ in our lowest mass bin, overall we find a good agreement between the mass dependency in our $\lambda_{\rm Edd}$ and the mass dependency reported for sSFR (e.g. Rodighiero et al., 2011; Ilbert et al., 2015). This suggests that, first AGN phases are concurrent with star-forming phases and, second, that AGNs and star formation are both triggered by a common gas reservoir. An accurate measure of average $\lambda_{\rm Edd}$ in low mass galaxies is necessary to put a better constraint on how $\lambda_{\rm Edd}$ evolves with stellar mass.

6.4 Discussion

6.4.1 Extending our mass-dependent model to higher redshifts

In this chapter, we infer the Eddington ratio distribution of star-forming galaxies by including a mass-dependency in our models. To do this, we first isolated the X-ray luminosity function for star-forming galaxies as predicted while using our previous model. We then fit this star-forming component of the X-ray luminosity function to optimise the mass-dependent Eddington ratio distribution. As mentioned previously, we used the empirical results from Georgakakis et al. (2014) to validate the model X-ray luminosity function split between star-forming and quiescent components out to $z\sim1$. However, beyond $z\sim1$ we do not have the empirical results to check the model X-ray luminosity function split between star-forming and quiescent galaxies, and we know that at $z\gtrsim2$ our previous model, from which we extract the star-forming component of the X-ray luminosity function to determine our mass-dependent Eddington ratio, is inconsistent with observations (i.e. too many AGNs in quiescent galaxies). Faced with this situation, where we cannot reliably exploit the star-forming component of our previous model, we now investigate whether we can fit the observed X-ray luminosity function at z=2.25 using both a mass-dependent star-forming component *and* a mass-independent (using a single broken power-law) quiescent component Eddington ratio distributions. This results in a total of 12 free parameters to optimise (i.e. eight parameters for the star-forming component and four parameters for the quiescent one). We use the same assumptions for the Eddington ratio distribution of star-forming galaxies as described in § 6.2, and demand that the normalisation of the Eddington ratio distribution for quiescent galaxies lies below that of star-forming galaxies (i.e. consistent with the lower redshift bins).

We show in Fig. 6.11 the results of this new model. Contrary to our previous model, we are now able to reproduce the total observed X-ray luminosity function at z=2.25 by placing the majority of AGNs in star-forming galaxies. In particular, we find that the X-ray luminosity function at z=2.25 is dominated by the highest mass star-forming galaxies, with a smaller contribution from medium mass star-forming galaxies. The contribution from our lowest mass bin is consistent with zero. Similarly, we can only place upper limits on the contribution from quiescent galaxies to the total X-ray luminosity function at z=2.25. We conclude, therefore, that while we are able to reproduce the total X-ray luminosity function using a mass-dependent Eddington ratio distribution for star-forming galaxies, this solution is degenerate

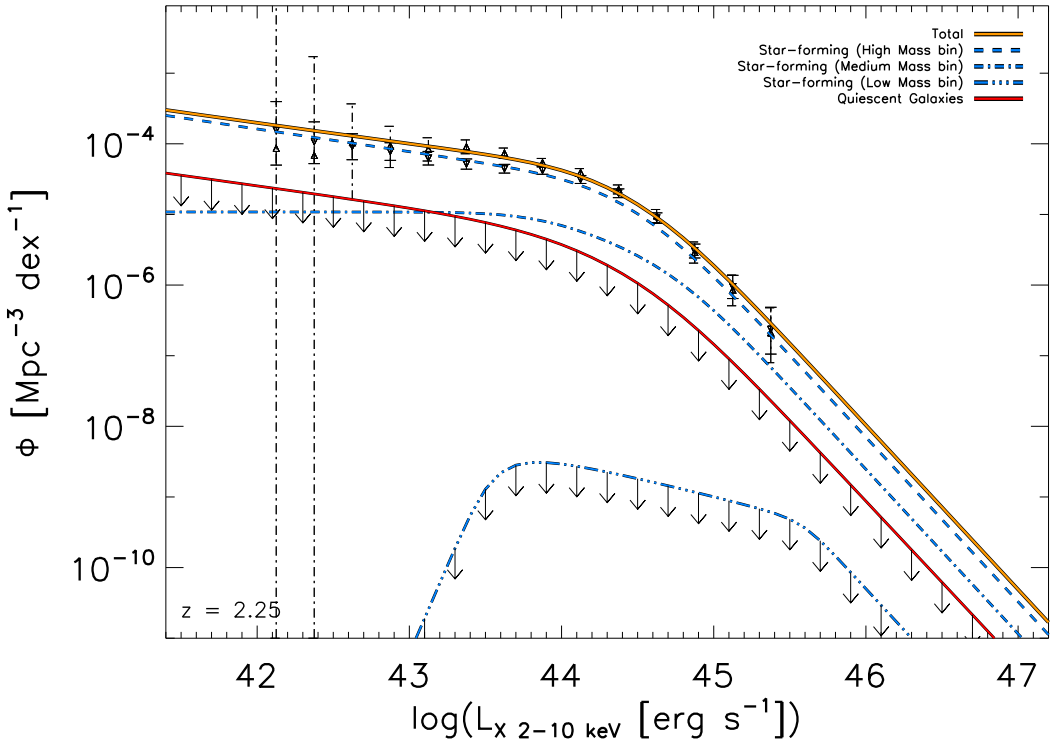

Figure 6.11: Fit of the X-ray luminosity function at z=2.25 of Aird et al. (2015) assuming a mass-dependent Eddington ratio distribution for star-forming galaxies and a mass-independent one for that of quiescent galaxies. The black downward and upward triangles show the X-ray luminosity function of Aird et al. (2015) for the soft and the hard band, respectively. The orange line shows the total X-ray luminosity function derived using our model, the blue lines are for that of the star-forming component in each different mass bin (see keys), and the quiescent component is shown with a red line. Downward black arrows indicate upper limits.

with the level of contribution from quiescent galaxies. Breaking this degeneracy will require the separation of the high-redshift X-ray luminosity function into quiescent and star-forming components (i.e. as performed by Georgakakis et al. (2014) at z<1).

6.4.2 Caveats

An obvious caveat of this mass-dependent model is that we are limited by our choice for the mass bins. Should we wish to probe in more detail how the Eddington ratio distribution changes with stellar mass, we would need to consider narrower mass bins. However, refining the number of mass bins is equivalent to adding further free parameters (i.e. one broken power-law for each new mass bin) in the model. While we are able to derive (within the given uncertainties) parameters for our mass-dependent

model, adding further free parameters would lead to a degenerate solution to the model. Our choice of three bins covering a wide range of masses (i.e. M_*=10^{8-12} $M_\odot$) aids in reducing the degeneracy of the model, whilst giving the possibility to investigate any large differences of the Eddington ratio distribution for various stellar masses.

Beyond being limited in the number of mass bins, this mass-dependent model also has similar caveats as for our previous model (described in Chapter 5, § 5.5.3). While deriving the Eddington ratio distribution, our model is limited by the functional form chosen for each mass component of the Eddington ratio distribution and the assumptions used to avoid degeneracies during fitting (see § 6.2). As such, again, we cannot explore the full range of possible Eddington ratio distributions. However, as stressed in § 6.2, all our assumptions are motivated by the findings of recent studies (e.g. Aird et al., 2017a). Furthermore, the results predicted by the mass-dependent model are in a very good agreement with many recent observational studies, i.e. the observed X-ray luminosity functions out to $z\sim2$ – including when split in terms of star-forming and quiescent galaxies (e.g. Georgakakis et al., 2014; Aird et al., 2015; Wang et al., 2017), the flat relationship between SFR and X-ray luminosity (e.g. Rosario et al., 2012; Stanley et al., 2015), the empirical Eddington ratio distribution at z=1 reported in Wang et al. (2017), and the enhancement of star-forming properties at higher $\lambda_{\rm Edd}$. As such our mass-dependent Eddington ratio distribution provides a simple means by which to explore the AGN-galaxy connection.

6.5 Conclusion

Motivated by the inability of our previous model (i.e. Eddington ratio distribution simply split between star-forming and quiescent galaxies) to reproduce the flat SFR/X-ray relationship, as well as by recent results reporting a mass-dependent Eddington ratio distribution for star-forming galaxies (e.g. Aird et al., 2017a), we attempt to accommodate a mass-dependency in our Eddington ratio distribution. To do this, we separate the Eddington ratio distribution for star-forming galaxies in three mass bins, i.e. a low mass bin ($8<\log(M_*/M_\odot)<10$), a medium mass bin ($10<\log(M_*/M_\odot)<11$), and a high mass bin ($11<\log(M_*/M_\odot)<12$). We find that by using this modelling approach we can still fit the X-ray luminosity function for star-forming galaxies (extracted from our previous model), the bulk of which is dominated by higher mass galaxies in our model at all redshifts. The fact that the X-ray luminosity function is dominated by massive galaxies could explain the findings of empirical studies that report a *mass-independent* Eddington ratio distribution, since

those empirical studies only probe higher stellar mass hosts. Although it is not a requirement of our model, after including a mass-dependency it naturally generates a flat relationship between SFR and X-ray luminosity when including the MS for star-forming galaxies, as suggested by recent observations. This is a result of the suppression of low $\lambda_{\rm Edd}$ AGNs in low mass galaxies. Further checks also demonstrate the ability for our mass-dependent model to mimic the enhancement of normalised average SFR at higher $\lambda_{\rm Edd}$ beyond $z{\sim}1.2$, as observed in our empirical results. Although the mass dependency is interesting, there is no obvious explanation on why the Eddington ratio distribution should be mass-dependent.

The overall conclusion of our work described in Chapter 5 and Chapter 6 is that our model Eddington ratio distributions are unable to reproduce both the X-ray luminosity functions and the flat relationship between SFR and X-ray luminosity, unless we introduce a mass dependency for the Eddington ratio of AGNs hosted in star-forming galaxies (see Chapter 7, § 7.1 for further discussions regarding the mass-dependent Eddington ratio distribution for star-forming galaxies).

Chapter 7

Conclusions

It is now widely regarded that AGNs have played an important role in shaping today's galaxies (e.g. Kormendy & Richstone, 1995; Magorrian et al., 1998; Marconi & Hunt, 2003; Ferrarese & Merritt, 2000; Gebhardt et al., 2000; Merritt, 2000; Tremaine et al., 2002; Kormendy et al., 2011). However, the precise mechanism of such role is still debated. One means to relate SMBHs to their host galaxies is via the energy released by AGNs directly impacting their host SFRs. Simulations of galaxy formation and evolution find that the predominant impact of such an interplay is the quenching of SFR via the energy released by the AGN (e.g. Di Matteo et al., 2005; Springel et al., 2005; Hopkins et al., 2008; Zubovas & King, 2012; Dubois et al., 2013). However, there is still no empirical consensus on these predictions. Overall, observational studies report that AGN host galaxies form a diverse population, with a slight preference for more massive, star-forming galaxies (e.g. Cisternas et al., 2011; Aird et al., 2012; Harrison et al., 2012; Kocevski et al., 2012; Mullaney et al., 2012; Rosario et al., 2012; Rovilos et al., 2012; Santini et al., 2012; Zinn et al., 2013; Shimizu et al., 2015, 2016). More importantly, many observational studies find that there is no evidence of a strong (anti-)correlation between X-ray luminosity (a proxy for AGN power) and SFR (e.g. Stanley et al., 2015, 2017). Therefore, there is still debate on the exact impact that AGNs have on their host galaxy SFRs. This thesis aims to investigate further the relationship between AGNs and the star-forming properties of their host galaxies.

Our initial hypothesis, tested in Chapter 2 and Chapter 3, was that a powerful AGN will have a greater impact on a low mass host galaxy than on a higher mass one. This is due to the relative depth of the induced potential well of a low mass compared to that of a high mass galaxy. Therefore, instead of using the X-ray luminosity as a measure of the AGN's ability to significantly impact its host galaxy SFR, we used the specific X-ray luminosity (i.e. the X-ray luminosity relative to the

host stellar mass, a proxy for Eddington ratio, $\lambda_{\rm Edd}$).

We first used a sample of 1620 X-ray selected AGNs, out to $z\sim3$, for which we have intrinsic X-ray luminosities spanning the range $10^{42} < L_X < 10^{46}$ erg s^{-1}. We derived their host stellar masses, using multi-component SED fitting to remove AGN contamination, and measured their $\lambda_{\rm Edd}$. We used HERSCHEL data to measure SFRs, performing stacking to include the HERSCHEL-undetected hosts, and measured their hosts' average IR SEDs in bins of redshift and $\lambda_{\rm Edd}$. Finally, we employed multi-component SED fitting (to remove AGN contamination from the IR SEDs), and multi-model inference to measure average SFRs in bins of redshift and $\lambda_{\rm Edd}$. Our main results indicate that there is a slight enhancement of normalised average SFR (i.e. the average SFR compared to that of a mock mass-matched sample of MS galaxies) at higher $\lambda_{\rm Edd}$. This is reinforced by our finding of a higher fraction of starburst galaxies at higher $\lambda_{\rm Edd}$. These results contradict our initial hypothesis of a suppression of SFR at higher $\lambda_{\rm Edd}$, as suggested by simulations. Furthermore, our results also suggest that the Eddington ratio distribution changes with the star-forming properties of their host galaxies. This supports recent findings of a different Eddington ratio distribution for star-forming and quiescent galaxy populations Georgakakis et al. (2014); Aird et al. (2017a); Wang et al. (2017). However, we cannot investigate this further with our empirical sample, since too many hosts are undetected by HERSCHEL.

Motivated by our findings of an Eddington ratio distribution that changes with the star-forming properties of host galaxies, we developed a model to infer the Eddington ratio distributions of star-forming and quiescent galaxies. Our hypothesis, tested in Chapter 5 and Chapter 6, was that the Eddington ratio distribution only depends upon the star-forming properties of host galaxies. To test this, we took an analytical approach to combine the mass function with the Eddington ratio distribution (split between star-forming and quiescent galaxies) to model the X-ray luminosity function. We performed MCMC optimisation to infer the parameters that define our Eddington ratio such that, once combined with the mass function, it provides a good fit to the observed X-ray luminosity function out to $z\sim3$. Interestingly, we found that to fit the observed X-ray luminosity function, we require a "peaky" distribution for the Eddington ratio distribution of star-forming galaxies. This is needed to reconcile the steep low-mass end of the mass function with the flat faint-end of the observed X-ray luminosity function. Furthermore, we found that although this model is able to reproduce the X-ray luminosity function (even when split between star-forming and quiescent galaxies at least out to $z\sim1$), it predicts a strong correlation between average SFR and X-ray luminosity, in contrast with recent observations. We demonstrated that this correlation is due to the narrowness of our inferred Eddington ratio

distribution combined with the mass function of star-forming galaxies. This generates a correlation between X-ray luminosity and stellar mass, that becomes a correlation between X-ray luminosity and SFR, since the latter is related to stellar mass via the MS.

Overall, there is a strong tension within our model that demands a "peaky" distribution for the Eddington ratio distribution of star-forming galaxies in order to reproduce the X-ray luminosity function, yet also requires a broader Eddington ratio distribution to reproduce the flat SFR/X-ray relationship.

As we found that our first model is unable to reproduce both the X-ray luminosity function and the flat SFR/X-ray relationship, and motivated by recent results reported in Aird et al. (2017b), we developed a model that can accommodate a mass-dependent Eddington ratio distribution for star-forming galaxies. We found that our mass-dependent model is able to fit the X-ray luminosity function out to $z{\sim}2$, *and* is able to reproduce the flat relationship between SFR and X-ray luminosity. Furthermore, our mass-dependent Eddington ratio distribution at $z{=}1$ is in agreement with empirical results of Wang et al. (2017) when split between star-forming and quiescent galaxies. Therefore, our results strongly suggest a mass-dependent Eddington ratio distribution. Again, while our initial hypothesis was that the Eddington ratio distribution simply depends upon the host star-forming properties, we find that the Eddington ratio distribution is likely to have a dependence on the stellar mass, as well as the star-forming properties of the host.

7.1 What does it mean for the AGN-galaxy connection?

Contrary to our initial expectations, our research has revealed an enhancement of the host star-forming properties at higher $\lambda_{\rm Edd}$. This suggests a positive impact of the AGN upon their host SFRs, or at least a concurrence of both AGN accretion and star formation (e.g. via a common triggering mechanism such as mergers), and contrasts to the so-called negative impact, where AGNs quench their host SFRs, as often predicted by simulations. One possibility to reconcile both simulations and observations is that the IR emission of the host galaxy measures SFRs on time scales of several hundreds of millions years. In contrast, AGNs vary by several orders of magnitudes on shorter time scales. Therefore, the IR luminosity might not be well-suited to measuring the quenching of SFR via the energy released by the AGN due to the large difference in the time scales involved for each mechanism. However, should

the quenching of SFR be the predominant impact of AGNs, then on average, perhaps we should expect to observe a suppression of SFR at higher $\lambda_{\rm Edd}$ in large sample of AGNs.

Another possibility is the time needed for a galaxy to transition from the MS to a fully quiescent galaxy, despite the negative impact of the AGNs on their galaxy SFRs. One scenario is that, once the gas supply exhausted, the AGN switches off more rapidly than the time needed for the SFR to be suppressed, although aided by AGN feedback. Since we use X-ray luminosities to observe AGNs, we do not capture galaxies that have recently had their AGN "switched off" which might, however, be undergoing a transition from MS to quiescence which has been triggered by the presence of a recent AGN activity.

None of the above explains why we appear to see an enhancement of AGN activity among strongly star-forming host galaxies. One possibility is that this is caused by the common gas reservoir that supplies both AGN and SFR. The findings of a higher contribution from the star-forming galaxies to the total X-ray luminosity function and Eddington ratio distribution could also be interpreted as supporting the common gas reservoir, since its suggests that there is a higher probability of finding an AGN (across a large range of X-ray luminosities and Eddington ratios) in a star-forming galaxy. However, this scenario does not account for the quenching of SFR suggested by simulations to successfully reproduce the observable Universe. Overall, a more realistic scenario is that a combination of both a common gas reservoir, followed by a longer term impact of the AGN upon the host star-forming properties is taking place. However, these two mechanisms might arise at different stages of the AGN-galaxy evolution, such that observations based on a combination of X-ray and Herschel data only capture one aspect of it: the active consumption of the common gas reservoir by both the SMBH and the galaxy.

Another interesting result from our Eddington ratio models, which has not been extensively explored, is the presence of a large proportion of AGNs in quiescent galaxies. At redshifts beyond $\approx$1.5, the mass function suggests that there are very few quiescent galaxies compared to star-forming galaxies (e.g. Davidzon et al., 2017). However, empirical results suggest a large contribution to the X-ray luminosity function from quiescent galaxies (e.g. Georgakakis et al., 2014; Wang et al., 2017). The large proportion of AGNs in quiescent galaxies contradicts observations that find average SFRs for AGN samples consistent with MS star-forming galaxies. Where are all these quiescent AGN host galaxies?

Our research, along with empirical results (e.g. Aird et al., 2017a), suggests that the Eddington ratio distribution is mass-dependent in such a way that, the Eddington

ratio is suppressed in smaller mass galaxies. On the face of it, this could be a problem for the formation of SMBHs at early epochs of the Universe, when they were predominantly hosted in low mass galaxies. However, although we find that the chance of finding an AGN with a given Eddington ratio hosted by a low mass galaxy is lower than for a higher mass one, these AGNs in low mass galaxies have an Eddington ratio distribution peaking at higher $\lambda_{\rm Edd}$. Therefore, should an AGN be located in a low mass galaxy, it will have a higher chance to be accreting at a higher rate than if located in a higher mass galaxy.

7.2 Future work

While investigating the star-forming properties of a sample of X-ray selected AGNs, we found a slight enhancement of normalised SFR (i.e. the SFR relative to that of the MS) at higher Eddington ratio (or X-ray luminosity relative to the host stellar mass). This indicates that we are witnessing the simultaneous apparition of AGN activity and SFR. Should it be AGN feedback, however, we do not know what is the mechanism generates this enhancement of the star-forming properties at higher Eddington ratios (e.g. a common gas reservoir, gas injection from the AGNs, shock-induced SFRs, etc). One of the most commonly used means to investigate such AGN feedback is to look at radio jets. As they extend to galactic scales, the provide an obvious means to inject energy back into the galaxy. Therefore, a realistic continuation of our empirical results is to look at the extended radio properties of our AGNs sample.

Another aspect of our study that has not been explored is the AGNs in quiescent galaxies. Our modelling of the X-ray luminosity function has flagged that we require that a very high fraction of quiescent galaxies host AGNs. This indicates that a large number of AGNs should be found in quiescent galaxies, which is against empirical studies that finds that AGNs preferentially reside in MS star-forming galaxies. Further investigations are needed on that aspect of our results.

The suppressed Eddington ratio in lower mass galaxies is puzzling when considering the formation of primordial galaxies and SMBHs. Today, it is extremely difficult to constrain the properties of sources in the early Universe. With the advent of the James Webb Space Telescope, it will be possible to have greater information on the formation of these primordial SMBHs, and test whether the suppression of Eddington ratio in low mass galaxies is also happening at early times in the Universe.

Bibliography

Aird J., et al., 2010, Monthly Notices of the Royal Astronomical Society, 401, 2531

Aird J., et al., 2012, Astrophysical Journal, 746, 90

Aird J., et al., 2013, Astrophysical Journal, 775, 41

Aird J., Coil A. L., Georgakakis A., Nandra K., Barro G., Pérez-González P. G., 2015, Monthly Notices of the Royal Astronomical Society, 451, 1892

Aird J., Coil A. L., Georgakakis A., 2017a, preprint, (arXiv:1705.01132)

Aird J., Coil A. L., Georgakakis A., 2017b, Monthly Notices of the Royal Astronomical Society, 465, 3390

Akaike H., 1973, Biometrika, 60, 255

Akaike H., 1974, IEEE Transactions on Automatic Control, 19, 716

Akaike H., 1985, in Atkinson A. C., Fienberg S. E., eds, , A Celebration of Statistics: The ISI Centenary Volume A Volume to Celebrate the Founding of the International Statistical Institute in 1885. Springer New York, New York, NY, pp 1–24, doi:10.1007/978-1-4613-8560-8˙1, http://dx.doi.org/10.1007/978-1-4613-8560-8_1

Akaike H., 1994, in Bozdogan H., Sclove S. L., Gupta A. K., Haughton D., Kitagawa G., Ozaki T., Tanabe K., eds, , Proceedings of the First US/Japan Conference on the Frontiers of Statistical Modeling: An Informational Approach: Volume 3 Engineering and Scientific Applications. Springer Netherlands, Dordrecht, pp 27–38, doi:10.1007/978-94-011-0854-6˙2, http://dx.doi.org/10.1007/978-94-011-0854-6_2

Alexander D. M., Hickox R. C., 2012, New Astronomy Reviews, 56, 93

Alexander D. M., et al., 2003, Astronomical Journal, 126, 539

Alexander D. M., Bauer F. E., Chapman S. C., Smail I., Blain A. W., Brandt W. N., Ivison R. J., 2005, Astrophysical Journal, 632, 736

Antonucci R., 1993, Annual Review of Astronomy and Astrophysics, 31, 473

Armus L., Heckman T., Miley G., 1987, Astronomical Journal, 94, 831

Arnouts S., et al., 2005, Astrophysical Journal Letters, 619, L43

Arnouts S., et al., 2007, Astronomy and Astrophysics, 476, 137

Assef R. J., et al., 2011, Astrophysical Journal, 728, 56

Azadi M., et al., 2015, Astrophysical Journal, 806, 187

Baldwin J. A., Phillips M. M., Terlevich R., 1981, Publications of the Astronomical Society of the Pacific, 93, 5

Barnes J. E., 2004, Monthly Notices of the Royal Astronomical Society, 350, 798

Barnes J. E., Hernquist L. E., 1991, Astrophysical Journal Letters, 370, L65

Barvainis R., Ivison R., 2002, Astrophysical Journal, 571, 712

Bauer F. E., Alexander D. M., Brandt W. N., Schneider D. P., Treister E., Hornschemeier A. E., Garmire G. P., 2004, Astronomical Journal, 128, 2048

Bell E. F., et al., 2012, Astrophysical Journal, 753, 167

Bernhard E., Béthermin M., Sargent M., Buat V., Mullaney J. R., Pannella M., Heinis S., Daddi E., 2014, Monthly Notices of the Royal Astronomical Society, 442, 509

Bernhard E., Mullaney J. R., Daddi E., Ciesla L., Schreiber C., 2016, Monthly Notices of the Royal Astronomical Society, 460, 902

Best P. N., Kauffmann G., Heckman T. M., Brinchmann J., Charlot S., Ivezić Ž., White S. D. M., 2005, Monthly Notices of the Royal Astronomical Society, 362, 25

Béthermin M., Dole H., Beelen A., Aussel H., 2010, Astronomy and Astrophysics, 512, A78+

Böhm A., Wisotzki L., 2007, in Metcalfe N., Shanks T., eds, Astronomical Society of the Pacific Conference Series Vol. 379, Cosmic Frontiers. p. 185

Bolton J. G., Stanley G. J., 1948, Nature, 161, 312

Boltzmann L., 1877, Über die Beziehung zwischen dem zweiten Hauptsatze des mechanischen Wärmetheorie und der Wahrscheinlichkeitsrechnung, respective den Sätzen über das Wärmegleichgewicht. Kk Hof-und Staatsdruckerei

Bonfield D. G., et al., 2011, Monthly Notices of the Royal Astronomical Society, 416, 13

Bouwens R. J., Illingworth G. D., Franx M., Ford H., 2007, Astrophysical Journal, 670, 928

Brightman M., Nandra K., Salvato M., Hsu L.-T., Aird J., Rangel C., 2014, Monthly Notices of the Royal Astronomical Society, 443, 1999

Bruzual G., Charlot S., 2003, Monthly Notices of the Royal Astronomical Society, 344, 1000

Burgarella D., Boquien M., Roehlly Y., Ciesla L., Buat V., 2015, in Biernacka M., Bajan K., Stachowski G., Flin P., eds, Introduction to Cosmology. pp 125–133

Burnham K., Anderson D., 2002, Model Selection and Multimodel Inference: A Practical Information-Theoretic Approach. Springer, `http://books.google.co.uk/books?id=fT1Iu-h6E-oC`

Burnham K. P., Anderson D. R., 2004, Sociological Methods & Research, 33, 261

Calzetti D., 2001, Publications of the Astronomical Society of the Pacific, 113, 1449

Calzetti D., et al., 2007, Astrophysical Journal, 666, 870

Caplar N., Lilly S. J., Trakhtenbrot B., 2015, Astrophysical Journal, 811, 148

Cen R., 2015, Astrophysical Journal Letters, 805, L9

Chabrier G., 2003, Publications of the Astronomical Society of the Pacific, 115, 763

Chary R.-R., Pope A., 2010, preprint, (`arXiv:1003.1731`)

Chen C.-T. J., et al., 2013, Astrophysical Journal, 773, 3

Ciesla L., et al., 2015, Astronomy and Astrophysics, 576, A10

Cisternas M., et al., 2011, Astrophysical Journal, 726, 57

Civano F., et al., 2012, Astrophysical Journal Supplements, 201, 30

Colbert E. J. M., Ptak A. F., 2002, Astrophysical Journal Supplements, 143, 25

Cole S., Lacey C. G., Baugh C. M., Frenk C. S., 2000, Monthly Notices of the Royal Astronomical Society, 319, 168

Conroy C., White M., 2013, Astrophysical Journal, 762, 70

Cuadra J., Nayakshin S., Springel V., Di Matteo T., 2006, Monthly Notices of the Royal Astronomical Society, 366, 358

Cuadra J., Nayakshin S., Martins F., 2008, Monthly Notices of the Royal Astronomical Society, 383, 458

Cucciati O., et al., 2012, Astronomy and Astrophysics, 548, A108

Czerny B., Elvis M., 1987, Astrophysical Journal, 321, 305

Daddi E., et al., 2007, Astrophysical Journal, 670, 156

Dai Y. S., Wilkes B. J., Bergeron J., Kuraszkiewicz J., Omont A., Atanas A., Teplitz H. I., 2015, preprint, (arXiv:1511.06761)

Dale D. A., Helou G., 2002, Astrophysical Journal, 576, 159

Davidzon I., et al., 2017, preprint, (arXiv:1701.02734)

Davies L. J. M., et al., 2015, Monthly Notices of the Royal Astronomical Society, 452, 616

Delvecchio I., et al., 2015, Monthly Notices of the Royal Astronomical Society, 449, 373

Di Matteo T., Springel V., Hernquist L., 2005, Nature, 433, 604

Dole H., et al., 2006, Astronomy and Astrophysics, 451, 417

Donley J. L., et al., 2012, Astrophysical Journal, 748, 142

Dubois Y., Gavazzi R., Peirani S., Silk J., 2013, Monthly Notices of the Royal Astronomical Society, 433, 3297

Dubois Y., Peirani S., Pichon C., Devriendt J., Gavazzi R., Welker C., Volonteri M., 2016, Monthly Notices of the Royal Astronomical Society, 463, 3948

Duc P.-A., Mirabel I. F., 1997, The Messenger, 89, 14

Dunlop J. S., McLure R. J., Kukula M. J., Baum S. A., O'Dea C. P., Hughes D. H., 2003, Monthly Notices of the Royal Astronomical Society, 340, 1095

Elbaz D., Cesarsky C. J., 2003, Science, 300, 270

Elbaz D., et al., 2007, Astronomy and Astrophysics, 468, 33

Elbaz D., et al., 2011, Astronomy and Astrophysics, 533, A119

Ellison S. L., Patton D. R., Simard L., McConnachie A. W., 2008, Astronomical Journal, 135, 1877

Ellison S. L., Mendel J. T., Scudder J. M., Patton D. R., Palmer M. J. D., 2013, Monthly Notices of the Royal Astronomical Society, 430, 3128

Ellison S. L., Patton D. R., Hickox R. C., 2015, Monthly Notices of the Royal Astronomical Society, 451, L35

Fabian A. C., 2012, Annual Review of Astronomy and Astrophysics, 50, 455

Fath E. A., 1909, Lick Observatory Bulletin, 5, 71

Ferrarese L., Merritt D., 2000, Astrophysical Journal Letters, 539, L9

Foreman-Mackey D., Hogg D. W., Lang D., Goodman J., 2013, Publications of the Astronomical Society of the Pacific, 125, 306

Forster M. R., 2000, Journal of Mathematical Psychology, 44, 205

Forster M. R., 2002, in Zellner A., Keuzenkamp H. A., McAleer M., eds, , Simplicity, Inference and Modelling: Keeping it Sophisticatedly Simple. Cambridge University Press, Cambridge, pp 83–119

Fritz J., Franceschini A., Hatziminaoglou E., 2006, Monthly Notices of the Royal Astronomical Society, 366, 767

Gebhardt K., et al., 2000, Astrophysical Journal Letters, 539, L13

Gelman A., Rubin D. B., 1992, Statistical science, pp 457–472

Georgakakis A., et al., 2014, Monthly Notices of the Royal Astronomical Society, 443, 3327

Georgakakis A., et al., 2015, Monthly Notices of the Royal Astronomical Society, 453, 1946

Goodman J., Weare J., 2010, Communications in applied mathematics and computational science, 5, 65

Griffin M. J., et al., 2010, Astronomy and Astrophysics, 518, L3+

Gruppioni C., et al., 2013, Monthly Notices of the Royal Astronomical Society, 432, 23

Haardt F., Maraschi L., 1991, Astrophysical Journal Letters, 380, L51

Haiman Z., Loeb A., 2001, Astrophysical Journal, 552, 459

Hanbury Brown R., Jennison R. C., Gupta M. K. D., 1952, Nature, 170, 1061

Harrison C. M., 2017, Nature Astronomy, 1, 0165

Harrison C. M., et al., 2012, Astrophysical Journal Letters, 760, L15

Hathi N. P., et al., 2010, Astrophysical Journal, 720, 1708

Hatziminaoglou E., et al., 2010, Astronomy and Astrophysics, 518, L33

Heinis S., et al., 2013, preprint, (arXiv:1310.3227)

Heinis S., et al., 2014, Monthly Notices of the Royal Astronomical Society, 437, 1268

Hernquist L., 1989, Nature, 340, 687

Hickox R. C., et al., 2009, Astrophysical Journal, 696, 891

Hickox R. C., Mullaney J. R., Alexander D. M., Chen C.-T. J., Civano F. M., Goulding A. D., Hainline K. N., 2014, Astrophysical Journal, 782, 9

Hogg D. W., Baldry I. K., Blanton M. R., Eisenstein D. J., 2002, ArXiv Astrophysics e-prints,

Hopkins P. F., Richards G. T., Hernquist L., 2007, Astrophysical Journal, 654, 731

Hopkins P. F., Hernquist L., Cox T. J., Kereš D., 2008, Astrophysical Journal Supplements, 175, 356

Hsu L.-T., et al., 2014, Astrophysical Journal, 796, 60

Hubble E. P., 1926, Astrophysical Journal, 63

Hwang H. S., et al., 2010, Monthly Notices of the Royal Astronomical Society, 409, 75

Ilbert O., et al., 2013, Astronomy and Astrophysics, 556, A55

Ilbert O., et al., 2015, Astronomy and Astrophysics, 579, A2

Jardel J. R., Gebhardt K., 2012, Astrophysical Journal, 746, 89

Jennison R. C., Das Gupta M. K., 1953, Nature, 172, 996

Jones M. L., Hickox R. C., Mutch S. J., Croton D. J., Ptak A. F., DiPompeo M. A., 2017, preprint, (arXiv:1706.00430)

Kauffmann G., et al., 2003, Monthly Notices of the Royal Astronomical Society, 346, 1055

Kelly B. C., Merloni A., 2012, Advances in Astronomy, 2012, 970858

Kennicutt Jr. R. C., 1998, Astrophysical Journal, 498, 541

Kocevski D. D., et al., 2012, Astrophysical Journal, 744, 148

Kormendy J., McClure R. D., 1993, Astronomical Journal, 105, 1793

Kormendy J., Richstone D., 1995, Annual Review of Astronomy and Astrophysics, 33, 581

Kormendy J., Bender R., Cornell M. E., 2011, Nature, 469, 374

Koss M., Mushotzky R., Veilleux S., Winter L. M., Baumgartner W., Tueller J., Gehrels N., Valencic L., 2011, Astrophysical Journal, 739, 57

Kuha J., 2004, Sociological Methods & Research, 33, 188

Kullback S., Leibler R. A., 1951, Ann. Math. Statist., 22, 79

Laigle C., et al., 2016, Astrophysical Journal Supplements, 224, 24

Lanzuisi G., et al., 2017, preprint, (arXiv:1702.07357)

Larson D., et al., 2011, Astrophysical Journal Supplements, 192, 16

Le Floc'h E., et al., 2005, Astrophysical Journal, 632, 169

Levenberg K., 1944, Quarterly of Applied Mathematics, 2, 164

Lora V., Sánchez-Salcedo F. J., Raga A. C., Esquivel A., 2009, Astrophysical Journal Letters, 699, L113

Lutz D., et al., 2008, Astrophysical Journal, 684, 853

Lutz D., et al., 2010, Astrophysical Journal, 712, 1287

Lutz D., et al., 2011, Astronomy and Astrophysics, 532, A90

Magnelli B., Elbaz D., Chary R. R., Dickinson M., Le Borgne D., Frayer D. T., Willmer C. N. A., 2011, Astronomy and Astrophysics, 528, A35+

Magnelli B., et al., 2013, Astronomy and Astrophysics, 553, A132

Magorrian J., et al., 1998, Astronomical Journal, 115, 2285

Maiolino R., Salvati M., Bassani L., Dadina M., della Ceca R., Matt G., Risaliti G., Zamorani G., 1998, Astronomy and Astrophysics, 338, 781

Malkan M. A., 1983, in Swings J.-P., ed., Liege International Astrophysical Colloquia Vol. 24, Liege International Astrophysical Colloquia. pp 433–436

Marconi A., Hunt L. K., 2003, Astrophysical Journal Letters, 589, L21

Marconi A., Risaliti G., Gilli R., Hunt L. K., Maiolino R., Salvati M., 2004, Monthly Notices of the Royal Astronomical Society, 351, 169

Marquardt D. W., 1963, Journal of the Society for Industrial and Applied Mathematics, 11, 431

Martini P., Weinberg D. H., 2001, Astrophysical Journal, 547, 12

Matt G., Fabian A. C., Guainazzi M., Iwasawa K., Bassani L., Malaguti G., 2000, Monthly Notices of the Royal Astronomical Society, 318, 173

Matthews T. A., 1963, Astronomical Journal, 68, 77

Matthews T. A., Sandage A. R., 1963, Astrophysical Journal, 138, 30

Merritt D., 2000, in Combes F., Mamon G. A., Charmandaris V., eds, Astronomical Society of the Pacific Conference Series Vol. 197, Dynamics of Galaxies: from the Early Universe to the Present. p. 221 (arXiv:astro-ph/9910546)

Metropolis N., Rosenbluth A. W., Rosenbluth M. N., Teller A. H., Teller E., 1953, The Journal of Chemical Physics, 21, 1087

Mullaney J. R., Alexander D. M., Goulding A. D., Hickox R. C., 2011, Monthly Notices of the Royal Astronomical Society, 414, 1082

Mullaney J. R., et al., 2012, Astrophysical Journal Letters, 753, L30

Mullaney J. R., et al., 2015, Monthly Notices of the Royal Astronomical Society, 453, L83

Mutua F. M., 1994, Hydrological Sciences Journal, 39, 235

Nandra K., et al., 2007, Astrophysical Journal Letters, 660, L11

Neistein E., Netzer H., 2014, Monthly Notices of the Royal Astronomical Society, 437, 3373

Netzer H., 2009, Monthly Notices of the Royal Astronomical Society, 399, 1907

Netzer H., et al., 2007, Astrophysical Journal, 666, 806

Nguyen H. T., et al., 2010, Astronomy and Astrophysics, 518, L5

Noeske K. G., et al., 2007, Astrophysical Journal Letters, 660, L43

Noguchi M., 1988, Astronomy and Astrophysics, 203, 259

Novikov I. D., Thorne K. S., 1973, in Dewitt C., Dewitt B. S., eds, Black Holes (Les Astres Occlus). pp 343–450

Oesch P. A., et al., 2010, Astrophysical Journal Letters, 725, L150

Oliver S. J., et al., 2012, Monthly Notices of the Royal Astronomical Society, 424, 1614

Page M. J., Stevens J. A., Ivison R. J., Carrera F. J., 2004, Astrophysical Journal Letters, 611, L85

Page M. J., et al., 2012, Nature, 485, 213

Pannella M., et al., 2015, Astrophysical Journal, 807, 141

Patton D. R., Ellison S. L., Simard L., McConnachie A. W., Mendel J. T., 2011, Monthly Notices of the Royal Astronomical Society, 412, 591

Pilbratt G. L., et al., 2010, Astronomy and Astrophysics, 518, L1+

Poglitsch A., et al., 2010, Astronomy and Astrophysics, 518, L2

Priddey R. S., Isaak K. G., McMahon R. G., Robson E. I., Pearson C. P., 2003, Monthly Notices of the Royal Astronomical Society, 344, L74

Rafferty D. A., Brandt W. N., Alexander D. M., Xue Y. Q., Bauer F. E., Lehmer B. D., Luo B., Papovich C., 2011, Astrophysical Journal, 742, 3

Ramos Almeida C., Ricci C., 2017, preprint, (arXiv:1709.00019)

Ranalli P., Comastri A., Setti G., 2003, Astronomy and Astrophysics, 399, 39

Reddy N. A., Steidel C. C., Pettini M., Adelberger K. L., Shapley A. E., Erb D. K., Dickinson M., 2008, Astrophysical Journal Supplements, 175, 48

Rees M., 1996, in Bender R., Davies R. L., eds, IAU Symposium Vol. 171, New Light on Galaxy Evolution. p. 303

Rodighiero G., et al., 2010, Astronomy and Astrophysics, 515, A8

Rodighiero G., et al., 2011, Astrophysical Journal Letters, 739, L40

Rodighiero G., et al., 2015, Astrophysical Journal Letters, 800, L10

Rosario D. J., et al., 2012, Astronomy and Astrophysics, 545, A45

Rosario D. J., et al., 2013, Astronomy and Astrophysics, 560, A72

Roseboom I. G., et al., 2010, Monthly Notices of the Royal Astronomical Society, 409, 48

Rovilos E., et al., 2012, Astronomy and Astrophysics, 546, A58

Ryle M., Smith F. G., 1948, Nature, 162, 462

Salim S., et al., 2005, Astrophysical Journal Letters, 619, L39

Salim S., et al., 2007, Astrophysical Journal Supplements, 173, 267

Salpeter E. E., 1955, Astrophysical Journal, 121, 161

Sanders D. B., Mirabel I. F., 1996, Annual Review of Astronomy and Astrophysics, 34, 749

Sanders D. B., Mazzarella J. M., Kim D.-C., Surace J. A., Soifer B. T., 2003, Astronomical Journal, 126, 1607

Santini P., et al., 2012, Astronomy and Astrophysics, 540, A109

Sargent M. T., Béthermin M., Daddi E., Elbaz D., 2012, Astrophysical Journal Letters, 747, L31

Schawinski K., Thomas D., Sarzi M., Maraston C., Kaviraj S., Joo S.-J., Yi S. K., Silk J., 2007, Monthly Notices of the Royal Astronomical Society, 382, 1415

Schreiber C., et al., 2015, Astronomy and Astrophysics, 575, A74

Schulze A., Wisotzki L., 2010, Astronomy and Astrophysics, 516, A87

Schwarz G., 1978, Ann. Statist., 6, 461

Schweitzer M., et al., 2006, Astrophysical Journal, 649, 79

Seyfert C. K., 1943, Astrophysical Journal, 97, 28

Shakura N. I., Sunyaev R. A., 1973, Astronomy and Astrophysics, 24, 337

Shao L., et al., 2010, Astronomy and Astrophysics, 518, L26

Shields G. A., Wheeler J. C., 1978, Astrophysical Journal, 222, 667

Shimizu T. T., Mushotzky R. F., Meléndez M., Koss M., Rosario D. J., 2015, Monthly Notices of the Royal Astronomical Society, 452, 1841

Shimizu T. T., Meléndez M., Mushotzky R. F., Koss M. J., Barger A. J., Cowie L. L., 2016, Monthly Notices of the Royal Astronomical Society, 456, 3335

Silverman J. D., et al., 2008a, Astrophysical Journal, 675, 1025

Silverman J. D., et al., 2008b, Astrophysical Journal, 679, 118

Silverman J. D., et al., 2009, Astrophysical Journal, 696, 396

Skelton R. E., et al., 2014, Astrophysical Journal Supplements, 214, 24

Slipher V. M., 1917, Lowell Observatory Bulletin, 3, 59

Springel V., et al., 2005, Nature, 435, 629

Stanley F., Harrison C. M., Alexander D. M., Swinbank A. M., Aird J. A., Del Moro A., Hickox R. C., Mullaney J. R., 2015, Monthly Notices of the Royal Astronomical Society, 453, 591

Stanley F., et al., 2017, preprint, (arXiv:1707.05334)

Steidel C. C., Adelberger K. L., Giavalisco M., Dickinson M., Pettini M., 1999, Astrophysical Journal, 519, 1

Stern D., et al., 2005, Astrophysical Journal, 631, 163

Symeonidis M., 2017, Monthly Notices of the Royal Astronomical Society, 465, 1401

Symeonidis M., Giblin B. M., Page M. J., Pearson C., Bendo G., Seymour N., Oliver S. J., 2016, Monthly Notices of the Royal Astronomical Society, 459, 257

Tadhunter C., 2016, Astronomy and Astrophysics Review, 24, 10

Tadhunter C., et al., 2011, Monthly Notices of the Royal Astronomical Society, 412, 960

Tadhunter C. N., Ramos Almeida C., Morganti R., Holt J., Rose M., Dicken D., Inskip K., 2012, Monthly Notices of the Royal Astronomical Society, 427, 1603

Thompson T. A., Quataert E., Murray N., 2005, Astrophysical Journal, 630, 167

Thorne K. S., Price R. H., 1975, Astrophysical Journal Letters, 195, L101

Treister E., Schawinski K., Urry C. M., Simmons B. D., 2012, Astrophysical Journal Letters, 758, L39

Treister E., Schawinski K., Volonteri M., Natarajan P., 2013, Astrophysical Journal, 778, 130

Tremaine S., et al., 2002, Astrophysical Journal, 574, 740

Urry C. M., Padovani P., 1995, Publications of the Astronomical Society of the Pacific, 107, 803

Valluri M., Ferrarese L., Merritt D., Joseph C. L., 2005, Astrophysical Journal, 628, 137

Vasudevan R. V., Fabian A. C., 2007, Monthly Notices of the Royal Astronomical Society, 381, 1235

Veale M., White M., Conroy C., 2014, Monthly Notices of the Royal Astronomical Society, 445, 1144

Vito F., et al., 2014, Monthly Notices of the Royal Astronomical Society, 441, 1059

Vollmer B., Beckert T., Davies R. I., 2008, Astronomy and Astrophysics, 491, 441

Volonteri M., Capelo P. R., Netzer H., Bellovary J., Dotti M., Governato F., 2015, Monthly Notices of the Royal Astronomical Society, 452, L6

Wang T., et al., 2017, Astronomy and Astrophysics, 601, A63

Weigel A. K., Schawinski K., Caplar N., Wong O. I., Treister E., Trakhtenbrot B., 2017, preprint, (arXiv:1707.05323)

Wuyts S., et al., 2011, Astrophysical Journal, 742, 96

Wyder T. K., et al., 2005, Astrophysical Journal Letters, 619, L15

Xue Y. Q., et al., 2010, Astrophysical Journal, 720, 368

Xue Y. Q., et al., 2011, Astrophysical Journal Supplements, 195, 10

Zahid H. J., Yates R. M., Kewley L. J., Kudritzki R. P., 2013, Astrophysical Journal, 763, 92

Zinn P.-C., Middelberg E., Norris R. P., Dettmar R.-J., 2013, Astrophysical Journal, 774, 66

Zubovas K., King A., 2012, Astrophysical Journal Letters, 745, L34

Acknowledgements

Firstly, I would like to thank James Mullaney for giving me the opportunity to do this PhD. James has been incredibly supportive throughout these four years. I also thank Clive Tadhunter for his welcomed encouragements and for accepting to be my internal examiner. Together, James and Clive have been a deep source of knowledge, and I feel grateful to be one of the people they have shared this with. I would also like to thank Dave Alexander for accepting to be my external examiner.

I could not have done this PhD without the support grant from the University of Sheffield.

I feel that Paul Kerry needs a special mention, as he is an invaluable asset for the Astro team of Sheffield. Thanks Pablo.

Now, of course, this is the time to thank all the people I have shared my office with during these years (bless them). I think I can now coin them as my friends (at least on Facebook). I can only remember the good times we had in the first E18 office with Liam, Martin, Pav, Dave, Chris, soon after joined by Dan and Rob (who calls himself *the galaxy hunter* for some reasons). Thanks guys for all the inspiring discussions we had about physics and astronomy (and also the chair racing, office cricket, office petanque, Nerf darts throwing, bullying me by trying to fit me in the rocket head cause I was the shortest, etc). I also thank the people who helped maintain a great working environment. Namely, Katie, Heloise, Jonny, Martin D, Becky, and all the rest of the PhD students. The staff of the full Astro team of Sheffield have also been a great help, especially the post-docs: Marvin, Claire, Steven, Saida, etc...

Special thanks to all the volunteers who accepted to proof-read this – precious – manuscript: Rob, Martin, Gemma, Katie, Heloise, Jonny, Marvin, Liam G, Vangy, Alex, and Gilly.

Four years in Sheffield is rather a long time and I met a lot of great (interesting?) people. A particular thanks to Calum for helping me to realise how bad my English was ("is" according to him). To Mike, Tom, and Will, who I shared my first house (Calum?) with, it has been a great time, and great BBQs (when it was not rainy).

Special thanks to Vangy of course, for accepting to share this flat with me now. To all my friends in general that started this journey with me, Dave, Amy, Jonny, those back home, Mika, Toine, Sofy, Renato, and many more, too many to mention here.

Thanks to Alex Bee for being such an amazing person. I understand it has been really hard to go through this with me, but we made it (well, one week away at the time of writing, surely you can make it). Thank you.

Finalement, je voudrais vous remercier, Papa, Maman, ainsi que Caro et Gab pour tout ce que vous avez fait pour moi. Sans vous je n'y serais jamais arrivé.

Merci a tous.

Appendix A

Insights into the demonstration of the AIC

In this appendix we give an insight of the demonstration of the AIC. This short demonstration is highly inspired from Burnham & Anderson (2004). The AIC is an information theory selection criterion based on the Kullback-Leibler (K-L) information loss (Kullback & Leibler, 1951), with K-L, itself following the Boltzmann's concept of entropy (Boltzmann, 1877). For f the full reality or truth, and g a probability distribution, or model defined by a set of parameters θ approximating f, the information lost, $\mathrm{I}(f,g)$, when g is used instead of f is written

$$\mathrm{I}(f,g) = \left[\int f(x)\log\frac{f(x)}{g(x|\theta)}dx\right] = \int f(x)\log f(x)dx - \int f(x)\log g(x|\theta)dx, \quad \text{(A.1)}$$

or,

$$\mathrm{I}(f,g) = \mathrm{E}_f[\log f(x)] - \mathrm{E}_f[\log g(x|\theta)], \quad \text{(A.2)}$$

where the expectation are with respect to the truth f.

Since the best model loses the least information, finding a good model is equivalent to minimise $\mathrm{I}(f,g)$ over the model g. Although we do not know f, we can carry out maximisation of the log likelihood (i.e. biased estimator) using a set of n observations $x = (x_1, x_2, ..., x_n)$ to estimate parameters $\hat{\theta}$ for the model g, and correct for the bias between the observed mean log-likelihood and the asymptotically (i.e. $n \to \infty$) unbiased one. Furthermore, since $\mathrm{E}_f[\log f(x)]$ only depends upon f, it is a constant, Cst, across the models as such only the cross-entropy $\mathrm{E}_f[\log g(x|\theta)]$ needs to be estimated, which is the expected log likelihood of the model's pdf $\hat{g}(x|\hat{\theta})$ with respect to $f(x|\text{data})$, i.e.,

$$\log \mathscr{L}(\hat{\theta}|\text{data}) = Cst - \hat{\text{E}}_{\hat{\theta}}[\text{I}(f, \hat{g})] \tag{A.3}$$

Akaike (1973, 1974, 1985, 1994) discovered a relationship between K-L and the likelihood theory, and found that the maximised log-likelihood bias was approximately equal to K, the number of free parameters (for technical details, see Burnham & Anderson, 2002, Chap. 7). Therefore, for large dataset, the asymptotically unbiased estimator is given by

$$\text{AIC} = -2 \log \mathscr{L}(\hat{\theta}|\text{data}) + 2\,\text{K}, \tag{A.4}$$

the multiplicative factor of -2 has been added for historical reasons. Furthermore, under the assumption of Gaussian distributed errors, the log of the likelihood values, $\log \mathscr{L}(\hat{\theta}|\text{data})$, are similar to the Chi square values (i.e. χ^2), as such, eq. A.5 can be written in a rather simple form, i.e.

$$\text{AIC} = -2\,\chi^2 + 2\,\text{K}. \tag{A.5}$$

Appendix B

Example of posterior distributions for each model

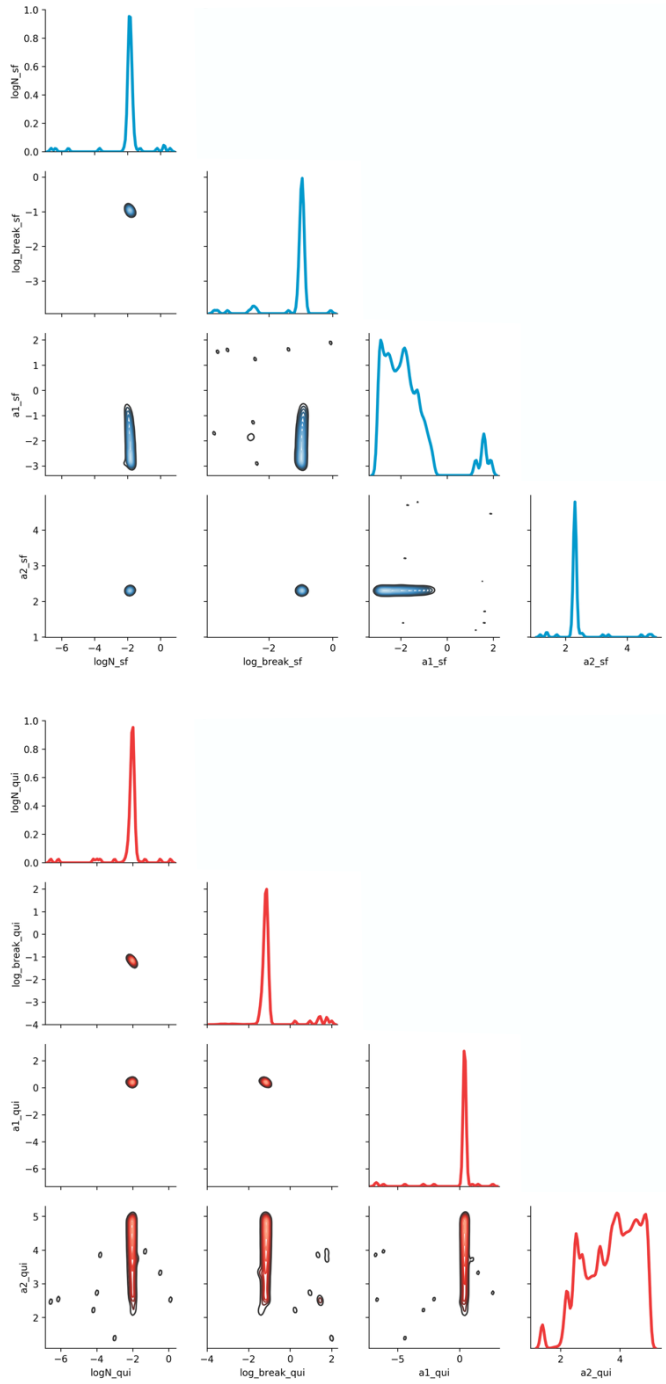

Figure B.1: Posterior distribution for our first model (i.e. assuming two broken power laws) at z=1. The top panel shows the parameters that define the model Eddington ratio distribution for star-forming galaxies (i.e. from left to right: the normalisation, the position of the break, the slope at low $\lambda_{\rm Edd}$, and the slope at high $\lambda_{\rm Edd}$), while the bottom panel shows these of the Eddington ratio distribution for quiescent galaxies.

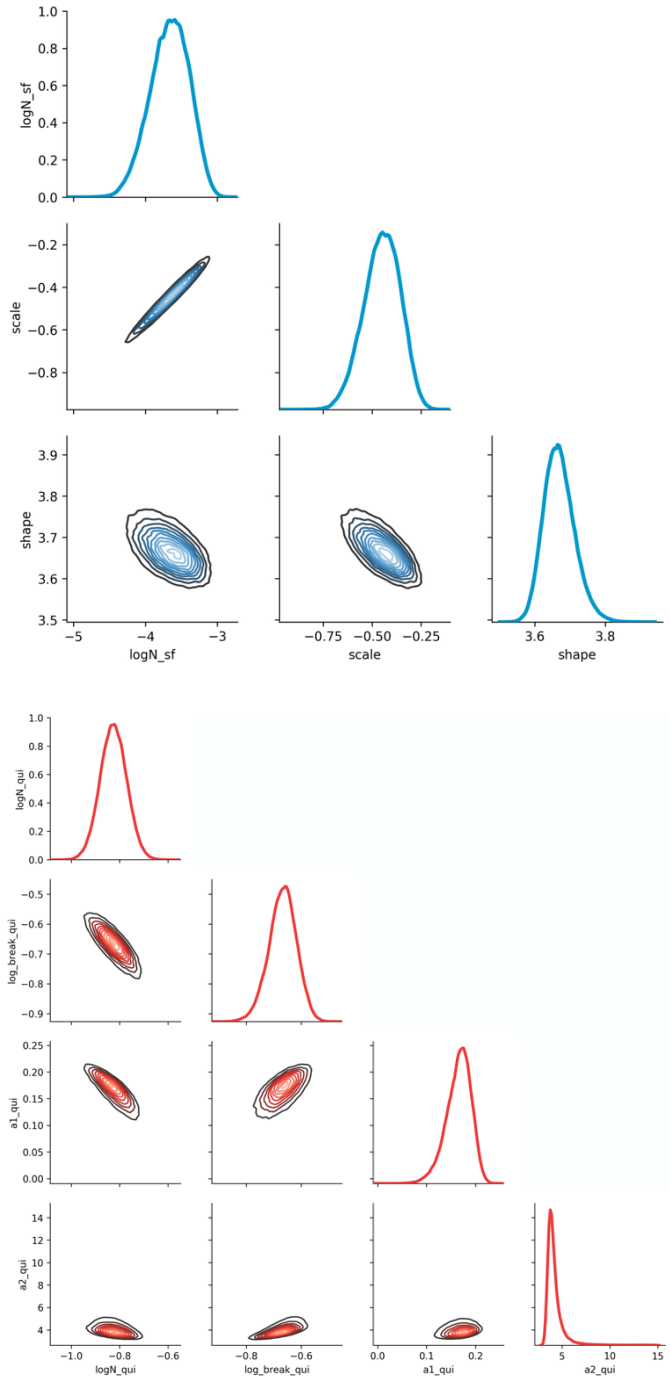

Figure B.2: Posterior distributions for our second model (i.e. using an inverse gamma distribution for the Eddington ratio distribution of star-forming galaxies) at z=2.2. The top panel shows the parameters that define the model Eddington ratio distribution for star-forming galaxies (i.e. from left to right: the normalisation, the scale, and the shape), while the bottom panel shows these of the Eddington ratio distribution for quiescent galaxies (i.e. from left to right: the normalisation, the position of the break, the slope at low $\lambda_{\rm Edd}$, and the slope at high $\lambda_{\rm Edd}$).

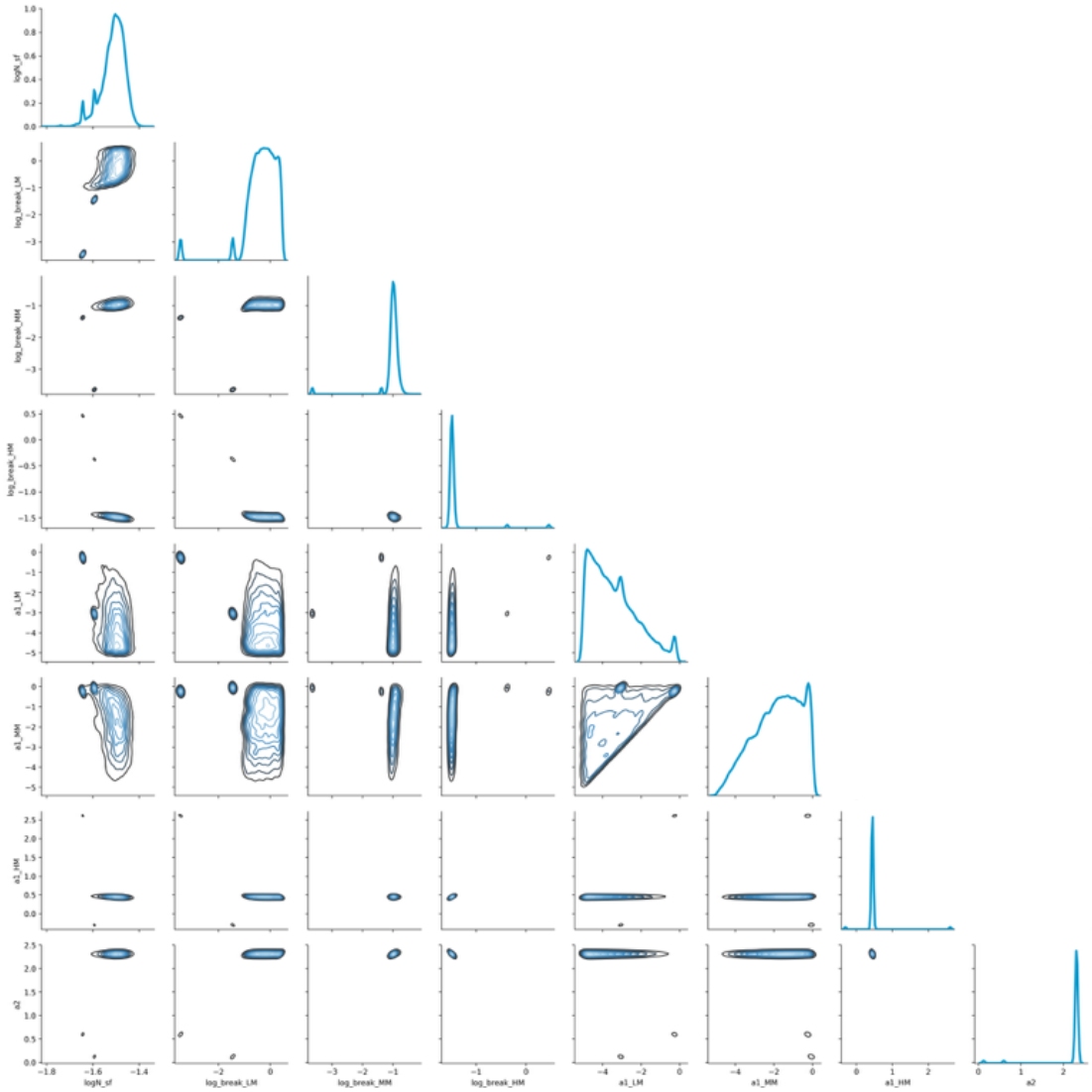

Figure B.3: Posterior distributions for our third model (i.e. assuming a mass dependency in the Eddington ratio distribution for star-forming galaxies) at z=0.5. Each distribution corresponds to a parameter that define the mass-dependent Eddington ratio distribution for star-forming galaxies, i.e. from left to right: the normalisation, the position of the break for low, medium, and high masses, the slope at low $\lambda_{\rm Edd}$ for low, medium, and high masses, and the slope at high $\lambda_{\rm Edd}$.